RL-TR-97-223
Final Technical Report
February 1998

ADAPTIVE PHASED ARRAY RADAR SIGNAL PROCESSING USING PHOTOREFRACTIVE CRYSTALS

University of Colorado

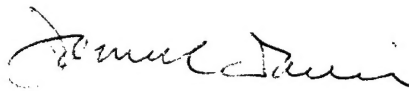Kelvin Wagner, Ted Weverka, Anthony Sarto, and Sam Weaver

19980415 091

**AIR FORCE RESEARCH LABORATORY
ROME RESEARCH SITE
ROME, NEW YORK**

DTIC QUALITY INSPECTED 3

This report has been reviewed by the Air Force Research Laboratory, Information Directorate, Public Affairs Office (IFOIPA) and is releasable to the National Technical Information Service (NTIS). At NTIS it will be releasable to the general public, including foreign nations.
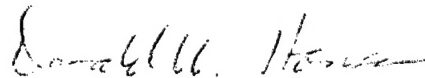
RL-TR-97-223 has been reviewed and is approved for publication.

APPROVED:

JAMES DAVIS
Project Engineer

FOR THE DIRECTOR:

DONALD W. HANSON, Director
Surveillance & Photonics

REPORT DOCUMENTATION PAGE

Public reporting burden for this collection of information is estimated to average 1 hour per response, including the time for reviewing instructions, searching existing data sources, gathering and maintaining the data needed, and completing and reviewing the collection of information. Send comments regarding this burden estimate or any other aspect of this collection of information, including suggestions for reducing this burden, to Washington Headquarters Services, Directorate for Information Operations and Reports, 1215 Jefferson Davis Highway, Suite 1204, Arlington, VA 22202-4302, and to the Office of Management and Budget, Paperwork Reduction Project (0704-0188), Washington, DC 20503.

1. AGENCY USE ONLY *(Leave blank)*	2. REPORT DATE	3. REPORT TYPE AND DATES COVERED
	February 1998	Final Jan 92 - Jan 96

4. TITLE AND SUBTITLE
ADAPTIVE PHASED ARRAY RADAR SIGNAL PROCESSING USING PHOTOREFRACTIVE CRYSTALS

5. FUNDING NUMBERS
C - F30602-92-C-0011
PE - 63726F
PR - 2863
TA - 92
WU - 43

6. AUTHOR(S)

Kelvin Wagner, Ted Weverka, Anthony Sarto, and Sam Weaver

7. PERFORMING ORGANIZATION NAME(S) AND ADDRESS(ES)

University of Colorado
Optoelectronic Computing Systems Center
Campus Box 525
Boulder CO 80309

8. PERFORMING ORGANIZATION REPORT NUMBER

N/A

9. SPONSORING/MONITORING AGENCY NAME(S) AND ADDRESS(ES)

Air Force Research Laboratory/SNDP
25 Electronic Pky
Rome NY 13441-4515

10. SPONSORING/MONITORING AGENCY REPORT NUMBER

RL-TR-97-223

11. SUPPLEMENTARY NOTES

Air Force Research Laboratory Project Engineer: James L. Davis/SNDP/(315) 330-4276

12a. DISTRIBUTION AVAILABILITY STATEMENT

Approved for public release; distribution unlimited.

12b. DISTRIBUTION CODE

13. ABSTRACT *(Maximum 200 words)*   This report covers the development, test and evaluation of an adaptive phased array optical processor. This system is designed to optimally process the wide band signals from large phased array antennas in real time, achieving a computational throughput approaching 10^{15} multiplies per second, demonstrating the potential of optical-based architectures to surpass performance achievable with conventional technology. The processor uses a three-dimensional volume hologram to create and store adaptive weights to simultaneously perform beam steering and jammer nulling functions. The adaptive processor consists of two sub-sections, the main-beam steering processor and the jammer-nulling processor. The nature of the architecture is that the number of processor components used is independent of the number of elements in the phased array. The report contains extensive treatment of models and analytical expressions developed to relate system parameters and to predict expected system behavior and performance of the experimental signal processors. A variety of jammer scenarios are described and analyzed. Experimental results obtained in a working hardware configuration of the processor are shown to verify the theoretical models. The models guided the development and evolution of the experimental optical hardware system with increasingly improved performance. By improving component stability, electronic gain, and feedback loop isolation, 45 dB jammer cancellation was demonstrated in the experimental system. Also described are results of main-beam formation experiments that did not require a priori knowledge of the angle-of-arrival of the desired signal. In addition, results from simultaneous operation of both the nulling processor and the main-beam processor are presented. The report contains extensive references and bibliography of the twenty technical papers published in conjunction with this program.

14. SUBJECT TERMS

Photorefractive Crystals, Signal Processing, Phased Array Radar

15. NUMBER OF PAGES
334

16. PRICE CODE

17. SECURITY CLASSIFICATION OF REPORT	18. SECURITY CLASSIFICATION OF THIS PAGE	19. SECURITY CLASSIFICATION OF ABSTRACT	20. LIMITATION OF ABSTRACT
UNCLASSIFIED	UNCLASSIFIED	UNCLASSIFIED	UL

DTIC QUALITY INSPECTED 3

I. Summary

This report is the final project summary for the contract Adaptive Phased-Array Radar Signal Processing using Photorefractive Crystals (Rome Labs, contract number F30602-92-C-0011). This report provides a complete technical review of the radar signal processing system developed during this contract.

All contract research statement of work items were successfully completed. There were 12 exchange visits between the University of Colorado at Boulder and Rome Laboratories. Additionally, collaborations with several companies, including Hughes, Rockwell, Optivision, and Martin Marietta, were initiated. For the duration of this contract, 40 monthly reports (11 per year), 2 annual reports, and this final report were submitted. The research has led to the publishing of 20 papers and the funding of 2 doctoral and 2 masters students. All of the former students are now working in industry.

We have successfully demonstrated an entirely new approach to adaptive array processing with several technical achievements. First, an adaptive main-beam steering system has been developed and demonstrated. Second, a jammer-nulling system has been demonstrated and characterized. The jammer-nuller uses optical polarization and angle multiplexing to achieve a record 45-dB null depth, while maintaining excellent agreement with dynamical analysis undertaken at the University of Colorado. The main-beam steering and jammer-nulling system were combined, which is the first such demonstration. Third, a wide-angular-aperture, low-time-delay acoustooptic device was invented. Finally, a novel and efficient true-time-delay adaptive algorithm was developed and implemented to control the experiment. Full details of each of these technical accomplishments are found in the body of this report.

II. Site visits and contract reviews

There were 12 site visits between Rome Laboratories and Professor Kelvin Wagner's group at the University of Colorado at Boulder during this contract. A synopsis of these meetings with dates and attendees is provided here.

1) <u>March 2, 1992</u>: University of Colorado at Boulder: kickoff meeting; Attendees from Rome Laboratories: Brian Hendrickson and Bob Kaminski.

2) <u>December 11, 1992</u>: visit to Rome Laboratories; Attendees from the University of Colorado at Boulder: Kelvin Wagner.

3) <u>February 8-19, 1993</u>: University of Colorado at Boulder: review and experiments; Attendees from Rome Laboratories: Dave Cordeiro.

4) <u>June 7-8, 1993</u>: University of Colorado at Boulder: annual site visit; Attendees from Rome Laboratories: Brian Hendrickson, Bob Kaminski, and Ernie Walge.

5) <u>April 11-14, 1994</u>: University of Colorado at Boulder: review and experiments; Attendees from Rome Laboratories: Ernie Walge.

6) <u>June 1, 1994</u>: Rome Laboratories: contractor review; Attendees from the University of Colorado at Boulder: Kelvin Wagner.

7) <u>September 22, 1994</u>: University of Colorado at Boulder; Attendees from Rome Laboratories: Paul Repak.

8) <u>March 9 1995</u>: University of Colorado at Boulder: annual site visit; Attendees from Rome Laboratories: Brian Hendrickson, Jim Davis, Joanne Maurice, and Paul Repak.

9) <u>March 29 1995</u>: University of Colorado at Boulder; Attendees from Rome Laboratories: George Brost and Kevin Madge.

10) <u>May 12 1995</u>: University of Colorado at Boulder; Attendees from Rome Laboratories: George Brost.

11) <u>August 4, 1995</u>: University of Colorado at Boulder: RF photonics discussions; Attendees from Rome Laboratories: Brian Hendrickson.

12) <u>January 11, 1996</u>: University of Colorado at Boulder: final contract review; Attendees from Rome Laboratories: Jim Davis, Joanne Maurice, and Paul Repak.

III. Statement of Work and Final Progress Report

Numerous system topologies were invented by the end of the contract (January 1996): a jammer-nulling processor, a beam-steering processor, a broad-band nuller, a true-time-delay resonator input, a true-time-delay architecture using bandpass filters, and an efficient true-time-delay adaptive algorithm. These systems are described briefly here: the statement of work for each item in the original contract, a short synopsis of the status of each item, and a brief description of the final progress for each item. Within the main body of this document, each aspect of the project is discussed in more detail.

Several spin-off technologies have resulted from this contract. A wide-angular-aperture, low-time-delay acoustooptic device was invented and investigated under a different Rome Laboratories grant (F30602-94-1-0013). Algorithms were developed for self-cohering imaging radar, leading to a publication in an SPIE proceedings. Range-angle-Doppler three-dimensional (3-D) imaging has been developed and reported in another SPIE proceedings. Finally, the true-time-delay adaptive algorithm was developed in the final year and has led to additional possibilities for future research.

1.   Phased array radar optical simulator

A.   Statement of Work:

A flexible phased-array radar optical simulator will be constructed on a movable breadboard that will be used in the subsequent system demonstrations. Two acoustooptic devices will be used to enter signal and jammer wavefronts, a beamsplitter will combine the wavefronts, a removable diffuser will simulate random fiber delays, and a Ronchi ruling will simulate the sampling of the antenna aperture. Electronic driving options will include CW jammers, RF sweepers, or a dual channel arbitrary waveform generator for flexible hopping jammer and spread spectrum signal simulation.

B.   Status

Done, first reported in 1994 and finished in 1995.

C.   Final Progress Report

In order to better understand the final system, an optical simulator for a large phased-array was developed. This simulation was able to handle 3 far-field sources, of which 2 can be moving. The algorithm included random phase behavior from fibers and a one dimensional (1-D) sampling aperture. The simulator can be multiply tapped for a simulated time-delayed multipath environment.

2.   Active processor demonstration

A.   Statement of Work

A prototype of the active processor will be constructed that allows different system configurations to be tested and compared. The capability of the system to point the simulated main beam towards the desired signal will be demonstrated, and its jammer nulling capabilities will be investigated. The results will be published.

B.   Status

Done, passive processor first reported in 1992 and completed in 1993 but with an improvement of jammer suppression from 35 dB to 45 dB in 1995, while the active processor was first reported in 1994 and finished by the final site review in early 1996.

C.   Final Progress Report

We have demonstrated a beam-steering processor that directs a main beam towards desired broadband signals while providing the full antenna spatial processing gain. We measured the beam width and array pattern to test the system, finding excellent agreement with expected results. Finally, photorefractive beam propagation has been modeled with extensive and detailed simulations to accurately characterize the adaptive weight matrix.

In order to implement the jammer-nulling processor, interferometric stability was required of the optical system. This requirement was realized with an actively stabilized feedback system to control the optical path length, resulting in a suppression value of 45 dB in the jammer-nulling process. The jammer-nulling processor has been fully characterized by considering the possibility of multiple jammers, jammer suppression versus loop gain, the capability for moving jammers, blinking jammers, the measured time response of the jamming procedure, and the measured antenna null pattern.

3.   System analysis

A.   Statement of Work

A nonlinear dynamic system analysis of the photorefractive phased-array processors will be performed. The effect of the various system parameters, such as loop gain, delay, grating phase, erasure rates, and detector gain and noise on stability,

response time, null depth, and dynamic range will be investigated. This information will be used to improve and optimize the optical phased array radar processor system design.

B.   Status

Done, first reported in 1992 and completed in 1995, but performance was improved from 30-dB null depth to 45 dB.

C.   Final Progress Report

An extensive model of the nonlinear behavior of the system was developed. The outcome was a set of nonlinear equations of motion with complex-valued excision solutions. This work incorporated multitone analysis for nulling multiple multipath jammers. The most important feature of this modeling was excellent agreement with our experiments, encouraging us that our understanding of the system was complete. For example, the frequency response solutions agree with experiment, which showed the importance of acoustic delay in the acoustooptic device (AOD). This effect led to a derivation of the relationship between AOD delay and nulling bandwidth. Second, the model allowed the inclusion of noise and feedthrough terms within the optical system, which in turn enables the choice of optimum beam ratios.

4.   Improved system demonstration

A.   Statement of Work

In the third year an optimized system, using improved components as well as a refined architecture will be constructed and tested.

B.   Status

Done, reported in 1994 with completion by final site review in 1996, but performance was improved from 20-dB null depth to 30 dB.

C.   Final Progress Report

The final system combined the beam-steering and the jammer-nulling processor with the use of 2 photorefractive crystals. In this configuration, the jammer on the first main beam sidelobe can be suppressed by 13 dB, while giving additional jammer-nulling suppression of 20 dB off the main beam sidelobe. Towards the end of the contract period, simulations were undertaken to demonstrate operation that includes true-time-delay.

5.   Zero time-delay acoustooptic Bragg cell

A.   Statement of Work

A zero time-delay acoustooptic Bragg cell operated in the wide angular aperture, parallel group velocity, beam-steering configuration will be designed and fabricated.

B.   Status

Done, first reported in 1992 but work continued during contract with completion by final site review in early 1996. Cracks within the AOD impaired low time delay measurement. A spin-off grant was awarded to address this problem.

C.   Final Progress Report

The system required time-delay characterization or the various components: acoustooptic devices (AODs), radio frequency (RF) devices, and lasers. It was found that there was only significant delay in AODs. Due to the nulling bandwidth limitations arising from time delay in the AODs, we investigated methods to reduce acoustic

propagation delay, especially for a wide angle aperture (WAA) device. A WAA, low-time-delay AOD was designed, fabricated, and experimentally characterized. Bevels and cracks within the AOD resulting from the fabrication process nullified the expected low time delay. This problem prompted the development of AODs made from TeO_2, which suffer from fewer material imperfections. The final step was to measure the phase noise of commercial Argon-ion and diode-pumped, doubled Nd:YAG lasers. It was noted that the solid-state laser, Nd:YAG, had a limited temporal coherence and 9-kHz and 50-kHz tones.

6.   Photorefractive polarization switching

A.   Statement of Work

An experimental demonstration of self aligned polarization switching diffraction in a cubic photorefractive sample of BSO will be performed. Later this will be duplicated in the near IR in the non-gyrotropic cubic photorefractive GaAs. Coherence detection and enhancement will be demonstrated with this technique.

B.   Status

Done, first reported in 1992 with BSO, but BSO was inappropriate, so in 1995, 45 degree cut $BaTiO_3$ was used instead when operating in the visible wavelength regime.

C.   Final Progress Report

Holographic multiplexing techniques were developed that allow the separation of the read and the write beams. Polarization switching of the beams within BSO was investigated as one possible method, but this type of switching is inappropriate for our application. Bragg degeneracy angle multiplexing was also studied, but the best method was polarization-angle multiplexing in 45 degree-cut $BaTiO_3$. This technique

was incorporated into the processor to improve null depth, with a final jammer suppression of 45 dB.

7. Test of wedged Fabry-Perot filter

A. Statement of Work

A high finesse wedged Fabry-Perot will be investigated for the space variant spectral filtering required on the feedback detector. The performance will be compared with that achievable with an integrated optoelectronic bandpass filter array.

B. Status

Done, done in 1995 and reported in the final site review early 1996. Fabry-Perot filters were less viable than a TDI electronic approach.

C. Final Progress Report

See Section III.9.C, Final Progress Report for time delay resonator demonstration.

8. Detector improvement

A. Statement of Work

Large transimpedance gain, large area, wide-band detectors will be fabricated and characterized for this application. The possibility of geometry optimized metal-semiconductor-metal interdigitated finger broadband detectors for this application will be investigated.

B. Status

Done, ongoing throughout the contract.

C.   Final Progress Report

Various detectors were investigated, but large transimpedance gain, large area, wide-band detectors were the best suited for this application

9.   Time delay resonator demonstration

A.   Statement of Work

A time-delay resonator will be constructed and evaluated. Multichannel time-delay behavior will be investigated, and if feasible this system will be incorporated into the prototype adaptive phased-array radar processor so that true-time-delay beam-forming without beam squint can be demonstrated.

B.   Status

Done, started in 1995 and completed by the final site review in early 1996. It was not necessary to incorporate this resonator into the processor since TDI on output was better.

C.   Final Progress Report

At the end of the contract, several true-time-delay resonators were investigated. The first was a input time delay line based on Herriot cells. The demonstration of this cell was limited by the short laser coherence length. The second was a wedged Fabry-Perot, but this configuration is limited by walkoff and diffraction. By implementing a fiber-based wedge with this configuration, ideal performance was obtained, though the fabrication was challenging. A third approach used the Fabry-Perot, but this time the system was tilted rather than wedged. This resonator is limited by the tradeoff between the quadratic frequency and the angle of the tilt. The final system is our invention of a true-time delay approach based on TDI detectors.

<u>10.</u>   <u>Reports</u>

A.   <u>Statement of Work</u>

Short monthly reports will be delivered in a timely fashion on the progress and problems being addressed during that time frame. Annual reports summarizing progress to date and plans for the upcoming year will be delivered towards the end of each funding year. Copies of all published papers resulting from this effort will be included in the reports.

B.   <u>Status</u>

Done, throughout the funding of this contract.

C.   <u>Final Progress Report</u>

40 monthly reports (11 per year), 3 annual reports, and this final report have been submitted.

IV. Work Schedule

Work was delayed by about 6 months due to changes in the funding profile, so as a comparison between the original and the modified budget:

	Year 1	Year 2	Year 3	Extension	Total
Original Budget	$244,946	$246,634	$248,652		$740,232
Modified Budget	$125,000	$250,000	$200,000	$165,232	$740,232

Therefore, the additional 6 months were at no additional cost to finish the project.

Year 1

During the first half of the first year, the major capital items required to perform the required system demonstration experiments will be obtained. The phased-array simulator will be constructed and finished by the ninth month of the first year. A zero time-delay acoustooptic Bragg cell will be designed and fabricated by the end of the first year. The initial system demonstration of the active processor will be carried out by the end of the first year. The nonlinear dynamical analysis of the photorefractive adaptive phased array processor will be begun immediately, and reported on by the sixth month. The improved detectors will be developed and tested before the processor is constructed. A final report will be submitted before the end of the first year.

Year 2

Experiments on the active processor will continue, and its performance capabilities will be investigated in the first half of the second year. During this period, some of the improved components will be tested, such as the zero time-delay acoustooptic device, the wedged Fabry-Perot detector, and the multichannel time-delay resonator, and if successful they will be incorporated in the processor. Other phased-array radar processor topologies, such as the broad band nuller will also be investigated before the end of the second year. The synergetic system analysis will continue and an optimized processor topology and component selection will be designed. A final report will be submitted before the end of the second year.

Year 3

The main task in the third year will be the demonstration of the improved next generation processor using improved components such as GaAs:Cr photorefractive material and diode pumped IR laser, in an optimized processor topology. the

components will be acquired in the first 6 months, and the processor will be constructed by month 9 and evaluated by years end.

V. Publications

Within the scope of this contract, 20 papers have been published in numerous journals and the proceedings of conferences. A bibliography of the publications is given here.

A. Journals and Proceedings

1) R.T. Weverka and K. Wagner, "Adaptive phased-array radar processing using photorefractive crystals," SPIE Proceedings, Vol. 1217, p. 173, Los Angeles CA, January, 1990.

2) Robert T. Weverka and Kelvin Wagner, "Wide angular aperture acoustooptic Bragg cell," SPIE Proceedings, Vol. 1563, San Diego, CA, July, 1991.

3) Robert T. Weverka and Kelvin Wagner, "Starting phased-array radar using photorefractive crystals," SPIE Proceedings, Vol. 1564-63, San Diego, CA, July, 1991.

4) Robert T. Weverka, Anthony Sarto, and Kelvin Wagner, "Starting phased-array radar using photorefractive crystals," DARPA/Rome Photonics in Antennas, Monterey, CA, November, 1991.

5) Ted Weverka, Kelvin Wagner, and Anthony Sarto, "Optical processing for self-cohering of phased-array imaging signals," SPIE Proceedings, Vol. 1703, Orlando, FL, April, 1992.

6) Robert T. Weverka, Anthony W. Sarto, and K. Wagner, "Photorefractive Phased-Array-Radar Processor Dynamics," DARPA/ROME meeting on Photonics for Antenna Applications, Monterey, CA, January, 1993.

7) Robert T. Weverka, Anthony W. Sarto, and K. Wagner, "Photorefractive Phased-Array-Radar Processor Dynamics," OSA Topical Meeting on Optical

Computing, Palm Springs, CA, March, 1993. {Highest Rated Paper by Optical Computing '93 Program Committee.}

8) Anthony W. Sarto, Robert T. Weverka, and Kelvin Wagner, "Photorefractive phased-array-radar processor dynamics," SPIE Proceedings, Vol. 2026, San Diego, CA, July, 1993.

9) Kelvin Wagner, "Adaptive Processing and Learning in Photorefractive Crystals," International Conference on Optical Information Processing, St. Petersburg, Russia, 1993.

10) Anthony W. Sarto, Robert T. Weverka, and Kelvin Wagner, "Active beam-steering photorefractive phased-array radar processor," SPIE Proceedings, Vol. 2155, Los Angeles, CA, January, 1994.

11) Robert T. Weverka, Anthony W. Sarto, and Kelvin Wagner, "3-dimensional holographic data processing and wavelength readout for range-Doppler-angle radar and synthetic aperture radar," SPIE Proceedings, Vol. 2155, Los Angeles, CA, January 1994.

12) Robert T. Weverka and Kelvin Wagner, "Hybrid electro-optic resonator for image classification," 1995 OSA Topical Meeting on Optical Computing, Salt Lake City, UT, March, 1995.

13) Anthony W. Sarto, Robert T. Weverka, and Kelvin Wagner, "Adaptive beam-steering and jammer-nulling photorefractive phased-array radar processor," 1995 OSA Topical Meeting on Optical Computing, Salt Lake City, UT, March, 1995.

14) Robert T. Weverka, Kelvin Wagner, and Anthony Sarto, "Three-dimensional photorefractive signal processing for radar applications," SPIE Proceedings, Vol. 2481, Orlando, FL, April ,1995.

15) K. Wagner, R. T. Weverka, A. W. Sarto, C. Garvin, T. Slagle, and S. Blair, "Adaptive Processing and Learning in Photorefractive Crystals," Invited Talk, Topical Meeting on Photorefractives, Estes Park, CO, June 12-14, 1995.

16) A. W. Sarto, R. T. Weverka, K. Wagner, and S. Weaver, "Wide angular aperture holograms in photorefractive crystals using orthogonally polarized write and read beams," Topical Meeting on Photorefractives, Estes Park, CO, June 12-14, 1995.

17) A. W. Sarto, K. H. Wagner, R. T. Weverka, S. Weaver, and E. K. Walge, "Wide Angular Aperture Holograms in Photorefractive Crystals using orthogonally polarized write and read beams," submitted to Applied Optics.

18) Tony Sarto, R.T. Weverka, and K. Wagner, "Phased-array radar processor jammer nulling dynamics."

19) Tony Sarto, R.T. Weverka, and K. Wagner, "Beam-steering/jammer nulling phased-array radar processor."

20) R.T. Weverka, Tony Sarto, and K. Wagner, "Noise and feedthrough in the dynamics of the photorefractive jammer nulling processor."

B.   Theses

1) A. W. Sarto, Ph.D., 1996, "Adaptive phased array radar optical processor."

2) Robert T. Weverka, Ph.D., in progress, "3-D adaptive optical processing."

3) Arnaud Brignon, MS, 1993, "Polarization and diffraction in photorefractive BSO."

4) Dave Finamore, MS, 1991, "A 130-MHz transimpedance amplifier for a high capacitance photodiode."

ABSTRACT

A high bandwidth, large degree-of-freedom, adaptive phased-array optical processor is described which uses three-dimensional volume holograms in photorefractive crystals to time-integrate the adaptive weights to perform beam-steering and jammer-cancellation signal processing tasks. The processor calculates the angle-of-arrival of a desired signal of interest and steers the antenna pattern in the direction of this desired signal, and simultaneously computes the angles-of-arrival of multiple interfering narrowband jammers and adaptively steers nulls in the antenna pattern in order to extinguish the jammers.

The adaptive phased-array processor is composed of two subsystems, the jammer-nulling processor, and the main-beam steering processor. A theoretical model developed for the jammer-nulling processor provides analytical expressions relating system parameters such as feedback gain and phase, optical intensities, and system noise to jammer suppression depth, convergence time, and processor signal-to-interference-plus-noise-ratio. The behavior of single and multiple planewave jammers are described, as well as jammers of arbitrary spatial profile. Holographic feedthrough is found to be the limit on processor null depth, and an improved holographic read-write multiplexing technique is described and incorporated in the processor. Experimental verification of the system behavior is presented, showing excellent agreement with the theoretical model and experimental jammer suppression as high as -45 dB. The adaptive array beam-forming process is described analytically in detail in terms of the holographic interaction within the photorefractive crystal. Experimental results of main-beam formation and measured array-functions are presented in addition to beam-propagation computer simulations demonstrating the spatio-temporal evolution of the holographic index grating and the resulting processor output. Experimental

results of simultaneous main-beam formation and jammer-nulling are also presented, which are the first known results of this type achieved with an optical-based, adaptive phased-array antenna processor.

CONTENTS

CHAPTER

CONTRACT INTRODUCTORY MATERIAL

REPORT INTRODUCTORY MATERIAL

CONTENTS

CONTENTS

CONTENTS

CONTENTS

CHAPTER

CONTENTS

FIGURES

Figure

FIGURES

FIGURES

FIGURES

FIGURES

FIGURES

FIGURES

1. Introduction

The adaptive phased-array antenna is recognized for its large aperture and corresponding high spatial resolution, and large antenna gain, as well as for the agility associated with electronic beam steering and adaptive interference cancellation provided by having multiple degrees of freedom (DOF) in the processing domain. These attributes are advantages over a single element, mechanically steeerable antenna, the trade-off comes with the processing complexity associated with the adaptive phased-array. In the simple case of narrowband processing, the output from each antenna element of the array is phase and amplitude controlled using an adaptive weight in order to form and steer a main-beam and to cancel unwanted interference. As the fractional bandwidth increases, true-time delay processing must be employed in order to maintain both a narrow beam pattern over the frequency band and low sidelobe levels at all frequencies. True-time delay processing uses a tapped delay-line behind each antenna element, which for a large phased-array can produce an unweildly number of adaptive weights[1].

What is meant here and throughout this thesis by an adaptive array, is an antenna and associated processing system which extracts information from the received signal environment and then in real-time alters the angular and frequency response of the system according to some desired output, optimum performance goal, or constraint. For example, using some *a-priori* information about a desired signal of interest to enable the array to locate and track that signal, while simultaneously using characteristics extracted from the received signal background to distinguish desired signal from interference such as jammers or multi-path signals, and adaptively removing these signals from the array response. Future generations of large, wide bandwidth adaptive phased-array antennas will consist of thousands of antenna elements and have GHz bandwidths, and will need to adaptively form and steer a main-beam while simultaneously nulling out interfering sources in a dynamic signal

1

environment. This can be an extremely demanding signal processing task because the number of adaptive weights (and DOFs) is now equal to $N \times M$, where N is the number of array elements and M is the the number of tapped delays behind each element. For example, an estimate of N is obtained by considering that the array of length L will have an element spacing capable of Nyquist sampling the RF center frequency ($\lambda_{rf}/2$), such that $N = 2L/\lambda_{rf}$. For the endfire case the number of required taps M (each with delay of $\tau = 1/B$) will be $M = BL/c = Bt_a$. Consider the specific example of simply reading out the adaptive weights of a 10,000 element array, with 100 time delay samples at each element, at a GHz rate. This requires 10^{15} multiplies per second, which exceeds the computing capabilities of even the most modern supercomputers. Current phased-arrays of modest size, for example less than 100 elements, can currently be processed using high-speed computers via standard DSP approaches. However, it is the processing task for very large phased-arrays which is by far the most challenging, and is the focus of the work presented in this thesis.

One possible representation of a received signal environment is a 3-D space is shown in figure 1.1, where two dimensions correspond to angle-of-arrival (AOA) and the third to temporal frequency. Nulling out the contribution of an interfering jammer can be viewed as having to place a null in this 3-D space corresponding to the AOA and frequency of the jammer. The time integrating properties of photorefractive volume holograms combined with their three-dimensions (3-D) and large number of accessible DOFs provide a unique computational media around which to construct highly parallel optical architectures for processing signals in complex signal environments. The beam-forming, jammer-nulling phased-array antenna processor presented in this thesis is actually one of several processors being developed[2,3,4,5,6,7,8] which maps the 3 dimensions of this signal environment representation into the 3 dimensions of the photorefractive media, where the adaptive weights are stored as Bragg selective, dynamic volume holograms.

2
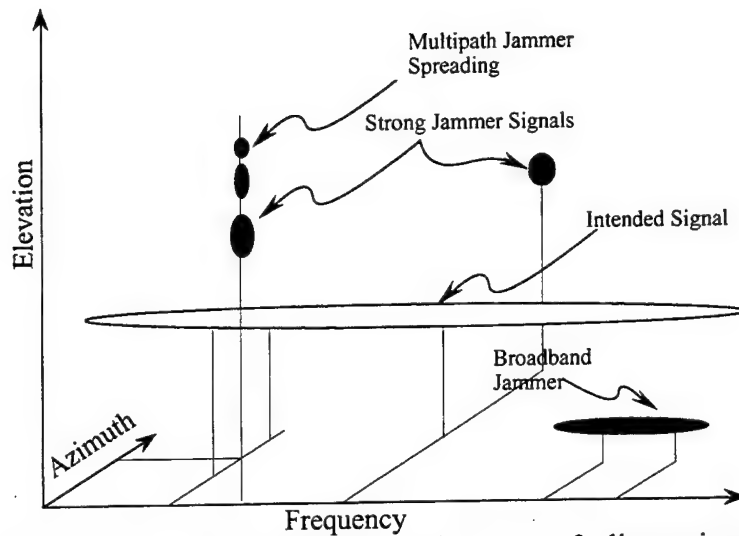
Figure 1.1. Received signal environment shown as 3-dimensional space, two dimensions of angle-of-arrival and one of temporal frequency.

The phased-array antenna processor presented in this thesis uses relatively simple components, one or two photorefractive crystals, two single-channel high-speed detectors, and one or two single channel acoustooptic (AO) Bragg cells. The bandwidth capabilities of these components approach 1 GHz, allowing the processing of wide-band phased-array signals. The most significant advantage to the architecture presented is that the required number of processor components used is independent of the number of elements in the phased-array. This attribute allows the processor to scale to processing applications for very large arrays. This is in marked contrast to traditional electronic or acousto-optic approaches, where the hardware complexity of the processor scales in proportion to the size of the array.

The phased-array processor is made up of two major processing subsystems, the beam-forming processor and the jammer-nulling processor. The beam-steering subsystem calculates the angle of arrival of a desired signal of interest and steers the antenna pattern in the direction of this desired signal by forming a dynamic holographic grating proportional to the correlation between the incoming signal of interest from the antenna array and the temporal waveform of the desired signal. This grating is formed

by repetitively applying the temporal waveform of the desired signal to a single acoustooptic Bragg cell and allowing the diffracted component from the Bragg cell to interfere with an optical mapping of the received phased-array antenna signal at a photorefractive crystal. The diffracted component from this grating is the antenna output modified by an array function pointed towards the desired signal of interest. This beam-steering task is performed with the only *a priori* information being that of the knowledge of a temporal waveform that correlates well with the desired signal and that the delay of the desired signal remains within the time aperture of the Bragg cell. This specific processing scheme is best suited for a communications scenario, as opposed to a radar scenario where quantitative range delay and AOA information is desired. The fundamental approach of using a photorefractive crystal to time integrate and store the adaptive weights is still applicable for a radar application, although a means of extracting the desired radar information would have to be implemented. The jammer-nulling subsystem computes the AOAs of multiple interfering narrowband jammers and adaptively steers nulls in the antenna pattern in order to extinguish the jammers by implementing a modified LMS algorithm in the optical domain. This task is performed in a second photorefractive crystal where holographic gratings are formed which are proportional to the correlation between the unprocessed antenna output and a delayed version of the formed main beam. The diffracted components from these gratings are jammer estimates which are subtracted from the formed main-beam signal producing a processor output with reduced jammer content.

1.1 Thesis Outline

This thesis presents the theory and experimental results of the beam-forming and jammer-nulling processors, as well as for the combined beam-forming and jammer-nulling processor. The thesis begins with a review of the traditional issues such as resolution and bandwidth associated with phased-array antenna processing, presented

in Chapter 2. The traditional approaches to beam-forming and adaptive interference suppression are discussed in Chapter 2, and it concludes with a derivation of the modified least-mean-square (LMS), hardware compressive algorithm which is implemented in the optical domain for the work performed in this thesis. It is shown that the modified algorithm performs the same as the LMS algorithm introduced by Widrow[1]. Chapter 3 presents previous work in LMS adaptive signal processing concepts with optical architectures, and work done in extending these architectures to adaptive processing of phased-arrays. Chapter 4 is a review of photorefractive holographic materials, with a particular emphasis on the dynamic nature of holographic grating formation. The dynamic holographic grating model presented in Chapter 4 serves as a foundation for the adaptive weight formation in both the jammer-nulling and beam-forming processors, in particular the performance characteristics of the jammer-nulling processor described in Chapter 7. Chapter 5 is dedicated to the discussion of two dynamic holographic read/write multiplexing techniques which have been used in both processors to simultaneously write and read out holographic gratings in photorefractive crystals. The two methods discussed are Bragg-angle degeneracy, and orthogonal polarization multiplexing, the latter of which has been demonstrated to exhibit extremely large phased-matched angular bandwidth[9,10], with possible applications to image processing and volume holographic storage. Experimental results are presented showing wide, Bragg matched angular bandwidth exceeding 18 x 9 degrees internal to the crystal, in agreement with a derived model and simulation results. The beam-forming processor is discussed in Chapter 6, where the primary emphasis is on demonstrating the analogy and equivalence of adaptive beam-formation method employed in this processor, and basic, dynamic volume holography. The Chapter begins with a derivation of the beam-forming process in terms of Fresnel propagation operators, which allows the process of the holographic beam-forming process to be ellucidated while suppressing the cumbersome task of calculating

multiple, embedded diffraction integrals. This analysis yields an analytical expression for the time integrated, 2-dimensional holographic grating formed in the dynamic holographic media. Simulations have also been done which demonstrate the beam-forming process using a split-step Fourier transform beam-propagation algorithm[11], coupled with a spatio-temporal model[12] for the photorefractive material. The photorefractive model takes into account non-linear behavior in the material such as angular and spatial-frequency response, two-wave mixing, and fanning. Chapter 7 presents the theoretical, simulation, and experimental investigations of the jammer-nulling processor. The theoretical investigation results in a dynamic model which describes the interference suppression performance of the jammer-nulling processor as a function of system parameters such as laser beam powers, photodetector responsivities, electrical gains, etc. The dynamic model is developed and modeled for the case of a single frequency planewave jammer, and extended to the more general case of multiple jammers with arbitrary spatial profiles. One of the more significant results of Chapter 7 is the distinction and tradeoffs between maximizing jammer suppression depth and maximizing the total array signal-to-interference-noise ratio (SINR), in terms of processor system parameters and noise. Experimental results of the processor are then presented, demonstrating 45 dB of suppression of a single narrowband jammer, and multiple jammer suppression results which agree well with the derived theory. The Chapter concludes with the first known experimental results of simultaneous phased-array beam-formation and jammer-suppression. Chapter 8 discusses in more detail some of the resonator based structures for optical processing of RF signals which are required in both the jammer-nulling and beam-forming processor. Finally, Chapter 9 is a summary of the thesis, with suggestions for future work.

References

[1]   R.T. Weverka and K. Wagner, "Adaptive phased-array radar processing using photorefractive crystals," in *Optoelectronic Signal Processing for Phased-Array Antennas II*, B.M. Hendrickson and G.A. Koepf, ed. Proc. Soc. Photo-Opt. Instrum. Eng. **1217**, 173-182 (1990).

[2]   R.T. Weverka and K. Wagner, "Staring phased-array radar using photorefractive crystals," in *Optical Information Processing Systems and Architectures III,* Proc. Soc. Photo-Opt. Instrum. Eng. **1564**, 676-684 (1991).

[3]   A.W. Sarto, R.T. Weverka, and K. Wagner, "Photorefractive phased-array radar processor dynamics," in *Photonics for Processors, Neural Networks, and Memories,* Proc. Soc. Photo-Opt. Instrum. Eng. **2026**, July 310-324 (1993).

[4]   A.W. Sarto, R.T. Weverka, and K. Wagner, "Beam-steering and jammer-nulling photorefractive phased-array radar processor," in *Optoelectronic Signal Processing for Phased-Array Antennas IV,* Proc. Soc. Photo-Opt. Instrum. Eng. **2155**, 378-388 (1994).

[5]   R.T. Weverka, K. Wagner, A.W. Sarto, and S. Weaver, "3-Dimensional holographic data processing and wavelength readout for range-doppler-angle radar, and synthetic aperture radar," in *Optoelectronic Signal Processing for Phased-Array Antennas IV,* B.M. Hendrickson, ed. Proc. Soc. Photo-Opt. Instrum. Eng. **2155**, 336-347 (1994).

[6]   R.T. Weverka, K. Wagner, and A.W. Sarto, "Adaptive phased-array radar processing using photorefractive crystals," Appl. Opt. **35**, no. 8, 1344-1366 March (1995).

[7]   A. W. Sarto, K. Wagner, R. T. Wagner, S. Blair, and S. Weaver, "Photorefractive phased-array antenna beam-forming processor," in *Radar Processing, Technology, and Applications,* SPIE **2845**, (1996).

[8]   B. Widrow, P.E. Mantey, L.J. Griffiths, and B.B. Goode, "Adaptive antenna systems," in , IEEE Proc. **55**, 2143-2161 (1967).

[9]   A.W. Sarto, R.T. Weverka, K.H. Wagner, and S. Weaver, "Wide angular aperture holograms in photorefractive crystals using orthogonally polarized write and read beams," in *Photorefractive materials, effects, and devices,* OSA/NIST, June 214-217 (1995).

[10]   A. W. Sarto, K. Wagner, R. T. Wagner, S. Weaver, and E. Walge, "Wide angular aperture holograms in photorefractive crystals by the use of orthogonally polarized write and read beams," Appl. Opt. **35**, no. 29, 5765-5775 Oct. (1996).

[11]   J. A. Fleck, J. R. Morris and M.D. Feit, "Time dependent propagation of high-energy laser beams through the atmosphere," Appl. Phys. **10**, 129-160 (1976).

[12]   M. Saffman, "Self-Organized Formation of Image Representations in Photorefractive Oscillators," Ph.D. thesis, University of Colorado, 1994.

2. Adaptive Phased-Array Antenna Processing

This chapter will review the fundamental signal processing methods used for adaptive phased-array antennas. The focus will be on main-beam formation and inteference cancellation. The chapter begins with a brief discussion of simple phase-shift and true-time delay beam formation, in the absence of any adaptive inteference suppression. Adaptive interference cancellation is then discussed, including the Widrow-Hopf[1,2] and Applebaum[3] least-mean-square (LMS) based algorithms, in addition to an overview of the classic sidelobe canceller[4]. Due to their applicability to large arrays, an emphasis is placed on LMS adaptive algorithms, which iteratively converge to the desired solution, taken to be the set of adaptive weights which optimize the signal-to-interference-plus-noise ratio; this is in marked contrast to algorithms which explicitly calculate the weights with a covariance matrix inversion technique[5,6]. The important performance metrics of signal-to-interference-noise-ratio and convergence time are discussed. The chapter concludes with a derivation of the optically-implemented delay-line compressive LMS algorithm for implementation in the optical phased-array processor discussed in this thesis.

2.1 Beam formation and steering

The fundamentals of phased-array beam formation and steering will be reviewed in this section, while adaptive algorithms for simultaneous interference suppression will be reserved for later sections. Main beam-steering alone represents a much simpler task than doing so with simultaneous interference cancellation. For an imaging example, the beam is simply scanned by varying the weight vector accordingly. A communications scenario requires the beam(s) to be pointed in specific directions. In both of these cases the weight vector can be directly calculated and implemented in an open-loop fashion.

2.1.1 Phase shift steering

A phase-shift steered, linear antenna array of N elements[1,7] is shown in figure 2.1. As shown in the figure, a far-field signal is received by the array at an angle θ. Multiplying the output signal of each antenna element x_n is an adaptive weight, denoted by w_n. The weighted antenna outputs are summed to yield the array output signal, which is written as

$$y(t) = \sum_{n=1}^{N} w_n x_n r(t) e^{i\omega_r t} = \underline{W}^T \underline{X} r(t) e^{i\omega_r t} \qquad 2.1$$

The weight and signal vectors in 2.1 are given by

$$\underline{W} = \left[w_1, w_2, w_3 \dots w_N \right] \text{ and } \underline{X}(u) = \left[1, e^{ikdu}, e^{i2kdu} \dots e^{ikNdu} \right] \qquad 2.2$$

where $u \equiv \sin(\theta)$, and the RF signal is $r(t)$ on a carrier ω_r. The individual weights compensate for the the phase shift between array elements produced by their physical separation, and adjust the response of the array to have a maximum at some particular angle. The interelement phase shift $\Delta\phi$ between array elements for a narrowband signal arriving at angle θ, is given by

$$\Delta\phi = \frac{2\pi d}{\lambda_{rf}} \sin(\theta) = \frac{2\pi d}{\lambda_{rf}} u \qquad 2.3$$

where λ_{rf} is the RF signal wavelength, and d is the array element spacing. For phase-shift steering, each w_n is simply a complex-valued multiplier, applying both an amplitude multiplication and a phase-shift of the form

$$w_n = a_n e^{i\phi_n} \qquad 2.4$$

For example, incrementally increasing the phase of each w_n would apply a linearly increasing phase shift across the array, steering the angle of the antenna response. The N adaptive weights provide N DOFs. For the single plane wave incident RF signal at
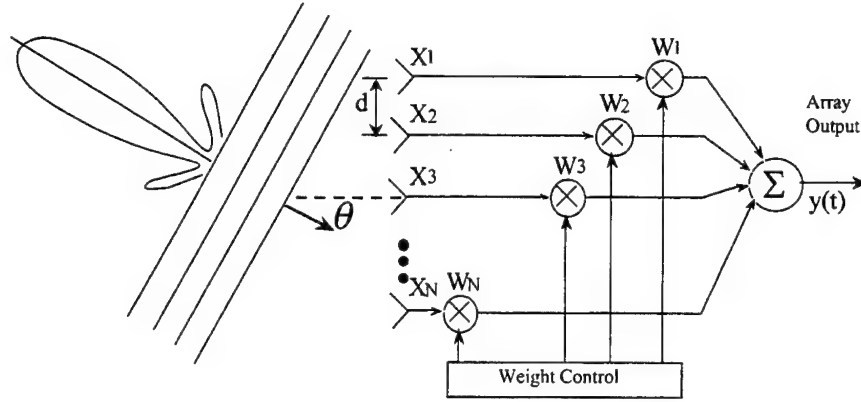
Figure 2.1. A phase-shift steered, linear phased-array antenna for narrowband array processing.

angle θ shown in figure 2.1, the weight vector which maximizes the antenna response in the signal direction is the complex-conjugate of the signal vector $\underline{X}(u)$,

$$\underline{W}(u) = \underline{X}^*(u) = \left[1, e^{-ikdu}, e^{-i2kdu} \ldots e^{-ikNdu}\right]$$ 2.5

It is evident that for this case $x_n w_n = 1$ for all n. There is now an array gain of N resulting from the sum of the N antenna elements, and a cross-range resolution given by the effective size of the array, $L\cos(\theta)$, where L is the length of the array and $\cos(\theta)$ is the steering angle. This linear array geometry provides the most straightforward example to further examine these properties of the formed beam. Initially assuming that the outputs of all N elements are uniformly weighted, in a receive scenario (essentially the same for transmit) the sum of all the element output voltages, E_{ar}, for a single frequency sinwave input at frequency ω will be[8,9]

$$E_{ar} = \sin(\omega t) + \sin(\omega t + \Delta\phi) + \sin(\omega t + 2\Delta\phi) + \cdots + \sin(\omega t + (N-1)\Delta\phi)$$
$$= \sin[\omega t + (N-1)\Delta\phi/2]\frac{\sin(N\Delta\phi/2)}{\sin(\Delta\phi/2)}$$ .2.6

10
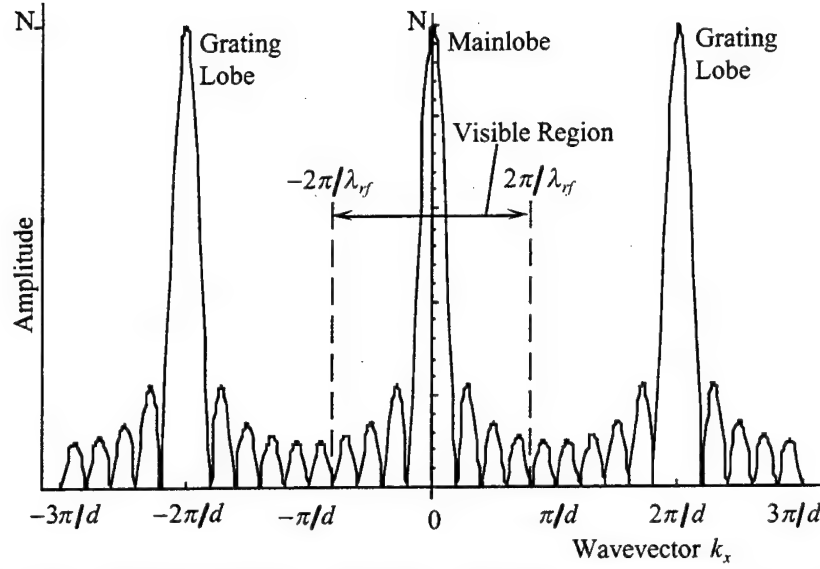
Figure 2.2. Array antenna pattern as a function of transverse wavevector component

where the interelement phase shift, $\Delta\phi$, is given by equation 2.3. The first factor is just a phase shifted sinewave of frequency ω, and the second is an aperture weighting function, which can be expressed in terms of the tranverse component of the incident wavevector, $k_x = k\sin(\theta)$, as

$$W(k_x) = \frac{\sin[N\Delta\phi/2]}{\sin[\Delta\phi/2]} = \frac{\sin[Nkd\sin(\theta)/2]}{\sin[kd\sin(\theta)/2]} = \frac{\sin[Nk_xd/2]}{\sin[k_xd/2]} \qquad 2.7$$

which is plotted in figure 2.2. As shown in figure 2.2, $W(k_x)$ is periodic with a period of $2\pi/d$. The heigth of the mainlobe is at $W(0)$, and is equal to N, the number of elements in the array, which again demonstrates spatial processing gain. The first zero occurs when the argument of the numerator is equal to π, corresponding to $k_x = 2\pi N/d$, and therefore the mainlobe width will be approximately $4\pi/Nd$. This demonstrates that increasing the number of array elements reduces the mainlobe width and improves the spatial resolution of the array. The secondary maxima shown in figure 2.2 would in general produce erronious, or at best confusing signal returns. These maxima are referredto as "grating lobes"[8, 9] and are produced whenever $\pi d\sin(\theta)/\lambda = 0, \pi, 2\pi\ldots$, or correspondingly whenever $k_x = \pm 2\pi/d$. For an incident

11

field of given wavelength λ_{rf}, $k_x = 2\pi \sin(\Delta\phi)/\lambda_{rf}$, and because $|\sin(\Delta\phi)| \leq 1$, k will have real values only between $k_x = \pm 2\pi/\lambda_{rf}$. This region is often referred to as "the visible region", or $\pm 90°$. The primary means of grating lobe avoidance is to select closely spaced elements $(d \leq \lambda/2)$, so that none of the grating lobes lie in real space[9, 10]. Irregular element spacing can also reduce grating lobes as well.

Normalizing the square of equation 2.7 and setting the element spacing to $d = \lambda/2$, produces the antenna radiation pattern

$$G(\theta) = \frac{\sin^2[N\pi \sin(\theta)/2]}{N^2 \sin[\pi \sin(\theta)/2]}.$$ 2.8

Approximating the sine function in the denominator of equation 2.8 by its argument under the assumption that N is large, results in a radiation pattern of

$$G(\theta) \approx \frac{\sin^2[N\pi \sin(\theta)/2]}{[N\pi \sin(\theta)/2]^2} = \text{sinc}^2(N\pi \sin(\theta)/2)$$ 2.9

Thus, for large N, the radiation pattern is essentially that of a uniform aperture, where the well-known sinc^2 far-field radiation pattern is related to the aperture via a Fourier transform relationship. In like fashion, the first sidelobe will be reduced from the power level of the main-lobe by approximately -13.5 dB. This result was based on the assumption that all of the elements were equally weighted before summation. Non-uniform weighting can be used to apodize the antenna and reduce sidelobe levels. For example the Dolphi-Chebyshev[11], Taylor[12], or cosine squared[13] apodization functions are well known to reduce sidelobes, but possibly at the expense of main-lobe width increase.

2.1.2 True-time delay beam formation

The inadequacy of phase-shift steering for broadband signal processing is exhibited by equation 2.3. The interelement phase shift $\Delta\phi$ is seen to be frequency

dependent; the higher the frequency, the higher the spatial phasor across the array which will be needed to control the beam. A different phase-shift is now required for each resolvable frequency over the signal bandwidth, however a single phase-shifter behind each antenna element provides only one. Thus each resolvable frequency is steered to a different angle, a condition known as "beam squint", which reduces the cross-range resolution of the array and increases sidelobe energy. An array can be considered broadband when the fractional bandwidth $F = B/v_{rf}$ of the array operating at center frequency $v_{rf} = c/\lambda_{rf}$ exceeds the center frequency wavelength divided by the antenna aperture L. In particular when

$$B/v_{rf} \geq \lambda_{rf}/L \text{ or when } LB \geq c, \qquad\qquad 2.10$$

the beam rotates resolvably over the RF frequency bandwidth, and for large broadband arrays, when $LB \gg c$, beam squint is over many beamwidths.

For broadband processing, time-delay elements are used to compensate for the actual time-of-flight difference of the signal between elements as the signal propagates across the array, which is the same for all frequencies. A simple example of true-time delay processing is shown in figure 2.3, where following each array element is a variable time-delay, and a real, multiplicative weight.

The approach shown in figure 2.3 is not an architecture traditionally embraced by the RF community, but nevertheless multiple implementations of this architecture based on optical processing methods have been provided by various researchers. A straightforward approach to implementing the architecture shown in figure 2.3 is to route a modulated laser beam down various lengths of optical fibers[14, 15, 16]. Other proposed methods include switching between free-space sections of variable lengths[17,18], exploiting the frequency dependence of highly dispersive optical fibers[19,20], and segmented mirror devices[21]. None of these approaches will be discussed in any detail here.
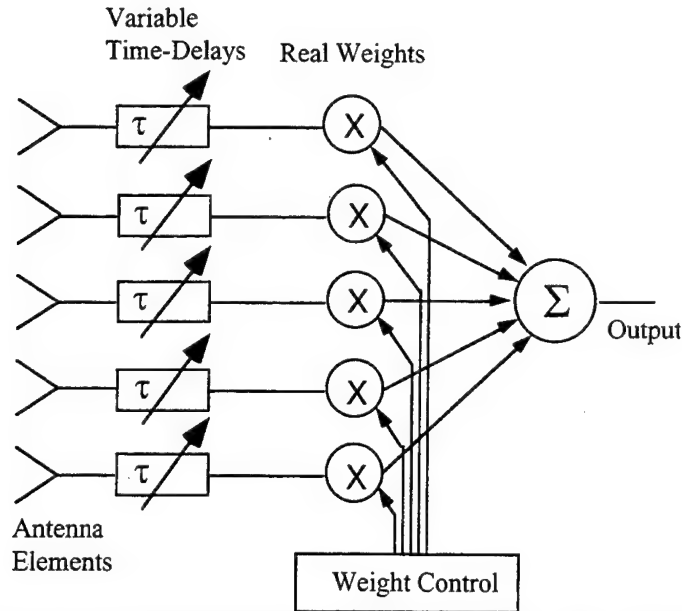
Figure 2.3. Variable time-delay architecture for broadband array processing.

The traditional approach to true-time delay processing is done using discretely tapped delay lines, also known as a transversal filter[1]. This approach is shown implemented into a linear, 1-D antenna in figure 2.4[22,7]. The true-time delay antenna in the figure can be viewed as a 1-D spatial array of transversal filters, each transversal filter providing the necessary temporal/frequency processing at each spatial sampling point along the aperture of the array. The function of the time-delays can be intuitively viewed as compensating for the time-of-flight variations across the array, which is most extreme for a signal arriving at endfire to the array. For the endfire case the array must be capable of processing signals over a time $t_a = L/c$, corresponding to the time-of-flight across the full array aperture, where L is the length of the array. The number of resolvable frequencies M, (equal to the number of required taps each with delay of $\tau = 1/B$) will then be

$$M = BL/c = Bt_a \qquad\qquad 2.11$$

When multipath delays (with a maximum time delay t_M) are also to be accounted for, M may need to be increased to Bt_M.

14
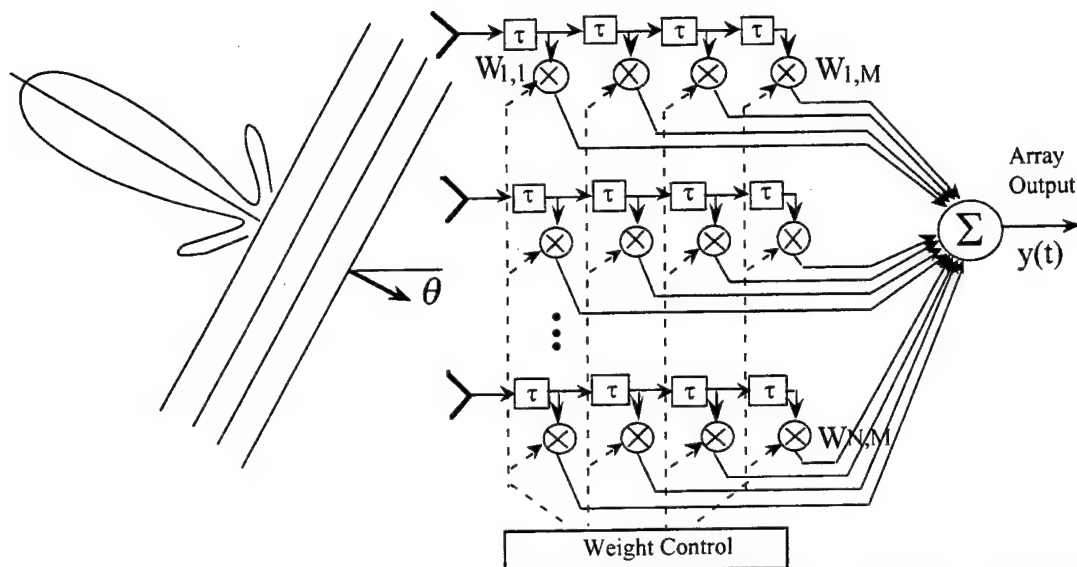
Figure 2.4. True-time delay implementation of phased-array antenna processes broadband signals.

Depending upon the application, the number of taps can become quite large because the number of adaptive weights (and DOFs) is now equal to $N \times M$. For the endfire case, an estimate of N is obtained by considering that the array of length L will have an element spacing capable of Nyquist sampling the RF center frequency ($\lambda_{rf}/2$), leading to

$$N = 2L/\lambda_{rf} \qquad\qquad 2.12$$

As an example, consider a 1-D antenna system operating at a center frequency of 10 GHz, with a bandwidth of 2 GHz ($F = 0.2$). For an array aperture of $L = 13.5$ meters, it follows that $N = 1000$, and $M = 100$. Thus this 1-D array would have a total of 100,000 weights, which is a formidable number to consider for real-time adaptive processing.

2.2 Adaptive Algorithms for Interference Cancellation

The true processing power of the adaptive phased-array comes from the ability to adaptively suppress interference, while simultaneously optimally receiving the desired signal with the full antenna gain. The adaptive weights provide the DOFs

necessary to move the location of the antenna pattern nulls in the direction of unwanted interference. In general, an adaptive array with N degrees of freedom will be capable of nulling out $N-1$ narrowband interfering sources, and still receive the desired signal. The primary performance metrics of the adaptive array are the signal-to-noise ratio (SNR) or the signal-to-interference-plus-noise ratio (SINR), and the convergence time. The SINR is often discussed in terms of the "improvement factor"[23, 24], or IF of the array, which is the ratio of the SINR of the adaptively formed output of the antenna to that of a single antenna element. In particular, the SINR and IF are defined as

$$SINR \equiv \frac{\text{Desired Signal Power}}{\text{Interference Power} + \text{Noise Power}} \qquad 2.13$$

and

$$IF \equiv \frac{\text{SINR}}{\text{SINR}_{element}} \qquad 2.14$$

While there are a multitude of algorithms for controlling the weights of an adaptive array, there are fundamentally two distinct approaches which are taken. Direct algorithms, based on some criteria or measurement, with a single computation explicitly calculate the optimal weights as determined by a Wiener solution[2] (i.e. those weights which maximize the SINR) and then implement these weights. Closed-loop algorithms are implemented recursively so that the system *converges* to the optimal weights for the given scenario. The former approach will be hereafter referred to as *direct* adaptive algorithms, and the latter as simply *adaptive* algorithms. The direct method is generally based on digitally computed signal statistics calculated over some finite temporal window and implemented open-loop, while the adaptive approach is generally error-driven and implemented closed-loop. As will be shown, the direct calculation of the optimal weights requires the calculation or estimation of correlation matrices as well as matrix inversions. If the number of weights NxM is small, a direct approach is sensible because the weights can be calculated and applied very efficiently in minimal time,

16

(although a finite temporal window is still necessary to estimate the correlation matrices). However, the matrix inversion operation is an order $(NxM)^3$ process, and if this number is large, the direct approach can become computationally impractical and an adaptive algorithm which converges to the optimum weights is more sensible. This chapter will emphasize adaptive, error driven algorithms. An additional advantage to an adaptive approach is that because the weights are updated incrementally, the correlation matrices and inverses are not calculated explicitly, but are instead estimated from instantaneous values. By not calculating these matrices, there is an enormous advantage in terms of reduced computational memory requirements with the adaptive approach. The primary tradeoff with the adaptive approach is in terms of convergence time, which for certain signal environments may be very slow.

2.2.1 Adaptive Weight Calculation for Known Signal Environment

When the properties of the signal environment are known, such as desired signal and noise spectra, and the AOAs of incident signals, the array output can be optimized by direct calculation of the optimum set of weights, $\underline{W}_{opt}$. As will be shown in this section, a direct calculation of $\underline{W}_{opt}$ requires the calculation of two correlation matrices and a matrix inversion.

Consider an N element, phase-steered array as shown in figure 2.1. The array output $y(t)$ can be written as the sum of the weighted antenna element outputs[25],

$$y(t) = \sum_N x_n(t)w_n = \underline{X}^T(t)\underline{W} = \underline{W}^T \underline{X}(t)$$

2.15

where the weight vector $\underline{W}$ is composed of the N individual weights, w_n,

$$\underline{W} = \left[w_1, w_2, \ldots w_N\right]^T.$$

2.16

The signal vector, $\underline{X}(t)$, is composed of the signals transduced from each array element,

$$\underline{X}(t) = \left[x_1(t), x_2(t), \ldots x_N(t)\right]^T$$

2.17

17

where the individual $x_n(t)$ are each composed of a desired signal component $D_n(t)$, and an undesired noise component $U_n(t)$, which can be made up of both jammers and broadband noise such as detector noise. Therefore,

$$x_n(t) = D_n(t) + U_n(t) \qquad 2.18$$

and

$$\underline{X}(t) = \underline{D}(t) + \underline{U}(t) \qquad 2.19$$

where again, using vector notation,

$$\underline{D}(t) = [D_1(t), D_2(t), \ldots D_N(t)]^T \qquad 2.20$$

and

$$\underline{U}(t) = [U_1(t), U_2(t), \ldots U_N(t)]^T. \qquad 2.21$$

A common metric used to evaluate the performance of the processor is the mean-square error, σ, produced between the processor output, and a reference, or target waveform $r(t)$, which must correlate well with the desired signal. Thus, some *a priori* information is needed in order to choose a reference signal. The error, $\varepsilon(t)$, is defined as

$$\varepsilon(t) = r(t) - y(t) \qquad 2.22$$

and the mean-square error σ, is taken to be the expectation value of $\varepsilon(t)$,

$$\sigma = E[\varepsilon^2(t)] \qquad 2.23$$

The expectation operator is denoted by $E[\bullet]$. Squaring equation 2.22 and using matrix notation, the expectation of the summed-squared-error is

$$E[\varepsilon^2(t)] = E[r^2(t)] - 2\underline{W}^T \underline{S} + \underline{W}^T \underline{\Phi} \underline{W} \qquad 2.24$$

18

where $\underline{\underline{\Phi}}$ is the received signal correlation matrix, and is defined as

$$\underline{\underline{\Phi}} = E\left[\underline{X}(t)\underline{X}^T(t)\right] = \int \begin{bmatrix} x_1(t)x_1(t) & x_1(t)x_2(t) & \cdots \\ x_2(t)x_1(t) & x_2(t)x_2(t) & \cdots \\ \vdots & \vdots & \ddots \end{bmatrix} dt \qquad 2.25$$

with ergodicity hypothesis allowing the expectation to be calculated with a time integration, and the cross-correlation vector $\underline{S}$ between the reference signal and received signal vector is defined as

$$\underline{S} \equiv E\left[\underline{X}(t)r(t)\right] \qquad 2.26$$

It is assumed that both the desired signal and the noise signal are zero-mean, random processes, as well as being uncorrelated with each other. Thus, the received signal correlation matrix $\underline{\underline{\Phi}}$, and the cross-correlation vector $\underline{S}$ can be written as the sums of the correlation matrices of the individual terms,

$$\underline{\underline{\Phi}} = \underline{\underline{\Phi}}_D + \underline{\underline{\Phi}}_U \qquad 2.27$$

and

$$\underline{S} = \underline{S}_D + \underline{S}_U \qquad 2.28$$

The optimum weight values are found by setting the gradient with respect to $\underline{W}$ of the summed-squared error given by equation 2.24 equal to zero. In particular, setting

$$\nabla_W \left\{ E\left[\varepsilon^2(t)\right] \right\} = 0 \qquad 2.29$$

Carrying out the gradient operation on equation 2.24 yields

$$\nabla_W \left\{ E\left[r^2(t)\right] - 2\underline{W}^T \underline{S} + \underline{W}^T \underline{\underline{\Phi}} \underline{W} \right\} = -2\underline{S} + 2\underline{\underline{\Phi}} \underline{W} \qquad 2.30$$

Setting equation 2.30 equal to zero yields the optimum weight vector, $\underline{W}_{opt}$,

$$\underline{W}_{opt} = \underline{\underline{\Phi}}^{-1} \underline{S} \qquad 2.31$$

The form of the optimum weight vector given in equation 2.31 is re-occuring[26] and fundamental, and is in fact one form of the Weiner solution[2], which yields the maximum SINR of the system. More generally, it can be shown that the Weiner solution corresponds to the condition when the cross-correlation between the error and the input vector $\underline{X}$ is equal to zero. Equation 2.28 can be simplified using the assumption that because the noise signal is not correlated with the desired signal, it will not be correlated with the reference signal either. Expanding equation 2.26, using equation 2.28 results in

$$\underline{S} = E[\underline{X}(t)r(t)] = E[\underline{D}(t)r(t) + \underline{U}(t)r(t)] = E[\underline{D}(t)r(t)] = \underline{S}_D \qquad 2.32$$

which indicates that under the assumptions of equation 2.32, $\underline{S}_U$ is equal to zero. Therefore equation 2.31 becomes

$$\underline{W}_{opt} = \underline{\underline{\Phi}}^{-1}\underline{S} = \underline{\underline{\Phi}}^{-1}\underline{S}_D \qquad 2.33$$

Thus, in theory, the weights could be calculated directly and applied to the array, using no adaptivity. Both the inverse of the received signal correlation matrix $\underline{\underline{\Phi}}^{-1}$, and the cross-correlation vector $\underline{S}_D$ could be calculated. However, the simplicity of this approach can be somewhat misleading. In particular, in order to construct the received signal correlation matrix given in equation 2.25, it is necessary to have full knowledge of the signal environment, including knowledge of the AOA of the desired source, as well as the AOAs and frequencies of all the interfering sources. If all of this information were available, it is likely that the antenna would not be needed. There are a multitude of signal estimation methods which could be used to analyze the received environment in an attempt to extract such information, such as MUSIC[27], ESPRIT[28], and IQML[29]. However, all of these methods are statistically based and again require signal correlation matrices to be calculated. For a small number of weights such an approach is reasonable, however the matrix inversion operation is an order $(NxM)^3$

process, and if the number of weights is large, the direct approach can become computationally impractical and require large memory. More commonly, there is some, albeit limited, *a priori* information available regarding the signal environment. This information is usually of a either temporal or spatial nature, and algorithms based on exploiting these two instances are discussed in following sections. The open-loop, direct matrix inversion method has additional disadvantages in terms of number of interfering sources. For example, if the number of interfering sources is $< N-1$, a unique inverse to the received signal matrix does not exist, or it may be singular with no inverse, although usually any real system with additive noise ensures against this.

It is important to point out that the mimimum error obtained from the approach outlined here will not be zero. Substituting equation 2.31 back into equation 2.24 yields this minimum error[30] ε^2_{min},

$$\varepsilon^2_{min} = E\left[r^2(t)\right] - 2\underline{W}^T_{opt}\underline{S} + \underline{W}^T_{opt}\underline{\underline{\Phi}}\underline{W}_{opt}.$$ 2.34

Noting that from equation 2.33 $\underline{S} = \underline{\underline{\Phi}}\underline{W}_{opt}$, it follows that the mimimum square error will be

$$\varepsilon^2_{min} = E\left[r^2(t)\right] - \underline{W}^T_{opt}\underline{\underline{\Phi}}\underline{W}_{opt}.$$ 2.35

It is instructive to use equation 2.35 to enable an arbitrary set of weights to be expressed in terms of ε^2_{min}. Solving equation 2.35 for $E\left[r^2(t)\right]$ and substituting the result into equation 2.24 yields a general expression for the error as a function of the weight values[30],

$$E\left[\varepsilon^2(t)\right] = \varepsilon^2_{min} + \left(\underline{W} - \underline{W}_{opt}\right)^T \underline{\underline{\Phi}}\left(\underline{W} - \underline{W}_{opt}\right)$$ 2.36

This form of the summed squared-error shows that the error surface is quadratic, and the fact that the summed squared-error is at a minimum when $\underline{W} = \underline{W}_{opt}$. The error
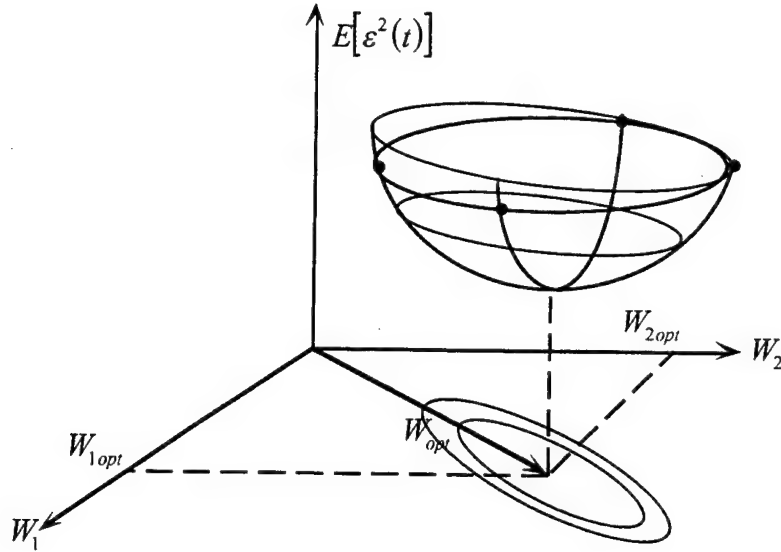
Figure 2.5. Quadratic error surface formed in weight space by two adaptive weights.

surface for a two weight system is shown in figure 2.5. A larger number of weights results in a higher dimensional surface quadratic error determined by $\underline{\underline{\Phi}}$.

In general, because the off-axis terms of $\underline{\underline{\Phi}}$ are non-zero, the principle axes of the error surface "bowl" are not parallel to the weight axis. A coordinate transformation is used to align the two axes. In particular, letting $\underline{\underline{R}}$ be an N x N rotation matrix, the weight vector can be written as

$$\underline{W} = \underline{\underline{R}}\,\underline{V} \qquad\qquad\qquad 2.37$$

where $\underline{V}$ is an N element column vector. If $\underline{\underline{R}}$ is chosen such that $\underline{\underline{R}}^T \underline{\underline{\Phi}}\underline{\underline{R}}$ is a diagonal matrix, then

$$\underline{\underline{R}}^T \underline{\underline{\Phi}}\underline{\underline{R}} = \begin{bmatrix} \lambda_1 & 0 & 0 & \cdots \\ 0 & \lambda_2 & 0 & \\ 0 & 0 & \lambda_3 & \\ \vdots & & & \ddots \end{bmatrix} \qquad\qquad 2.38$$

where the λ_i are the eigenvalues of $\underline{\underline{\Phi}}$ and the elements of $\underline{V}$ are the normal coordinates of the error surface. The eigenvalues play an important role in the convergence behavior of the Widrow-Hopf LMS algorithm discussed below.

2.2.2 Error minimization and the Widrow-Hopf LMS algorithm

The Widrow-Hopf LMS algorithm is a closed-loop, adaptive algorithm which converges to the ideal weight values given by equation 2.31. In particular, the algorithm makes use of a gradient descent technique to reduce the summed squared error in incremental steps, and track the bottom of the error surface bowl. The incremental approach allows correlation estimates to be replaced by instantaneous measured values, which dramatically reduces both computation and memory requirements.

The gradient descent operation implemented with the Widrow-Hopf LMS algorithm incrementally updates the adaptive weights by moving down-hill in the steepest direction of the error surface[1],

$$\frac{dW}{dt} = -k\nabla_w\left\{E\left[\varepsilon^2(t)\right]\right\} \qquad\qquad 2.39$$

where k is a positive feedback gain constant. The negative sign multiplying the gradient in equation 2.39 causes the weights to move in the direction of steepest descent towards the bottom of the error surface bowl shown in figure 2.5, and the quadratic form of the summed squared-error causes the weights to evolve more quickly when they are farther from the error minima. The gradient with respect to the weights of the of the squared-error is given by equation 2.30, and is repeated here

$$\nabla_w\left\{E\left[\varepsilon^2(t)\right]\right\} = \nabla_w\left\{E\left[r^2(t)\right] - 2\underline{W}^T\underline{S} + \underline{W}^T\underline{\underline{\Phi}}\underline{W}\right\} = -2\underline{S} + 2\underline{\underline{\Phi}}\underline{W}. \qquad 2.40$$

Substituting this value into the gradient descent rule of 2.39 yields[30]

$$\begin{aligned}
\frac{dW}{dt} &= -2k\left[\underline{S} + \underline{\underline{\Phi}}\underline{W}\right] \\
&= -2k\left\{E\left[\underline{X}(t)\underline{X}^T(t)\right]\underline{W} - E\left[\underline{X}(t)r(t)\right]\right\} \\
&= 2kE\left\{\underline{X}(t)\left[r(t) - \underline{X}^T(t)\underline{W}\right]\right\} \\
&= 2kE\left[\underline{X}(t)\varepsilon(t)\right]
\end{aligned} \qquad 2.41$$

23

The actual implementation of the algorithm instantaneous values for $\underline{X}(t)$ and $\varepsilon(t)$ instead of the time-averaged values resulting from the expectation operator. Dropping the expectation operator yields

$$\frac{d\underline{W}}{dt} = 2k\left[\underline{X}(t)\varepsilon(t)\right] \qquad\qquad 2.42$$

The significance of the approximation made in dropping the expectation values as in equation 2.42 is that the ε^2 surface is allowed to fluctuate about its mean, and hence the weight values also fluctuate, varying about the mean producing weight "jitter". The fluctuations can be caused by the changing signal environment, as well as noise internal to the processor. This fluctuation of the weights can be kept small by limiting the magnitude of the feedback gain constant k in equations 2.39 and 2.42. The value of k greatly affects convergence, and is discussed in more detail below.

At steady-state, the time derivative in equation 2.42 equals zero, which implies that at steady-state $\underline{X}(t)$ and $\varepsilon(t)$ are orthogonal. In addition, at steady-state, the weights converge to the optimum weight values given by equation 2.31. To show this, recall that the error can be written as

$$\varepsilon(t) = r(t) - \underline{W}^T \underline{X}(t) \qquad\qquad 2.24$$

substituting this result into equation 2.42 yields

$$\frac{d\underline{W}}{dt} + k\underline{\underline{\Phi}}\,\underline{W} = k\underline{S}$$
$$2.43$$

Setting $d\underline{W}/dt = 0$, the steady-state weight values $\underline{W}_{ss}$ are given by[31]

$$\underline{W}_{ss} = \underline{\underline{\Phi}}^{-1}\underline{S} \qquad\qquad 2.44$$

in agreement with the expression for the optimum weights given by equation 2.31.

The effects of dropping the expectation operator in the LMS algorithm means that the feedback constant k must be chosen carefully. Too large of k results in the weight values possibly overshooting the error surface minima and not converging, and too small of k produces an impractically long convergence time. The convergence behavior of the LMS algorithm is related to the eigenvalues of the correlation matrix $\underline{\underline{\Phi}}$, which depend upon signal power, the number of signals, signal AOAs, and the number of adaptive weights. The convergence behavior is most straightforwardly demonstrated by examining the temporal evolution of the weight vector as given in equation 2.43. The transient solution of equation 2.43 is a sum of decaying exponentials[30] which can be written in the form of

$$\underline{W}(t) = \sum_{j=1}^{N} \underline{C}_j e^{-k\lambda_j t} + \underline{\underline{\Phi}}^{-1} \underline{S} \qquad 2.45$$

where the λ_j are the eigenvalues of the correlation matrix $\underline{\underline{\Phi}}$, and the *jth* time constant is given by

$$\tau_j = \frac{1}{k\lambda_j} \qquad 2.46$$

The $\underline{C}_j$ are constants, and are determined by the initial weight values. The expression for the time constant given in equation 2.46 demonstrates the important result that the convergence time of the LMS array is inversely proportional to feedback gain. Because of the inevitable spread in eigenvalues, there are many possible choices for k. Widrow et al.[1] have shown that convergence is assured when k is chosen such that

$$0 < k < \frac{1}{\lambda_{max}} \qquad 2.47$$

where λ_{max} is the largest eigenvalue of the correlation matrix $\underline{\underline{\Phi}}$. When there is a wide range of signal powers incident upon the array, it can be difficult to choose a value for the feedback constant k. The possibility of having eigenvalues equal to zero, resulting

in a singular covariance matrix, is generally not a concern in any real system because thermal noise will be present.

2.2.3 Narrowband Implementation of the Widrow-Hopf LMS Algorithm

The expression given by equation 2.42 describing the gradient descent rule can be implemented using a feedback loop as shown in figure 2.6, where one such loop is required for both quadrature components of each weight. By having a single weight as shown in the figure, the loop is by definition narrowband. However, as shown in the following section this simple loop forms the building block for the broadband implementation. The figure is shown with the unprocessed array output $x_n(t)$ for the *nth* array element expressed as the sum of a desired signal $D_n(t)$ and an interference term $U_n(t)$. The output of the processor is then $y_n(t) = x_n(t)w_n$. The feedback loop, and the evolution of the single weight can be viewed as a single component of the weight vector given in equation 2.42. Thus the discrete weight will evolve according to

$$\frac{dw_n}{dt} = 2kx_n(t)\varepsilon(t)$$

2.48

The feedback loop is often referred to as a correlation cancellation loop, because the loop effectively takes the product of x and ε and integrates the result, while reducing the error, i.e. cancelling out the undesired signal component from the processor output. The time integrated correlation for the *nth*, single adaptive weight can be written as the integral of equation 2.48,

$$w_n = 2k \int_{-\infty}^{t} x_n(\eta)\varepsilon(\eta)dr$$

2.49

The steady-state weight can be obtained from equation 2.49 by letting $t \to \infty$. Substituting in the expression for the error, the steady-state weight is given by

$$w_{n_{ss}} = 2k \int_{-\infty}^{\infty} x_n(\eta)[r(\eta) - wx_n(\eta)]d\eta$$

2.50

26
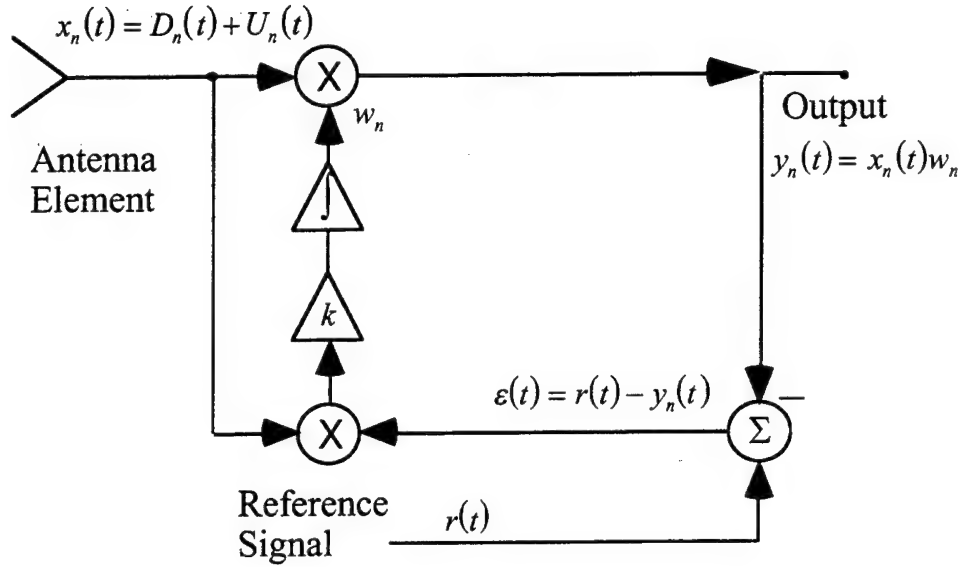
Figure 2.6. Correlation cancellation loop implements the gradient descent algorithm.

which can by assuming ergodicity, be alternatively be expressed in terms of expectation operators as

$$w_{n_{ss}} = 2kE[x_n(t)r(t)] - 2kE[x_n(t)w_{n_{ss}}x_n(t)]$$ 2.51

Under the assumption that $2k \gg 1$ (for convergence), the steady-state weight becomes

$$w_{n_{ss}} = \frac{E[x_n(t)r(t)]}{E[x_n(t)x_n(t)]}$$ 2.52

which is seen to be identical to equation 2.44, but here there is only one element in $\underline{\underline{\Phi}}$ and $\underline{S}$.

2.2.4 Broadband Implementation of the Widrow-Hopf LMS Algorithm

This analysis of the time evolution of a single adaptive weight can be extended to the more general, true-time delay array processing architecture shown in figure 2.7, and that the processor of figure 2.7 will produce an array output $y(t)$ which is strongly correlated with the input reference signal $r(t)$. It will also be shown that the expression for the optimum weight values is very similar to that derived in Section 2.2.1.

27
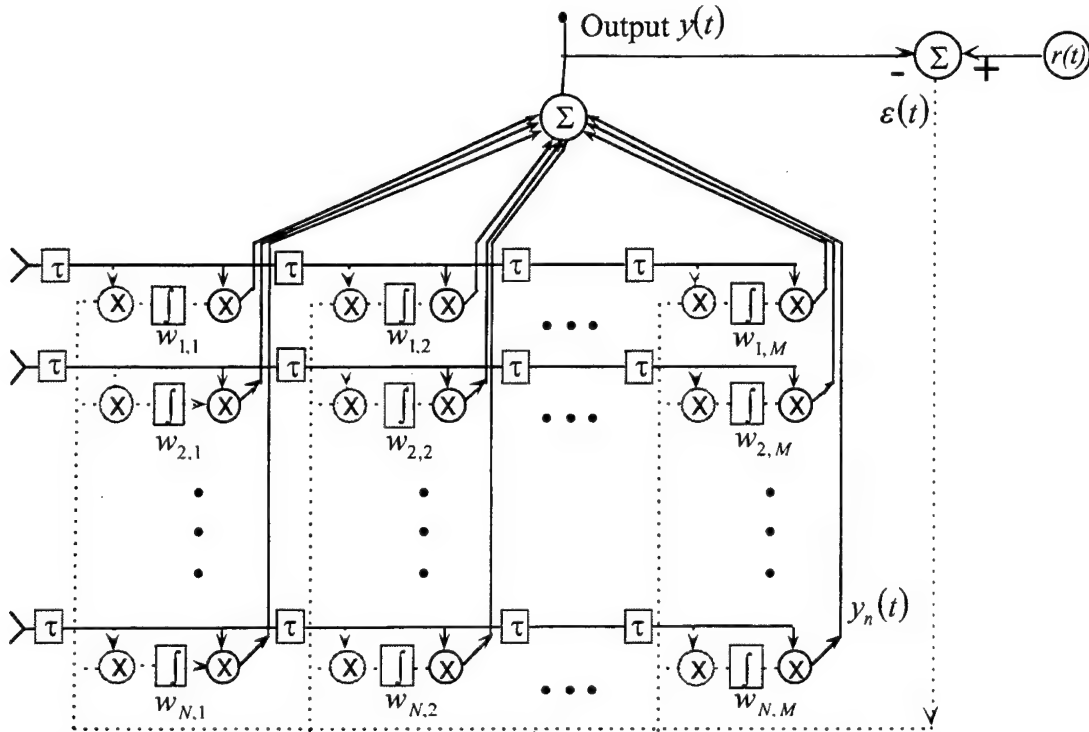
Figure 2.7. Tapped-delay line phased-array implementation of LMS architecture.

Referring to figure 2.7, each of the N array elements, has an M element tapped delay line behind it, where each delay is separated by a temporal delay of τ and $\tau = 1/B$, for a signal bandwidth of B. As shown in figure 2.7, each weight is proportional to the time integration between the feedback error term, and a delayed version of the input signal. Deriving the optimum weights begins by proceeding as in Section 2.2.1, where the weight vector will now be increased from an N element long vector to an NxM element long vector[25],

$$\underline{W} = \left[w_1, w_2, \ldots w_{NM} \right]^T .$$

2.53

Similarly the signal vector will also be an NxM element long vector, given by

$$\underline{X}(t) = \left[x_1(t), x_2(t), \ldots x_{NM}(t) \right]^T$$

2.54

where the signal from the *nth* element contains a desired signal $D(t)$ and an interference term $U(t)$ as in equation 2.18, again assumed to be zero-mean, random

28

processes which are uncorrelated with each other. The processed antenna output can then be written as

$$y(t) = \underline{X}^T(t)\underline{W} = \underline{W}^T \underline{X}(t).$$ 2.55

Again choosing the sum-square error between the array and a reference signal $r(t)$ as processing performance metric, $\varepsilon(t) = r(t) - y(t)$, an expression identical in form to equation 2.24 is obtained for the squared-error,

$$E[\varepsilon^2(t)] = E[r^2(t)] - 2\underline{W}^T \underline{S} + \underline{W}^T \underline{\underline{\Phi}} \underline{W}.$$ 2.56

where as in section 2.2.1,

$$\underline{\underline{\Phi}} = E[\underline{X}(t)\underline{X}^T(t)]$$ 2.57

and

$$\underline{S} = E[\underline{X}(t)r(t)].$$ 2.58

Taking the gradient with respect to $\underline{W}$ of equation 2.56, yields,

$$\nabla_W \{ E[r^2(t)] - 2\underline{W}^T \underline{S} + \underline{W}^T \underline{\underline{\Phi}} \underline{W} \} = -2\underline{S} + 2\underline{\underline{\Phi}} \underline{W} = 0.$$ 2.59

with the optimum weight vector given by

$$\underline{W}_{opt} = \underline{\underline{\Phi}}^{-1} \underline{S}.$$ 2.60

which is identical in form to result of Section 2.2.1, in equation 2.31.

Expansion of the expression for the array output $y(t)$, given by equation 2.55 yields

$$y(t) = \underline{X}^T(t)\underline{W} = [x_1(t), x_2(t), \ldots x_{NM}(t)] \cdot [w_1, w_2, \ldots w_{NM}]^T$$ 2.61

which can also be written in terms of partitioned vectors such that

$$y(t) = [\underline{X}_1(t) \mid \underline{X}_2(t) \mid \ldots \underline{X}_N(t)] \cdot [\underline{W}_1 \mid \underline{W}_2 \mid \ldots \underline{W}_N]^T$$ 2.62

where the components of the partioned vectors of length M are given by

$$\underline{X}_n(t) = \left[x_1(t-\tau), x_2(t-2\tau), \ldots x_M(t-m\tau) \right]^T \qquad \qquad 2.63$$

for the received signal vector, and the unique time delay between samples has now been indicated. The partitioned weight vectors are given by

$$\underline{W}_1 = \left[w_1, w_2, \ldots w_M \right]^T \qquad \qquad 2.64$$

The individual partitions as chosen correspond to signal and weight values for a given element n of the array. It follows that the array output can be written as

$$
\begin{aligned}
y(t) &= \underline{X}_1^T(t)\underline{W}_1 + \underline{X}_2^T(t)\underline{W}_2 + \ldots + \underline{X}_N^T(t)\underline{W}_N \\
&= \sum_{n=1}^{N} \underline{X}_n^T(t)\underline{W}_n \\
&= \sum_{n=1}^{N}\sum_{m=1}^{M} x_n(t)w_{nm} \\
&= \sum_{n=1}^{N}\sum_{m=1}^{M} x_n(t-m\tau)w_{nm}
\end{aligned}
\qquad \qquad 2.65
$$

which is clearly the sum of all of the delayed and weighted output taps in the array. The temporal correlation for the n-mth weight is also a discrete function of delay, $m\tau$, which allows the $nmth$ weight to be expressed as

$$w_{nm} = \int_{-\infty}^{t} x_n(\eta - m\tau)\varepsilon(\eta)d\eta. \qquad \qquad 2.66$$

Substituting this expression for w_{nm} into equation 2.65, yields an expression for the total array output given by

$$y(t) = \sum_{n=1}^{N}\sum_{m=1}^{M} x_n(t-m\tau)w_{nm} = \sum_{n=1}^{N}\sum_{m=1}^{M} x_n(t-m\tau)\int_{-\infty}^{t} x_n(\eta - m\tau)\varepsilon(\eta)d\eta \qquad 2.67$$

This expression ellucidates the adaptive process in terms of sums of products of time-integrated correlations and delayed ouputs, which can also be viewed as a convolution process between the adaptive weights and the antenna outputs.

2.2.5 Constrained Array Processing and the Howells-Applebaum Algorithm

Another method of weight calculation is based on the concept of a constraint. A constraint is often introduced in the form of a steering vector corresponding to the AOA of the desired signal. Thus, where the Widrow-Hopf algorithm used *a priori* temporal information in the form of a reference signal, the constrained approach makes use of spatial information. For example, a steering vector for a narrowband desired signal source $D(t)$, in direction θ can be written as

$$\underline{U}^T = \left[1, e^{i\Delta\phi}, e^{i2\Delta\phi} \dots e^{i(N-1)\Delta\phi}\right] \qquad 2.68$$

where $\Delta\phi$ is the interelement phase shift given by equation 2.3.

To maximize the response of the antenna in the direction of the signal $D(t)$, the system is constrained such that the array output from this signal is unity, while the interference power is minimized. For a given steering vector $\underline{U}$, the weight vector can be constrained according to

$$\underline{W}^T \underline{U} = 1 \qquad 2.69$$

The Lagrange multiplier method can be used to minimize the average output power subject to the constraint given by equation 2.69, which allows a direct calculation of the optimum weights. The method of Lagrange requires defining a cost function, $H(\underline{W})$, of the form

$$H(\underline{W}) = P + \lambda\left(1 - \underline{W}^T \underline{U}\right) \qquad 2.70$$

where λ is an arbitrary constant, and the average power, P, is defined as the expected value of the array output,

$$P = E\left[\underline{Y}\underline{Y}^*\right] = \underline{W}^T \underline{\underline{\Phi}}\,\underline{W} \qquad 2.71$$

31

Where $\underline{\underline{\Phi}}$ is the received signal correlation matrix defined as in equation 2.25. Differentiating equation 2.70 with respect to $\underline{W}$ and equating to zero to find the extremum (which is a minimum), yields the following expression for the optimum weight vector $\underline{W}_{opt}$,

$$\underline{W}_{opt} = \frac{\underline{\underline{\Phi}}^{-1}\underline{U}^*}{\underline{U}^T\underline{\underline{\Phi}}^{-1}\underline{U}^*} \qquad\qquad 2.72$$

and corresponding value for the array output power of

$$P_{opt} = \frac{1}{\underline{U}^T\underline{\underline{\Phi}}^{-1}\underline{U}^*} \qquad\qquad 2.73$$

The optimum weight vector given by equation 2.72 is seen to be the product of the inverse of the signal correlation matrix and the steering vector, normalized by the array output power.

The concept of a constraint forms the basis for the Howells-Applebaum adaptive array[31,3], and as with the LMS algorithm, the Howells-Applebaum array converges to a solution which maximizes the SINR of the array. The SINR for a desired narrowband signal $D(t)$ can be written as[31]

$$SINR = E\left[|D|^2\right]\frac{\left|\underline{W}^T\underline{U}_D\right|}{\underline{W}^\dagger\underline{\underline{\Phi}}_{NN}\underline{W}} \qquad\qquad 2.74$$

with an optimum weight vector which is given by

$$\underline{W}_{opt} = \mu\underline{\underline{\Phi}}_{NN}^{-1}\underline{U}_D^* \qquad\qquad 2.75$$

where $\underline{\underline{\Phi}}_{NN}$ is the correlation matrix of the undesired interference and noise terms only, $\underline{U}_d$ is the steering vector, and μ is an abitrary constant. The derivation of equations 2.74 and 2.75 is lengthy and will not be included here. A feedback loop for a single weight which implements the Howells-Applebaum algorithm is shown in figure 2.8, and it differs from the LMS loop of figure 2.6 primarily in the location of the

32
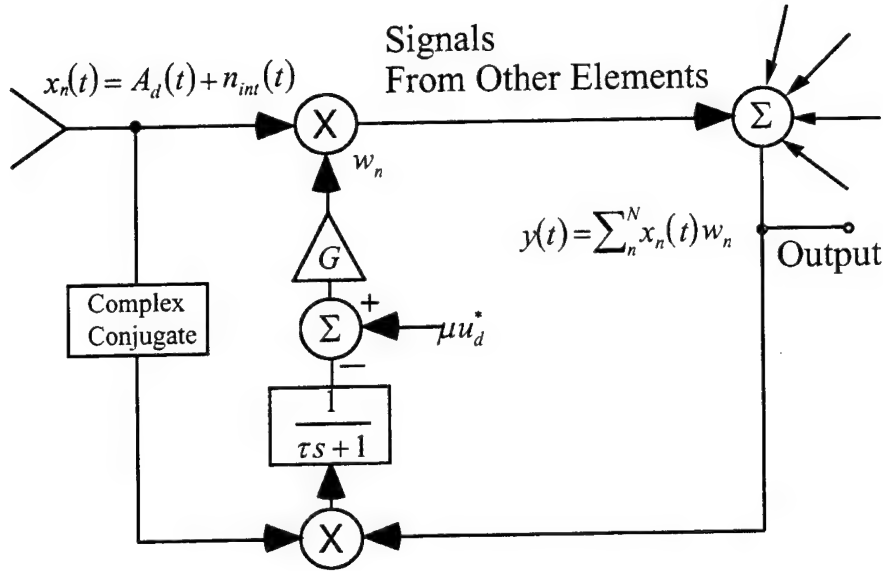
Figure 2.8. The narrowband Howells-Applebaum feedback loop.

differencing node. As shown in the figure, the error is the difference between the product of the element output $x^*(t)$ and the processed array output $y(t)$, and the desired signal steering vector element μu_D.

To include all of the adaptive loops of the array, the weight update rule can be expressed as

$$\frac{\tau}{G}\frac{d\underline{W}}{dt}+\left[\frac{1}{G}\underline{\underline{I}}+\underline{\underline{\Phi}}\right]\underline{W}=\mu\underline{U}_d^*$$

2.76

where G is the feedback gain. The steady-state weight values are thus

$$\underline{W}_{ss}=\left[\frac{1}{G}\underline{\underline{I}}+\underline{\underline{\Phi}}\right]^{-1}\mu\underline{U}_d^*$$

2.77

which for sufficiently large gain G becomes approximately

$$\underline{W}_{ss}\approx\mu\underline{\underline{\Phi}}^{-1}\underline{U}_d^*$$

2.78

While this set of steady-state weights differs from equation 2.75 in that the signal correlation matrix is $\underline{\underline{\Phi}}$ instead of $\underline{\underline{\Phi}}_{NN}$, they are actually related to each other by a

33

scalar[31], and are approximately the same when the interference is much stronger than the desired signal. Comparing equation 2.76 to the previously derived Widrow-Hopf LMS relation given by equation 2.43,

$$\frac{d\underline{W}}{dt} + k\underline{\underline{\Phi}}\,\underline{W} = k\underline{S}$$

2.43

it is clear that these two algorithms are quite similar, and are in fact identical if $\mu\underline{U}_d^* = \underline{S}$. The choice between the algorithms is determined by whether the *a priori* information is spatial or temporal.

2.2.6 The Sidelobe Canceller

One of the simplest forms of an adaptive array is the sidelobe canceller[4], used to remove interference incident upon the sidelobes of an antenna. The sidelobe canceller is shown in figure 2.9, and is typically composed of a highly directional primary antenna element and either one or a group of omni-directional, auxillary elements whose weighted outputs are first summed together, and then subtracted from the primary element output. The primary element is configured to form a beam in the direction of the desired signal, and the auxillary elements adaptively construct an antenna pattern in the direction of interfering sources. The adaptive scheme is based on minimizing the error between the primary and auxillary outputs, which is actually the same as minimizing the total array output power, subject to the constraint of the primary antenna. The primary output can be considered as the reference signal, while the auxillary output is that of an adaptive filter, configured as a matched filter for the incident interference. Because the primary element is pointed in the direction of the desired signal, i.e. constrained, the sidelobe canceller is in fact a simplified implementation of the Howells-Applebaum array[31].

The sidelobe canceller reduces the contributions of unwanted interference sources which are incident on the primary antenna element pattern's sidelobes by
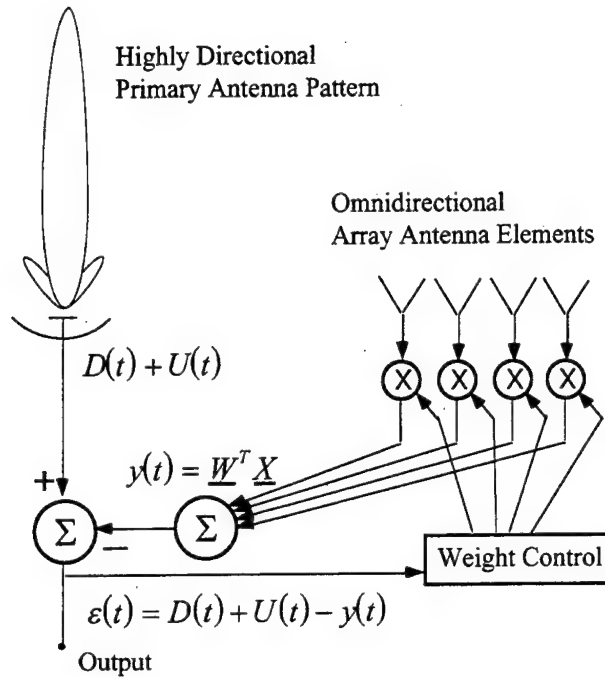
Figure 2.9. Sidelobe canceller removes interference incident on primary antenna sidelobes.

essentially taking the difference between the desired and interference antenna patterns. This is shown conceptually in figure 2.10, where the auxillary beam pattern is pointed towards the interference source corresponding to an incident direction of $\overline{k}_{int}$, and has a scaled amplitude such that, when subtracted from the primary antenna pattern signal pointed at the desired signal in direction $\overline{k}_d$, the contribution of the inteference signal will be reduced in the output. Adaptively minimizing the difference between these two antenna patterns is analogous to redistributing the nulls of the antenna pattern in angle-space towards the directions of the interfering sources.

It can be shown that the highest SNR is obtained when the total output power of the sidelobe canceller is minimized. As shown in figure 2.9, the auxillary output $y(t)$ is represented as the inner product of the input signal vector, $\underline{X}(t)$, and the weight vector $\underline{W}$. The signals making up $\underline{X}(t)$ are assumed to be inteference sources only, where the interference is correlated between array elements (thermal noise is neglected here). This assumption of only interference power contained in the array elements is based on the

35
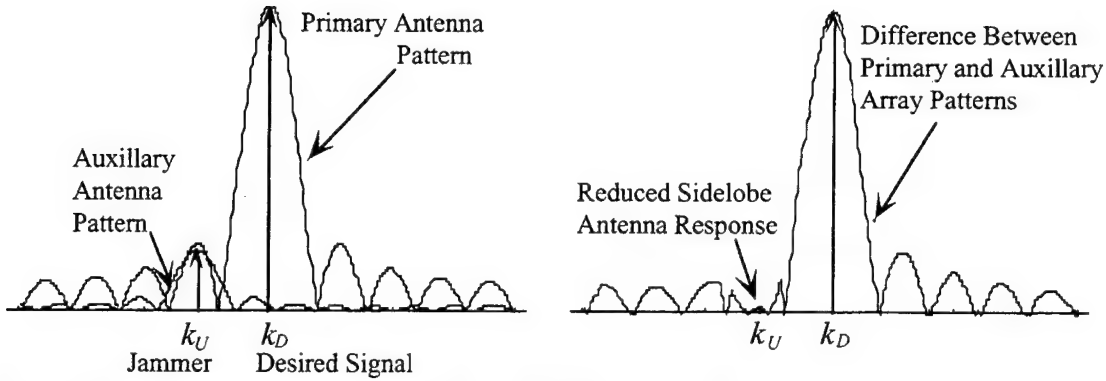
Figure 2.10. Conceptual represenation of sidelobe cancellation.

fact that usually the desired signal is much weaker than the interference, and that the omnidirectional acceptance pattern of the auxilliary array elements causes very little desired signal to be present in the received power from these elements. The signal output of the primary element is the sum of the desired signal $D(t)$, and the interference source terms designated as $U(t)$. The signals $D(t)$ and $U(t)$ are uncorrelated with each other, but $U(t)$ is correlated with the interference sources of $y(t)$ because they are from the same source. Note here that the processer output is the difference, or error, between the primary and auxillary antenna components. This error is given by

$$\varepsilon(t) = D(t) + U(t) - y(t) \qquad\qquad 2.79$$

The weights are adjusted so as to minimize the expectation value of the squared error, and from equation 2.79, the expectation of the squared error is

$$E\left[\varepsilon^2(t)\right] = E\left[D^2(t)\right] + E\left[\left[U(t) - y(t)\right]^2\right] + 2E\left[D(t)\left[U(t) - y(t)\right]\right] \qquad 2.80$$

The cross-product term $2D(t)\left[U(t) - y(t)\right]$ goes to zero because $D(t)$ is uncorrelated with both $U(t)$ and $y(t)$, resulting in

$$E\left[\varepsilon^2(t)\right] = E\left[D^2(t)\right] + E\left[\left[U(t) - y(t)\right]^2\right] \qquad\qquad 2.81$$

36

In order to minimize the residual error, it must be that the last term of equation 2.81 must be minimized, because $D(t)$ is independent of $\underline{W}$, and there would be no SNR advantage to minimizing $D(t)$. Therefore,

$$E\left[\varepsilon_{min}^2\right] = E\left[D^2(t)\right] + E\left[\left(U(t) - y\right)_{min}^2\right] \qquad 2.82$$

Equation 2.82 yields the intuitive result that the error will be minimized when the auxillary output $y(t)$ is the best possible replica of the interference term $U(t)$. The fact that the SNR is at a maximum when the total error is minimized is made evident by rewriting equation 2.79 as

$$\varepsilon(t) - D(t) = U(t) - y(t) \qquad 2.83$$

Thus, minimizing $U(t) - y(t)$ is equivalent to minimizing the difference between the error and the desired signal, and therefore the minimum value of the error will be

$$E\left[\varepsilon_{min}^2(t)\right] = E\left[D^2(t)\right] \qquad 2.84$$

The result of equation 2.84 states that the minimum possible error is in fact the desired signal, and correspondingly the SNR will be a maximum when this occurs.

It is important to point out that the implementation of the sidelobe canceller is based on two *a priori* pieces of information; the direction of the desired signal is known, and the strength of the desired signal is small compared to the integrated noise and interference power. The known signal direction allows the primary antenna to be pointed in the direction of the desired signal, and the weak signal assumption insures that the desired signal contribution from the auxillary elements is minimal. If the desired signal is strong enough, with a significant contribution to the power received in the auxillary elements, the sidelobe canceller will null this signal as well.

2.3 Optically Implemented Phased-Array Processing Algorithm

The optically implemented phased-array processor developed in this thesis uses a modified version of the LMS algorithm to perform simultaneous beam formation and jammer cancellation. The intention of the algorithm is to provide a practical means of processing signals from very large phased-arrays, and is in part met by dramatically decreasing the number of required delay lines from N, where N is the number of array elements, to only 2. Optical implementation of conventional (tapped) delay line structures for array processing as shown in figure 2.4 is often done with multichannel acousto-optic (AO) devices, one transducer per each antenna element, and therefore the number of AO channels required is equal to the number of antenna array elements. As a result, the limitations of multichannel AO technology[32] typically limits the number of elements which can be processed to at most 32. In contrast, the delay line reduced, optically implemented LMS algorithm presented in this thesis, uses the inherent delay available in optical resonator cavities to achieve the required time delays necessary for wideband phased-array processing. This section demonstrates the equivalence between the adaptive weights of the optically implemented, modified LMS algorithm, and the weights used in the traditional tapped-delay line architecture presented in Section 2.2.4. It is important to point out how the modified algorithm closely resembles the Widrow-Hopf and Applebaum algorithms; the adaptive weights which are formed and the array output are equivalent, and the modified LMS algorithm produces the required number of DOFs to perform broadband, spatial-temporal processing for phased-arrays. However, there are important differences which are addressed at the end of this section.

A schematic diagram of the modified LMS algorithm is shown in figure 2.11. The set of N tapped delay lines on the antenna elements that is used to produce the relative delayed output taps of the Widrow-Hopf algorithm of figure 2.7, have been replaced by a single tapped-delay line in the feedback, and distributed to all the elements in parallel. As in figure 2.7, the time integrated weights are calculated between the

incoming array signals and the relatively delayed feedback error signal. The weight w_{nm} corresponds to the weight for the *nth* antenna element, at the *mth* delay, where now *m* corresponds to the relative delay of the feedback signal. The delay is implemented with a single AO device, and the weights are represented by the diffraction efficiencies of the time-integrated holographic gratings in the PRC. The products of the incoming unprocessed array signals and the weights at a particular delay are added, and these sums are Fourier transformed in space across delay value. Each output of the spatial Fourier transform is passed through a bandpass filter, and the outputs of the bandpass filters are summed to produce an output which is correlated with the reference signal $r(t)$. The center frequency of the bandpass filters varies linearly across the filter array, and tuned so as to pass the signal which would have appeared at that position had instead the tapped delay line been used as the Fourier transform input. The Fourier transform operation is done simply in the optical domain with a lens, and the array of bandpass filters is obtained from a tilted or wedged Fabry-Perot resonator structure as discussed in more detail in Chapter 8.

The adaptive network of figure 2.11 is shown being used as a jammer canceller. The delay, τ_e, that the reference signal passes through serves to decorrelate desired signals, which are assumed to be of broader bandwidth than the jamming sources. In this manner, while the broadband signals are present in the feedback signal, because they are delayed with respect to the incoming signals, they are decorrelated with the desired signals at the input of the array and do not build up appreciable weights. This suggests τ_e should be chosen such that $\tau_e \gg 1/B$, where B is the desired signal bandwidth.

Using an AO cell for the feedback signal delay line results in the discrete weights of equation 2.66 becoming a continuous function of delay, where the delay is a proportional to the spatial variable ξ along the AO aperture, divided by the acoustic

Figure 2.11. Schematic of optically implemented LMS algorithm.

velocity V of the AO cell. These continuous adaptive weights can be described by the time integral[33]

$$w_n^*(\xi) = \int_{-\infty}^{t} x_n^*(t_2)\varepsilon(t_2 - \xi/V)dt_2 \qquad 2.85$$

where it is to be emphasized that the delay is now on the feedback error signal, $\varepsilon(\eta - \xi/V)$ in contrast to the Widrow-Hopf alogorithm. These weights are multiplied by the instantaneous output signals from the array, and summed (vertically in figure 2.11) over the N antenna elements to give

$$y(t,\xi) = \sum_{n=1}^{N} x_n(t)w_n^*(\xi) \qquad 2.86$$

This sum is Fourier transformed spatially across ξ giving

40

$$\tilde{y}(t,u) = \int_0^L y(t,\xi)e^{iu\xi}d\xi \qquad 2.87$$

The total array output is then the integral of the bandpass filtered versions of these signals $\tilde{y}(t,u)$ over the output variable u of the spatial Fourier transform,

$$y(t) = \int_{M/L}^{2M/L} \int_0^T \tilde{y}(t-t_3,u)e^{iuVt_3}dt_3du \qquad 2.88$$

A temporal filter with a linearly increasing center frequency $\omega = uV$ in space, scaled by the acoustic velocity V and a constant bandwidth $B = 1/T$ has been implemented, and the limits of integration of M/L to $2M/L$ define an octave bandwidth for this system, where the spatial aperture of the Bragg cell is L and M is the time-bandwidth product. Substituting equations 2.85 through 2.87 into equation 2.88, and interchanging orders of summation and integration, it follows that

$$
\begin{aligned}
y(t) &= \int_{M/L}^{2M/L} \int_0^T \int_0^L \sum_{n=1}^N x_n(t-t_3) \int_{-\infty}^{t-t_3} x_n^*(t_2)\varepsilon(t_2-\xi/V)dt_2 e^{iu\xi}d\xi e^{iuVt_3}dt_3du \\
&= \sum_{n=1}^N \int_0^T dt_3 x_n(t-t_3) \int_{-\infty}^{t-t_3} dt_1 \int_0^L d\xi x_n^*(t-t_3)\varepsilon(t_1-t_3-\xi/V) \int_{M/L}^{2M/L} due^{iu\xi}e^{iuVt_3} \\
&= \sum_{n=1}^N \int_0^T dt_3 x_n(t-t_3) \int_{-\infty}^{t-t_3} dt_1 x_n^*(t-t_3) \times \\
&\qquad \int_0^L d\xi \frac{M}{L} e^{i(\xi+Vt_3)3M/2L} \text{sinc}\left[\frac{M}{2L}(\xi+Vt_3)\right]\varepsilon(t_1-t_3-\xi/V)
\end{aligned}
\qquad 2.89
$$

where $t_1 - t_3 = t_2$, and the integral over u has been performed. It has also been assumed that that the error signal has a finite bandwidth which is contained within the bandwidth of the sinc function, which is taken to be the same as the input bandwidth of the processor. This assumption allows the convolution of $e^{i(\xi+Vt_3)3M/2L}\varepsilon(t_1-t_3-\xi/V)$ with

$\mathrm{sinc}\left[\dfrac{M}{2L}(\xi + Vt_3)\right]$ to be treated as a convolution with the delta function $\delta\big((\xi + Vt_3)M/2L\big)$, giving

$$y(t) = \sum_{n=1}^{N} \int_0^T x_n(t - t_3) \int_{-\infty}^{t} x_n^*(t - t_3)\varepsilon(t_1)\,dt_3 dt_1 \qquad\qquad 2.90$$

This result is equivalent to that of Widrow-Hopf algorithm given by equation 2.67, but here the delay is continuous. Recalling that the total delay line interval is $T = L/V$, and allowing the delay line to become a discrete function of position, equation 2.90 becomes

$$y(t) = \sum_{n=1}^{N}\sum_{m=1}^{M} x_n(t - m\tau) \int_{-\infty}^{t} x_n^*(t_1 - m\tau)\varepsilon(t_1)\,dt_1 \qquad\qquad 2.91$$

which agrees identically with the expression for the true-time delay output given by the Widrow-Hopf algorithm in Section 2.2.4.

The processor shown in figure 2.11 uses a temporal reference signal $r(t)$ to correlate with the incoming signals. As discussed in more detail in later chapters, this reference signal is actually derived from the output of the beam-forming processor which steers the main-beam of the antenna towards the desired signal. The complete algorithmic structure is shown in figure 2.12, where the structure at the left performs jammer cancellation, and the structure on the right is a similar beam-forming processor. The details of the beam-forming and jammer-nulling processors are reserved for Chapters 6 and 7 respectively, however it is worthwhile to discuss the overall, combined functionality between them here. As shown in figure 2.12, the beam-forming processor uses a temporal reference signal, $r_s(t)$, to time integrate weights such that the main-beam of the antenna is steered towards the desired signal. In this case the reference signal $r_s(t)$ is well correlated with the desired signal. The summed output from the beam-forming processor becomes the reference signal input $r(t)$ to the
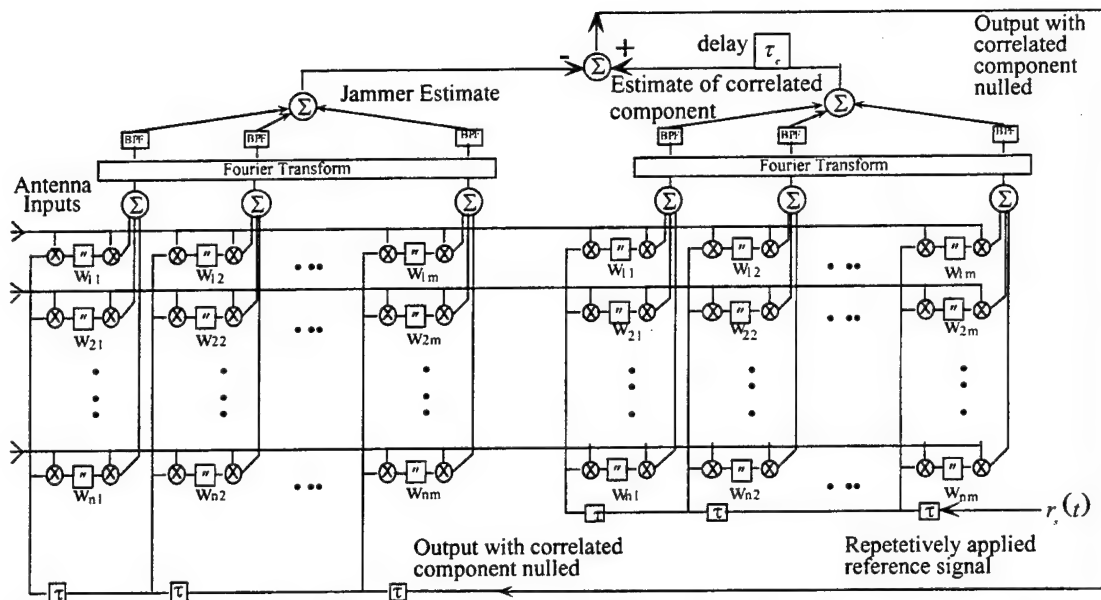
Figure 2.12. Schematic of combined optically implemented jammer-nulling and beam-forming processors.

jammer-nulling processor. Due to the decorrelation delay τ_e and the assumption that desired signals are of broader bandwidth than jammers, the reference signal $r(t)$ in the jammer-nulling processor is effectively composed only of interference terms; the broadband desired components presumably pass through the jammer-nulling processor unaffected, extracted at the feedback error output, which is also the net processor output. This is a significant departure from the Widrow-Hopf algorithm where the reference signal is the desired signal. Directly coupled with this alternative strategy of using the interference as a reference signal is the fact that the final processed array output is the feedback error term of the jammer-nulling processor. The adaptive weights in the jammer-nulling processor serve to maximize the jammer-nulling processor output for the jammer as with traditional LMS, but here the output is the error signal, the difference between the beam-forming and jammer-nulling processors.

It is important to note that the beam-forming processor is open-loop, there is no error driven feedback. It is adaptive in the sense that it will find and track the desired signal over angle space, and it does provide the spatial processing gain associated with

the array. However, it it is not adaptive in the sense of maximizing the SINR of the array output. The full adaptive functionality of beam-steering and interference cancellation is achieved when the two processors are combined. In this sense the optically implemented algorithm is a great deal like a sidelobe canceller; a primary antenna is pointed towards the desired signal (by the beam-forming processor) eeven though its AOA is unknown,.and a second set of adaptive weights are constructed to minimize interference (by the jammer-nulling processor), and the final array output is the difference between the two constructed antenna functions. Distinct advantages of this modified implementation over traditional sidelobe cancellers is that in addition to the dramatic reduction in the number of required delay lines, the main-beam-former is adaptive and not just a single element, and also a strong desired signal will not null itself out. The details of the processor operations which ellucidate the adavantages of this processing method over more traditional processing methods are given in following chapters.

References

[1]   B. Widrow and S.D. Stearns, *Adaptive Signal Processing*. Prentice Hall, 1985.

[2]   B. Widrow, "Adaptive noise canceling: principles and applications," Proc. IEEE **63**, no. 12, 1692-1719 Dec (1975).

[3]   S.P. Applebaum, "Adaptive arrays," IEEE Trans. Ant. Prop. **AP-24**, 585-598 (1976).

[4]   P.W. Howells, "Explorations in fixed and adaptive resolution at GE and SURC," IEEE Trans. Ant., Prop. **AP-24**, no. 5, 575-584 Sept. (1976).

[5]   J. Capon, R. J. Greenfield and R.J. Kolker, "Multi-dimensional maximum likelihood processing of a large aperture seismic array," Proc. IEEE **55**, 192-211 Feb. (1967).

[6]   L.J. Griffiths, "A comparison of multi-dimensional Weiner and maximum-likelihood filters for antenna arrays," Proc. IEEE **55**, 2045-2047 Nov. (1967).

[7]   R.J. Mailloux, "Phased array theory and technology," Proc. IEEE **70**, no. 3, 246-293 March (1982).

[8]   B. D. Steinberg, and H. M. Subbaram, *Microwave Imaging Techniques.* John Wiley & Sons, 1991.

[9]   M.I. Skolnik, *Introduction to Radar Systems.* (McGraw-Hill, 1962), chap. 7, pp. 294-329.

[10]   D. H. Johnson and D.E. Dudgeon, *Array Signal Processing, Concepts and Techniques.* (Prentice Hall, 1993), chap. 3, pp. 84-106.

[11]   C.L. Dolph, "A current distribution for broadside arrays which optimizes the relationship between beamwidth and sidelobe level," Proc. IRE **34**, 335-345 (1946).

[12]   T.T. Taylor, "Design of line source antennas for narrow beamwidth and low sidelobes," IEEE Trans. Ant. Prop. **AP-3**, 16-28 (1955).

[13]   T.T. Taylor, "Design of circular apertures for narrow beamwidth and low sidelobes," IRE Trans. Ant. Prop. **AP-8**, 17-22 (1960).

[14]   H. W. Yen, M. Wechsberg, J. J. Lee, and A. E. Popa, "EHF fiber-optic based antenna array," in *Optoelectronic Signal Processing for Phased-Array Antennas,* SPIE **886**, 218-222 (1988).

[15]   A. Goutzoulis and K. Davies, "Compressive 2-D delay line architecture for time steering of phased-array antennas," in *Optoelectronic Signal Processing for Phased-Array Antennas II,* SPIE **1217**, 270-283 (1990).

[16]   A. P. Goutzoulis, D. K. Davies and J.M. Zomp, "Hybrid electronic fiber optic wavelength-multiplexed system for true time-delay steering of phased array antennas," Opt. Eng. **31**, no. 11, 2312-2322 Nov. (1992).

[17]   D. Dolfi, F. Michel-Gabriel, S. Bann, and J. P. Huignard, "Two-dimensional optical architecture for time-delay beam forming in a phased-array antenna," Opt. Lett. **16**, no. 4, 255-257 Feb. (1991).

[18]   N.A. Riza, "Transmit-receive time-delay beam-forming optical architecture for phased-array antennas," Appl. Opt. **30**, no. 32, 4594-95 Nov. (1991).

[19]   R. D. Esman, M. Y. Frankel, J. L. Dexter, L. Goldberg, M. G. Parent, D. Stilwell, and D. G. Cooper, "Fiber-optic prism true time-delay antenna feed," IEEE Phot. Tech. Lett. **5**, no. 11, 1347-1349 Nov. (1993).

[20]   A. Molony, C. Edge and I. Bennion, "Fibre grating time delay element for phased array antennas," Elec. Lett. **31**, no. 17, 1485-1486 Aug. (1995).

[21]   E. N. Toughlian and H. Zmuda, "Variable time-delay system for broadband phased array and other transversal filtering applications," Opt. Eng. **32**, no. 3, 613-617 March (1993).

[22]   B. Widrow, P. E. Mantey, L. J. Griffiths, and B. B. Goode, "Adaptive antenna systems," Proc. IEEE **55**, no. 12, 2143-2161 Dec. (1967).

[23] A. Farina, *Antenna-Based Signal Processing Techniques for Radar Systems*. (Artech House, Inc., 1992), chap. 5.

[24] B. Widrow and S.D. Stearns, *Adaptive Signal Processing*. (Prentice Hall, 1985), chap. 12.

[25] L.J. Griffiths, "A simple adaptive algorithm for real-time processing in antenna arrays," Proc. IEEE **57**, no. 10, 1696-1704 Oct. (1969).

[26] J.W.R. Griffiths, "Adaptive array processing," IEE Proc. **130**, no. 1, 3-10 Feb (1983).

[27] R.O. Schmidt, "Multiple emitter location and signal parameter estimation," IEEE Trans Ant. and Prop. **AP-34**, no. 3, 276-280 March (1986).

[28] R. Roy and T.K. K., "ESPRIT- estimation of signal parameters via rotational invariance techniques," Opt. Eng. **29**, no. 4, 296-313 April (1990).

[29] R. Kumaresan, L. L. Scharf, and A. K. Shaw, "An algorithm for pole-zero modeling," IEEE Trans. Acoust., Speech, Signal Process **34**, 637-640 (1986).

[30] R.T. Compton, *Adaptive Antennas*. (Prentice Hall , 1988), chap. 2.

[31] R. T. Compton, *Adaptive Antennas*. (Prentice Hall, 1988), chap. 3, pp. 120.

[32] D. R. Pape, P. Wasilousky and P.M. Payson, "A high performance apodized phased-array Bragg cell," in *Proc. SPIE vol. 789,* (1987).

[33] R. T. Weverka, K. Wagner and A.W. Sarto, "Photorefractive processing for large adaptive phased-arrays," Appl. Opt. **35**, no. 8, 1344-1366 March (1996).

3. Optical Processing for Adaptive Phased-Arrays

This Chapter will present a brief overview of previous work done on optical processing for adaptive phased-arrays. While much work has been done in this area, the emphasis here will be on systems and architectures which attempt to address the complex problem of real-time adaptive array processing. In particular, the emphasis will be on processors capable of adaptive interference cancellation. This Chapter will also elucidate the fact that the vast majority of the published work on optical processing of phased-arrays does not scale efficiently to very large arrays, which is a major advantage of the work presented in this thesis. In addition, a review of the published literature reveals that the work presented in this thesis is the only published work on simultaneous, real-time, adaptive beam-steering and jammer-cancellation performed to date.

3.1 Optical Adaptive Filtering Techniques

Some of the early work in optically implemented, single channel adaptive filters provided the fundamental building blocks and structures which would later be implemented into higher-dimensional adaptive array processors. Much of this early work consisted of adaptive linear prediction algorithms and correlation cancellation loop (CCL) implementations using 1-D transversal filters for adaptive interference suppression. These processors generally relied on acousto-optic Bragg cells for the wideband transversal filters, but implemented correlation and convolution operations via a wide range of methods including processing in the temporal and frequency domains using either space or time integrating architectures.

The adaptive filter demonstrated by Rhodes[1] consisted of a CCL, temporal domain structure for performing linear prediction of RF signals. The processor demonstrated linear prediction by adaptively producing an estimate, $o(t)$, of a given input RF signal, $s(t)$. Assuming that the input signal $s(t)$ consisted of a broadband

desired component and strong narrowband frequency components which are uncorrelated with the desired signal, the processing operation was based upon first performing a correlation between the difference between the estimated signal $o(t)$ and the processor input $s(t)$ to produce the set of adaptive weights, and then convolving these weights with the processor input $s(t)$ to produce the adaptive matched filter and optimize the processor output for $s(t)$. This is classic linear prediction[2], where an estimate of a signal is obtained from the weighted sum of past values. However, by changing the error term to be the difference between some reference signal $r(t)$ and the signal estimate $o(t)$, the 1-D adaptive signal canceller of the previous chapter is implemented.

The time integrated correlation operation was implemented by first using a single Bragg cell with electrical input $s(t)$, and illuminated by an optical beam electro-optically modulated by the error signal $\varepsilon(t) = s(t) - o(t)$. This provided the multiple delayed products between $s(t)$ and the error signal, given by $\varepsilon(t)s(t-x/V)$, where x is the spatial coordinate along the Bragg cell aperture and V is the acoustic velocity in the cell. An optically addressed liquid crystal light-valve (OASLM) is then used to time integrate these products to complete the correlation operation. Thus, the adaptive weight vector, $w(x)$, is a continuous function of the spatial coordinate x,

$$w(x) = \int \varepsilon(t)s(t-x/V)dt$$

3.1

The OASLM stores the weights in the form of a spatially varying charge which modulates the polarization of the reflected (readout) light off of the OASLM. Reading out the light-valve is done with a second optical beam, and the polarization state is converted to an intensity variation using a polarizer. This readout beam illuminates a second Bragg cell, whose electrical input is $s(t)$. This operation again forms the set of multiply delayed products, $w(x)s(t-x/V)$. Using a lens to spatially integrate these

48

multiple products onto a photomultiplier tube is seen to be the required convolution operation, and yields the processor output,

$$o(t) = \int w(x)s(t - x/V)dx$$ 3.2

Substituting equation 3.1 into equation 3.2 yields an expression for the processor output of

$$o(t) = \int\int \varepsilon(t)s(t - x/V)s(t - x/V)dtdx$$ 3.3

The error term is then updated in the electrical domain according to $\varepsilon(t) = s(t) - o(t)$, and the processor output ideally converges to a replica of the input signal $s(t)$, which is equivalent to driving the error term $\varepsilon(t)$ to zero. The results of the processor[1] were encouraging, but suffered from several equipment and stability related shortcomings. Architectural issues which limited performance were primarily caused by the fact that because information is carried in the processor by the light intensity, rather than amplitude, negative values cannot be represented. To accommodate this, The Bragg cells and light valve were operated on top of a DC bias, which generally introduced a loss in signal dynamic range[3].

A Fourier domain, adaptive optical processor was proposed by Vander Lugt[4], which implemented a linear prediction algorithm in the Fourier domain with a space integrating architecture using three Bragg cells. Again the basis of the adaptive signal estimation was that of a correlation and convolution operation, although the Fourier implementation allowed the two operations to be performed non-sequentially, in a 2-D folded format as discussed below.

Proceeding in like fashion to the processor discussed above, and again assuming a broadband desired signal in the presence of uncorrelated, strong, narrowband interference, the weight vector is determined from the correlation between the error signal $\varepsilon(t)$, and the processor input $s(t)$, which can be represented by[4]

$$w(\tau) = G \int_{t-T_1}^{t} \varepsilon(u)s(u-\tau)du$$

<div align="right">3.4</div>

where T_1 is the integration time of the correlation loop, G is the feedback gain, and again the error signal is the difference between the input of the processor and the calculated estimate, $\varepsilon(t) = s(t) - o(t)$. The correlated estimate is then determined from the convolutional process given by

$$o(t) = \int_{0}^{T} w(\tau)s(t-\tau)d\tau$$

<div align="right">3.5</div>

where T is the length of the Bragg cell time delay. Substituting equation 3.4 into equation 3.5 yields the processor output expressed in the time domain,

$$o(t) = G\int_{0}^{T}\int_{t-T_1}^{t} \varepsilon(u)s(u-\tau)w(\tau)s(t-\tau)dud\tau$$

<div align="right">3.6</div>

The Fourier representation of equation 3.6 can easily be obtained[4] by the convolution theorem,

$$o(t) = G\int_{-\infty}^{\infty} E_T(\omega,t)|S_T(\omega,t)|^2 e^{i\omega t} dt$$

<div align="right">3.7</div>

where $E_T(\omega,t)$ and $S_T(\omega,t)$ the instantaneous Fourier transforms of $\varepsilon(t)$ and $s(t)$ within the time aperture of the Bragg cell, T. The error signal is then updated, and at steady-state the error is driven to zero. The frequency domain representation elucidates how the estimate signal $o(t)$ evolves, in particular, the term $|S_T(\omega,t)|^2$ puts a strong weighting on the dominant spectral components of the correlated interference, and hence acts as a filter which separates the interference form the desired signal.

A simplified system schematic is shown in figure 3.1, which is essentially an interferometer between the two branches, 1 and 2. The three Bragg cells overlap in a
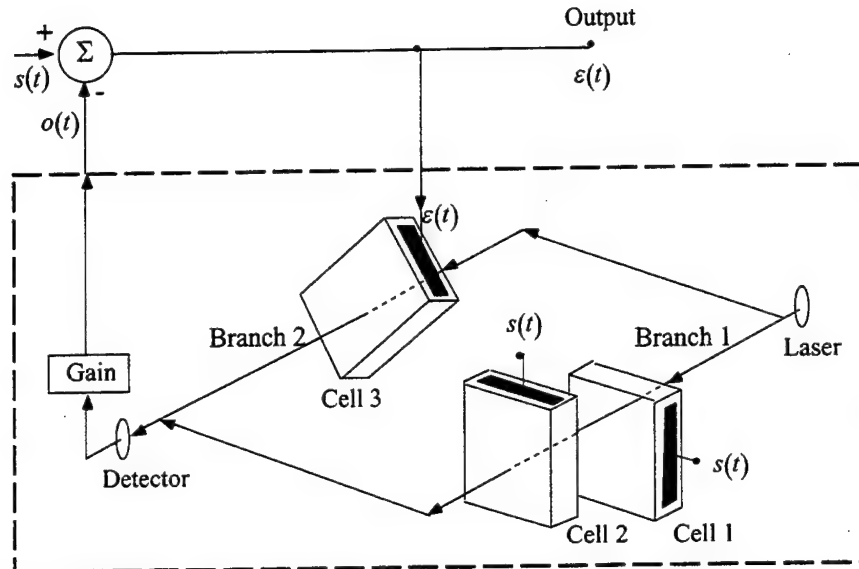
Figure 3.1. Simplified schematic of Fourier domain adaptive filter.

(a)   (b)
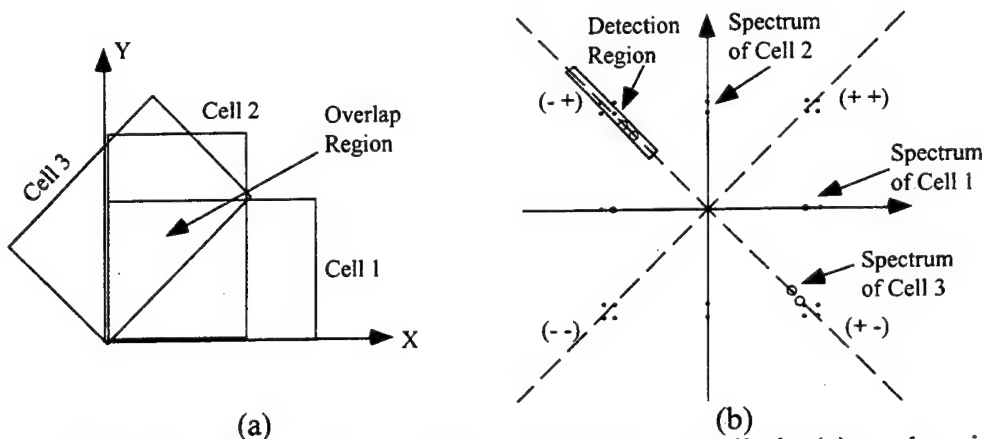
Figure 3.2. Region of spatial overlap of the three Bragg cells in (a), and region of spectral overlap in (b), showing reduced area of photodetection.

plane (external to the interferometer) as shown in figure 3.2a, and figure 3.2b shows the Fourier plane of the overlap plane, where the Fourier plane corresponds to the plane of the photodetector. As shown in the figure, the photodetected area is limited to the diagonal slice. The two orthogonal Bragg cells, both which have $s(t)$ as an input, produce the term $|S_T(\omega,t)|^2$, which then selects the interference components from the spectra of $E_T(\omega,t)$, and uses these as feedback signals in the cancellation loop. This implementation where Bragg cells 1 and 2 are given $s(t)$ as an input, and Bragg cell 3 the error signal $\varepsilon(t)$, yields the same output as driving Bragg cells 1 with $s(t)$ and

51

Bragg cell 2 with $\varepsilon(t)$ to perform the correlation given by equation 3.4, and then interfering and integrating this signal with the output of Bragg cell 3, driven by $s(t)$, to perform the convolution of equation 3.5.

Architecturally, this system offered several advantages over the time integrated processor reported in reference 1; the space-integrating, Fourier domain implementation allows full use of the wide bandwidth of the Bragg cells, the use of signal amplitude instead of intensity eliminates the need for any bias signals, and there was no time integrating device in the system to introduce unwanted bias buildup[4, 3]. The 2-D, folded nature of the processor made this processor difficult to scale to array architectures, simply because the second spatial dimension is already used; scaling would require that each array element have its own 2-D processing domain.

An experimental demonstration of the processor[5] achieved approximately 32 dB of narrowband jammer suppression. The dynamical behavior of the processor was derived and particular emphasis placed upon the stability of the system. The stability of the processor was then experimentally characterized, and the issues of time delay and resulting frequency dependent phase shift around the feedback loop were borne out of this investigation. The authors identified that the residual delay in the processor was caused by the fact that the beam illuminating the Bragg cells, because of the birefringent AO interaction, is a finite distance away from the Bragg cell transducer edge. Hence, there is always a time delay at each Bragg cell produced by the distance the acoustics must travel before interacting with the illuminating beam. This same issue exists in the jammer-nulling processor discussed in this thesis, the characterization is presented in Chapter 7.

In 1984, Psaltis and Hong[6] proposed a set of adaptive processors, named the "passive" and "active" processors, each of which performed correlation and convolution operations, implemented in time domain, space integrating architectures. The passive processor performed narrowband jammer suppression, and the active
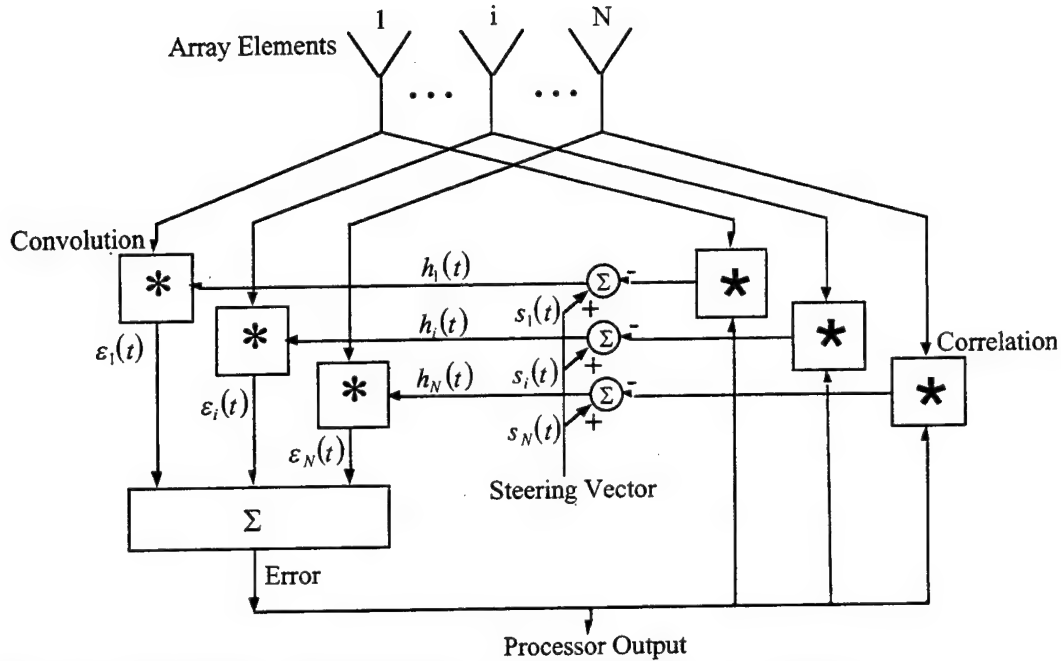
Figure 3.3. Algorithm implemented by 3-D space-time array processor

processor was designed to perform adaptive matched filtering for a desired signal of interest. The 2-D design of this system allowed its 3-D extension to a space-time version intended for phased-array radar processing[7]. The algorithm implemented by the space-time version of the active processor is shown in figure 3.3, where the array look direction is determined by the signal $s^*(-\tau)$, which is also the temporal reference signal used to detect the desired signal. The filter function for the *ith* element, $h_i(t)$, must be adaptively determined, and then applied to each element.

The matched filtering operation which is performed for each array channel of figure 3.3 can be seen by examining the error signal $\varepsilon(t)$, given by the combination of correlation and convolutions[6]

$$\varepsilon(t) = \int_{-\infty}^{\infty} x(t-\tau)s^*(-\tau)d\tau - G\int\int_{-\infty}^{\infty} x(t-\tau)x^*(\alpha)\varepsilon(t+\alpha)d\alpha d\tau \qquad 3.8$$

where G is the feedback gain, and the signal into the processor, $x(t)$, is the sum of a broadband, desired signal $s(t)$, and uncorrelated, narrowband interference terms $n(t)$.
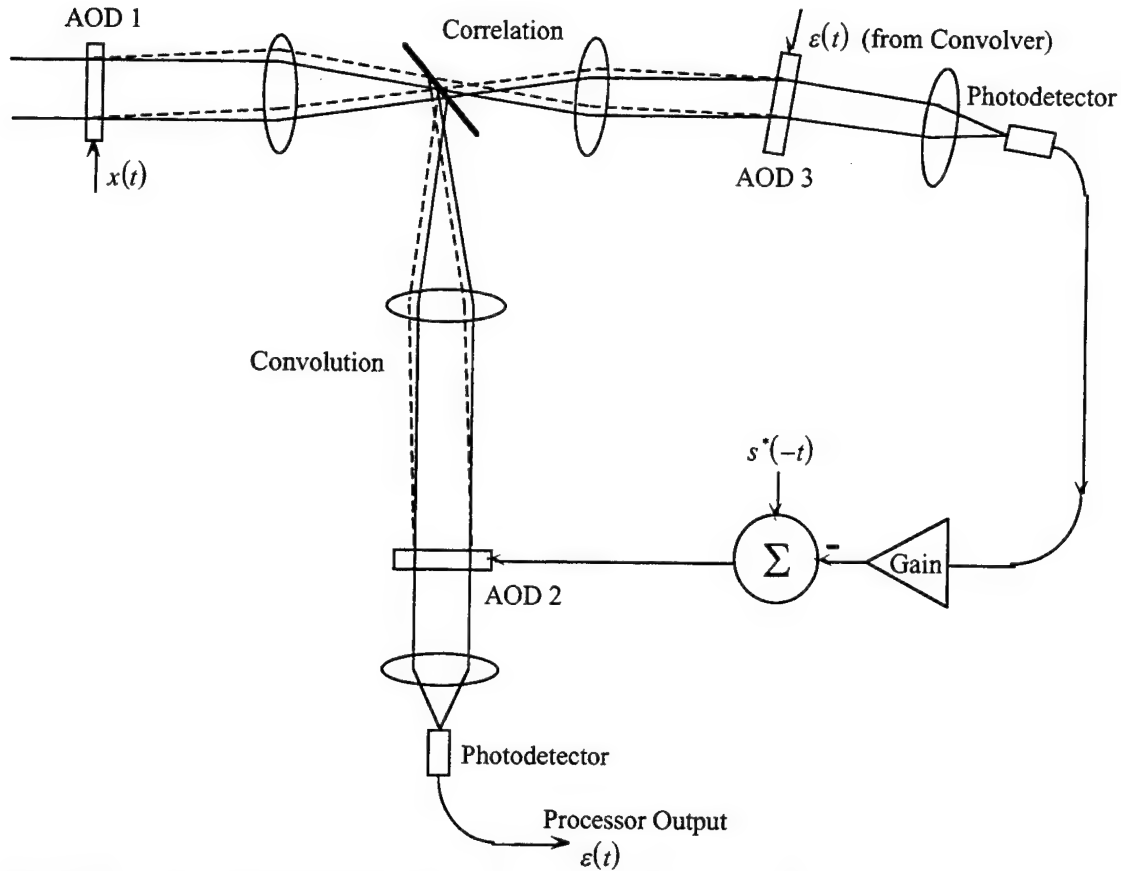
Figure 3.4. Optical implementation of a single channel of the space-time processor shown in figure 3.3.

Assuming that the desired signal component in the array input is weak compared to the interference, equation 3.8 can be approximated by

$$\varepsilon(t) \cong \int_{-\infty}^{\infty} x(t-\tau)s^*(-\tau)d\tau - G\int_{-\infty}^{\infty}\int n(t-\tau)n^*(\alpha)\varepsilon(t+\alpha)d\alpha d\tau$$

.3.9

Taking the Fourier transform of equation 3.9 yields the expression for the matched filter[6, 8], where $X(\omega)$, $S(\omega)$, and $N(\omega)$ are the spectra of the input, steering, and noise signals respectively.

$$E(\omega) \cong \frac{X(\omega)S^*(\omega)}{1 + G|N(\omega)|^2}.$$

3.10
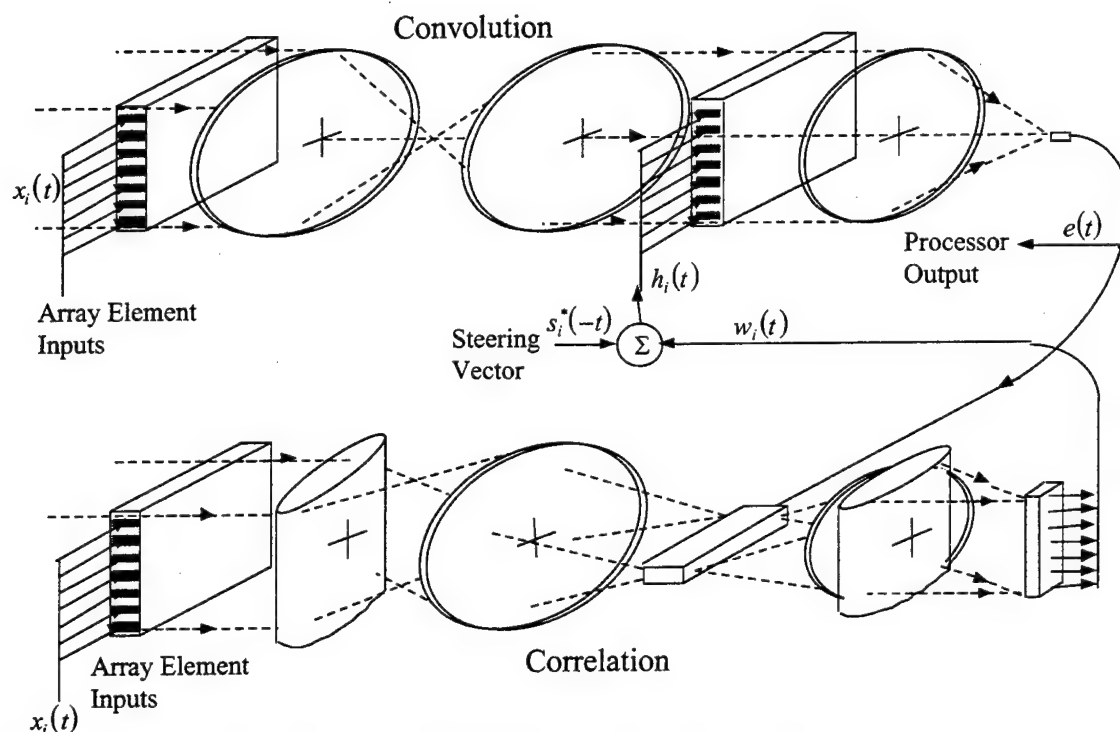
Figure 3.5. Optical implementation of 3-D space-time optical processor

The single channel optical implementation of this processor is shown in figure 3.4, where the space integrating convolver and correlator are identified. As discussed in reference 6, the output of the convolver is compressed in time by a factor of two, and therefore the correlator input must be compatible with the temporally scaled input. The implementation shown in figure 3.4 provides for the scaling factor, however in general the temporal scaling reduces the flexibility of convolver and correlator architectures somewhat. Unlike the space integrating processor of reference 4, this system scales well for the multi-channel, 3-D, space-time implementation proposed for adaptive array processing, primarily by invoking multi-channel Bragg cells, and parallelizing the electronics as shown in figure 3.5. The proposed 3-D active processor system nulling bandwidth was still limited by the inverse of the feedback loop delay time for the acoustics to propagate to the optical window. To avoid this limitation, a time integrating correlator was investigated[9, 10] that used a photorefractive crystal to integrate the weights, and the lack of DC spatial frequency response was used
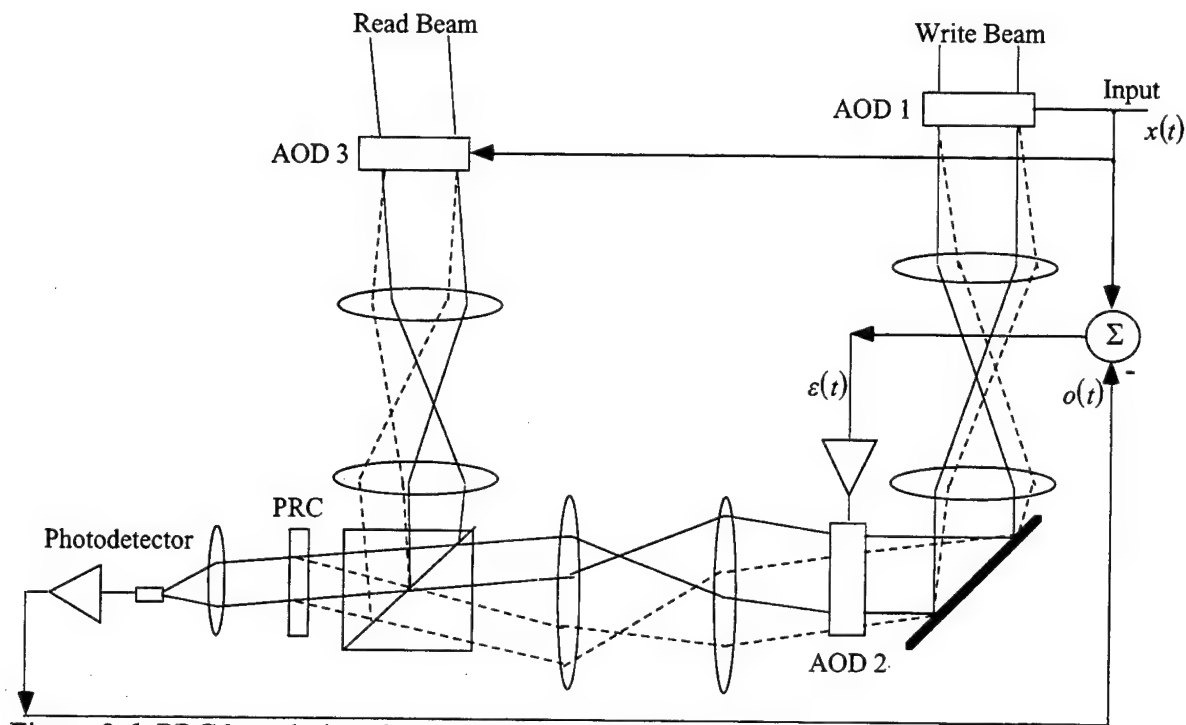
Figure 3.6. PRC based, time-integrating adaptive filter.

advantageously to avoid bias buildup of the weights. A schematic diagram for a space-time adaptive filter based on the photorefractive correlator is shown in figure 3.6. Except for the fact that a PRC is used instead of an OASLM and the read beam is a different wavelength, this architecture is essentially the same as that reported in reference 1. The operation of the processor can be described by the same, very general set of equations given by equations 3.2 through 3.3. Architecturally, the only significant difference with the implementation using the PRC is that a different wavelength (HeNe) is used to read out the weights and perform the final convolution. A small crystal thickness relaxes the Bragg selectivity.

Although the interference suppression results of approximately 15 dB reported in reference 10 were somewhat modest, the introduction of a new, bias-free time-integrating element, with optical input and output represented a significant contribution to the field. The time integration technique offers distinct advantages because while Bragg cells can have large bandwidths, their finite time aperture limits the integration

56

period available for space-integrating architectures. The longer integration period of the time integrating processors allows a significant improvement of the processing gain[11]. In addition to the lack of bias terms traditionally produced by time integrating elements such a light-valves and CCDs, the photorefractive element promised much higher spatial resolution, a response time which can be controlled by intensity level, the simplicity of being a single component rather than a complex device, and an optical, coherent output. It should be noted that bias terms do exist in the sense that the spatially DC terms of the illumination at the photorefractive reduce the diffraction efficiency of the holographic gratings by the erasure mechanism, however the bias signals are not present in the photodetected output. Photorefractive crystals are used as time-integrating elements in the adaptive phased-array processor discussed in this thesis, and the time-integrating properties are discussed in more detail in Chapter 4.

In 1988 multi-channel phased-array beam-forming, and simultaneous pulse compression was demonstrated based on the space integrating correlation architecture presented in references 6 and 7. A schematic of the top-view of the experimental set-up is shown in figure 3.7, where the acoustics propagate into the plane of the paper. The optical implementation uses the multi-channel Bragg cells to perform the multi-delayed multiplication between the array element signals and the time delayed reference signals. The lens and detector perform the spatial integration needed to complete the correlation process. As shown in the figure, the experimental implementation used a mirror to reflect the optical signal back through the same Bragg cell in order to assure good matching of acoustic channel widths[9]. Thus, the signals from the array elements, $x_i(t)$, are correlated with the time-delayed reference signals, $s(t)$, and coherently summed to yield the beam-forming output.

Experimental results from the processor were obtained for a one, two, three, and four channel array, in the presence of narrow and wideband jammers. While not truly adaptive, the results of this experiment demonstrated spatial beam-forming gain,

57
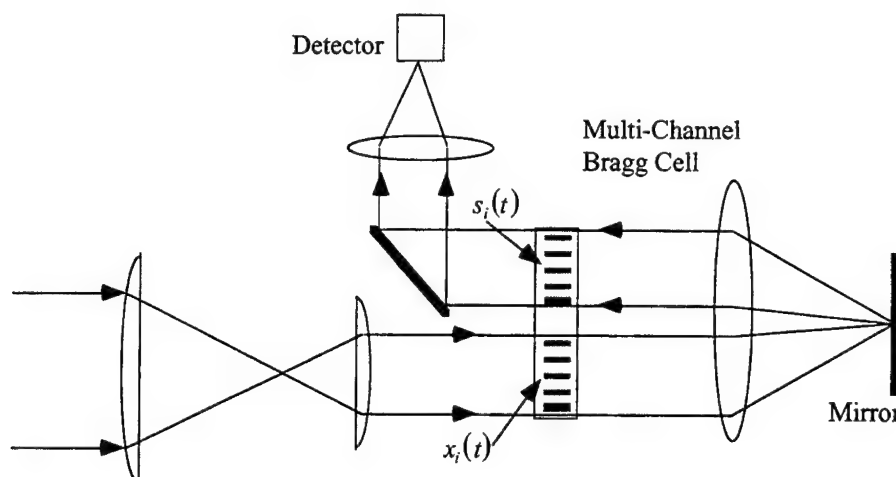
Figure 3.7. Top view of experimental set-up for multi-channel beam-forming processor

and a corresponding robustness in the presence of both narrow and broadband jammers. The authors noted that this same architecture can be used to simultaneously form multiple beams, and could be made truly adaptive by generating an appropriate error signal for use in a closed-loop implementation.

3.2 Optical Processing for Adaptive Phased-Arrays

There are few efforts done with adaptive phased-arrays which are directly comparable to the work presented in this thesis, and this is because only a few groups have approached the true multi-dimensional nature of the phased-array processing problem using adaptive, optically based processors. While many architectures have been proposed, very few systems have actually been built and experimentally demonstrated. As was shown, not all of the architectures of the previous section scaled well from a single channel adaptive filter to the space-time architectures needed for array processing. In this light, the discussion of this section will be restricted to the work presented by three groups, R.M Montgomery, et al.[12, 13, 14], at Harris Microwave Corp., Penn et al.[15,16], at General Electric Corp., and Keefer, et al. at

58

Rome Laboratory[17]. Both of these groups demonstrated adaptive jammer cancellation, but not adaptive beam-forming.

In 1990, while at Harris Microwave Corp., R. M. Montgomery proposed an acousto-optic/photorefractive, adaptive phased-array processor for implementing the LMS algorithm[12]. The processor was based on using a Bragg cell for implementing multiple time delays, and a PRC for calculating and storing the time-integrated weights. While architecturally similar in principle to the work presented by Hong[9, 10], in that the weights were time integrated in a PRC and read out using a space integrating structure, and the writing of the weights was done with one wavelength, and read-out was done with another, a significant difference with the Montgomery approach was the concept of a single, monolithic device which performed both the acousto-optic and photorefractive functions. The proposed monolithic device was to be constructed of bulk GaAs (which is both acousto-optic and photorefractive when properly doped), and the write and read lasers were to be at 1.2 and 1.3 microns respectively. While elegant and compact, the monolithic device was never demonstrated, and the follow-on paper where jammer suppression results were presented[13] used a discrete, conventional AO device and a GaAs photorefractive crystal. A simplified schematic of the experimental architecture is shown in figure 3.8. As shown in the figure, the product of the output of the modulated write laser and the diffracted component form the Bragg cell interfere at the PRC, and the product is time integrated by the PRC. The general expression for the weights can thus be described by equation 3.1. The read laser then illuminates the Bragg cell, the diffracted and undiffracted components propagate through the crystal, probe the holographic weights, and interfere at the photodetector. This performs the convolution described by equation 3.2, and the detected signal is then subtracted from the incoming signal from the array element to generate the feedback error signal. The fact that the write and read wavelengths are reasonably close, and the small crystal thickness
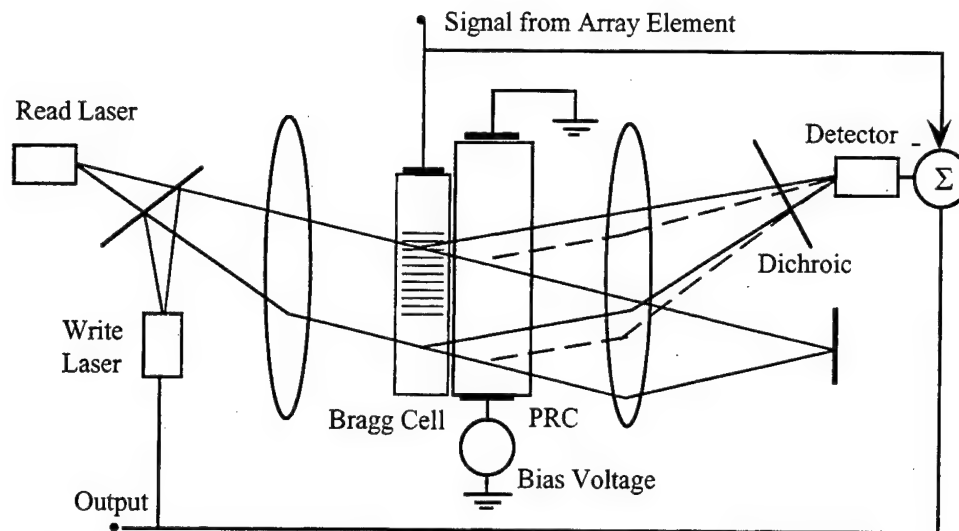
Figure 3.8. Adaptive phased-array processor (single element shown) of Montgomery, et al.[13]

relaxes the Bragg selectivity. The beams were separated using polarization isolation and a dichroic filter.

Narrowband suppression results reported for the single antenna element architecture of figure 3.8 were approximately 40 dB[13], over a nulling bandwidth of approximately 10 MHz. Montgomery noted that the nulling bandwidth was limited to the inverse of the feedback loop-delay time, a limitation common to the processor discussed in this thesis as well.

In later work by Montgomery, et al.[14], the architecture was extended to the true phased-array problem of multiple elements. The single Bragg cell was replaced with a six element device, which simulated a modest array of six elements. Reduction of the feedback loop-delay time to 9 nsec extended the narrowband nulling bandwidth to approximately 32 MHz. Scanning over frequency resulted in a periodic jammer nulling bandwidth, similar to that reported for the jammer-nulling processor of this thesis.

In 1990, while at General Electric Corp., Penn, et al.[16] presented results for an optical adaptive multipath canceller which implemented the LMS algorithm. The first reference to this processor was actually in 1982[15], although the paper was a concept
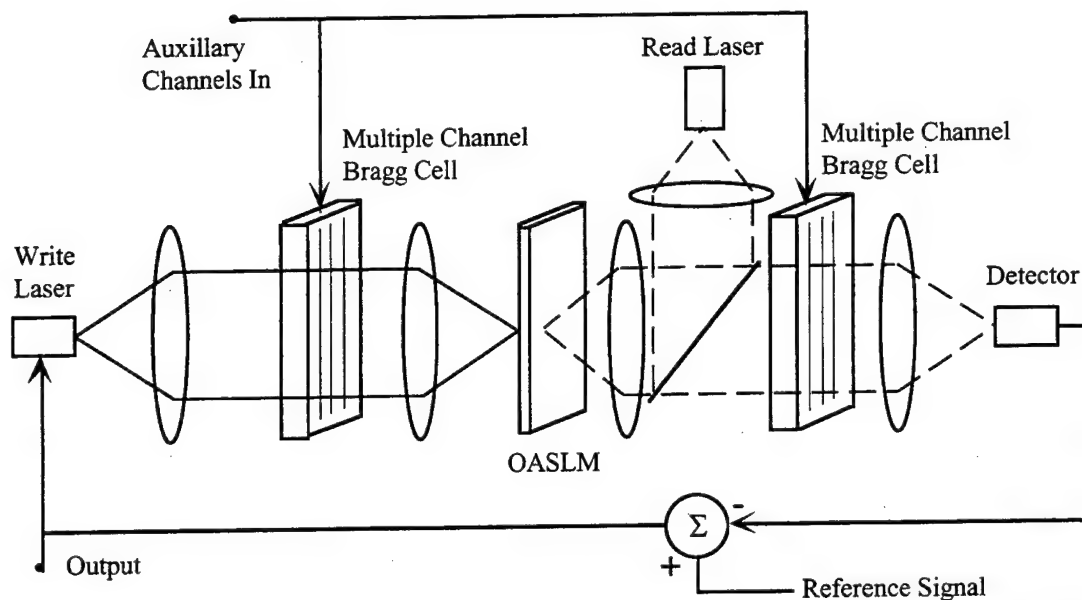
Figure 3.9. Adaptive, optical phased-array radar processor proposed by Penn, et al.[16]

paper only. The architecture is shown in figure 3.9, and although the architecture is shown with multiple channel Bragg cells, the experimental results were obtained using single channel devices. The only difference between this architecture and that proposed by Hong[10] and Montgomery[14] is that now an OASLM is used to time integrate the weights. In fact, the single channel acousto-optic device is architecturally identical to that of Rhodes[1] discussed at the beginning of this chapter, and can be described by the same set of equations.

Using the single channel version of the processor of figure 3.9, approximately 30 dB of suppression for a narrowband jammer was obtained over a six MHz bandwidth, and approximately 15 dB suppression of a 1 MHz wide jammer. This same architecture was outfitted with a PRC as the time-integrating element by Keefer, et al.[17] at Rome Laboratory in 1992 (and later again with a CCD device[18] and an electronic processor that applies the weights). The weights in the PRC were probed by reading out the grating from the back side of the crystal. The performance of the system, again for a single channel, was improved somewhat to approximately 25 dB of narrowband

61

cancellation over a 2 MHz wide bandwidth, while suppression performance for wideband jammers did not improve appreciably. In 1993, researchers at General Electric proposed a Brass-board demonstration for an adaptive processor based on a very similar architecture[19], this time with a HeNe laser used for the readout. This concept appears to have never been built.

It is clear that the architectures discussed in this section are essentially the same; they are all based on time integrating the adaptive weights, and then reading out these weights using a space integrating structure. Moreover, none of the processors described in this chapter scale easily to large phased-arrays. This is due to the use of one Bragg cell per antenna channel, which quickly becomes a problem as the number of antenna channels increases. Current mulit-channel acousto-optic devices are limited to approximately 32 channels[20]. Aside from the work in this thesis, there seems to have been no other demonstrations of either truly adaptive beam-forming, or simultaneous beam-forming and jammer-cancellation of a phased-array using an optical processor.

References

[1]   J.F. Rhodes, "Adaptive filter with a time domain implementation using correlation cancellation loops," Appl. Opt. **22**, no. 2, 282-287 Jan (1983).

[2]   S. Haykin, *Adaptive Filter Theory*. (Prentice Hall, 1991), chap. 6.

[3]   J.D. Cohen, "Optical adaptive linear predictors," Appl. Opt. **24**, no. 23, 4247-4259 Dec. (1985).

[4]   A.VanderLugt, "Adaptive optical processor," Appl. Opt. **21**, no. 22, 4005-4011 Nov. (1982).

[5]   A. M. Bardos, W. R. Beaudet and A.VanderLugt, "Stability considerations for adaptive filtering," Appl. Opt. **25**, no. 14, 2314-2325 July (1986).

[6]   D. Psaltis and J. Hong, "Adaptive acoustooptic filter," Appl. Opt. **23**, no. 19, 3475-3481 Oct. (1984).

[7]   D. Psaltis and J. Hong, "Adaptive acoustooptic processor," in *Analog Optical Processing and Computing*, SPIE **519**, 62-68 (1984).

[8]   W. Davenport and W. Root, *Introduction toTheory of Random Processes and Noise*. McGraw Hill, 1967.

[9]   D. Psaltis, J. Yu and J. Hong, "Bias-free time integrating optical correlator using a photorefractive crystal," Appl. Opt. **24**, no. 22, 3860-3865 Nov. (1985).

[10]   J. Hong, S. Hudson, J. Yu, and D. Psaltis, "Photorefractive crystals as adaptive elements in acoustooptic filters," in *Optical Technology for Microwave Applications III,* SPIE **789**, 136-144 (1987).

[11]   P. Kellman, "Time integrating optical signal processing," Opt. Eng. **19**, no. 3, 370-375 May (1980).

[12]   R.M. Montgomery, "Acousto-optic, photorefractive processor for adaptive antenna arrays," in *Optoelectronic Signal Processing for Phased-Array Antennas II,* SPIE **1217**, 207-217 (1990).

[13]   R. M. Montgomery and M.R. Lange, "Photorefractive adaptive filter structure with 40-dB interference rejection," Appl. Opt. **30**, no. 20, 2844-2849 July (1991).

[14]   R. M. Montgomery, W. R. Beaudet and M.R. Lange, "Photorefractive adaptive sidelobe canceler for phased-array antennas," in *Optical Technology for Microwave Applications,* SPIE **1703**, 405-410 (1992).

[15]   W. Penn, "Optical adaptive array processing," in *Proc. LIA Conf.,* LIA **34,** (1982).

[16]   W. Penn, R. Wasiewicz and R.M. Iodice, "Optical adaptive multipath canceller for surveillance radar," in *Optoelectronic Signal Processing for Phased-Array Antennas II,* SPIE **1217**, 151-160 (1990).

[17]   C. W. Keefer, J. E. Malowicki and P.M. Payson, "Wideband operation of a photorefractive based adaptive processor," in *Analog Photonics,* SPIE **1790**, 145-156 (1992).

[18]   M. C. Budge, R. J. Berinato and M.C. Zari, "Acousto-optic applications for multichannel adaptive optical processor," Tech. Rep., 1992.

[19]   D. B. Friedman, D. P. Dwyer and R.M. Iodice, "Acousto-optic null steering processor (AONSP)," in *Transition of Optical Processors into Systems,* SPIE **1958**, 83-97 (1993).

[20]   D. R. Pape, P. Wasilouski and M. Krainak, "A high performance apodized phased-array Bragg cell," in *Optical Technology for Microwave Applications III,* SPIE **789**, 117-126 (1987).

4 Photorefractive Volume Holography

This chapter will review volume holography in photorefractive media. The chapter begins with a review of dynamic holograms as signal processing elements. Volume holographic readout via the coupled mode equations in static media is then presented. Following is a review of the fundamentals of the photorefractive effect and volume holography in photorefractive media. A differential equation describing the time-evolution of the photorefractive photoinduced space-charge field is derived, and transformed into an equation describing the grating diffraction efficiency used in later chapters for modeling the phased-array jammer-nulling processor dynamics.

4.1 Volume Holography for Signal Processing

The 3-D nature of volume holograms leads to many characteristics and applications uniquely different from those possible with 2-D media. The most significant difference between 2 and 3-D media is that within volume holographic media, due to its thickness, wave propagation is best described by electromagnetic propagation in periodic media. The resulting Bragg diffraction phonemena[1,2,3] leads to high angular and spectral selectivity between holograms as well as the capability for extremely high diffraction efficiency. These properties can be exploited for a variety of applications such as holographic-optical-elements[4,5], (HOEs), data storage[1,6], and storage of multiple images[7,8].

Dynamic holograms formed in photorefractive crystals (PRCs) have been used as processing elements in optical computing architectures for such applications as image processing, neural networks, and signal processing. Image processing applications have included dynamic correlation and convolution[9,10] image amplification[11] and subtraction[12,13] spatial light modulation[14,15] incoherent-to-coherent optical

conversion[16], and optical novelty filters[17]. These applications often use either energy exchange through beam coupling or the phase-conjugation properties of photorefractives via four-wave mixing[18,19,20]. Neural network and signal processing applications often use PRCs as processing elements in the form of multipliers and finite response-time integrators, where the holographic gratings function as an array of complex adaptive weights[21,22,23].

Processors using PRCs addressing radar and communications signal processing applications have been used for performing temporal signal correlation[24], frequency lock-in detection[25], conversion of RF signals[26], and adaptive filtering for phased-array-radar[27,28,29,30]. The adaptive phased-array applications typically implement a modified Least-Mean-Square (LMS)[31] algorithm in the optical domain where the PRCs are used as arrays of complex, time integrated adaptive weights. The phased-array applications are particularly challenging because of the large number of adaptive weights required. For example, a two-dimensional (2D) array with 100 elements in each dimension, each with a 1000 element tapped delay-line requires 10^7 adaptive weights. This large number of required degrees of freedom can easily exceed the computational capabilities of traditional digital signal processing approaches. Using appropriate optical architectures these applications can exploit the large number of degrees-of-freedom available in 3D dynamic volume holographic media. In the phased-array processor presented in this thesis [27,28,32] the adaptive weights are used to implement correlation cancellation loops and matched filtering operations to perform antenna beam steering and spatio-temporal interference cancellation. The adaptive weights are proportional to the crosscorrelation between the unadapted array output, and an error term derived from the difference between the processed array output and a reference signal. Time-integrating correlation is used to calculate the adaptive weights as modulated holographic gratings in the PRC, and the amplitude of each input signal diffracted by these modulated gratings is multiplied by the grating strength, thereby

implementing the adaptive weight calculation and weight multiplication that forms the antenna array function entirely in the optical domain.

4.2 Diffraction by Volume Holographic Gratings: the Coupled-Mode Equations in Static Media

A standard method of solution of electromagnetic propagation in periodic media is by means of coupled mode equations[2]. The coupled-mode equations are appropriate for analyzing the reconstruction of volume holograms because the holographically induced perturbation is distributed over a volume. The "periodic" nature is derived from the index variation resulting from the interference pattern between particular plane wave components of a reference and an object field. This solution method yields straightforward expressions for diffraction efficiency and Bragg selectivity as a function of angle and wavelength. It is important to note that the applicability of the coupled-mode equations to the study of volume holographic diffraction is justified under the assumption of linearity where a complex interference pattern can be considered the result of interference from the linear superposition of angularly diverse plane wave components. This further implies small modulation depth such that the total material response and resultant coupling remains linear.

The coupled-mode solution technique treats the variation of the refractive index or dielectric tensor of the media as a perturbation which couples the unperturbed normal modes of the structure. Material properties determine the physical mechanism which produces the index perturbation, i.e. photorefraction[33,34], photoabsorption[35], photoanisotropy[36] etc. Consider a rectangular slab of holographic recording media of dimensions L_x, L_y, and L_z as shown in figure 4.1 which has an index perturbation in it produced by an interference pattern between optical reference and object wavefronts. The resulting interference pattern shown in the figure is indicative of a single sinusoidal grating as would be produced by two plane waves. Static, or fixed holograms can be

66
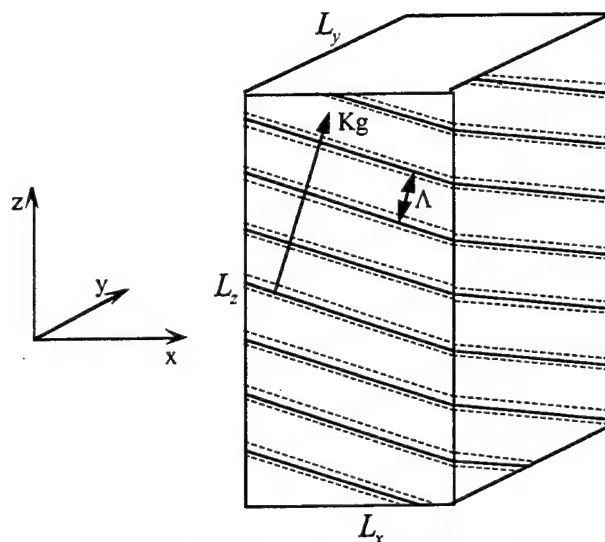
Figure 4.1. Three dimensional slab of holographic recording media of dimensions L_x, L_y, and L_z, with static recorded interference pattern recorded in it.

formed in such materials as photographic emulsions, photopolymers, dichromated gelatin, or specially processed photorefractive materials[37,38]. In static materials the hologram is read out by illuminating it with an incoming reference beam at the proper angle which interacts with the recorded dielectric perturbation, and a single diffracted object output beam is produced. In contrast, in dynamic materials such as photorefractive materials, the writing and reading processes occur simultaneously, exhibiting "self-diffracting" effects. The dynamic energy exchange between the writing and diffracting beams as they propagate through the material produce more complicated diffraction phonomena as discussed in later sections.

The 1-D coupled mode equations will be solved for the case of static media. Although much less rigorous than the true 3-D case, the salient features of Bragg selectivity and high diffraction efficiency can still be elludicated when the interaction region is reduced from truly volumetric to one that is thick in at least one dimension. The volume holographic region of figure 4.1 is reduced to the 2-D planar region as shown in figure 4.2, where the dielectric perturbation is now periodic in the x direction,

67
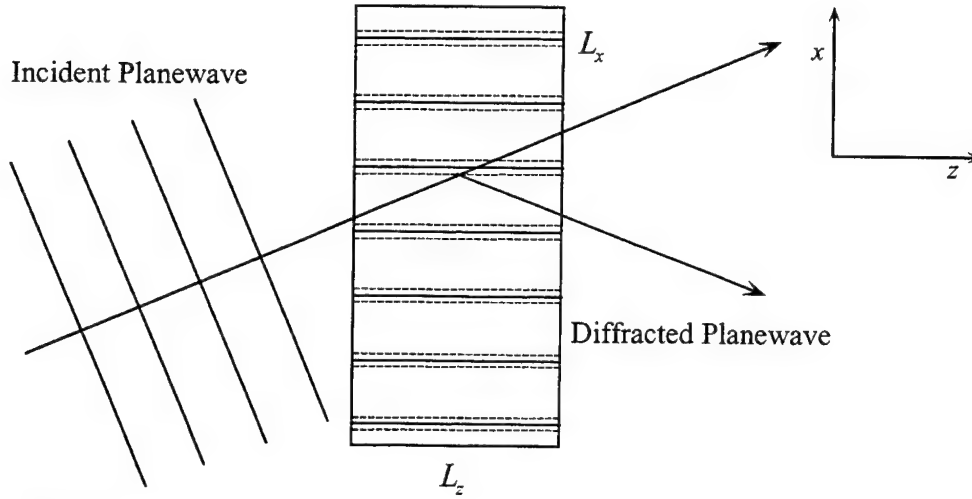
Figure 4.2. Two-dimensional holographic interaction region of dimensions L_x, L_y, and L_z, with periodic dielectric perturbation in x direction. Incident readout plane wave produces a diffracted output wave.

and the interacting wavefronts are propagating nominally in the z direction. The 1-D coupled-mode approximation arises from assuming small-angle Bragg interaction and a semi-infinite x dimension. Thus, the interacting waves are taken to be essentially infinite plane waves in x, whose modal amplitudes vary only as a function of the propagation direction z.

The optical illumination which produced the dielectric perturbation can be described by an interference pattern of the form

$$I(x) = I_o\left[1 + m\cos\left(K_g x\right)\right] \qquad 4.1$$

where the modulation index $m = 2A_1A_2 / \left(A_1^2 + A_2^2\right)$ for two writing beams A_1 and A_2. The interaction of the electric field $\overline{E}$ and the dielectric perturbation can be modeled as an induced polarization wave $\overline{P}$ and subsequent driving term in the wave equation,

$$\nabla^2\overline{E} - \mu_o\varepsilon_o\underset{=}{\overset{\cdot}{\varepsilon_r}}\frac{\partial^2\overline{E}}{\partial t^2} = \mu_o\frac{\partial^2\overline{P}}{\partial t^2} \qquad 4.2$$

where $\overline{P} = \varepsilon_o \underline{\underline{\Delta\varepsilon}}_r \overline{E}$, and the static dielectric perturbation in this example consists of a single spatial frequency or Fourier component denoted by K_g with modulation amplitude $\underline{\underline{\varepsilon_1}}$,

$$\underline{\underline{\Delta\varepsilon}}_r \approx \frac{\underline{\underline{\varepsilon_1}}}{2} e^{iK_g x} + c.c. \tag{4.3}$$

In the above notation both $\underline{\underline{\varepsilon}}_r$, the relative optical dielectric tensor, and $\underline{\underline{\Delta\varepsilon}}_r$, the perturbation of the dielectric tensor are unitless tensor quantities. Noting that $\partial/\partial t \to i\omega$, equation 4.2 becomes

$$\nabla^2 \overline{E} + \frac{\omega^2}{c^2} \underline{\underline{\varepsilon}}_r \overline{E} = -\frac{\omega^2}{c^2} \underline{\underline{\Delta\varepsilon}}_r \overline{E}. \tag{4.4}$$

The electric field is now considered an expansion of the perturbed normal modes of the media, in particular

$$\overline{E} = \sum_p A_p(z) \hat{e}_p e^{i\omega t} e^{-ik_o(\alpha_p x + \beta_p z)} \tag{4.5}$$

where $\hat{e}_p$ is a unit vector in the direction of the *pth* electric field component with z varying amplitude $A_p(z)$, and α and β are the direction cosines of the x and z components respectively of the (internally) propagating wavevector of magnitude $k_o = 2\pi/\lambda_o$. Substituting 4.3 and 4.5 into the wave equation yields the general expression for the coupling between the *pth* and *qth* electric field modes,

$$\sum_p \left[\frac{d^2}{dz^2} A_p(z) - 2ik_o \alpha_p \frac{d}{dz} A_p(z) \right] \hat{e}_p e^{i\omega t} e^{-ik_o(\alpha_p x + \beta_p z)} = -\frac{\omega^2}{c^2} \sum_q \underline{\underline{\Delta\varepsilon}}_r A_q(z) \hat{e}_q e^{i\omega t} e^{-ik_o(\alpha_q x + \beta_q z)} \tag{4.6}$$

where the assumption of infinite plane waves in the x direction allows the approximation that $\nabla^2 \to \partial^2/\partial z^2$. For a weak dielectric perturbation this second derivative can be neglected (slowly-varying envelope approximation), resulting in

$$-2ik_o \alpha_p \sum_p \left[\frac{d}{dz} A_p(z) \right] \hat{e}_p e^{i\omega t} e^{-ik_o(\alpha_p x + \beta_p z)} = -\frac{\omega^2}{c^2} \sum_q \underline{\underline{\Delta\varepsilon}}_r A_q(z) \hat{e}_q e^{i\omega t} e^{-ik_o(\alpha_q x + \beta_q z)}. \tag{4.7}$$

In the case of Bragg interactions only one phase synchronous interaction occurs, so the above sum is reduced to coupling between only two modes, designated as 1 and 2,

$$2ik_o\alpha_1\frac{d}{dz}A_1(z)\hat{e}_1e^{i\omega t}e^{-ik_o(\alpha_1 x+\beta_1 z)} + 2ik_o\alpha_2\frac{d}{dz}A_2(z)\hat{e}_2e^{i\omega t}e^{-ik_o(\alpha_2 x+\beta_2 z)} = \frac{\omega^2}{c^2}\underline{\underline{\Delta\varepsilon_r}}\overline{E} \qquad 4.8$$

where $\overline{E}$ can now be considered as the sum between an incident plane wave $\hat{e}_1 A_1(z)$ and diffracted plane wave $\hat{e}_2 A_2(z)$,

$$\overline{E} = \hat{e}_1 A_1(z)e^{i\omega t}e^{-ik_o(\alpha_1 x+\beta_1 z)} + \hat{e}_2 A_2(z)e^{i\omega t}e^{-ik_o(\alpha_2 x+\beta_2 z)}. \qquad 4.9$$

The coupled-mode equations are obtained by using the orthogonality of the propagating modes. More specifically, multiplying equation 4.8 first by $\hat{e}_1^* A_1(z)e^{i\omega t}e^{-ik_o(\alpha_1 x+\beta_1 z)}$ and integrating over all x and t, followed with multiplication by $\hat{e}_2^* A_2(z)e^{i\omega t}e^{-ik_o(\alpha_2 x+\beta_2 z)}$ and integration over all x and t while invoking the definition

$$\int_{-\infty}^{+\infty} e^{ia\xi}d\xi \equiv \delta(a) \quad or \quad \begin{cases} 0, & a \neq 0 \\ 1, & a = 0 \end{cases} \qquad 4.10$$

results in the familiar coupled mode equations[39]

$$\frac{d}{dz}A_1(z) = -i\kappa_{12}A_2(z)e^{i\Delta kz} \qquad 4.11$$

$$\frac{d}{dz}A_2(z) = -i\kappa_{21}A_1(z)e^{-i\Delta kz}. \qquad 4.12$$

The coupling constants are proportional to the magnitude of the dielectric perturbation ε_1. In particular,

$$\kappa_{12} = \frac{\omega}{4cn_1\cos(\theta_1)}\hat{e}_1^* \cdot \underline{\underline{\varepsilon_1}}\hat{e}_2 \qquad 4.13$$

$$\kappa_{21} = \frac{\omega}{4cn_2\cos(\theta_2)}\hat{e}_2^* \cdot \underline{\underline{\varepsilon_1}}\hat{e}_1 \qquad 4.14$$

where θ_1 and θ_2 are the internal angles of incidence of A_1 and A_2 respectively, and n_1 and n_2 are the respective background refractive indices. The momentum mismatch in the z direction is given by

$$\Delta k = k_o(\beta_1 - \beta_2) = k_o\left[\cos(\theta_1) - \cos(\theta_2)\right] \qquad 4.15$$

while it has been assumed that the Bragg condition has been satisfied in the x direction. This assumption requires that $k_o\alpha_2 = k_o\alpha_1 \pm K_g$, which can also be stated as

$$\sin(\theta_2) = \sin(\theta_2) \pm \lambda_o/\Lambda \qquad 4.16$$

where Λ is the grating wavelength. When illumination is precisely at the Bragg angle, the momentum mismatch is zero. In an isotropic medium this will occur when $\theta_1 = -\theta_2 = \theta_B$. In this case equation 4.16 yields the familar expression for the Bragg condition,

$$\sin(\theta_B) = \frac{K_g}{2k_o}. \qquad 4.17$$

More generally there will be some phase mismatch in the z direction as a result of not reading out the grating at precisely the Bragg angle. Therefore it is useful to express Δk specifically in terms of the readout angle. In this case $\theta_1 = -\theta_B + \Delta\theta$ and $\theta_2 = \theta_B + \Delta\theta$ where $\Delta\theta$ is the deviation from the Bragg angle. Substituting the above perturbed expressions for θ_1 and θ_2 into equation 4.15 yields

$$\Delta k(\Delta\theta) = -2k\Delta\theta\sin(\theta_B) = -K_g\Delta\theta. \qquad 4.18$$

It is precisely this angularly selective behavior which is exploited for angularly multiplexed holographic storage applications.

Alternatively the momentum mismatch can be produced by a change in the readout wavelength. Let the wavelength of the illumination beam change from λ_o to

71

$\lambda_o + \Delta\lambda$, where $\Delta\lambda \ll \lambda_o$. This will produce a corresponding change from the Bragg condition given by equation 4.17 to

$$2\Lambda \sin(\theta_B + \Delta\theta) = \lambda_o + \Delta\lambda . \qquad 4.19$$

Taking $\cos(\Delta\theta) \approx 1$ and $\sin(\Delta\theta) \approx \Delta\theta$, it follows that

$$\Delta\theta(\Delta\lambda) = \frac{\Delta\lambda}{2\Lambda\cos(\theta_B)} = \left(\frac{\Delta\lambda}{\lambda}\right)\tan(\theta_B). \qquad 4.20$$

This value of the effective angular deviation can be used in equation 4.18 to yield a wavelength dependent momentum mismatch of

$$\Delta k(\Delta\lambda) = -K_g\left(\frac{\Delta\lambda}{\lambda}\right)\tan(\theta_B). \qquad 4.21$$

Consider now a simple example where the hologram is illuminated by a single plane wave reference beam and thus the diffracted term is initially zero. Using the boundary condition $A_2(0) = 0$ for the diffracted beam, the solution of equations 4.11 and 4.12 is given by

$$A_1(z) = e^{i(\Delta k/2)z}\left[\mathrm{Cos}(sz) - i\frac{\Delta k}{2}\sin(sz)\right] \qquad 4.22$$

$$A_2(z) = e^{-i(\Delta k/2)z}\left[-i\frac{\kappa_{21}}{s}A_1(0)\sin(sz)\right] \qquad 4.23$$

where

$$s^2 = \kappa_{12}\kappa_{21} + \left(\frac{\Delta k}{2}\right)^2 . \qquad 4.24$$

At a given distance L in the media, the intensity diffraction efficiency is

$$\eta = \frac{|A_2(L)|^2}{|A_1(0)|^2} = \frac{|\kappa_{12}\kappa_{21}|}{|\kappa_{12}\kappa_{21}| + (\Delta k/2)^2}\sin^2\sqrt{|\kappa_{12}\kappa_{21}| + (\Delta k/2)^2}\,L . \qquad 4.25$$

For small momentum mismatch Δk equation 4.25 predicts a $\sin^2$ dependence with κL, while for small coupling constant κ, there is a sinc^2 dependence with Δk. The intensity

diffraction efficiency in the small coupling limit is an important parameter which is used throughout this thesis, given by

$$\eta \cong L^2 |\kappa_{12}\kappa_{21}| \text{sinc}^2\left(\frac{\Delta k L}{2\pi}\right)$$

4.26

where $\text{sinc}(\xi) \equiv \sin(\pi\xi)/\pi\xi$. Momentum mismatch Δk and corresponding phase mismatch produces non-resonant coupling between the incident and diffracted wave resulting in reduced amplitude of the diffracted wave. Equation 4.26 shows that optimum coupling is achieved when the momentum mismatch $\Delta k = 0$. In fact, when $\Delta k = 0$ very high diffraction efficiency, theoretically 100%, can be obtained (absorption and Fresnel surface reflections have been neglected in this analysis). The first zero of the sinc^2 function will occur at $\Delta k = 2\pi/L$, and the -4 dB point of the diffracted outout power will occur at $\Delta k = \pm\pi/L$. The momentum mismatch and its angular selectivity as given by equation 4.18 play a key role in the evaluation of holographic diffraction efficiency in Chapter 5.

4.3 Photorefractive Volume Holograms

4.3.1 The Photorefractive Effect

The photorefractive effect is caused by a change in the dielectric constant due to spatial variation of photo-induced electronic charge density within the medium. In coherent processing the spatially varying charge density is produced by the interference of two or more optical beams. In regions of brightness electrons are photo-generated into the conduction band from donor sites formed by dopant or impurity sites within the band-gap of the material, leaving behind them positively charged ion centers. These electrons migrate to darker regions where they can be subsequently caught by empty traps within the band-gap. These traps can be formed either by impurities of the same type as the donors but of a different valence state, different impurity species entirely, or positively charged photo-ionized centers. The transport of charge carriers occurs by

73

diffusion, and/or drift due to the presence of an electric field. The electric field can be applied externally to the crystal or produced internally due to photovoltaic effects. Photovoltaic effects will not be included in the discussion presented here. It is important to note that while the photo-induced charge carriers are mobile, the ionized impurity sites are not. Ignoring beam coupling by assuming the hologram is thin in the nominal propagation direction in addition to assuming short carrier transport lengths, the steady-state result is a modified space-charge distribution within the material with the same spatial modulation as the incident illuminating intensity pattern. This spatially modulated charge distribution produces an internal electric space charge field E_{sc}, which modulates the dielectric constant via the linear electro-optic effect. This physical description of the photorefractive process is known as the band transport model[19,20] and is of course applicable to materials where either holes or electrons are the dominant photoinduced charge carrier. An alternative model, the "Hopping model"[40], based on the statistical behavior of photo-induced charge carriers hopping into vacant capturing sites has been shown to produce similar results, but will not be discussed further here. The dielectric modulation produced in the material is equivalent to a refractive index modulation which for low absorption acts as a holographic phase-only grating. Due to the anisotropic nature and tensoral properties of the electro-optic coefficients characteristic of most photorefractive materials, there is a significant angular and spatial frequency dependence for the strength of the holographic response. In order to analyze the physics of holographic grating creation within a PRC, again linearity is assumed, that is that a complex interference pattern can be considered as the linear superposition of its spatial frequency components. In this light, the basic physical processes contributing to the formation of a complex hologram can be studied by analyzing one spatial frequency at a time. It should be emphasized that the photorefractive effect is inherently nonlinear and a complete analysis must include these nonlinear effects, but much can be ascertained from the analysis presented here. In addition, the
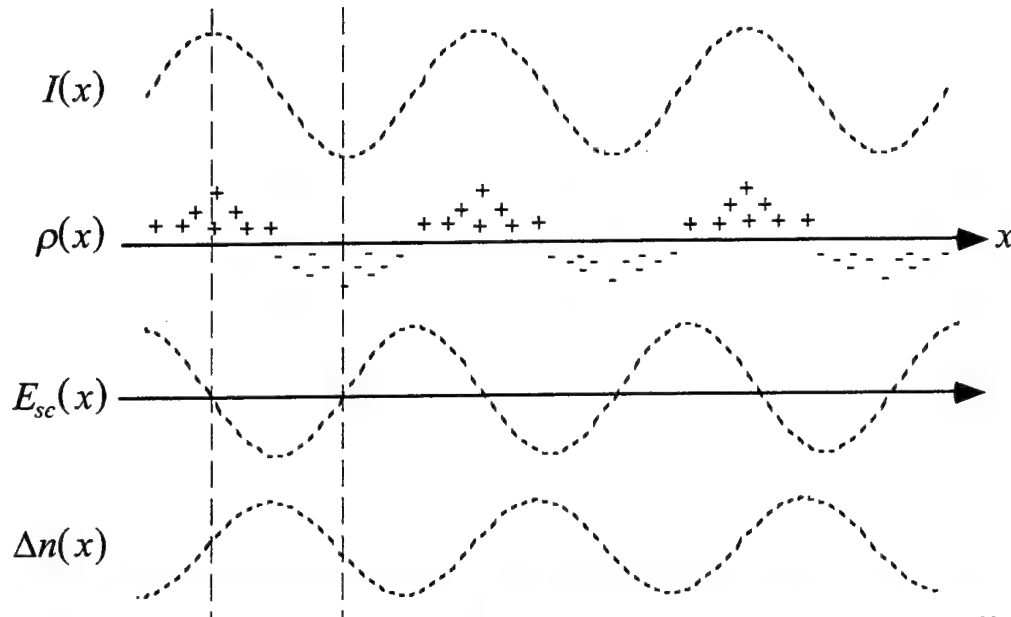
Figure 4.3. Schematic representation of the photorefractive effect in the diffusion dominated regime. Sinusoidal illumination pattern produces spatially varying charge density within material and corresponding space-charge electric field.

photorefractive effect differs significantly from other nonlinear processes in that photorefractivity is driven by the spatial variation of the incident intensity, and not the absolute intensity.

The photorefractive effect can be reviewed in the context of the diffusion field and drift field dominated cases. The photorefractive diffusion dominated charge transport process is shown schematically in figure 4.3. A sinusoidal modulated spatial intensity pattern is incident on a slab of photorefractive material as shown in the upper portion of figure 4.3. This optical illumination can be described as in equation 4.1

$$I(x) = I_o\left[1 + m\cos\left(K_g x\right)\right] \qquad 4.1$$

where the modulation index $m = 2A_1 A_2 / \left(A_1^2 + A_2^2\right)$ for two writing beams A_1 and A_2 propagating nominally along the z axis. The light intensity is assumed uniform along the y axis. It is assumed that there is no external applied (drift) field present.

75
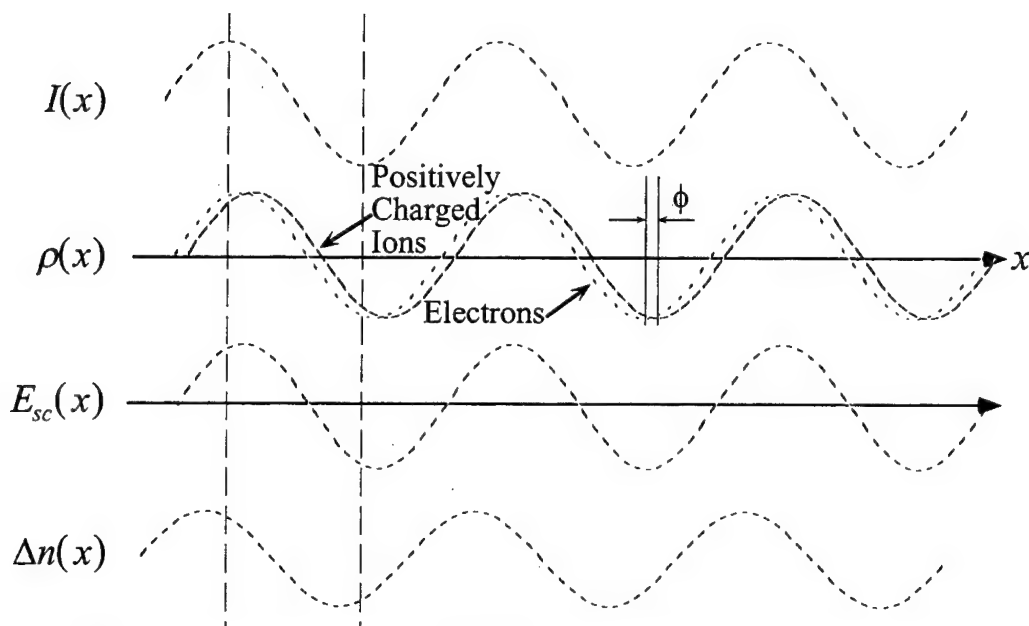
Figure 4.4. Schematic representation of the photorefractive effect in the drift dominated regime. In this regime the sinusoidal illumination pattern results in a refractive index perturbation approximately in phase with the incident illumination pattern.

The diffusion process can be thought of as giving rise to three charge gratings; the first is a grating of stationary positively charged donor ions, and the second and third are gratings of negatively charged traps, one which is due to electrons moving to the right, and the other due to an equal number of electrons moving towards the left. The photo-excitation of the electrons into the conduction band cause them to effectively migrate from regions of brightness and accumulate in regions of darkness, leaving behind the stationary positively charged ions. When the diffusion transport length of the migrating electrons is shorter than the grating wavelength, after multiple cycles of photoexcitation and recombination, the charge distribution will obtain the same spatial distribution as the input illumination pattern[41]. The space-charge field builds up to the point that it inhibits charges from being redistributed and the steady-state charge density distribution $\rho(x)$ shown in figure 4.3 results. The important point is that for this diffusion dominated case the charge density is nearly in phase with the incident illumination.

The induced electric field can be calculated from Poisson's equation, $\nabla \cdot \underline{\underline{\varepsilon_{dc}}} \overline{E}(x) = \rho(x)$, where $\underline{\underline{\varepsilon_{dc}}}$ is the low frequency dielectric tensor. The resulting steady-state space charge field will have a sinusoidal dependence, 90 degrees out of phase with the incident illumination pattern as shown in figure 4.3. This space-charge field then produces a dielectric perturbation via the linear electrooptic effect, also 90 degrees out of phase with the incident illumination pattern.

In contrast, in the drift dominated regime produced by an applied electric field E_o, both the amplitude and phase of the space-charge field is modified. As one would expect the photoinduced carriers move in a preferential direction. An electron will move an average drift length $L_E = \mu \tau E_o$ before becoming trapped, where μ is the electron mobility and τ is the recombination lifetime. Assuming the same $\cos(K_g x)$ dependent illumination pattern as for the diffusion case, the preferential drift of the electrons due to the applied field will result in a drifted electron distribution proportional to $\cos(K_g x + \phi)$ as shown in figure 4.4. For small phase shift ϕ (small transport length), the net charge distribution produced between the photoinduced electrons and the stationary positively charge ions will be approximately sinusoidal. The resulting space-charge field from Poisson's equation and the resulting dielectric perturbation will then be approximately cosinusoidal, nearly in phase with the incident illumination pattern.

More generally, the steady-state space-charge field produced by this single frequency sinusoidal illumination pattern can be described in terms of a complex steady-state space-charge field amplitude E_{sc}^{ss} and grating phase shift ϕ

$$E_{sc}(x) = E_{sc}^{ss} \frac{m}{2} e^{iK_g x} + c.c. \qquad\qquad 4.27$$

where E_{sc}^{ss} is given by[42]

$$E_{sc}^{ss} = E_q \left[\frac{E_o^2 + E_D^2}{E_o^2 + \left(E_D + E_q\right)^2} \right]^{1/2} e^{-i\phi} \qquad\qquad 4.28$$

77

and the grating phase shift ϕ is given by

$$\tan(\phi) = \frac{E_D}{E_o}\left(1 + \frac{E_D}{E_q} + \frac{E_o^2}{E_D E_q}\right).$$

4.29

The trap density-limited space-charge field is defined as $E_q = qN_A/\varepsilon_{dc}K_g$, and $E_D = k_B T K_g/q$ is the diffusion field, E_o is the applied field, where k_B is Boltzman's constant, T is temperature in kelvins, q is the electronic charge, and N_A is the crystal acceptor dopant density. It is important to note that the saturated space-charge field E_{sc}^{ss} is a complex quantity due to the fact that there is a phase-shift of the field with respect to the optical illumination pattern. This is fundamental to energy-coupling characteristics between beams in photorefractive materials.

For the case of pure diffusion, $E_o = 0$, the phase shift is 90 degrees, and the the (linearized) steady-state space-charge field is given by[41]

$$E_{sc}(x) = \left(\frac{E_D}{1 + K_g^2/K_d^2}\right) m\sin(K_g x)$$

4.30

where the Debye wavevector K_D is defined as $K_D = q\sqrt{N_A(N_D - N_A)/(N_D\varepsilon_{dc}k_B T)}$ and N_D is the crystal dopant doping density.

In the case of a large applied field, the drfit dominated (linearized) steady-state space-charge field becomes[41]

$$E_{sc}(x) = E_o\left(\frac{1}{1 + E_o^2/E_q^2}\right)^{1/2} m\cos[K_g x].$$

4.31

Equation 4.31 indicates that the phase of the space-charge field can be in phase with the incident illumination pattern. Examination of equation 4.28 shows that the effects of the externally applied field on the space-charge field amplitude is much more significant at larger grating periods than at smaller grating periods. Recall that both

equations 4.30 and 4.31 are based on the assumption of short charge carrier transport lengths. Long transport lengths can significantly alter the grating phase[43,44].

It is instructive to examine the behavior of the steady-state saturation space-charge complex field amplitude E_{sc}^{ss} with respect to doping density and grating wavelength Λ. Much of the characteristic behavior can be attributed to the fact that E_q is directly proportional to dopant density and grating wavelength Λ, while E_D is independent of dopant density and inversely proportional to grating wavelength Λ. For the case of no applied field charge transport is dominated by diffusion. Here E_{sc}^{ss} increases linearly as a function of Λ for small Λ, reaches a peak at the Debye wavelength Λ_D, where $\Lambda_D = 2\pi/K_D$, and then falls off as $1/\Lambda$. The peak occurs when $E_D = E_q$. The amplitude of this peak is directly proportional to the acceptor dopant density N_A. From the definition of E_q and E_D it is evident that for large grating spacing (small K_g) $E_D << E_q$, and then E_{sc}^{ss} can be approximated by $E_{sc}^{ss} \cong iE_D$. The presence of the "i" indicates the characteristic $\pi/2$ phase shift between the incident illumination and the dielectric perturbation for the case of $E_o = 0$, as evidenced by equation 4.30. For the other limiting case of small grating spacing (large K_g) E_{sc}^{ss} becomes $E_{sc}^{ss} \cong iE_q$, which is directly proportional to dopant density and grating spacing. Thus when charge transport is dominated by diffusion, the steady-state space-charge field can be either diffusion field limited or saturation field (dopant) limited depending on the grating spatial frequency.

4.3.2 Coupled-Mode Equations in Photorefractive Media

In dynamic media such as photorefractives, the two beams that write the grating are also simultaneously diffracting off of the grating, and thus the grating itself is modified as the beams propagate through the media. As expected, the coupled-mode solutions for this case exhibit more inter-dependent characteristics because the form of

the dielectric perturbation $\underline{\underline{\Delta\varepsilon}}$ depends on the modulation depth of the interference pattern of the interacting waves.

An optical illumination pattern of the same form as equation 4.1 will induce a space-charge field and resulting dielectric perturbation as described in section 4.3.1, and again the electric field E is taken to be the sum of two modes (incident and diffracted beams) as given by equation 4.9. The induced dielectric perturbation is related to the space-charge field via the linear electrooptic effect. In particular, a unitless relative dielectric perturbation can be defined by[45]

$$\underline{\underline{\Delta\varepsilon}} = \frac{\underline{\underline{\varepsilon}}_1}{2}\frac{\hat{e}_1 \cdot \hat{e}_2^* A_1 A_2}{I_o}e^{-i\bar{K}_g \cdot \bar{r}} + c.c. \tag{4.32}$$

with

$$\underline{\underline{\varepsilon}}_1 = \underline{\underline{\varepsilon}}_r\left(\underline{\underline{r}}\,E_{sc}^{ss}\right)\underline{\underline{\varepsilon}}_r \tag{4.33}$$

where $\underline{\underline{r}}$ is the third rank electro-optic tensor, and $\underline{E}_{sc}^{ss}$ is the photoinduced steady-state space-charge complex field. The DC intensity term in the denominator of equation 4.32 is given by $I_o = |A_1|^2 + |A_2|^2$.

The expressions for the optical field and the dielectric perturbation (equations 4.9 and 4.32 respectively) are substituted into the wave equation 4.2 and the slowly varying envelope approximation is invoked. Applying the Bragg matching constraint of $\pm\bar{K}_g = \bar{k}_2 - \bar{k}_1$, followed by setting similar rapidly time varying components separately equal to zero, the coupled-mode equations for photorefractive media are

$$\frac{d}{dz}A_1(z) = -i\kappa_{12}\frac{A_1(z)|A_2(z)|^2}{I_o}e^{i\Delta kz}\left(\hat{e}_1^* \cdot \hat{e}_2\right) - \frac{\tilde{\alpha}}{2}A_1(z) \tag{4.34}$$

$$\frac{d}{dz}A_2(z) = -i\kappa_{21}\frac{A_2(z)|A_1(z)|^2}{I_o}e^{-i\Delta kz}\left(\hat{e}_2^* \cdot \hat{e}_1\right) - \frac{\tilde{\alpha}}{2}A_2(z) \tag{4.35}$$

where $\tilde{\alpha}$ is an absorption constant, and the coupling constants are[46,40,47]

$$\kappa_{i,j} = \left(\frac{\omega k_B T}{cq2\cos\theta_B}\right)\hat{e}_i^* \underline{\underline{\varepsilon}}^r \underline{r}\hat{\underline{K}}_g \underline{\underline{\varepsilon}}^r \hat{e}_j \left[\frac{K_g}{\left(1 + K_g^2/K_D^2\right)}\right].$$

4.36

The sign of κ will determine the direction of the two-beam coupling gain, and is dependent upon the orientation of the beams with respect to the crystal axis, the polarization of the beams, and the material electro-optic coefficients.

Equations 4.34 and 4.35 can be solved for the intensities of the two signals by letting $A_1 = \sqrt{I_1}e^{-i\phi_1}$ and $A_2 = \sqrt{I_2}e^{i\phi_2}$. This yields the steady-state coupled intensity equations[48]

$$\cos(\theta_1)\frac{d}{dz}I_1(z) = -\left(\frac{\varepsilon_1\pi\sin(\phi)}{\lambda n_o}\right)\frac{I_1(z)I_2(z)}{I_o} - \tilde{\alpha}I_1(z)$$

4.37

$$\cos(\theta_2)\frac{d}{dz}I_2(z) = +\left(\frac{\varepsilon_1\pi\sin(\phi)}{\lambda n_o}\right)\frac{I_1(z)I_2(z)}{I_o} - \tilde{\alpha}I_2(z)$$

4.38

where ϕ is the spatial phase-shift between the dielectric perturbation and the incident intensity illumination pattern, typically 90 degrees. The intensity equations solved for the transmission grating geometry yield

$$I_1(z) = I_1(0)e^{-\tilde{\alpha}z/\cos\theta_1}\frac{I_1(0) + I_2(0)}{I_1(0) + I_2(0)e^{\Gamma z/\cos\theta_1}}$$

4.39

$$I_2(z) = I_2(0)e^{-\tilde{\alpha}z/\cos\theta_2}\frac{I_1(0) + I_2(0)}{I_1(0)e^{-\Gamma z/\cos\theta_2} + I_2(0)}$$

4.40

where the gain constant Γ is defined such that $\Gamma = \varepsilon_1\pi\sin(\phi)/\lambda n_o$.

The above equations indicate that for positive Γ, beam 2 undergoes coherent gain at the expense of beam 1, limited only by absorption. It is important to note that for $\phi = \pi/2$ energy can be transferred entirely from one beam to the other. This asymmetric beam-coupling behavior can be exploited for real-time signal and image processing applications. The phases of the two beams are coupled via

81

$$\cos(\theta_1)\frac{d\phi_1}{dz} = \left(\frac{\varepsilon_1 \pi \cos(\phi)}{\lambda n_o}\right)\frac{I_2(z)}{I_o} \qquad \text{4.41}$$

$$\cos(\theta_2)\frac{d\phi_2}{dz} = \left(\frac{\varepsilon_1 \pi \cos(\phi)}{\lambda n_o}\right)\frac{I_1(z)}{I_o} \qquad \text{4.42}$$

which indicates that for $\phi = \pi/2$ (diffusion dominated case), while there is energy exchange via the coupled intensity equations, there is no fringe curvature or phase coupling.

The assymetric beam-coupling behavior is directly related to the phenomena of photorefractive fanning[49,50]. Fanning can be described as directional, amplified optical noise that is inherent in all photorefractive crystals, but obviously more significant in those crystals with high gain. The fanning process is generally considered to be initially induced by scattering centers either internal to the crystal or on the crystal surface. The incident beam is scattered off of these centers and the scattered beam components write photorefractive gratings with each other and the incident beam. Energy is exchanged through (multi) beam coupling, and is enhanced in directions where ΓL is positive. When the crystal is illuminated by a single incident beam, the result is a scattered cone or "fan" of light which builds up over time with a preferential orientation, towards the c-axis of the crystal. This scattering is generally a source of unwanted noise in most experimental situations. However, most experiments involve interaction of at least two reasonably strong beams, and when a second strong beam is introduced much of the energy is diverted from the fanning gratings, and the fanning pattern can be seen to rapidly collapse. Smaller beam profiles help reduce the amount of fanning because there is less spatial overlap with the incident beam and the scattered components of the incident beam. Working with non-focused beams, which have less spatial frequency content than a focused beam also minimzes fanning.

4.3.3 Dynamics of Photorefractive Grating Formation

The band transport model can provide analytic solutions for both the dynamic and steady-state behavior of the photo-induced space-charge field. Given the space-charge field behavior and coupled-mode equations which describe the optical fields, the spatial and temporal behavior of the photorefractive process can be completely described by a set of coupled differential equations. Due to the nonlinear behavior of the photorefractive effect, obtaining analytic solutions is possible only if certain approximations can be made. A very common assumption which is often employed is that of a strong undepleted pump beam[51,52,53,54]. Fourier and Laplace transform techniques have been used to derive the transfer function and impulse response for two[55] and four-wave mixing[42] under the undepleted pump approximation. The emphasis of this section will be to present an outline for the derivation of the spatio-temporal evolution of the space-charge field via the Band-transport model. The dynamical expression for the space-charge field is then transformed into an equation describing the temporal evolution of the grating strength, useful for modeling the phased-array processor jammer suppression dynamics.

We seek the time evolution of the electric field amplitude E_{sc} in a photorefractive crystal under optical illumination. In particular the photorefractive index grating will be formed by the interaction of two plane waves A_1 and A_2 propagating in the nominal z direction which produce a simple intensity modulation pattern of the form of equation 4.1. Following references [56], [42] and [19], the fundamental material equations describing the photorefractive charge transport are

$$\frac{\partial N_D^+}{\partial t} = sI\left(N_D - N_D^+\right) - \gamma_R N_D^+ n_e \qquad 4.43$$

$$\frac{\partial n_e}{\partial t} - \frac{\partial N_D^+}{\partial t} = \frac{1}{q}\nabla \cdot \bar{J} \qquad 4.44$$

83

$$\bar{J} = q\mu n_e \bar{E}_{sc} + \mu k_B T \nabla n_e \qquad\qquad 4.45$$

$$\nabla \cdot \underline{\underline{\varepsilon_{dc}}} \bar{E}_{sc} = q\left(n_e + N_A - N_D^+\right) \qquad\qquad 4.46$$

where

N_D^+ = number density of ionized donor ions s = ionization rate

N_D = number density of donor ions q = electronic charge

n_e = number density of photoinduced electrons μ = mobility constant

N_A = number density of acceptor ions k_B = Boltzman constant

$\bar{E}_{sc}$ = space-charge field I = optical intensity

γ_R = recombination rate $\bar{J}$ = current density

$\underline{\underline{\varepsilon_{dc}}}$ = low frequency dielectric tensor T = temperature (Kelvins)

Equations 4.43 and 4.44 are the continuity equations for the (immobile) ionized donors and the photo-induced electron density respectively. Equation 4.45 is the current density which is the sum of diffusion and drift current terms, and equation 4.46 is Poisson's equation.

Several approximations will be made in order to obtain an analytic solution. The first assumption will be that of an undepleted pump beam. The undepleted pump approximation is assumed in modeling the phased-array jammer nulling processor dynamics, and therefore it is useful to employ it here. A second assumption is a quasi-cw approximation, that is that the time scale of the grating formation and erasure is much longer than the free carrier lifetime. This allows the time derivative term $\partial n_e / \partial t$ in equation 4.44 to be neglected. The n_e term in Poisson's equation is also dropped by assuming that $n_e \ll N_A$. Also invoked is the assumption of linearity, that is that the fundamental spatial frequency component of the intensity pattern formed between the two incident plane waves is the only spatial frequency component formed in the photorefractive grating. Spectrally rich approaches which maintain the full nonlinear

coupling behavior between spatial frequencies have been developed[57], but will not be implemented here. The assumption of linearity is equivalent in its outcome to assuming small modulation depth m between the two incident beams, and allows the spatial variation of all quantities to be written as the sum of a constant zeroth order term and a small sinusoidal perturbation term. This produces the following set of equations

$$N_D^+(t,z) = N_A(t) + \text{Re}\left[N_{D1}^+(t)\exp(iK_g z)\right] \qquad 4.47$$

$$n_e(t,z) = n_{eo}(t) + \text{Re}\left[n_{e1}(t)\exp(iK_g z)\right] \qquad 4.47$$

$$j_e(t,z) = j_{eo}(t) + \text{Re}\left[j_{e1}(t)\exp(iK_g z)\right] \qquad 4.49$$

$$E_{sc}(t,z) = E_{sco}(t) + \text{Re}\left[E_{sc1}(t)\exp(iK_g z)\right]. \qquad 4.50$$

Substituting these equations into the material equations (4.43 - 4.46), and neglecting quadratic and higher order products of the perturbation terms yields a linearized differential equation for the time evolution of the space-charge field[42]

$$\frac{\partial E_{sc}(\bar{r},t)}{\partial t} = -\frac{E_{sc}(\bar{r},t)}{\tau} + \frac{E_{sc}^{ss}}{\tau I_o}\left[A_1(t)A_2^*(\bar{r},t)\right] \qquad 4.51$$

where $I_o = I_1 + I_2$ is the spatially D.C. component of the incident intensity, and the steady-state saturation space-charge complex field amplitude E_{sc}^{ss} is defined in equation 4.28. The intensity dependent time constant[58] τ can be approximated by $\tau \approx \tau_o / I_{dc}^x$, where $x \leq 1$, and τ_o is a function of material parameters[42]. Therefore equation 4.51 becomes

$$\frac{\partial E_{sc}(\bar{r},t)}{\partial t} = -\frac{E_{sc}(\bar{r},t)I_{dc}}{\tau_o} + \frac{E_{sc}^{ss}}{\tau_o}\left[A_1(t)A_2^*(\bar{r},t)\right]. \qquad 4.52$$

Recalling that the interacting optical fields are plane waves which propagate nominally in the z direction, and that the induced grating is in the x-direction, the modal amplitude of the space-charge field will then vary spatially only in the z direction,

$$\frac{\partial E_{sc}(z,t)}{\partial t} = -\frac{E_{sc}(z,t)I_{dc}}{\tau_o} + \frac{E_{sc}^{ss}}{\tau_o}\left[A_1(t)A_2^*(z,t)\right]. \qquad 4.53$$

A useful form of equation 4.53 which is used extensively in chapter 7 for modeling the phased-array jammer nuller processor dynamics is in terms of a unitless grating perturbation $G(t)$. This quantity is actually the grating amplitude diffraction efficiency because in the jammer-nulling processor dynamics analysis the diffracted term is modelled as the product $G(t)A(t)$. The transformation from $\partial E_{sc}/\partial t$ to $\partial G/\partial t$ is obtained by first defining a unitless amplitude diffraction efficiency per unit-length $g(z,t)$, proportional to $E_{sc}(z,t)$ by

$$g(z,t) = \frac{\pi n^3 r_{eff} E_{sc}(z,t)}{\lambda} \qquad 4.54$$

where n is the background material refractive index and r_{eff} is the effective electrooptic coefficient. Substitution of $g(z,t)$ into 4.53 yields

$$\frac{\partial g(z,t)}{\partial t} = -\alpha g(z,t)I_{dc} + bA_1(t)A_2^*(z,t) \qquad 4.55$$

where

$$\alpha = \frac{1}{\tau_o} \qquad 4.56 \qquad\qquad b = \frac{\pi n^3 r_{eff} E_{sc}^{ss}}{\lambda \tau_o}. \qquad 4.57$$

Recalling that equation (4.25) predicted a sinusoidal holographic diffraction efficiency for small coupling and negligible momentum mismatch. Assuming equal coupling coefficients, the diffraction efficiency can be written as

$$\eta \approx \sin^2(\kappa L). \qquad 4.58$$

Noting that $g(z,t)$ is amplitude diffraction efficiency/length, more generally the amplitude diffraction efficiency can be expressed as

$$G(t) \approx \sin\left(\int_0^L g(z,t)dz\right). \qquad\qquad 4.59$$

In the Born approximation, $g(z,t)$ is very small and approximately constant along the length L of the crystal. Assuming realistic values of L, and approximating the sin function by its argument, $G(t)$ can then be expressed as

$$G(t) = \int_0^L g(z,t)dz \approx g(t)L \qquad\qquad 4.60$$

Using this definition, equation 4.55 can be written as

$$\frac{\partial G(t)}{\partial t} = -\alpha G(t)I_{dc} + \beta A_1(t)A_2^*(t) \qquad\qquad 4.61$$

where in the Born approximation it is also assumed that $A_2(z,t)$ varies negligibly over the crystal length L, and β is defined as

$$\beta = \frac{\pi n^3 r_{\it eff} E_{sc}^{ss} L}{\lambda \tau_o}. \qquad\qquad 4.62$$

In the steady-state equation 4.61 yields

$$G = \frac{A_1 A_2^*}{I_{dc}}\left(\frac{\beta}{\alpha}\right) \qquad\qquad 4.63$$

which when using the definition[59] of $\Delta n = n^3 r_{\it eff} E_{sc}/2$ and equation 4.27 for the space-charge field can be written as

$$G = \frac{A_1 A_2^*}{I_{dc}}\left(\frac{\pi n^3 r_{\it eff} E_{sc}^{ss} L}{\lambda}\right) = \frac{\pi \Delta n L}{\lambda} \qquad\qquad 4.64$$

and it is evident that G is the diffraction efficiency in the small-signal limit due to an interaction length[2] of L. The function $G(t)$ and it's steady-state value will prove useful in estimating performance limits of the jammer-nulling processor in subsequent chapters.

87

The analogy between $G(t)$ and a that of a time-integrated weight is apparent when $G(t)$ is expressed in integral form. As discussed further in Chapters 6 and 7, one of the hologram writing beams is passed through a continuous delay-line, allowing $G(t)$ to be expressed as a temporal correlation between the two writing beams with a decay term proportional to grating strength,

$$G(t) = -\alpha I_{dc} \int_0^t G(t)dt + \beta \int_0^t A_1(t)A_2^*(t-\tau)dt.$$

4.65

The grating diffraction efficiency builds-up in proportion to the time integrated product of the spatially varying portion of the intensity, and suffers from a decay due to the D.C. intensity term.

The speed of the photorefractive grating process is often characterized in terms of the intensity dependent photorefractive time constant τ. In the phased-array jammer nulling processor, one of the two writing beams incident on the PRC is derived from an amplified error signal between the desired array response and the actual jammer corrupted received array signal. This error signal is highly amplified in the RF domain before being shifted up to an optical carrier and incident on the PRC. Due to the fact that we are implementing a feedback system with gain, the convergence time to jammer suppression can be much faster than the characteristic steady-state grating response time characterized by the time constant τ. For this reason we are not in general concerned with the time constant for writing a grating fully to saturation, but instead more interested in the photorefractive sensitivity, a measure of the amount of change in refractive index for a given amount of absorbed energy density. The photorefractive sensitivity is defined as[60]

$$S = \frac{\Delta n}{\alpha I \tau}$$

4.66

where I is the incident power density. From equation 4.66 it is apparent that materials most desirable for our purposes do indeed have a small time constant, but in addition also have a large Δn, which is essentially proportional to the dopant density. Increased sensitivity can be obtained by using 45 degree-cut $BaTiO_3$ crystals[61,62] which allow more efficient access to the large r_{42} electrooptic coefficient.

References

[1]   P.J. van Heerden, "Theory of Optical Information in Solids," Appl. Opt. **2**, no. 4, 393-400 April (1963).

[2]   H. Kogelnik, "Coupled wave theory for thick hologram gratings," Bell. Syst. Tech. J. **48**, 2909-2945 (1969).

[3]   D. Gabor and G.W. Stroke, "The theory of deep holograms," Proc. Roy. Soc. **A304**, 275 (1968).

[4]   W.C. Sweatt, "Designing and constructing thick holographic optical elements," Appl. Opt. **17**, no. 8, 1220-1227 April (1978).

[5]   M.R.B. Forshaw, "The imaging properties and aberrations of thick transmission holograms," Opt. Acta **20**, no. 9, 669-686 (1973).

[6]   J.F. Heanue, M.C. Bashaw, and L. Hesselink, "Volume holographic storage and retrieval of digital data," Science **265**, 749-737 August (1994).

[7]   E.N. Leith, A. Kozma, J. Upatniks, J. Marks, and N. Massey, "Holographic data storage in three-dimensional media," Appl. Opt. **5**, no. 8, 1303-1311 August (1966).

[8]   F.H. Mok, "Angle-multiplexed storage of 5000 holograms in lithium niobate," Opt. Lett. **18**, no. 11, 915-917 (1993).

[9]   J. White and A. Yariv, "Real-time image processing via four-wave mixing in a photorefractive medium," Appl. Phys. Lett. **37**, 5-7 (1980).

[10]   L. Pichon and J.P. Huignard, "Dynamic joint-Fourier transform correlator by Bragg diffraction in photorefractive Bi12SiO20 Crystals," Opt. Commun. **36**, 277-280 (1981).

[11]   V. Markov, S. Odoulov, and M. Soskin, "Dynamic holography and optical image processing," Opt. Laser Tech. **11**, 95-99 (1979).

[12]   P. Yeh, D. Zhang, and C. Gu, "Parallel subtraction of Fourier power spectrum using holographic interferometry," Opt. Lett. **17**, 70-72 (1992).

[13]   A.E. Chiou and P. Yeh, "Parallel image subtraction using a phase-conjugate Michelson interferometer," Opt. Lett **11**, 306-308 (1986).

[14]   D.S. Oliver, P. Vohl, R.E. Aldrich, M.E. Behrndt, W.R. Buchan, R.C. Ellis, J.E. Genthe, J.R. Goff, S.L. Hou, and G. m Daniel, "Image storage and optical readout in a ZnS device," Appl. Phys. Lett. **17**, 416-418 (1970).

[15]   M.P. Petrov, A.V. Khomenko, M.V. Krasin'kova, V.I. Marakhonov, and M.G. Shylyagin, "The PRIZ image converter and its use in optical data processing systems," Sov. Phys.-Tech. Phys **26**, 816-821 (1981).

[16]   Y. Shi, D. Psaltis, A. Marrakchi, and J. A.R. Tanguay, "Photorefractive incoherent-to-coherent optical converter," Appl. Opt. **22**, 3665-3667 (1983).

[17]   D.Z. Anderson and J. Feinberg, "Optical Novelty Filters," IEEE J. Quant. Elec. **25**, 635-647 (1989).

[18]   D.L. Staebler and J.J. Amodei, "Coupled-wave analysis of holographic storage in LiNbO3," J. Appl. Phys. **43**, 1043-1049 (1972).

[19]   N. Kukhtarev, V. Markov, S. Odoulov, M. Soskin, and V. Vinetski, "Holographic storage in electrooptic crystals. I. Steady-state," Ferroelectrics **22**, 946-960 (1979).

[20]   N. Kukhtarev, V. Markov, S. Odoulov, M. Soskin, and V. Vinetski, "Holographic storage in electrooptic crystals.II. Beam-coupling-light amplification," Ferroelectrics **22**, 5061-5076 (1979).

[21]   K. Wagner and D. Psaltis, "Multilayer optical learning networks," Appl. Opt. **26**, 5061-5076 (1987).

[22]   Y. Owechko, "Cascaded-grating holography for artificial neural networks," Appl. Opt. **32**, 1380-1398 (1993).

[23]   I.M. Bel'dyugin, M.V. Zolotarev, and K.A. Sviridov, "Optical neural computers based on photorefractive crystals," Sov. J. Quant. Electron. **22**, 384-399 (1992).

[24]   D. Psaltis, J. Yu, and J. Hong, "Bias free time-integrating optical correlator using a photorefractive crystal," Appl. Opt. **24**, 3860-3865 (1985).

[25]   J. Khoury, V. Ryan, C. Woods, and M. Cronin-Golomb, "Photorefractive optical lock-in detector," Opt. Lett. **16**, 1442-1444 (1991).

[26] J. Khoury, V. Ryan, and M. Cronin-Golomb, "Photorefractive frequency converter and phase-sensitive detector," J. Opt. Soc. Am. B **10**, 72-82 (1993).

[27] R.T. Weverka and K. Wagner, "Adaptive phased-array radar processing using photorefractive crystals," in *Optoelectronic Signal Processing for Phased-Array Antennas II,* B.M. Hendrickson and G.A. Koepf, ed. Proc. Soc. Photo-Opt. Instrum. Eng. **1217**, 173-182 (1990).

[28] A.W. Sarto, R.T. Weverka, and K. Wagner, "Beam-steering and jammer-nulling photorefractive phased-array radar processor," in *Optoelectronic Signal Processing for Phased-Array Antennas IV,* Proc. Soc. Photo-Opt. Instrum. Eng. **2155,** 378-388 (1994).

[29] R.M. Montgomery and M.R. Lange, "Photorefractive adaptive filter structure with 40-dB interference rejection," Appl. Opt. **30**, 2844-2849 (1991).

[30] F. Vachss, J. Hong, and C. Keefer, "Adaptive signal processing using a photorefractive time integrating correlator," DARPA/Rome Labs Proc. **PSAA-91**, 127-132 (1991).

[31] B. Widrow and S.D. Stearns, *Adaptive signal Processing.* Prentice-Hall Inc, N.J., 1985.

[32] R.T. Weverka, K. Wagner, and A.W. Sarto, "Adaptive phased-array radar processing using photorefractive crystals," Submitted to Appl. Opt..

[33] J.P. Huignard and P. Gunter, *Photorefractive Materials and their Applications*, vol. 61, Topics in Applied Physics. Berlin: Springer-Verlag, 1989.

[34] J.P. Huignard and P. Gunter, *Photorefractive Materials and their Applications*, vol. 62, Topics in Applied Physics. Berlin: Springer-Verlag, 1989.

[35] F. Seitz, "Color Centers in Alkali Halide Crystals II," Rev. Modern Phys. **26**, no. 1, 7-94 Jan (1954).

[36] T. Huang, "Physics and Applications of Photoanisotropic Organic Volume Holograms," Ph.D. thesis, University of Colorado, 1993.

[37] J.J. Amodei and D.L. Staebler, "Holographic pattern fixing in electro-optic crystals," Appl. Phys. Lett. **18**, no. 12, 540-542 June (1971).

[38] F. Micheron and G. Bismuth, "Electrical control of fixation and erasure of holographic patterns in ferroelectric materials," Appl. Phys. Lett. **20**, no. 2, 79-81 January (1972).

[39]   A. Yariv and P.Yeh. , *Optical waves in crystals.* (John Wiley & Sons, N.Y., 1984), chap. ch. 9.

[40]   J. Feinberg, D. Heiman, J. A. R. Tanguay, and R.W. Hellwarth, "Photorefractive effects and light-induced charge migration in barium titanate," J. Appl. Phys. **51**, no. 3, 1297-1305 March (1980).

[41]   J.J. Amodei, "Analysis of transport processes during holographic recording in insulators," RCA review **32**, 185-198 June (1971).

[42]   G.C. Papen, B.E.A. Saleh, and J.A. Tataronis, "Analysis of transient phase conjugation in photorefractive media," J. Opt. Soc. Am. B **5**, no. 8, 1763-1774 August (1988).

[43]   M.G. Moharam, T.K. Gaylord, and R. Magnusson, "Holographic grating formation in photorefractive crystals with arbitrary electron transport lengths," J. Appl. Phys. **50**, no. 9, 5642-5651 Sept. (1979).

[44]   L. Young, W.K.Y. Wong, M.L.W. Thewalt, and W.D. Cornish, "Theory of phase holograms in lithium niobate," Appl. Phys. Lett. **24**, no. 6, 264-265 March (1974).

[45]   P. Yeh, *Introduction to Photorefractive Nonlinear Optics.* New York: (John-Wiley & Sons, 1993), chap. 4.

[46]   Y. Fainman, E. Klancnik, and S.H. Lee, "Optimal coherent image amplification by two-wave coupling in photorefractive BaTiO3," Optical Engineering **25**, no. 2, 228-234 February (1986).

[47]   J. Feinberg, D. Heiman, J. A. R. Tanguay, and R.W. Hellwarth, "Photorefractive effects anf light-induced charge migration in barium titanate, erratum," J. Appl. Phys. **52**, no. 1, 537 January (1981).

[48]   J.O. White, S.K. Kwong, and M. Cronin-Golomb, *Photorefractive Materials and their Applications*, vol. 62, Topics in Applied Physics. (Springer-Verlag, 1989), chap. 4, pp. 106.

[49]   M. Segev, Y. Ophir, and B. Fischer, "Nonlinear multi two wave mixing, the fanning process and its bleaching in photorefractive media," Opt. Comm. **77**, no. 2.3, 265-274 June (1990).

[50]   G. Zhang, Q.X. Li, P.P. Ho, S. Liu, Z.K. Wu, and R.R.A. , "Dependence of specklon size on the laser beam size via photo-induced light scattering in $LiNbO_3$:Fe," Appl. Opt. **25**, no. 17, 2955-2958 Sept (1986).

[51]   N. Kukhtarev, V. Markov, and S. Odulov, "Transient energy transfer during hologram formation in LiNbO3 in external electric field," Opt. Comm. **23**, no. 3, 338-343 December (1977).

[52]   J.M. Heaton and L. Solymar, "Transient energy transfer during hologram formation in photorefractive crystals," Opt. Acta **32**, no. 4, 397-408 (1985).

[53]   M. Cronin-Golomb, "Analytic solution for photorefractive two-beam coupling with time-varying signals," in *Digest of Topical Meeting on Photorefractive Materials, Effect and Devices,* Optical Society of America, 142 (1987).

[54]   M. Horowitz, D. Kligler, and B. Fischer, "Time-dependent behavior of photorefractive two- and four-wave mixing," J. Opt. Soc. Am. B **8**, no. 10, 2204-2217 Oct. (1991).

[55]   A. Hermanns, C. Benkert, D.M. Lininger, and D.Z. Anderson, "The transfer function and impulse response of photorefractive two-beam coupling," IEEE Journ. Quant. Elec. **28**, no. 3, 750-756 March (1992).

[56]   F.P. Strohkendl, J.M.C. Jonathan, and R.W. Hellwarth, "Hole-electron competition in photorefractive gratings ," Optics Letters **11**, no. 5, 312-314 May (1986).

[57]   M. Saffman, "Self-Organized Formation of Image Representations in Photorefractive Oscillators," Ph.D. thesis, University of Colorado, 1994.

[58]   S. Ducharme and J. Feinberg, "Speed of the photorefractive effect in a BaTiO3 single crystal," J. Appl. Phys. **56**, no. 3, 839-842 August (1984).

[59]   P. Yeh, *Introduction to Photorefractive Nonlinear Optics.* New York: (John Wiley & Sons, 1993), chap. 1.

[60]   J.P. Huignard and P. Gunter, *Photorefractive Materials and their Applications*, vol. 62, Topics in Applied Physics. Berlin: (Springer-Verlag, 1989), chap. 6, pp. 205-206.

[61]   J.E. Ford, Y. Fainman, and S.H. Lee, "Enhanced photorefractive performance from 45 degree-cut BaTiO3," Appl. Opt. **28**, no. 20, 4808 (1989).

[62]   M.H. Garrett, J.Y. Chang, H.P. Jenssen, and C. Warde, "High photorefractive sensitivity in an n-type 45 degree-cut BaTiO3 crystal," Opt. Lett. **17**, no. 2, 103-105 January (1992).

5. Simultaneous Holographic Write/Read Techniques in Photorefractive Crystals

This chapter will discuss two methods for separating and extracting the diffracted term from the writing beams in dynamic volume holographic interactions. In conventional dynamic holographic geometries the write beams and diffracted beams are co-propagating. In order to extract the diffracted output a method of separating the diffracted term from the write beam is necessary. Common methods of reading out the weights are by probing the grating from the back side with a different beam from the write beams in a phase conjugate geometry[1], or by forming a Bragg matched readout with another wavelength and using spectral filtering to extract the desired component[2]. These weight values are then available to multiply an RF signal at the appropriate time delays, for example by using an acousto-optic Bragg cell implemented as a space-integrating transversal filter[3,4]. The LMS algorithm requires feedback with gain, and hence a read-out method which provides a high degree of isolation between the write and read components is critical, because write-beam leakage can drive the system into oscillation. To avoid oscillation at a given level of isolation, a maximum feedback gain will be allowed which limits processor performance by compromising convergence time and interference rejection depth. In addition, the angular bandwidth over which Bragg matched readout is possible (due to Bragg selectivity) is of interest when processing is done with wavefronts containing diverse angular spectra such as images. Wide angular bandwidth is especially important with PRCs due to the small crystal size, since the product of angular bandwidth and crystal size must exceed the number of resolvable degrees-of-freedom.

Two different write/read, or multiplexing, techniques with high write/read isolation for dynamic holographic media will be discussed in this chapter. The two methods, angle multiplexing using Bragg degeneracy, and orthogonal polarization write/read have both been used extensively in our optical phased-array radar processor.

The latter method has potential applications in image processing because of the extremely wide angular aperture over which phase-matching can occur. The chapter begins with an introduction to momentum space, or k-space, followed by a discussion of the two multiplexing techniques.

5.1 Introduction to Momentum Space

A momentum space, or k-space approach for analyzing the angular dependence of the diffracted beams in holograms is valid in the low diffraction efficiency regime[5,6,7,8]. This method of analysis leads to a clear geometric interpretation of the interacting beams and a convenient method for rapidly approximating diffraction properties. Momentum space is used extensively in this chapter and thus a brief introduction to momentum space is warranted. A frequently used parameter used in this chapter is the momentum mismatch ΔK, which was also developed in the previous chapter's discussion of the 1-D coupled-mode equations.

In an anisotropic crystal there are two allowed eigenmodes of propagation with distinct polarization phase velocities and polarization orientation for any given propagation direction within the crystal[9]. Associated with each of these eigenmodes is a distinct eigenvalue for the magnitude of the momentum vector $\left|\vec{k}\right|$. For a uniaxial crystal, the $\vec{k}$ vectors are confined to two surfaces of revolution, a sphere and an ellipse, referred to as momentum surfaces. These surfaces are proportional by the vacuum momentum $k_o = 2\pi/\lambda_o$ to the index surfaces which are characterized by the ordinary index n_o and the extraordinary index n_e, and are the loci of allowed propagation values and directions within the crystal. The momentum surfaces can be derived by first assuming a planewave propagating in an anisotropic media, with electric and magnetic field components described by

$$\overline{E} = E e^{i(\vec{k}\cdot\vec{r}-\omega t)} \qquad 5.1 \qquad\qquad \overline{H} = H e^{i(\vec{k}\cdot\vec{r}-\omega t)}. \qquad 5.2$$

Substitution into Maxwell's equation and elimination of the magnetic component yields

$$\bar{k} \times (\bar{k} \times \overline{E}) + \omega^2 \mu_o \underline{\underline{\varepsilon}} \overline{E} = 0 \qquad 5.3$$

where in the principal coordinate system the dielectric tensor is.

$$\underline{\underline{\varepsilon}} = \begin{bmatrix} \varepsilon_{11} & 0 & 0 \\ 0 & \varepsilon_{22} & 0 \\ 0 & 0 & \varepsilon_{33} \end{bmatrix} \qquad 5.4$$

Rewriting equation (5.3) as

$$\left[k_i k_j - \delta_{ij} k^2 + \omega\mu\varepsilon_{ij} \right] E_j = 0 \qquad 5.5$$

Nontrivial solutions will exist only when the determinant of the matrix in the brackets of equation (5.5) is equal to zero,

$$\det\left[k_i k_j - \delta_{ij} k^2 + \omega\mu\varepsilon_{ij} \right] = 0. \qquad 5.6$$

Expanding the determinant yields Fresnel's equation

$$k^2\left(\varepsilon_{11} k_1^2 + \varepsilon_{22} k_2^2 + \varepsilon_{33} k_3^2\right) - \left[\varepsilon_{11} k_1^2\left(\varepsilon_{22} + \varepsilon_{33}\right) + \varepsilon_{22} k_2^2\left(\varepsilon_{11} + \varepsilon_{33}\right) + \varepsilon_{33} k_3^2\left(\varepsilon_{11} + \varepsilon_{22}\right)\right] k_o^2$$
$$+ \varepsilon_{11}\varepsilon_{22}\varepsilon_{33} k_o^4 = 0. \qquad 5.7$$

In a uniaxial crystal, equation (5.7) simplifies to

$$\left[k^2 - \varepsilon_{11} k_o^2\right]\left[\varepsilon_{11}\left(k_1^2 + k_2^2\right) + \varepsilon_{33} k_3^2 - \varepsilon_{22}\varepsilon_{33} k_o^2\right] = 0 \qquad 5.8$$

which can be factored into two quadratic equations defining a sphere corresponding to the ordinary polarization with radius

$$k_{ord} = k_o\sqrt{\varepsilon_{11}} = k_o n_o \qquad 5.9$$

and an ellipsoid of revolution about the k_3 axis corresponding to the extraordinary polarized eigenmode, described by

$$\left[\left(k_1^2 + k_2^2\right)/\varepsilon_{33}\right] + k_3^2/\varepsilon_{11} = k_o^2 \qquad\qquad 5.10$$

which can be described in the x-z plane as

$$k_{ext}(\theta) = k_o\left[\sin^2(\theta)/n_e^2 + \cos^2(\theta)/n_o^2\right]^{-1/2} = k_o n_e(\theta) \qquad\qquad 5.11$$

where θ is the angle measured from the z-axis. The two wavevectors described by equations (5.9) and (5.11) correspond to the two eigenmodes of propagation within the crystal. The 3-D surfaces mapped out by these wavevectors in k-space are thus the loci of allowed propagation modes within the crystal.

Alternatively one can view k-space as a reciprocal space, related to real space by a Fourier transform relationship[10]. In this light, any point in momentum space corresponds to an infinite planewave in real space, and thus planewaves are represented as delta functions in momentum space, often drawn as a vector propagating at a corresponding angle in momentum space usually defined with respect to the C-axis of the crystal. Figure 5.1 shows two planewaves $\bar{k}_{w1}$ and $\bar{k}_{w2}$ incident upon a slab of isotropic holographic recording media. The center portion of the figure is the momentum space representation where a hologram is read out with plane wave $\bar{k}_r$ producing diffracted plane wave $\bar{k}_d$. These two plane waves are represented as vectors in momentum space which ideally intersect the k-space surface. Each spectral component of the hologram formed in the media is represented as a single grating vector, with there only being one shown in the figure.

In order to read out the grating inside the media, the incident read-out beam must satisfy the Bragg condition $\lambda = 2\Lambda \sin(\theta_B/2)$, where Λ is the grating spacing. This condition is only precisely true for infinitely thick media. In a holographic media of finite dimensions, the Bragg matching constraint can be relaxed. This results in a

97
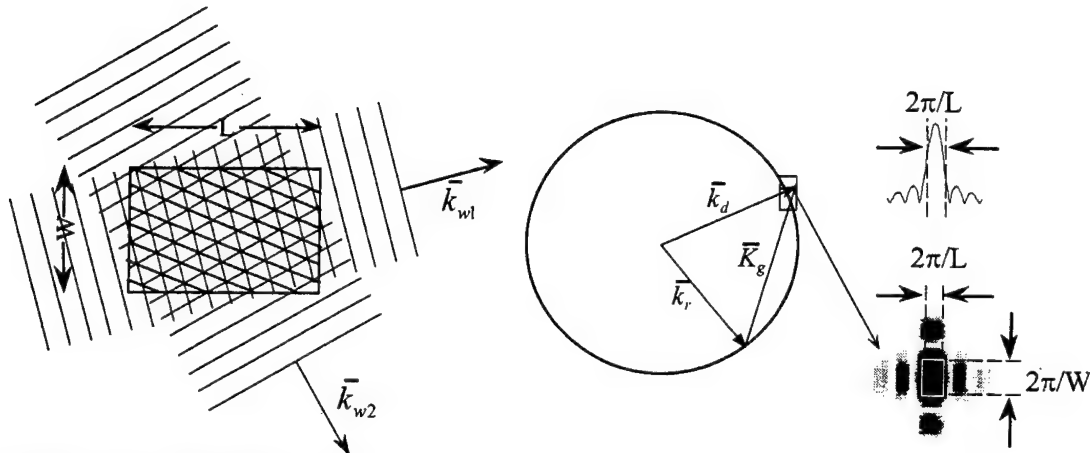
Figure 5.1. Rectangular holographic interaction region of dimensions LxW creates two-dimensional sinc^2 in Fourier space. The half-width to the first zero in each dimension of the sinc^2 function, corresponding to $2\pi/L$ and $2\pi/W$, define the momentum uncertainty box in two dimensions.

finite resolvability in diffraction angles, which is analogous to tolerance with respect to incident phase-matching angles. Equation 4.25 of Section 4.1.1 describes the diffraction efficiency of a single volume holographic grating as determined from the coupled mode theory. When read out at precisely the Bragg angle, i.e. when the momentum mismatch $\Delta K = 0$, 100% diffraction efficiency can theoretically be obtained. This is in accordance with the exact Bragg matching condition stated above. Deviations away from this ideal incident angle result in a sinc^2 dependent roll-off in the diffraction efficiency with momentum mismatch as derived in section 4.1.1. The momentum and phase matching tolerances depend on the physical dimensions of the holographic interaction region. Insight into the role played by the crystal dimensions can be gained by a momentum space analysis, and the same sinc^2 result for the diffraction efficiency behavior can be obtained as was done using the 1-D coupled-mode analysis.

In general, momentum matching tolerances must be met for all three dimensions of a finite media. In particular, the diffraction properties of the diffracted wave will be determined by the momentum matching conditions in three dimensional k-space. The

98

circular region of allowed propagation values for 2-D shown in figure 5.1 must be extended to 3-D, corresponding to either the spherical or ellipsoidal k-space surfaces of revolution, depending upon the polarization of the eigenmode. In addition, the Fourier transform relationship between real space and k-space causes a given dielectric perturbation which is confined to finite boundaries in real space to become a smoothed function in k-space. It is this smoothing operation, manifested as a convolutional operation between the spatial frequency content of the grating and the Fourier transform of the media boundaries which significantly alters the angular selectivity and response from that predicted by the classic Bragg condition.

The diffracted wave can be expressed as a transverse Fourier expansion of its plane wave components k_x and k_y in the unperturbed media, which propagate nominally in the z direction,

$$\bar{E}_d(\bar{r}) = \int \tilde{E}_d\Big[k_x,k_y,k_{dz}\big(k_x,k_y\big)\Big]e^{i(k_x x+k_y y)}e^{ik_{dz}(k_x,k_y)z}dk_x dk_y \qquad 5.12$$

where the z component of the propagation vector k_{dz} for the field is expressed as a function of its transverse components, given by $k_{dz}(k_x,k_y) = \sqrt{k_d^2 - k_x^2 - k_y^2}$ for isotropic media, where $k_d = 2\pi n_o/\lambda_o$ is the magnitude of the diffracted wave vector. This form for the diffracted wave can be substituted into the wave equation given by (4.4), where the electric field is the sum of an incident and diffracted term, $\bar{E} = \bar{E}_i + \bar{E}_d$. A coupled-mode solution followed by a transverse Fourier transform in x and y, results in an expression describing the field of the diffracted wave at a distance L in the media containing the dielectric perturbation[7],

$$\tilde{E}_d\big(k_x,k_y,L\big) = \frac{i\omega^2}{2c^2 k_{dz}\big(k_x,k_y\big)}\int \delta\Big[k_z - k_{dz}\big(k_x,k_y\big)\Big]FT\{\Delta\varepsilon(\bar{r})E_i(\bar{r})\}dk_z \qquad 5.13$$

where FT is a 3-D Fourier transform defined by

$$FT\{f\} \equiv \int_{-\infty}^{\infty} f(x,y,z)e^{-i(k_x x+k_y y+k_z z)}dxdydz \qquad 5.14$$

99

Equation 5.13 shows that the angular spectra of the diffracted wave $\tilde{E}_d\left(k_x, k_y, L\right)$ for a crystal of length L is proportional to the 3-D Fourier transform of the product of the incident read beam amplitude $E_i(\bar{r})$ and the dielectric perturbation $\Delta\varepsilon(\bar{r})$, evaluated on the surface of allowed propagation modes, i.e. on the momentum surface corresponding to the eigenmode of the diffracted wave.

As an example, consider a dielectric perturbation consisting of a single spatial frequency and corresponding grating vector denoted by $\bar{K}_g = 2\pi/\Lambda$ with modulation amplitude $\Delta\varepsilon_{K_g}$, bounded by the rectangular interaction region with dimensions L_x, L_y, and L_z. This dielectric perturbation can be expressed as

$$\Delta\varepsilon(\bar{r}) = \text{rect}(x/L_x)\text{rect}(y/L_y)\text{rect}(z/L_z)\Delta\varepsilon_{K_g} e^{i(\bar{K}_g \cdot \bar{r})}. \qquad 5.15$$

An incident planewave field with constant amplitude expressed as $A_i e^{i[k_{ix}x + k_{iy}y + k_{iz}z]}$ is now used to read out the hologram. The Fourier transform term of equation (5.13) becomes

$$FT\{\Delta\varepsilon(\bar{r})E_i(\bar{r})\} = FT\left\{\left(\Delta\varepsilon_{K_g}\text{rect}(x/L_x)\text{rect}(y/L_y)\text{rect}(z/L_z)e^{i(\bar{K}_g \cdot \bar{r})}\right)A_i e^{i[k_{ix}x + k_{iy}y + k_{iz}z]}\right\}. 5.16$$

This can be expressed as a convolution of the Fourier transforms

$$FT\{\Delta\varepsilon(\bar{r})E_i(\bar{r})\} = FT\{\Delta\varepsilon(\bar{r})\} * FT\{E_i(\bar{r})\} \qquad 5.17$$

where the Fourier transform of the dielectric perturbation can also be expressed as a convolution between the Fourier transforms of the interaction region and the grating vector.

$$FT\{\Delta\varepsilon(\bar{r})\} = FT\{\Delta\varepsilon_{K_g}\text{rect}(x/L_x)\text{rect}(y/L_y)\text{rect}(z/L_z)\} * FT\{e^{i(\bar{K}_g \cdot \bar{r})}\}. \qquad 5.18$$

The resulting Fourier transform is then

$$FT\{\Delta\varepsilon(\bar{r})E_i(\bar{r})\} = \tag{5.19}$$

$$\Delta\varepsilon_{K_g} A_i L_x L_y L_z \, \text{sinc}\left[\frac{k_x - \left(K_{gx} - k_{ix}\right)}{2\pi/L_x}\right] \text{sinc}\left[\frac{k_y - \left(K_{gy} - k_{iy}\right)}{2\pi/L_y}\right] \text{sinc}\left[\frac{k_z\left(k_x,k_y\right) - \left(K_{gz} - k_{iz}\right)}{2\pi/L_z}\right].$$

Substituting equation (5.19) into equation (5.13) and carrying out the integration over dk_z results in

$$\tilde{E}_d\left(k_x,k_y,L\right) = \tag{5.20}$$

$$\frac{i\omega^2 \Delta\varepsilon_{K_g} A_i L_x L_y L_z}{2c^2 k_{dz}\left(k_x,k_y\right)} \, \text{sinc}\left[\frac{k_x - \left(K_{gx} - k_{ix}\right)}{2\pi/L_x}\right] \text{sinc}\left[\frac{k_y - \left(K_{gy} - k_{iy}\right)}{2\pi/L_y}\right] \text{sinc}\left[\frac{k_{dz}\left(k_x,k_y\right) - \left(K_{gz} - k_{iz}\right)}{2\pi/L_z}\right]$$

where it is re-emphasized that k_{dz} is a function of its transverse coordinates.

Equation 5.20 predicts maximum diffracted power when for perfect Bragg matching when the sinc argument is equal to zero, and a sinc^2 power roll-off with increasing momentum mismatch ΔK. For 1-D, this result is in agreement with the sinc^2 response predicted by the 1-D coupled mode theory as in equation 4.26. Evaluating the function given by equation (5.20) at a particular incidence angle will yield the relative amplitudes of the Fourier spectrum components given by the intersection of the k-space surface and the Fourier distribution. While the sidelobes of the sinc functions extend to infinity, choosing a convenient cutoff point such as the half-width to the first zero of the sinc^2 diffraction pattern in each dimension of the three dimensional sinc^2 function allows one to capture a significant amount of the diffracted angular power spectrum. This region bounded by the half power points defines the "momentum uncertainty box", as shown for the two dimensional interaction region in figure 5.1. The cutoff point corresponds to $\Delta K_j = k_j - K_{gj} - k_{ij} = \pm\pi/L_i$, for $j = x$, and y. Note the inverse dependence of the volume size on the crystal dimensions. For example, as the dimensions get very small, the sinc width gets very large, implying adequate readout for a wide angular spread of readout angles, as in planar holographic material.

Conversely, as the dimensions get infinitely large, the sinc functions approach delta functions and equation (5.17) can be written

$$\tilde{E}_d\left(k_x, k_y, L\right) = \frac{i\omega^2 A_i \Delta\varepsilon_{K_g}}{2c^2 k_{zd}\left(k_x, k_y\right)} \delta\left(\Delta K_x\right)\delta\left(\Delta K_y\right)\delta\left(\Delta K_z\right). \qquad 5.21$$

Equation 5.21 implies no allowable angular deviation from the exact Bragg matching angle, indicating that the classical Bragg condition is in fact only truly valid for infinite media. Any real sample will have finite dimensions and hence a corresponding allowable amount of phase mismatch which translates to a reduction of angular resolvability. Angular selectivity is important for the two multiplexing techniques described in this section because it determines the number of resolvable holographic gratings which can be implemented.

5.2 Angle Multiplexing using Bragg Degeneracy
5.2.1 Bragg Degeneracy

This multiplexing method involves writing two gratings between three beams and reading them out in the direction of Bragg degeneracy, producing diffracted output beams which are angularly separable from the write beams. Bragg degenerate gratings are gratings which can be accessed by more than one input-output pairs of k-vectors. Figure 5.2 shows a simple case for two distinct pairs of input-output k-vectors in 3-D momentum space. The optical wave vectors $\bar{k}_1$, $\bar{k}_2$, $\bar{k}_3$, and $\bar{k}_4$ are clearly independent, however the two gratings written $\bar{K}_{g12}$ and $\bar{K}_{g34}$ are essentially translated versions of the same grating, and hence Bragg matched to both input-output pairs of writing vectors. There are in fact an infinite number of input-output pairs which satisfy the degeneracy condition, forming "cones of Bragg degeneracy"[11] as shown in figure 5.2.Degenerate gratings are typically the bane of optical interconnect researchers. In the interconnect scenario a 2D input plane is interconnected to a 2D output plane via a 3D volume hologram. Full independent interconnection between the 2-D input and the 2-D
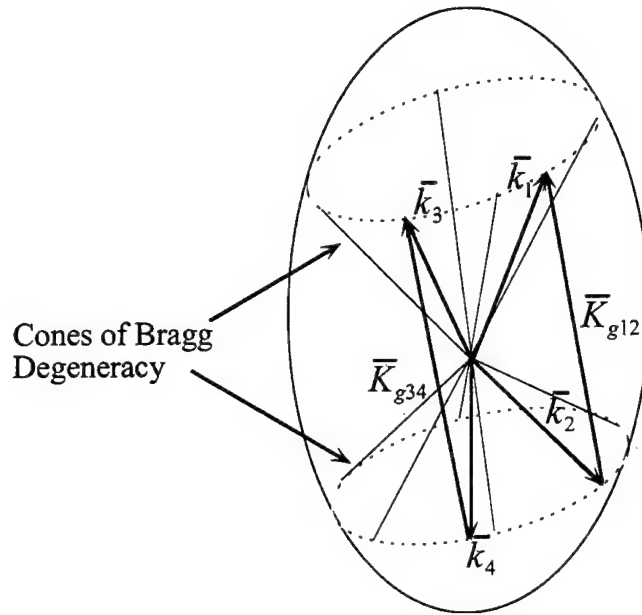
Figure 5.2. Momentum-space representation of Bragg degenerate gratings $\overline{K}_{g12}$ and $\overline{K}_{g34}$ formed between two independent sets of input-output k-vectors $\overline{k}_1$ and $\overline{k}_2$, and $\overline{k}_3$ and $\overline{k}_4$. Infinite number of possible input-output k-vector pairs map out "cones of Bragg degeneracy".

output requires a 4D interconnection. However, the actual interconnection matrix formed in a volume hologram is restricted to only 3D. The result is that some interconnections are not unique because they are related by degenerate holographic gratings. Attempts at eliminating these degenerate interconnection pairs involve sparse or fractal[12] sampling of the input-output arrays. While Bragg degeneracy is undesirable from the standpoint of interconnects, it can provide a unique method for real time holographic read/write multiplexing because an existing grating can be probed by a different (angularly resolvable) read-out beam from those which wrote the grating.

5.2.2 Implementation

The angle-multiplexing using Bragg degeneracy technique used here involves writing two gratings and reading them out in the direction of Bragg degeneracy. As discussed in more detail in following chapters, in the phased-array radar processor the
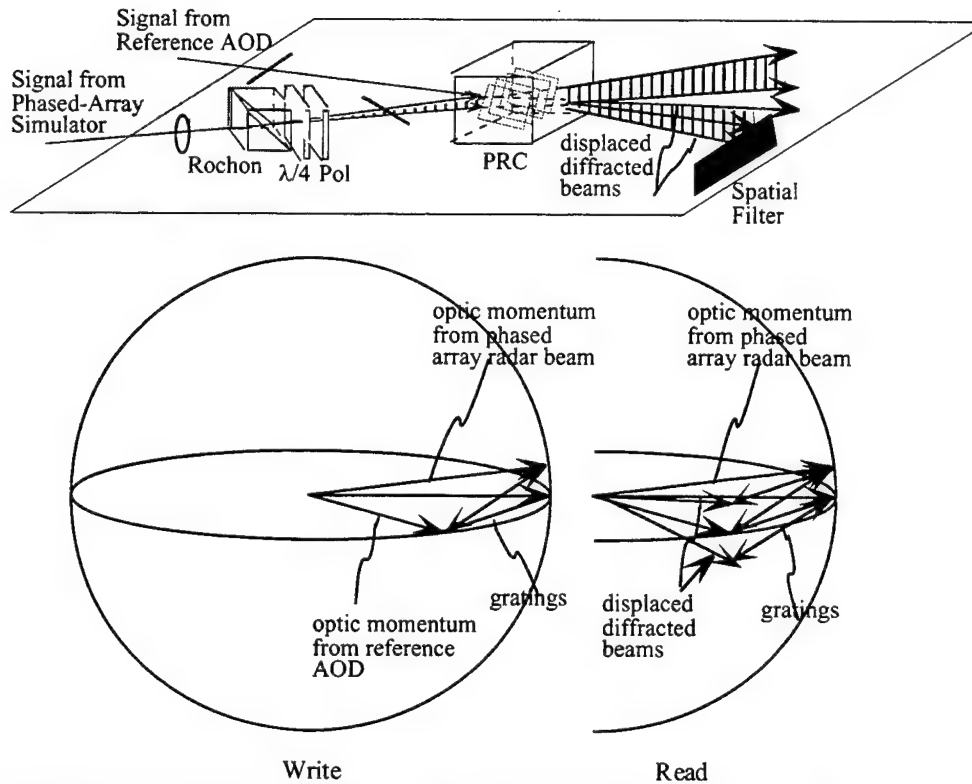
Figure 5.3. Schematic representation of angle multiplexing in Bragg degeneracy shown in real space above, and in momentum space below.

two gratings are written between the diffracted component from a reference Bragg cell and two beams from the phased-array simulator. This technique is represented in figure 5.3, where the upper figure shows three beams incident on the PRC; one from the reference AOD and two from the phased array simulator. The two beams from the simulator are replicas of each other, produced by a Rochon prism and polarization optics, and are angularly diverging from each other in the direction of Bragg degeneracy (vertical here). Each of these beams writes a grating with the reference beam. The vertical displacement of the one write beam in the Bragg degeneracy direction places the two gratings on the cone of Bragg degeneracy for the other beam. Both of the gratings produced can diffract each of the three writing beams to produce a total of 5 diffracted output beams. The read and write scenario described is shown in momentum space in the lower portion of figure 5.3. As shown in the figure, when each of the two angularly diverging beams from the simulator diffract off the grating written

104

between the other beam and the reference, two diffracted beams which are angularly separated are produced in a vertical plane from the reference beam. The angular separation of the diffracted beams allows the desired diffracted signal to be separated from the writing beams by spatial filtering in the vertical direction.

The angle multiplexing in Bragg degeneracy technique has been successively implemented in both the phased-array jammer nulling processor and the beam-steering processor. From the narrowband jammer results obtained, this read/write technique has isolation between the diffracted component and the write beam on the order of 35dB. There are several problems with this technique which limit its performance which are discussed below.

5.2.3 Performance Limitations

The primary problem is corruption of the desired diffraction term due to higher order diffractions of the reference write beam. The angle multiplexing scheme is shown in figure 5.4, where the write beams B, A_1, and A_2 are propagating in the nominal z direction (into the page) and writing gratings $G_1(A_1 B^*)$ and $G_2(A_2^* B)$. The problem arises when reference signal B diffracts first off of $G_1(A_1 B^*)$ and then off of $G_2(A_2^* B)$, resulting in some reference signal that is co-propagating with the vertically displaced diffracted beams, heterodyne detected and added with the wrong phase into the jammer estimate signal.

As shown in figure 5.4, the signal collected at the jammer estimate detector consists of the jammer estimate $A_1 G_2(A_2^* B)$, obtained by signal A_1 diffracting off of grating $G_2(A_2^* B)$ formed between A_2^* and B, and the doubly diffracted noise term of $f_2 B G_1(A_1 B^*) G_2(A_2^* B)$. The coupling coefficient f_2 accounts for the fact that there are two phased-matched interactions occurring to produce the double diffracted term. This noise term can be significant and sets a limit on the amount of isolation between the read and write beams. A more detailed treatment of the manner in which this noise term

Diffracted Term 1

$$A_1 G_2 \left(A_2^* B \right) + f_2 B G_1 \left(A_1 B^* \right) G_2 \left(A_2^* B \right)$$
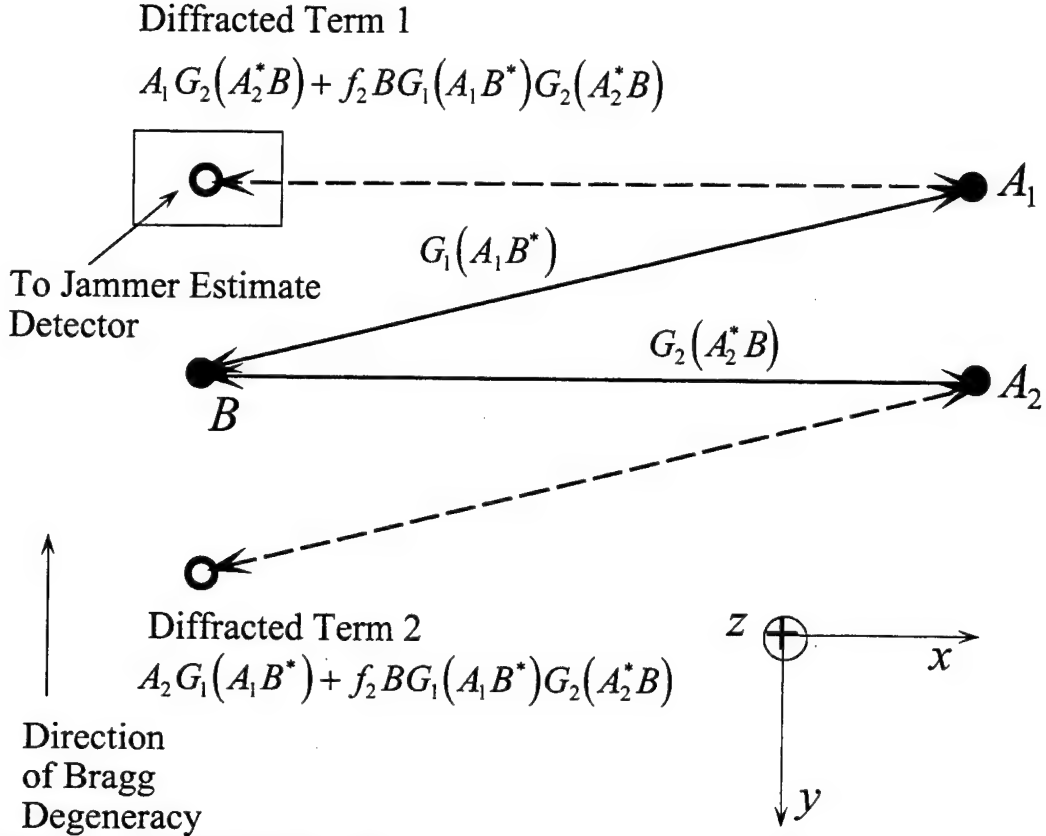
Figure 5.4. Planar representation of angle multiplexing using Bragg degeneracy technique. Write beams B, A_1, and A_2 propagate in the nominal z direction (into the page) and produce gratings $G_1 \left(A_1 B^* \right)$ and $G_2 \left(A_2^* B \right)$. A_1 and A_2 diffract off these gratings to produce the spatially and angularly separable diffracted beams at the left of the figure.

affects the SINR is treated in Chapter 6, although it is useful here to derive an estimate of the coupling coefficient f_2. Consistent with the nomenclature of the previous chapter, G is the amplitude diffraction efficiency of the grating. The amplitude diffraction efficiency η_a from a thick holographic grating can be approximated by

$$G \approx \sin \left(\int_0^z g(z) dz \right) \approx \int_0^z g(z) dz \qquad 5.22$$

where $g(z)$ is the diffraction efficiency per unit length, and the sin function has been approximated by its argument. The double diffracted term can then be modeled as

$$f_2 B G_1 G_2 = \int_0^L g_2(z) dz \int_0^z B g_1(z') dz'. \qquad 5.23$$

106

In the Born approximation the function $g(z)$ can be assumed a constant, and performing the integral of equation (5.23) yields the diffraction efficiency from a single grating as $G = gL$. Therefore equation 5.23 becomes

$$f_2 B G_1 G_2 = \frac{L^2}{2} B g_1 g_2 = \frac{B}{2} G_1 G_2$$

5.24

where it is evident that $f_2 = 1/2$. This result is consistent with results derived by Hecht [13] describing cross-modulation effects in multi-frequency acousto-optic diffraction in the small signal limit. As an example, for a grating diffraction efficiency of 5%, the leakage signal is on the order of 32 dB below the desired term and could set the lower limit on isolation.

A second problem is due to photorefractive fanning. All the optical beams used are extraordinary polarized and the fanning produced by these beams produces unwanted scattering, designated as f_o in later chapters, which can be difficult to spatial filter from the desired diffracted term. Lower frequency gratings written between the beams in the direction of Bragg degeneracy has also been observed experimentally, especially with very high gain photorefractive crystals. The result is that instead of three distinct spots being observed along the direction of Bragg degeneracy, there are now several. Up to 6 such spots have been observed using a 45 degree cut BaTiO3 crystal. Fundamentally these gratings represent a power loss with respect to the desired diffracted term, however they are presumed to be extremely small. Lastly, beam coupling effects can affect the temporal and spatial characteristics of the gratings.

5.3 Polarization-Angle Multiplexing
5.3.1 Read/write geometry

This second method uses orthogonally polarized read and write beams, and parallel tangent diffraction geometry near the condition of equal curvatures to provide spatially

separable orthogonally polarized diffracted output beams with high isolation and wide Bragg matched angular bandwidth[14] with high Bragg selectivity. The orthogonal polarization states assure no interference between the read and write beams. The write beams are ordinary polarized to reduce fanning and beam coupling effects, and the read beam is extraordinary polarized to achieve strong diffraction efficiency. The ordinary write beams and extraordinary diffracted read beams are angularly separated and easily isolated with a spatial filter and polarizer.

The polarization-angle multiplexing technique involves writing gratings with ordinary polarization and reading them out with extraordinary polarization. This is shown in figure 5.5, where a 2D momentum space diagram for an x-z cross-section of a negative uniaxial crystal with reading and writing beams in the wide-angular aperture readout geometry is shown. The degree of birefringence between the ordinary and extraordinary surfaces has been greatly exaggerated in the figure for clarity. The C-axis is along $\hat{z}$, which is an axis of rotational symmetry of the momentum surfaces. A set of grating vectors are shown written between two ordinary polarized beams; a planewave $\bar{k}_{w1}$ at θ_{w1}, and a finite angular spectra of $\bar{k}$ vectors centered at $\bar{k}_{w2}$ at angle θ_{w2}. The holographic grating $\bar{K}_g = \bar{k}_{w1} - \bar{k}_{w2}$ formed in the PRC between the ordinary planewave and one spatial component of the angular spectra of the input image is emphasized in the figure. The spectrum of grating vectors is read out by an extraordinary planewave $\bar{k}_r$ at θ_r, producing a diffracted output spectra near the parallel tangents condition[15] with central $\bar{k}$ vector $\bar{k}_e$ at θ_e, where θ_e is the angle of equal curvatures of the two momentum surfaces.

The parallel tangents condition can be achieved in a PRC when an existing spectrum of gratings is read out with an orthogonal polarization from that which wrote the gratings. In particular, this occurs at an extraordinary diffraction angle where the spectrum of gratings is tangent to the ordinary momentum surface. This condition provides first-order phase-matching over large angular bandwidth and is related to the
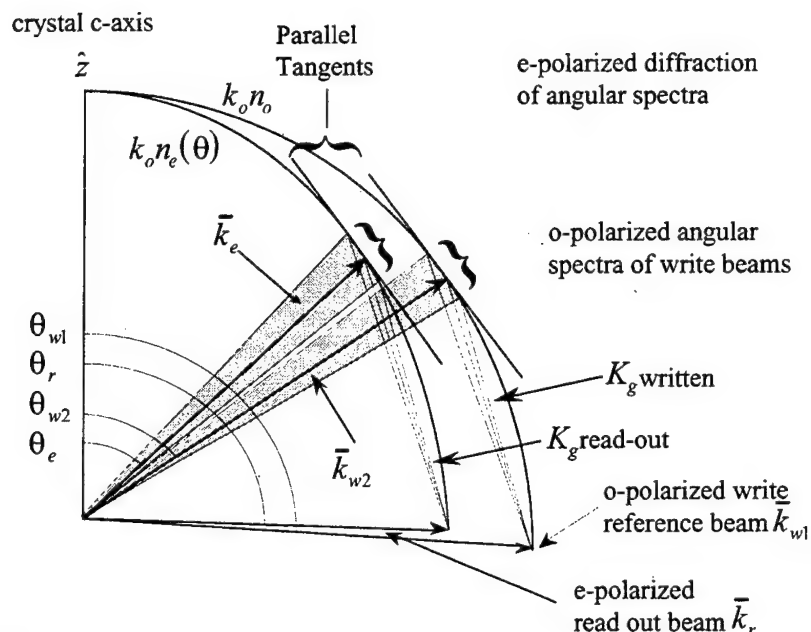
Figure 5.5. 2D momentum space diagram of a negative uniaxial photorefractive crystal, with a write reference planewave and an angularly diverse object beam. The extraordinary polarized read-out beam produces an extraordinary polarized diffracted spectra in a parallel tangents condition.

geometry of noncollinear tunable acousto-optic filters[15](TAOF). However, the write/read geometry described here should not be confused with the TAOF condition where the input and output surfaces have parallel tangents. Instead the geometry used here is more analogous to the acoustooptic geometry of tangential beam steering[16,17,18] where the locus of dielectric perturbations in momentum space is brought into tangency with the output momentum surface.

As described in Chapter 4, the holographic phase grating formed by the interference between two planewaves in a PRC is modeled as an index or permittivity perturbation in the media induced by the photogeneration of free carriers and subsequent charge transport and the linear electro-optic effect. When read out with planewave $\bar{k}_r$, each spectral component K_g gives rise to an induced polarization vector field with wave vector $\bar{k}_p = \bar{k}_r + \overline{K}_g$ in direction θ_p. Because of the orthogonally polarized readout geometry this polarization wave vector does not necessarily intersect
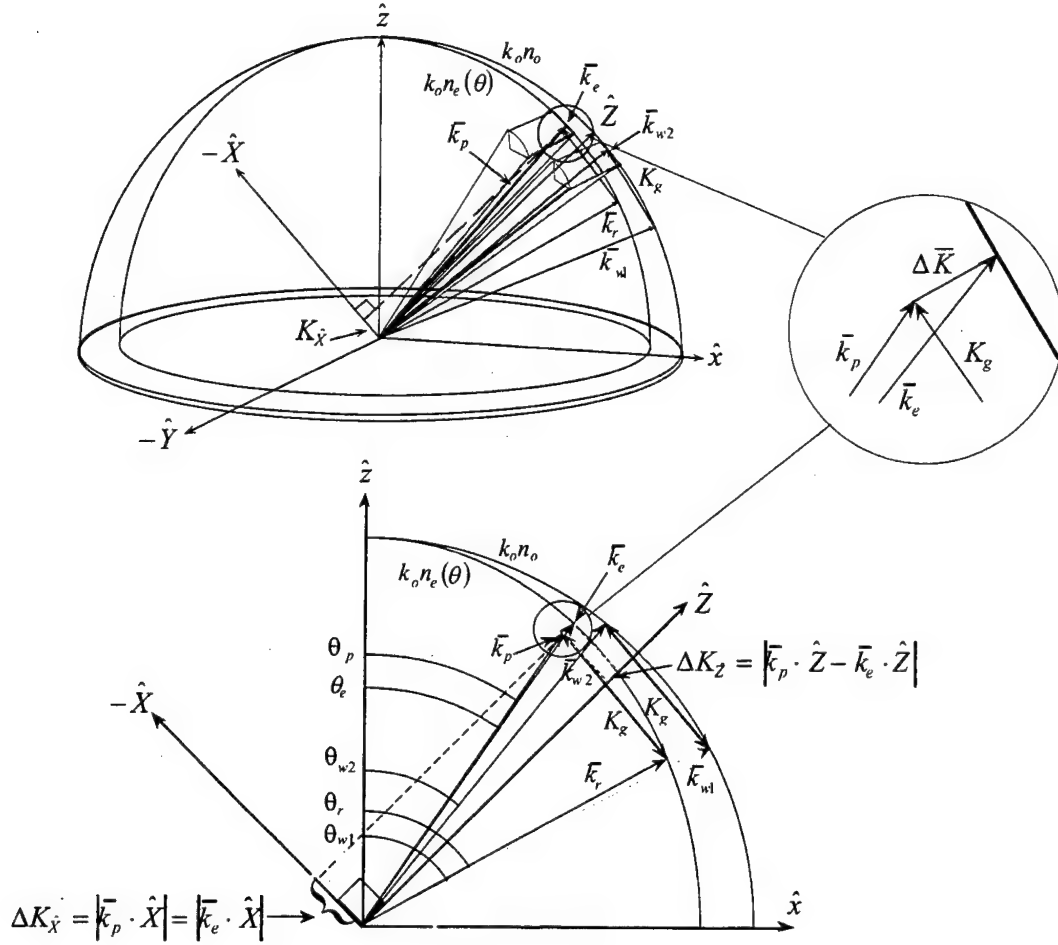
Figure 5.6. Read/write geometry in both 3 and 2D momentum space showing grating vector $\overline{K}_g$ written between $\overline{k}_{w1}$ and $\overline{k}_{w2}$ and read out by $\overline{k}_r$. Bragg mismatch results in momentum mismatched component $\Delta\overline{K}$, shown in figure inset.

the momentum surface and there will be some momentum mismatch $\Delta\overline{K}$ between this wave vector and the actual diffracted wave vector $\overline{k}_e$. Momentum mismatch and corresponding phase mismatch produces non-resonant coupling between the incident and diffracted wave resulting in a reduction of the amplitude of the diffracted wave.

The induced polarization wave is modeled as a driving vector field in the wave equation which is proportional to the product of the dielectric perturbation $\Delta\varepsilon$ formed by the interaction of the two ordinary write beams with the extraordinary readout beam electric field vector,

$$\overline{P}(x,z) \propto \Delta\varepsilon(x,z)\overline{E}(x,z).$$ 5.25

Figure 5.6 depicts the same write/read geometry as in figure 5.5, but now in 3-D, where the diffracted wave is propagating in a direction near to the crystal normal, i.e. the $\hat{Z}$ direction for a 45 degree-cut crystal, and $\hat{X}$ and $\hat{Y}$ ($\hat{Y}$ into the plane of figure) are the dimensions orthogonal to $\hat{Z}$. We assume that the two orthogonal dimensions of the crystal are much larger than that in the $\hat{Z}$ direction. This implies high Bragg selectivity in the $\hat{X}$ and $\hat{Y}$ dimensions and an intensity diffraction efficiency proportional to a sinc^2 with momentum mismatch $\Delta\overline{K}_z$, consistent with the 1-D analysis of Section 4.2. This assumes that the electric field amplitudes vary only along the $\hat{Z}$ direction and the coupling is small. Thus it is assumed that significant momentum mismatch exists only in the $\hat{Z}$ direction. After substituting the induced polarization into the wave equation, a coupled mode solution allows the diffraction efficiency η to be calculated via equation 4.20, where the coupling constant κ is obtained from equation 4.31.

5.3.2 Tangents and Curvatures

The parallel tangents condition can be derived for the x-z plane by equating the slopes of the two momentum surfaces expressed as functions of angle θ from the C-axis, where θ_{w2} and θ_e are the angles measured from the C-axis of the crystal for the ordinary and extraordinary surfaces respectively. The extraordinary momentum surface ellipse k_e and the ordinary momentum surface k_o can be expressed in the x-z plane as

$$\frac{k_x^2}{n_e^2} + \frac{k_z^2}{n_o^2} = |k_o|^2 = \left(\frac{2\pi}{\lambda}\right)^2$$ 5.26

and

$$\frac{k_x^2}{n_o^2} + \frac{k_z^2}{n_o^2} = |k_o|^2 = \left(\frac{2\pi}{\lambda}\right)^2$$ 5.27

111

respectively, where λ is the optical wavelength in vacuum. We transform to a polar coordinate system by noting that $k_x = k\sin(\theta)$ and $k_z = k\cos(\theta)$. Taking differentials of equations (5.26) and (5.27), it follows that the slopes of the momentum surfaces are given by

$$\frac{dk_z}{dk_x} = -\frac{k_x}{k_z}(n_o/n_e)^2 = -(n_o/n_e)^2 \tan(\theta_e) \qquad 5.28$$

$$\frac{dk_z}{dk_x} = -\frac{k_x}{k_z} = -\tan(\theta_{w2}) \qquad 5.29$$

for the extraordinary and ordinary surfaces respectively. For a given ordinary angle θ_{w2} internal to the crystal, the internal extraordinary angle θ_e satisfying parallel tangents condition is found by equating equation (5.28) and (5.29), yielding[15]

$$\theta_e = \tan^{-1}\left[(n_e/n_o)^2 \tan(\theta_{w2})\right] \qquad 5.30$$

Note that for every ordinary write beam angle between 0 and 90 degrees from z there is a corresponding parallel tangents extraordinary angle, thus allowing a first-order momentum matching condition at virtually any angle. A particularly interesting case is obtained by choosing a parallel tangents set of ordinary and extraordinary angles such that the extraordinary angle corresponds to the angle where the curvatures of the ordinary and extraordinary momentum surfaces in the x-z plane are also equal . At this extraordinary equal curvature angle, of which there is only one between 0 and 90 degrees, second-order momentum matching is also obtained[19]. By simultaneously satisfying the parallel tangents and equal curvature condition, holograms with extremely large angular bandwidth can be written and read out between orthogonal polarizations.

To determine the equal curvature condition, the curvature ρ of a Cartesian function $y = f(x)$ is defined as the rate of change of the slope of the tangent to the curve with respect to arc length, in general given by

$$\rho = \frac{|f''|}{\left[1 + (f')^2\right]^{3/2}}$$

5.31

where the primes denote differentiation. Taking a similar approach to that for deriving the parallel tangents condition, the curvature of the extraordinary momentum ellipse in the θ direction is

$$\rho(\theta)_{ext} = \frac{\left(n_o/n_e^2\right)}{k_o\left[1 + \left[n_e(\theta)\sin(\theta)\right]^2 \left(n_o^2 - n_e^2\right)/n_e^4\right]^{3/2}}$$

5.32

where the extraordinary index $n_e(\theta)$ is

$$n_e(\theta) = \left[\frac{\cos^2(\theta)}{n_o^2} + \frac{\sin^2(\theta)}{n_e^2}\right]^{-1/2}.$$

5.33

Due to its spherical symmetry, the curvature of the ordinary momentum surface is constant with angle θ, thus

$$\rho_{ord} = 1/k_o$$

5.34

The extraordinary angle satisfying the equal curvature condition is found by setting equations (5.32) and (5.34) equal and solving for θ_{eqcurv}. After considerable algebra, the equal curvature condition is found to be[20]

$$\cos\left(2\theta_{eqcurv}\right) = \frac{n_o^{10/3} - n_o^{2/3}n_e^{8/3} - n_e^{10/3}}{n_o^{10/3} + n_o^{2/3}n_e^{8/3} + n_e^{10/3}}.$$

5.35

For small birefringence $\Delta n = n_e - n_o$, this equicurvature angle approaches 54.736 degrees as Δn vanishes, and it is always within a few degrees of this angle for typical birefringence values. In addition, the equicurvature angles are independent of fractional birefringence n_e/n_o.

Our experiments have been done with BaTiO$_3$ at 514 nm with estimated values[21] of ordinary index $n_o = 2.469$ and the extraordinary index $n_e = 2.390$.

113
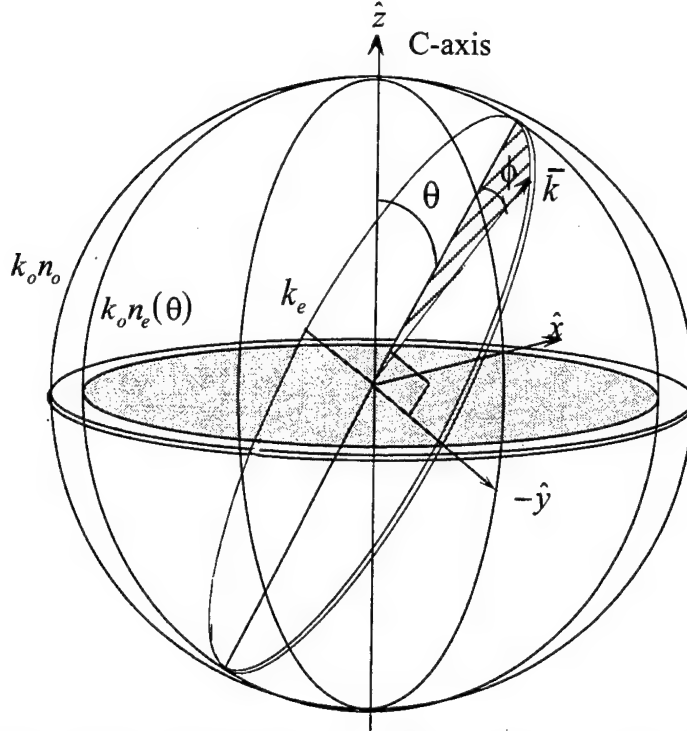
Figure 5.7. Uniaxial crystal 3D momentum surfaces showing ellipse formed between axes $k_e(\theta)$ and the $\hat{Y}$ axis. Ellipse is in plane inclined at angle θ from C-axis, and angle ϕ moves vector $\bar{k}$ along elliptical path.

Equation 5.35 yields an equal curvature angle of 53.409 degrees from the C-axis for this material. For a standard cut crystal with faces parallel and perpendicular to the C-axis, it is impossible to externally access this angle from air due to the high refractive index of the material. For this reason a 45 degree cut crystal is used to allow external access to the internal equal curvature angle which is accessible at approximately 24 degrees external from the crystal face normal. In $BaTiO_3$, operating near the equal curvature angle fortuitously allows access to the large r_{42} electro-optic coefficient and corresponding peak diffraction efficiency. The simultaneous operation at maximum diffraction efficiency with wide angular aperture can not be achieved in other PRCs such as $LiNbO_3$ or SBN that rely on large r_{33} coefficients because the equal curvature condition (which is always near 55 degrees) does not correspond to a region of peak diffraction efficiency.

114
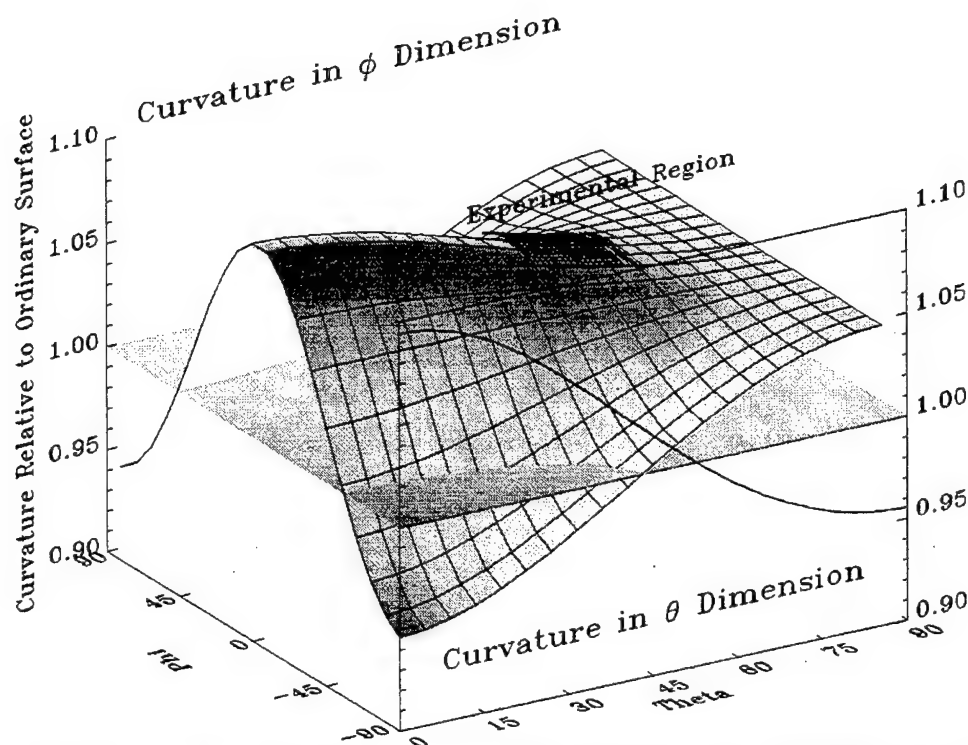
Figure 5.8. Extraordinary curvature as function of θ and ϕ normalized by constant ordinary curvature, shown as a plane at unity, with extraordinary curvature in θ direction projected onto front face. The parameters used are those for BaTiO3 at 514 nm, with $n_o = 2.469$ and $n_e = 2.390$. The hatched-in region between $\theta = \{45, 63\}$ and $\phi = \{-9, 9\}$ degrees corresponds to where the calculations and experiments were done with a 45 degree-cut crystal as presented in section 5.3.4.

Processing two-dimensional information requires examination of phase matching behavior in the angular dimension orthogonal to θ. For any angle θ, components in the direction orthogonal to θ, defined as the ϕ direction, will have a different curvature and phase matching behavior. Due to the fact that both the ordinary and extraordinary surfaces are surfaces of revolution about the C-axis, the tangent lines in the ϕ dimension are always parallel. Thus first-order phase-matching is obtained automatically. The curvature in the ϕ direction is the curvature of the ellipse in the plane formed by a particular ordinary write beam spectral component and the $\hat{Y}$ axis. This ellipse is shown in figure 5.7 where it is evident that the $\hat{Y}$ axis of the ellipse is constant, while the magnitude of the other axis, $k_e(\theta)$, varies with θ. The curvature of

this ellipse, defined as the change in arc length around the ellipse as a function of the angle ϕ, can be described by an equation similar to equation (5.32)

$$\rho_\theta(\phi)_{ext_\phi} = \frac{\left(n_e(\theta)/n_e^2\right)}{k_o\left[1+\left[n_e(\theta)\sin(\phi)\right]^2\left(n_e^2(\theta)-n_e^2\right)/n_e^4\right]^{3/2}}$$ 5.36

where $n_e(\theta)$ is given by equation (5.33).

A plot of this function using the parameters of BaTiO$_3$ normalized by the constant ordinary curvature value over the range of $\theta = \pm\pi/2$, and $\phi = \pm\pi/4$ is shown in figure 5.8. The surface is intersected with a plane at unity, corresponding to the normalized curvature of the ordinary momentum sphere. The figure demonstrates that the equal curvature condition in the ϕ dimension can be achieved in several regions, but not in the region of which our experiments were done. The normalized curvature in the θ dimension given by equation (5.32) is shown projected onto the front face where the equal curvature condition is achieved at 53.409 degrees. The hatched-in region between $\theta = \{45, 63\}$ and $\phi = \{-9,9\}$ degrees corresponds to where the calculations and experiments were done with a 45 degree-cut crystal as presented in section 5.3.4.

The possibilities of writing and reading at or near a wide angular aperture configuration with different wavelengths has also been investigated. In the ideal case this would allow writing a large angular spectra of gratings using ordinary polarized light, and then reading out the gratings non-destructively with extraordinary polarized light at a wavelength outside of the absorption band of the photorefractive material. Such a capability is very attractive from the standpoint of optical memory storage in PRCs[22]. The equal curvature condition in the θ direction for different write and read wavelengths is given by

$$\cos\left(2\theta_{eqcurv,\lambda}\right) = \frac{n_e^4 - \beta n_{ow}^{2/3}\left(n_o^{2/3}n_e^{8/3} + n_e^{2/3}n_o^{8/3}\right) + n_o^4}{\left(n_o^2 - n_e^2\right)\left(n_e^2 - \beta n_{ow}^{2/3}n_o^{2/3}n_e^{2/3} + n_o^2\right)}$$ 5.37
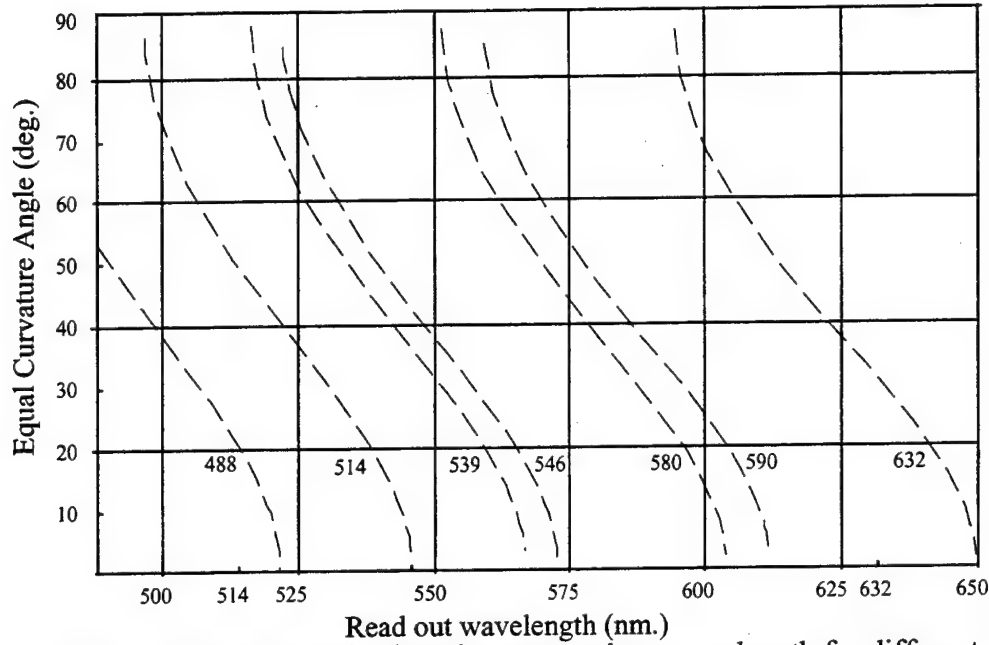
Figure 5.9. Equal curvature angle plotted versus read out wavelength for different write beam wavelengths.

where the parameter β is defined as

$$\beta = \left(\frac{\lambda_{write}}{\lambda_{read}}\right)^{2/3} \qquad\qquad 5.38$$

and n_e, n_o are the extraordinary and ordinary read beam indices, and n_{ow} is the ordinary write beam index.

The wavelength range that can be accommodated in this curvature matched orthogonally polarized non-destructive read out geometry is limited by the material birefringence. For example, gratings written with ordinary polarized light at 514 nm in BaTiO$_3$ can only be read out using extraordinary light at a wavelength up to approximately 550 nm, while the material sensitivity extends well beyond 600 nm. Results are shown below in figure 5.9. The horizontal axis is the read wavelength which is extraordinary polarized with index n_e, and the vertical axis is the equal curvature angle in degrees. Each of the family of curves corresponds to an ordinary polarized write wavelength with index n_{ow}. Dispersion is taken into account by making the indices n_o and n_e functions of the write

117

and read wavelengths, for this plot the dispersion was taken to be linear over the range of wavelengths used in the calculations. For example, the second curve from the left corresponds to a write wavelength of 514 nm, and at a read wavelength of 514 nm the curve passes through approximately 53 degrees which agrees with the result from monochromatic result given by equation (5.35).To utilize this technique to achieve non-destructive read out, materials having both larger birefringence and sharp edges to their spectral sensitivity regimes will be required.

5.3.3 Wide Angular Aperture Diffraction Efficiency

The diffraction efficiency of the read beam over the two dimensions of angular aperture of gratings for any read/write beam angular combinations can be calculated by finding the momentum mismatch and grating vector amplitude. The calculations take into account Bragg matching, the angularly dependent electro-optic coupling coefficient, and the variations of the response of the induced space-charge field in the photorefractive material with grating spatial frequency. Calculations are presented for a 2mm thick, 45 degree cut BaTiO$_3$ crystal (n_o = 2.469, n_e = 2.390) with a two-dimensional angular write spectra spanning 18.3 degrees internal to the crystal, chosen to approximate the experimental parameters. The center of the ordinary write spectra is at θ_{w2} = 55.174 degrees from the C-axis which is the parallel tangents angle corresponding to the extraordinary equal curvature angle of θ_e = 53.409 degrees.

The two angles θ_{w2} and θ_e corresponding to the central angles of the angular spectra are defined by the equal curvature and parallel tangents conditions, in the following discussion it is shown how to choose the planewave reference write and read beam angles. The angles θ_{w1} and θ_r are found by first translating the ordinary momentum surface by $\Delta\overline{R}$ such that the points of parallel tangency coincide. This is shown in figure 5.10, where $\Delta\overline{R}$ is given by

$$\Delta\overline{R} = R_x\hat{x} + R_z\hat{z} = \left[k_o\sin(\theta_{w2}) - k_e(\theta_e)\sin(\theta_e)\right]\hat{x} + \left[k_o\cos(\theta_{w2}) - k_e(\theta_e)\cos(\theta_e)\right]\hat{z} \quad 5.39$$

118
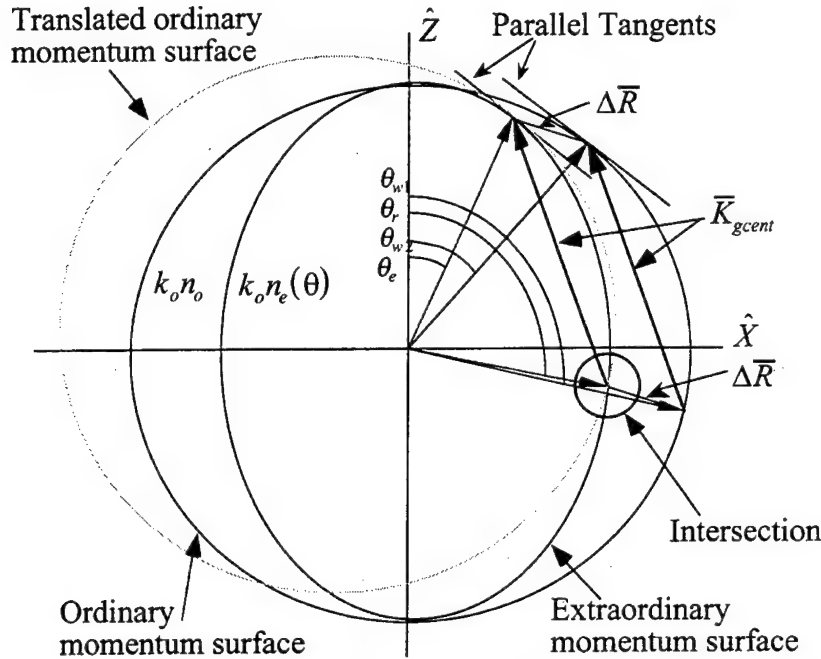
Figure 5.10. Ordinary momentum surface is translated by $\Delta\overline{R}$ such that points of parallel tangency coincide. Point of intersection (or difference of $\Delta K \approx \pi/L$)between translated ordinary surface and extraordinary surface determines extraordinary plane-wave read-out angle θ_r. Ordinary planewave write beam angle at θ_{w1} is then determined by translation back by $\Delta\overline{R}$.

Thus $\Delta\overline{R} = \overline{k}_o(\theta_{w2}) - \overline{k}_e(\theta_e)$ is just the difference vector between the parallel tangents.

As shown in figure 5.10, there is a distinct point of intersection between the extraordinary and translated momentum surfaces. The angle at which this intersection occurs is chosen to be θ_r, the extraordinary planewave reference beam angle, with associated momentum vector $\overline{k}_e(\theta_r)$. The ordinary planewave reference beam $\overline{k}_o(\theta_{w1})$ is now found by translating by $-\Delta\overline{R}$, i.e.

$$\overline{k}_e(\theta_r) - \Delta\overline{R} = \overline{k}_o(\theta_{w1}).$$ 5.40

Determination of these four primary angles defines the write/read beam geometry. In reality, there is significant latitude in choosing θ_r as long as the resulting momentum mismatch between the extraordinary and translated ordinary momentum surfaces is less than approximately π/L.

119

In order to determine the diffraction angle θ_e from each component of the grating spectra, it is assumed that the projection of the momentum vectors $\bar{k}_p$ and $\bar{k}_e$ in the directions orthogonal to $\hat{Z}$ are equal, i.e. K_X in the $\hat{X}$ direction, and K_Y in the $\hat{Y}$ direction. This is consistent with the assumption of $\Delta\overline{K} \approx \Delta\overline{K}_Z$ as discussed in section 5.3.1. Having determined the angle of the diffracted beam, the component of the momentum mismatch in the $\hat{Z}$ direction is then

$$\Delta K_Z = \left| \left(\bar{k}_e - \bar{k}_p \right) \cdot \hat{Z} \right|. \qquad 5.41$$

The incident and diffracted momenta are then used to determine the electric field polarizations by solving for the known linearly propagating eigenmodes in anisotropic media. These polarization directions are then used along with published values for $\underline{\underline{\varepsilon}}$, and $\underline{\underline{r}}$, and calculated values of $\overline{K}_g$ (parallel to $\underline{E}$) in equation 4.36 to determine a normalized coupling constant κ for each grating read/write pair over the full 2-D angular spectra of gratings.

Calculation results are shown in figures 5.11a-c, plotting diffraction efficiency as calculated from equations 4.26 and 4.36 in dB of the extraordinary diffracted spectra on the vertical axis, versus the two dimensions θ and ϕ of angular aperture. The ordinary planewave write beam angle, which is the same throughout the sequence, is 64 degrees from the C-axis.

Figure 5.11b is optimally Bragg matched for extraordinary read-out at the equal curvature condition, demonstrating large, uniform diffraction efficiency over a large angular range. Figures 5.11a and 5.11c show the results of reading out the same spectra of gratings written by the ordinary beams from a slightly different extraordinary planewave readout angle θ_r, i.e. detuning away from the optimum Bragg angle. The set of figures indicate that the Bragg matching constraints are different for the two dimensions of angular aperture. Surprisingly, the read-out angular bandwidth is
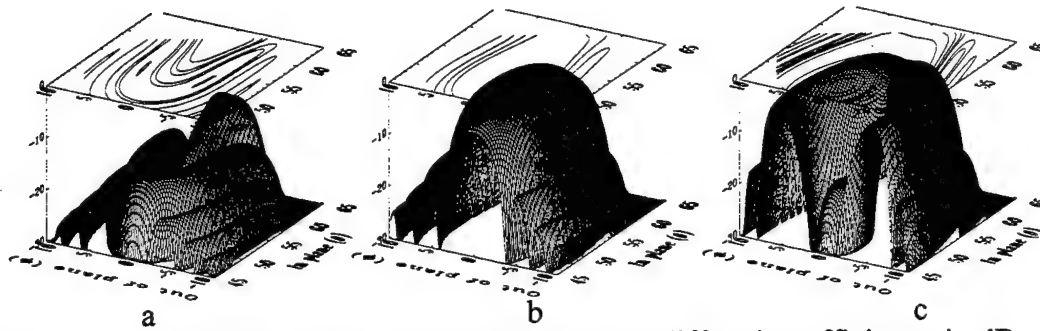
Figure 5.11. Three calculation results of normalized diffraction efficiency in dB over two dimensions of angular aperture. Figure b, near the exact Bragg matched equal curvature condition, shows a broad region of high diffraction efficiency thereby achieving large angular aperture. A and c show behavior as read beam is detuned on either side of the optimum Bragg matching angle.

narrower in the ϕ direction (direction of Bragg degeneracy) than the θ direction when the read-out beam is Bragg matched near the optimum equal curvature parallel tangents angle. As the read-out beam angle is detuned in the θ direction away from the optimum, as shown in figures 5.11a and 5.11c, it is evident that the Bragg matching behavior is also quite different depending upon the direction of detuning. A trade-off exists between maximum bandwidth in a given dimension and overall diffraction efficiency uniformity, which may be advantageous for certain applications.

The Bragg matching behavior as the extraordinary read beam is detuned away from the optimum Bragg matching angle can be understood by considering the surface area of the elliptical extraordinary momentum surface which is subtended by the angular spectra of gratings sliding along the inside of the spherical ordinary momentum surface as the read beam angle is rotated. The intersection of the two surfaces at a given read beam angle forms a locus of points which defines perfect Bragg matching along that locus, where the resulting diffraction efficiency is high. At other points, which correspond to different spectral components, the extraordinary ellipse either protrudes through the ordinary surface as in figure 5.11c or is underneath the ordinary surface as in figure 5.11a. Areas where this displacement is large occur where the grating vectors are severely Bragg mismatched and the diffraction efficiency has been dramatically

121

reduced. For example, in figure 5.11b where the grating spectra is optimally Bragg matched, there is a large area where the two surfaces conform well to each other with the extraordinary surface just barely protruding through by $|\Delta \overline{K}| < \pi/L$ in the central region. Over this broad region, before the first zero of the sinc^2 diffraction efficiency, the total separation of the two surfaces is such that $|\Delta \overline{K}| \leq 2\pi/L$. In figures 5.11a and c the momentum mismatch is much larger for a greater portion of the grating spectra, where the lobe structure of the diffraction patterns indicate the sinc^2 function rapidly passes through several zeros. This interpretation is complicated by the fact that while the extraordinary surface is sliding along the ordinary surface more or less tangentially as the read out beam is rotated, the two surfaces have different curvatures in both angular dimensions.

While the read out angular aperture of the hologram is large, there is still high Bragg selectivity for the diffraction efficiency of the total integrated intensity of the hologram. An approximately 0.2 degree detuning of the read beam angle from the optimum Bragg matching angle reduces the overall diffraction efficiency by approximately 30dB. It should be noted that the overall diffraction efficiency is asymmetric with read-out detuning angle and does not fall off as a sinc^2 function in detuning angle. This is the case because on one side the extraordinary ellipse protrudes through the ordinary sphere leaving a locus of high diffraction efficiency, while on the other side it pulls away resulting in a rapid drop-off of diffraction efficiency. From figure 5.11 it is evident that the angular selectivity of an individual spectral component of the hologram is quite high, yielding a -30 dB width of approximately 0.05 degrees which is typical for a 2 mm crystal in this writing geometry. The high angular selectivity of the overall diffraction efficiency indicates that the ability to angularly multiplex multiple holograms has not been seriously compromised.

5.3.4 Experimental Demonstration of Wide Angular Aperture Readout

Experiments have been done in a 2 mm-thick, 45 degree cut BaTiO$_3$ crystal, reading out gratings written between a planewave and a wavefront with a very large angular spectra of approximately 0.42 numerical aperture (N.A.) corresponding to a full-angle of approximately 49 degrees. The write beam geometry chosen is shown in figure 5.12. The central angle of the write angular bandwidth is at approximately 55 degrees (internal) from the C-axis. As in the calculations, this angle is near the parallel tangents angle corresponding to the equal curvature condition as determined by equation (5.35). The 49 degree external angular spectra, designated $\Delta\theta$ in the figure, produces a refracted internal spectra of approximately 18 degrees full angular width. The ordinary planewave write beam is at 64 degrees (internal) to the C-axis. The extraordinary read-out angle was then varied about the optimum Bragg matching angle as was done in the calculations.

The experimental set-up is shown in figure 5.13. Two ordinary polarized Argon ($\lambda = 514$ nm) beams are incident upon the 5mm x 5mm x 2mm thick BaTiO$_3$ crystal. One beam is sent through the lens, (f = 4.5mm, N.A.= 0.556) brought to a focus and allowed to diverge onto the crystal which is mounted on a calibrated rotation stage with a motorized actuator. The reflected component of the first beamsplitter is sent through a half-wave plate and the polarizing beamsplitter to produce two orthogonally polarized planewaves approximately 7 mm in diameter, each with an adjustable incidence angle. First with S1 closed and S2 and S3 open, the ordinary polarized planewave interferes with the angular spectra diverging from the high N.A. lens to write the spectra of gratings, and then with S1 open and S2 and S3 closed, the extraordinary planewave is used to read out these gratings. The crystal is then rotated on the stage through several angles to examine the effects of off-angle Bragg readout on the available angular aperture and its angular selectivity. Because of the short focal length and working distance of this high N.A. lens, the lens has to be moved back slightly from the crystal

123
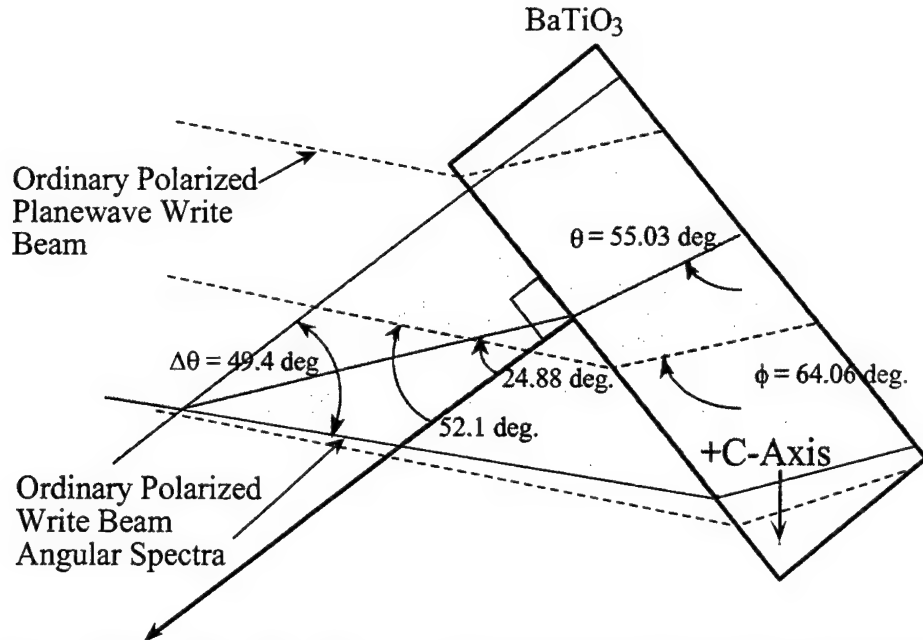
Figure 5.12. Write beam geometry, showing crystal and beam orientation between angular spectra and planewave write beam.
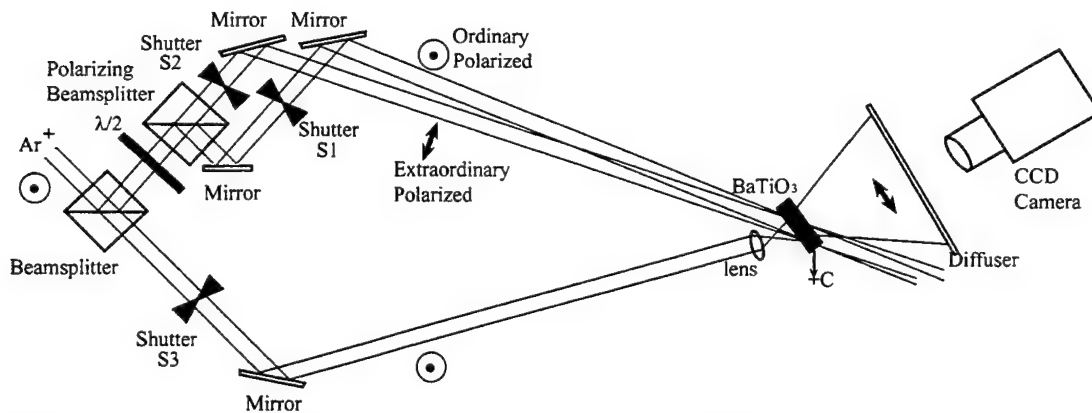
Figure 5.13. Experimental set-up for orthogonal polarization multiplexing experiment. The extraordinary beam is blocked during writing, and the ordinary write beams are blocked with shutters during extraordinary readout.

to allow the other write-beam to pass by the lens and reach the crystal unobstructed. Moving the lens back effectively reduced the available N.A. to that limited by the aperture of the crystal. This reduced N.A. was measured to be approximately 0.42. The diffracted spectra propagates a short distance to a diffuser, and is then imaged onto a CCD camera and digitized with an 8-bit frame-grabber board. Log-scaled experimental diffraction patterns and corresponding calculations are shown side by side in figure
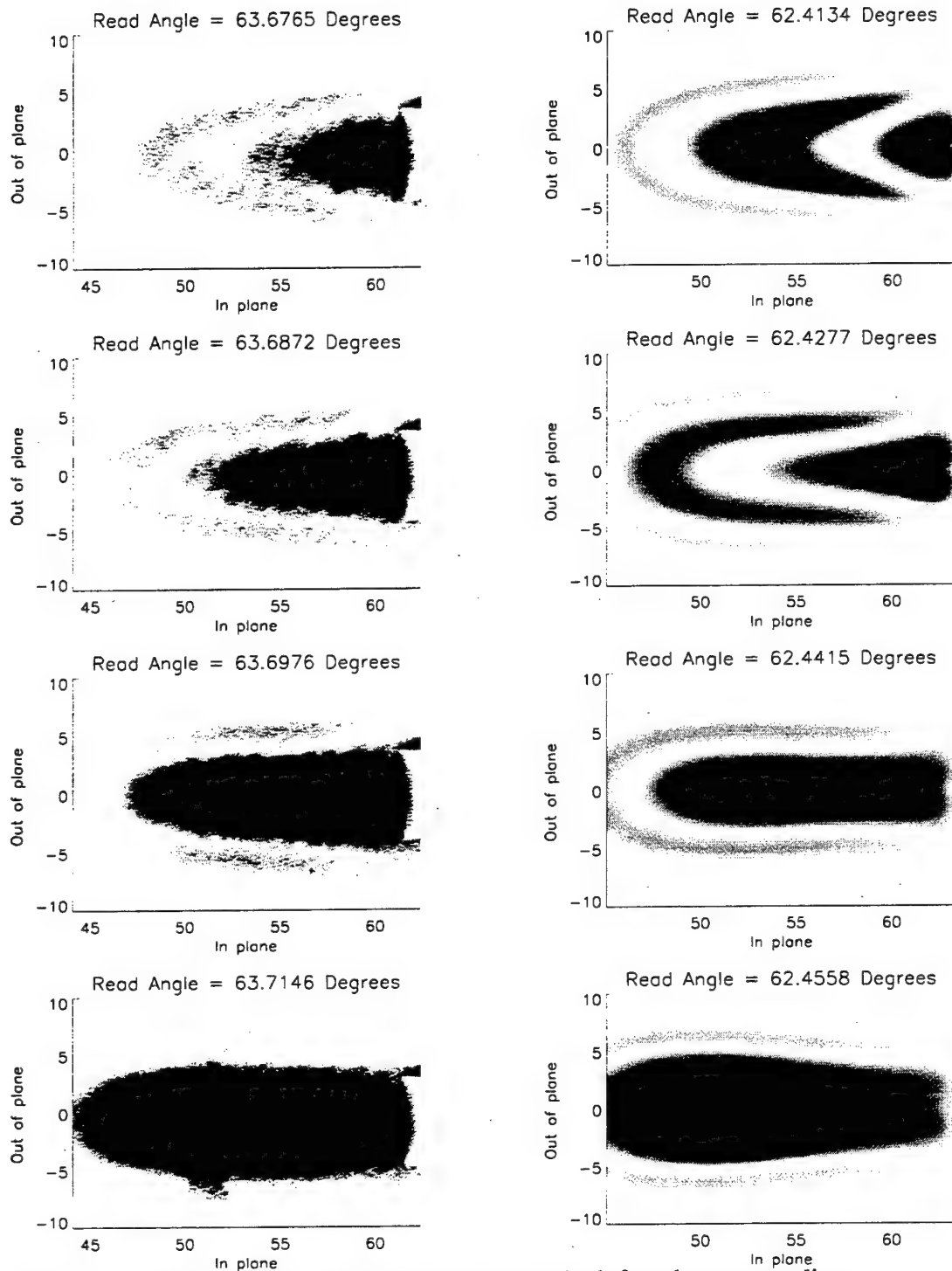
Figure 5.14. Experimental diffraction patterns on the left and corresponding calculations of holographic readout on the right.

125
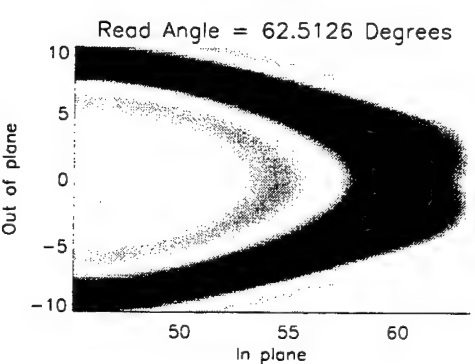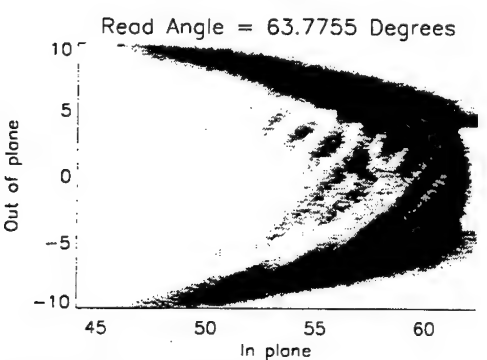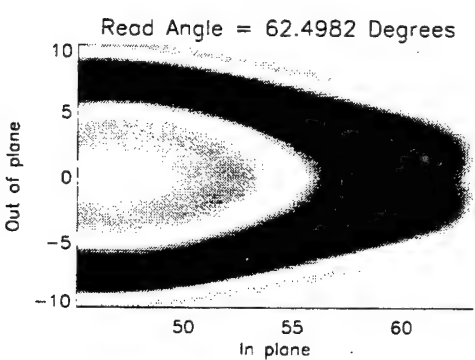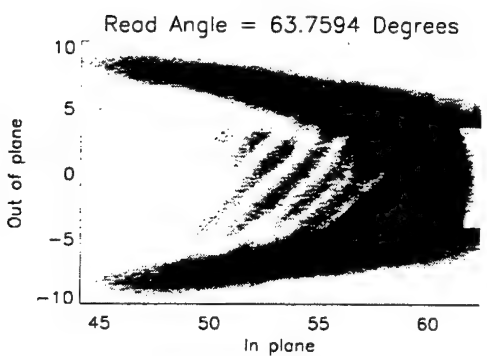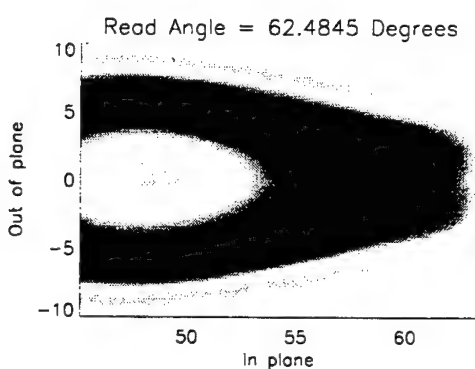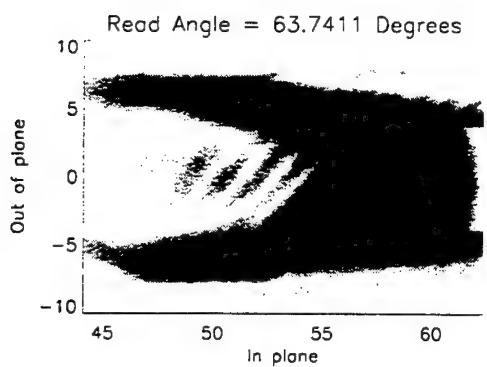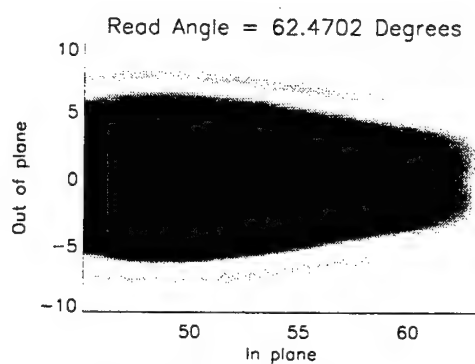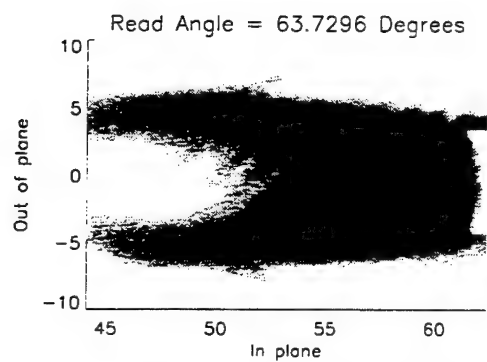
Figure 5.14 continued.

126

5.14. The two axes span the angular aperture of the angularly diverse diffracted beam. The sequence begins with the readout angle adjusted slightly off the optimum Bragg matching angle. As expected, when the readout beam angle is varied, the readout angular bandwidth passes through a maximum and then decreases again on the other side of the optimum angle. The experimental results have good qualitative agreement with the calculations, with both having very similar two-dimensional structural variation and shape as a function of extraordinary read-out angle. The total change in read-out angle of approximately 0.1 degrees from high to extremely low overall diffraction efficiency is the same for both the theoretical and experimental results. There is also good agreement for the rate at which the diffraction efficiency of individual spectral components within the angular spectra degrade with varying read-out angle. There is a finite offset between the calculated and experimental readout angle values that is most likely due to the fact that it is very difficult to measure the beam angles and angular spectra to within a fraction of a degree with the current experimental set-up. In addition, the refractive index values of the crystal are only approximate as these values can vary from boule to boule and with dopant concentration, and the 45 degree cut condition is only approximate.

The 4th figure in the calculation sequence is near the optimum read-out angle, demonstrating the wide angular aperture which can be obtained. The experimental result shown is not precisely the optimum condition, but the angular bandwidth is still quite large. As shown, nearly the entire 18 degrees of internal angular spectra of written gratings have been reconstructed in the θ dimension, and approximately 6 degrees have been reconstructed in the ϕ dimension. The best results observed in the lab exceeded 18 x 9 degrees. It is important to note that the 18 degrees of angular aperture in the θ dimension was limited by the lens N.A. and working distance, and not by Bragg matching constraints. In our calculations shown on the right-hand side of figure 5.14 a value of 5×10^{16} cm^{-3} has been chosen for the crystal acceptor density for best
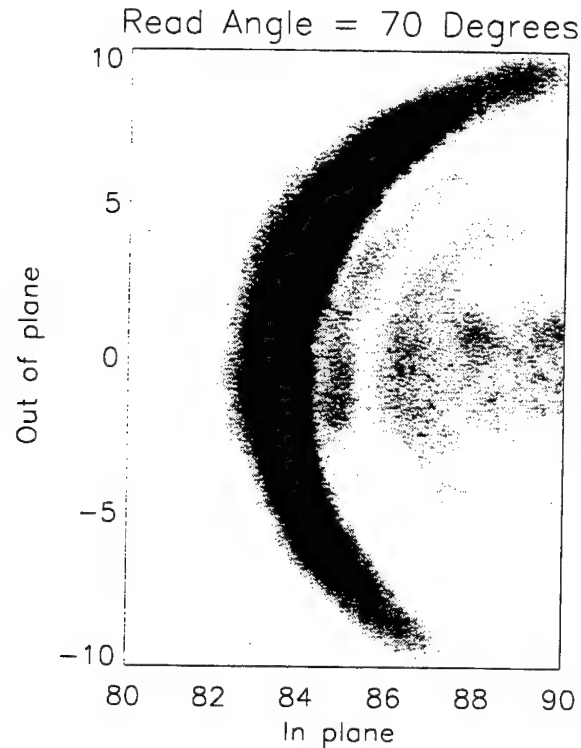
Figure 5.15. Experimental result for the case of reading out the same wide angular spectra of gratings far from both the equal curvature and parallel tangents condition. The central angle of the write angular spectra and the planewave write beam angle were at approximately 65 and 80 degrees respectively.

agreement with the experimental results. This acceptor density estimate is widely accepted in the literature.

Figure 5.15 shows an experimental result for the case of writing and reading the same wide angular spectra of gratings as above, but now far from both the equal-curvature and parallel tangents condition. The central angle of the angular spectra and the planewave angle were approximately 65 and 80 degrees (internal) from the crystal C-axis respectively. It is evident that only a small portion of the angular spectra is phase matched, producing the "arc" shown in the figure which is in marked contrast to the results displayed in figure 5.14.

References

[1] F. Vachss, J. Hong, and C. Keefer, "Adaptive signal processing using a photorefractive time integrating correlator," DARPA/Rome Labs Proc. **PSAA-91**, 127-132 (1991).

[2] R.M. Montgomery and M.R. Lange, "Photorefractive adaptive filter structure with 40-dB interference rejection," Appl. Opt. **30**, 2844-2849 (1991).

[3] J. Hong, S. Hudson, J. Yu, and D. Psaltis, "Photorefractive crystals as adaptive elements in acoustooptic filters," in *Optical Technology for Microwave Applications III*, SPIE, 136-144 (1987).

[4] J. Rhodes, "Adaptive filter with a time-domain implementation using correlation cancellation loops," Appl. Opt. **22**, no. 2, 282-287 January (1983).

[5] P.P. Ewald, "Crystal optics for visible light and x-rays," Reviews of modern physics **37**, no. 1, 46-56 January (1965).

[6] V.V. Aristov and V.S. Shekhtman, "Properties of three-dimensional holograms," Soviet Physics Uspekhi **14**, no. 3, 263-277 November (1971).

[7] R.T. Weverka, K.H. Wagner, R.R. McLeod, K. Wu, and C. Garvin, *Acousto-optic Signal Processing: Theory and Implementation*, 2. (Marcel Dekker, 1995), chap. 15.

[8] R.R. Mcleod, "Spectral-domain analysis and design of three-dimensional optical switching and computing systems," Ph.D. thesis, University of Colorado, Boulder, 1995.

[9] A. Yariv and P. Yeh, *Optical waves in crystals*. (John Wiley & Sons, N.Y., 1984), chap. ch. 4.

[10] J.M. Cowley, *Diffraction Physics*. (North-Holland, Amsterdam, 1981), pp. 31.

[11] D. Gabor and G.W. Stroke, "The theory of deep holograms," Proc. Roy. Soc. **A304**, 275 (1968).

[12] D. Psaltis, X.G. Gu, and D. Brady, *An Introduction to Neural and Electronic Networks*. San Diego: (Academic Press Inc., 1990), chap. 17.

[13] D.L. Hecht, "Multifrequency Acoustooptic Diffraction," IEEE Trans. Sonics and Ultrasonics **SU-24**, no. 1.

[14]   A.W. Sarto, R.T. Weverka, K.H. Wagner, and S. Weaver, "Wide angular aperture holograms in photorefractive crystals using orthogonally polarized write and read beams," in *Photorefractive materials, effects, and devices,* June 214-217 (1995).

[15]   I.C. Chang, "Noncollinear acousto-optic filter with large angular aperture," Appl. Phys. Lett. **25**, 370-372 (1974).

[16]   G.A. Coquin, J.P. Griffin, and L.K. Anderson, "Wide-band acousto-optic deflectors using acoustic beam steering," IEEE Trans. Sonics and Ultrasonics **SU-17**, 34-40 (1970).

[17]   D.A. Pinnow, "Acouto-optic light deflection: Design considerations for first order beam steering," IEEE Trans. Sonics and Ultrasonics **SU-18**, 209-214 (1971).

[18]   A. Korpel, R. Adler, P. Desmares, and W. Watson, "A television display using acoustic deflection and modulation of coherent light," Appl. Opt. **5**, 1667-1675 (1966).

[19]   J. Xu and R. Stroud, *Acousto-optic devices*, Wiley series in pure and applied optics. (Wiley-Interscience, 1992), chap. 7, pp. 413-424.

[20]   R.T. Weverka and K. Wagner, "Wide angular aperture Acoustooptic Bragg cell," in *Devices for Optical Processing,* D.M. Gookin, ed. Proc. Soc. Photo-Opt. Instrum. Eng. **1562**, 66-72 (1991).

[21]   H. Landolt and R. Bornstein, *Numerical Data and Functional Relationships in Science and Technology, New series: Ferro- and Antoferroelectric Substances*, vol. 3.   Berlin: (Springer-Verlag, 1975).

[22]   M.P. Tarr and M. Cronin-Golomb, "Birefringent phase matching for nonvolatile readout of holographic memories," in *Photorefractive materials, effects, and devices,* 435-438 (1995).

6 Adaptive Phased-Array Beam-Forming Processor.

The beam-steering phased-array processor calculates the angle of arrival of a desired RF signal of interest and steers the main lobe of the antenna array pattern towards this signal of interest. The chapter begins with an overview of the beam-steering processor operation, followed by a derivation which demonstrates that the holographic interaction in the PRC which is implemented is equivalent to adaptive array beam-formation. In addition, an analytical expression for the holographic grating formed in the PRC is derived. Simulation results of the beam-forming processor using an explicit photorefractive model are also presented, followed by experimental results of beam-formation on a broadband signal of interest.

6.1 Beam-Forming Processor

6.1.1 Holographic Beam-Forming Process

The photorefractive phased-array antenna beam-forming processor calculates the AOA of a desired signal of interest and steers the antenna-array pattern in the direction of this desired signal by forming a dynamic holographic grating which is proportional to the correlation between the incoming signal of interest from the antenna array and the temporal waveform of an estimate of the desired signal. The Bragg selectivity of the photorefractive crystal (approximately 10^4 beams, estimated by the addressable angular aperture of the hologram divided by the holographic angular Bragg aperture) is substantially larger than the required array function (10^3 beams), so the grating produced by the correlation process only requires a fraction of the crystal volume to achieve the necessary Bragg selectivity to implement the desired beam steering operation with the full resolution of the array. This grating is algorithmically and functionally equivalent to an array of adaptive weights, and the Bragg matched

131
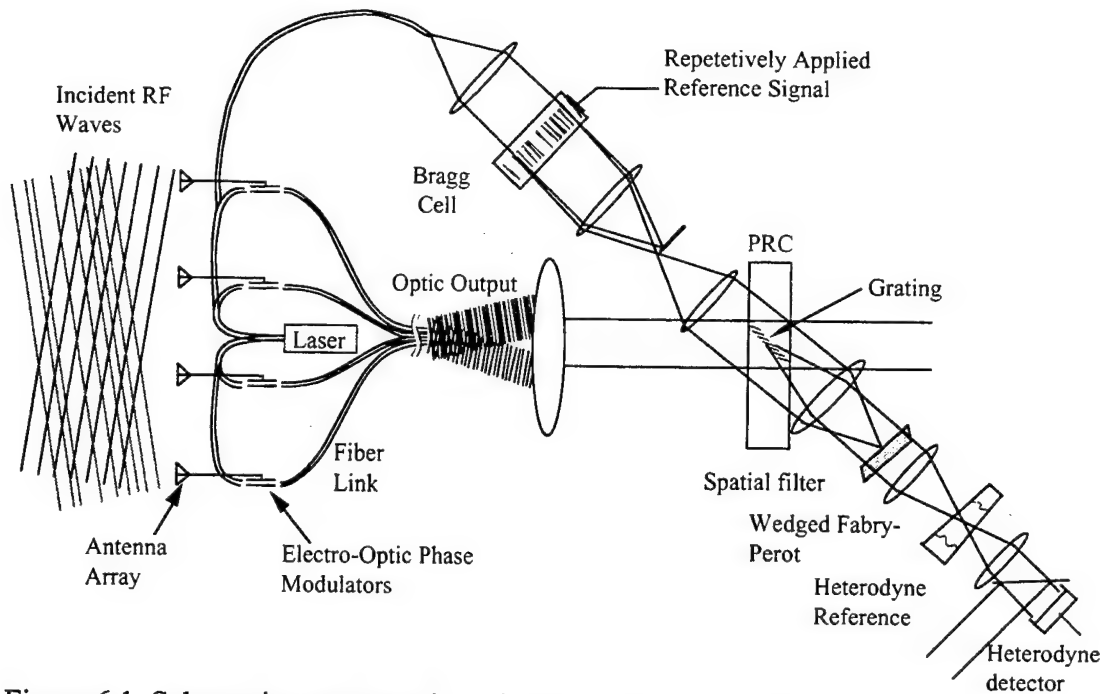
Figure 6.1. Schematic representation of beam-forming phased-array radar processor

diffracted component from this grating is the antenna output modified by an array function pointed towards the desired signal of interest.   The main-beam forming processor is shown schematically in figure 6.1. The figure shows a broadband signal of interest and a narrowband jammer incident upon an RF phased array antenna. The outputs from the antenna elements are converted to the optical domain using electro-optic modulators fed by a common distributed laser and coupled to an optical fiber for delivery to the processor. The analysis is simplified by assuming single sideband electro-optic modulators, but conventional phase modulators or amplitude modulators can be used with nearly equivalent results (although reduced diffraction efficiency due to the additional bias terms on the PRC and smaller fraction of power in the desired sideband). Ideally, each fiber is cut to precisely the same length (e.g. to within $\lambda/10$), preserving in the optical domain the same phase relationship that exists between the array elements of the antenna. It will be shown that the processor forms a main beam even if the spatial phase profile of the optical topological mapping has been modified by fibers cut to unequal lengths or even with a shuffled spatial order, provided that they

132

are the same length to within a fraction of the radar signal bandwidth (c/bandwidth), and within a laser coherence length. The diffracted component from the Bragg cell, whose input is a repetetive application of an estimate of the desired signal, interferes with the optical mapping of the phased-array at the PRC. The estimate of the desired signal must be well correlated with the desired signal at a delay within the Bragg cell aperture, and for simplicity, here it is taken to be the desired signal itself. When the optical mapping of the phased-array and the diffracted component from the Bragg cell are interfered in the PRC, this effectively forms a bank of time-integrating correlators multiplexed throughout the volume of the crystal. For each antenna element, a strong correlation peak will exist between the desired signal and the reference signal corresponding to some particular time delay in the Bragg cell and delay at each antenna element, and the element to element variation of the correlation peak delay indicates the AOA of the signal. A stationary interference pattern will arise at a corresponding position in the PRC, and over time a holographic grating will build up in the crystal. The spatial-temporal grating strength $g(x,z,t)$ in the PRC is proportional to the time integrated correlation between the electric fields of the two optical fields $E_{ARr}(x,z,t)$ and $E_{BCr}(x,z,t)$. These signals are taken to be from the optical mapping of the phased-array and the diffracted component from the Bragg cell respectively. The grating term will be given by,

$$g(x,z,t) \propto \int E_{AR}(x,z,t')E_{BC}^*(x,z,t' - x_o/V)dt' \qquad 6.1$$

where V is the acoustic velocity of the Bragg cell. Equation 6.1 has a correlation peak at x_o/V, and the positions of these gratings will form a 2-D slice in the 3-D volume of the crystal as shown in figure 6.1. This is also shown in figure 6.2 for the more intuitive case where the inputs are in a 90 degree holographic geometry taht will be analyzed in the following section, but this analysis applies to arbitrary geometry through an appropriate conformal transform.

6.1.2 Holographic Beam-Forming Process for Desired Signal only

The holographic beam-forming process will first be analyzed for the case of only a desired signal incident upon the array. Figure 6.2 shows the two interfering fields, $E_{ARr}(x,z,t)$ and $E_{BCr}(x,z,t)$, which write the grating in the PRC, as well as the fact that the top edge of the crystal is in an image plane of the Bragg cell. The optical mapping of the phased-array antenna at the ouput face of the fiber-optic cable bundle can be described as the combined field arising from the sum over N antenna elements, in which the RF waveform s_n at the nth fiber of the desired signal $r(t)$ transduced by the nth element can be represented by the product between an envelope term and carrier terms delayed by an AOA dependent and linearly increasing delay, resulting in

$$s_n(t) \approx \tilde{r}\left(t - na\sin\left(\theta_{rf}\right)/c\right)e^{i\omega_r\left[t - na\sin(\theta_{rf})/c\right]} + c.c. \qquad 6.2$$

where $\tilde{r}(t)$ is the single sideband analytic modultion.

The simplest optical mapping to consider is that of a linear RF array coherently mapped into a linear array of fiber-optic ouputs, as shown in figure 6.1 and in more detail in figure 6.3. The incident RF wave with propagation vector k_{rf}, will have a transverse component, k_x^{rf} projected onto the array, given by

$$k_x^{rf} = \frac{\omega_{rf}}{c}\sin\left(\theta_{rf}\right) \qquad 6.3$$

where θ_{rf} is the angle of incidence of the RF wave with respect to the array normal. The mapping of k_x^{rf} from an array with element spacing a, into an optical fiber bundle made up of single-mode fibers spaced by D, results in a conserved transverse optical propagation vector component k_x^{opt} which is equal to k_x^{rf} times the ratio of antenna spacing a to fiber spacing D.

$$k_x^{opt} = \frac{a}{D}k_x^{rf} = \frac{\omega_{rf}a}{cD}\sin\left(\theta_{rf}\right). \qquad 6.4$$

134
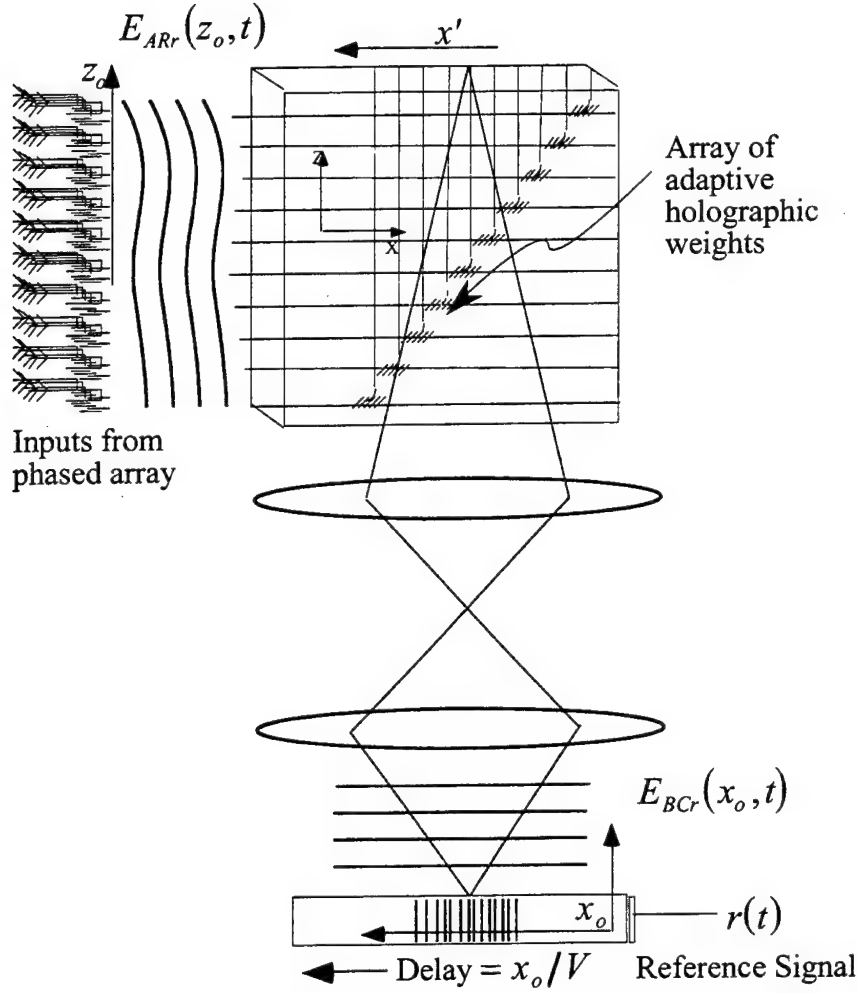
Figure 6.2. Beam interaction geometry for holographic beam-forming process, showing 2-D grating slice formed in the volume of the PRC.

Equation 6.4 yields a scaled optical angle θ_{opt} given by

$$\theta_{opt} = \sin^{-1}\left[\sin(\theta_{rf})\omega_{rf}a/\omega_{opt}D\right]. \qquad 6.5$$

Consider now a single incident desired signal given by $\tilde{r}\left(t - \tau - na\sin(\theta_{rf})/c\right)$, at some unknown range delay τ and within the AO time aperture. Taking into account 6.5, the array input field launched by N fibers of core diameter d, spaced by D, and propagating nominally in the x direction into the processor can be expressed as

$$E_{ARr}\left(x=x_{do}, z_o, t\right) = \left[\tilde{r}(t-\tau)e^{i\omega_r\left[t-\tau-z_o a\sin(\theta_{rf})/cD\right]}e^{i\omega_o t}e^{i\Phi(z_o)}\right]\Pi\left[\frac{z_o}{ND}\right]\text{comb}\left[\frac{z_o}{D}\right]*g\left[\frac{z_o}{d}\right] + c.c.$$

$$6.6$$

135

$$\vec{k}_{rf} = \frac{\omega_{rf}}{c}\left[\sin\left(\theta_{rf}\right)\hat{x} + \cos\left(\theta_{rf}\right)\hat{z}\right]$$
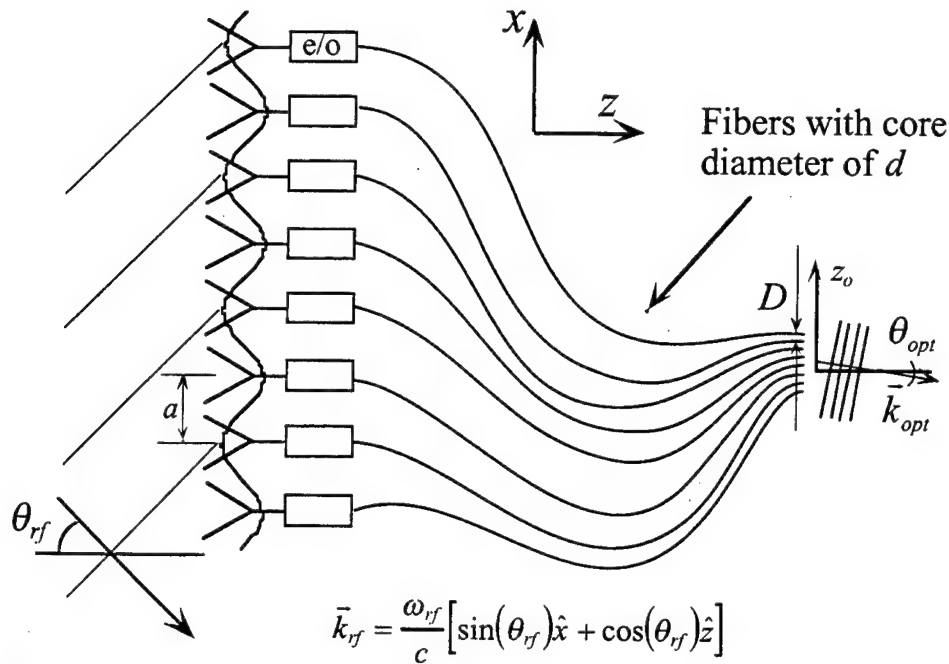
Figure 6.3. Optical mapping of incident RF signal onto array results in scaled optical angle at fiber array output.

where the desired signal modulation is now approximated by $\tilde{r}(t-\tau)$, implying the signal is narrowband compared to the time-of-flight time across the array. z_o is the transverse coordinate at the fiber input plane at $x=x_{do}$, and the light propagates nominally in the x direction. The assumption of the plane wave to plane wave mapping, which requires fibers cut to the exact same length, has been relaxed here by introducing a random phase delay function $\Phi(z)$ along the array aperture. The finite aperture of the optical fiber bundle is taken into account by choosing a finite length comb function which describes the position of each fiber, and the illumination from each fiber is modeled a Gaussian aperture function $g[z_o/d] \equiv \exp\left[-(z_o/d)^2\right]$. The array input field will interfere at the PRC with the diffracted output from the reference Bragg cell. This diffracted term, propagating nominally in the z direction, can be expressed as

$$E_{BCr}\left(x_o,z=z_{do},t\right) = e^{i\omega_o t}\Pi\left[\frac{x_o}{X}\right]\tilde{r}\left(t - x_o/V\right)e^{i\omega_r\left(t-x_o/V\right)} + c.c.. \qquad 6.7$$

The function $\Pi[x_o/X]$ describes the finite, uniformly illuminated aperture of the AO device. Analagous to the field from the array, but now propagating in the z direction, the field from the Bragg cell is described by the initial field as a function of x_o at the plane x_o, at the initial propagation position $z = z_{do}$.

The analysis of the holographic write and read process due to the interaction of the two diffracting fields in the PRC is aided by introducing the Fresnel operator $£\{•\}$, to express the Fresnel propagation of the fields. The Fresnel propagation of the x propagating field of the optical mapping of the phased-array field from x_{do} to x_{d1} is given by equation 6.6. In terms of this Fresnel operator this is expressed as

$$£_x\{E_{ARr}(x = x_{do}, z_o, t)\} = E_{ARr}(x_{d1}, z_1, t) = \int E_{ARr}(x = x_{do}, z_o, t)\frac{e^{ikx}}{i\lambda x}e^{\frac{i\pi}{\lambda x}(z_1 - z_o)^2}dz_o \quad 6.8$$

where the resulting field, whose amplitude is a function of the coordinate z_1, is now at the position x_{d1} after propagating a distance x, and λ is the material wavelength λ_o/n. Similarly, using the operator notation, after propagating a distance z, the Bragg cell field can be expressed as

$$£_z\{E_{BCr}(x_o, z = z_{do}, t)\} = E_{BCr}(x_1, z = z_{d1}, t) = \int E_{BCr}(x_o, z = z_{do}, t)\frac{e^{ikz}}{i\lambda z}e^{\frac{i\pi}{\lambda z}(x_1 - x_o)^2}dx_o . 6.9$$

The Fresnel operator approach allows the propagating fields to be manipulated according to the standard rules of linear operators, and provides both a compact notation to describe the Fresnel integral equations. The three most important properties of these linear operators used in this derivation will be additivity, $£_{z1}\{£_{z2}\{A\}\} = £_{z1+z2}\{A\}$, phase conjugate imaging, $£_z\{£_{-z}\{A\}\} = A$, and conjugation, $[£_z\{A\}]^* = £_{-z}\{A^*\}$.

In the operator notation, the spatio-temporal evolution of the grating inside the PRC created by the interference of the fields can be expressed as

137

$$g(x,z,t) = \int_{-\infty}^{t} \left[\pounds_x \left\{ E_{ARr}\left(x = x_{do}, z_o, t'\right) \right\} \right]^{*} \cdot \pounds_{-z} \left\{ E_{BCr}\left(x_o, z = z_{do}, t'\right) \right\} dt' \qquad .6.10$$

where it is noted to be the time-integrated correlation between the two writing fields. Referring to the geometry of figure 6.2, which was chosen for simplicity, the exit face of the crystal is an image plane of the Bragg cell, but any equivalent geometry could be similarly analyzed. The entrance face of the crystal is thus some intermediate field between the object and the image, and hence complex to describe. However, knowing that the exit face is an image plane (assumed to be a one-to-one telescopic magnification), at any position in the crystal, propagating the image field backwards through the crystal is the same as propagating the object field forward. This simplifies the analysis because the field from the Bragg cell which interferes with the array field can then be represented as the image of the object field travelling backwards through the crystal, as indicated by the $\pounds_z$ operator which has a negative sign on the z-subscript. The grating formed is then read out with the x propagating array field $E_{ARr}\left(x = x_{do}, z_o, t\right)$, and produces a diffracted field propagating in the (positive) z direction towards the Bragg cell image plane. Integrating this 2-D field in the z dimension over the length L of the crystal produces the final field at the x' output plane at position z', at the edge of the crystal. The final field should be at an image plane of the Bragg cell, temporally modulated by the desired RF signal which has been extracted from the input from the phased-array and spatially modulated by the autocorrelation function of the reference and array signal. The final diffracted field at the image plane is

$$E_D'(x',t) = \int_{0}^{L} \pounds_z \left\{ \pounds_x \left\{ E_{ARr}\left(x_{do}, z_o, t\right) e^{i\Delta\beta z} \right\} \cdot g(x,z,t) \right\} dz. \qquad 6.11$$

It is important to note that the array field which reads out the time-integrated grating is taken to be instantaneous time, and is designated by the temporal variable t, different from t', representing previous time, appearing in the grating evolution integral equation

138

6.10. The additional phasor term of $e^{i\Delta\beta z}$ allows for the readout array field to be slightly angularly shifted with respect to the array field which wrote the grating in order to characterize the Bragg selectivity of the readout as a manifestation of the angular array beam steering response. In the following section, this phasor term will allow the anlysis of off boresight interfering jammers. Expanding out equation 6.11 yields

$$E'_D(x',t)=$$
$$\int_0^L\int_{-\infty}^t \pounds_z\left\{\pounds_x\left\{E_{ARr}(x=x_{do},z_o,t)e^{i\Delta\beta z}\right\}\left[\left[\pounds_x\left\{E_{ARr}(x=x_{do},z_o,t')\right\}\right]^* \pounds_{-z}\left\{E_{BCr}(x_o,z=z_{do},t')\right\}\right]\right\}dt'dz$$
6.12

for the squint-free narrowband case. The array field $E_{ARr}(x_{do},z_o,t)$ given by equation 6.6 can be written as a separable function in space and time, such that

$$E_{ARr}(x=x_{do},z_o,t)=L_r(x=x_{do},z_o)M_r(t-\tau) \qquad 6.13$$

where the spatial function is given by

$$L_r(x_{do},z_o)=e^{i\Phi(z_o)}e^{-i\omega_r z_o a\sin(\theta_{rf})/cD}\Pi\left[\frac{z_o}{ND}\right]comb\left[\frac{z_o}{D}\right]*g\left[\frac{z_o}{d}\right] \qquad 6.14$$

and the temporal function is

$$M_r(t-\tau)=e^{i\omega_o t}\tilde{r}(t-\tau)e^{i\omega_r(t-\tau)}. \qquad 6.15$$

This simplification is not necessary for beam steering but does simplify the analysis considerably. The separable nature of the array field allows equation 6.12 to be written as

$$E'_D(x',t)=$$
$$\int_0^L\int_{-\infty}^t \pounds_z\left\{\pounds_{-z}\left\{E_{BCr}(x_o,z=z_{do},t')\right\}\cdot\pounds_x\left\{L_r(x=x_{do},z_o)e^{i\Delta\beta z}M_r(t-\tau)\right\}\left[\pounds_x\left\{L_r(x=x_{do},z_o)M_r(t'-\tau)\right\}\right]^*\right\}dt'dz$$
6.16

when $\Delta\beta=0$, a purely real intensity term $I_{ARr}(x,z)$ can be defined such that

$$I_{ARr}(x,z)\equiv\pounds_x\left\{L_r(x=x_{do},z_o)\right\}\left[\pounds_x\left\{L_r(x=x_{do},z_o)\right\}\right]^*=\left|\pounds_x\left\{L_r(x=x_{do},z_o)\right\}\right|^2\approx constant. 6.17$$

139

It is important to note that at this point the random phase delay produced by $\Phi(x)$, has been eliminated due to the complex conjugate multiplication between the array read out field and the corresponding random phase delay profile recorded in the holographic grating. In addition, the phasor due to the AOA of the incident RF wave has been eliminated, and thus the specific interelement phase information from the array is no longer used. From Parseval's theorem[1], the intensity represented by equation 6.17 will be a constant for any z-slice taken along the propagation direction x so that the final z integral of equation 6.11 will produce a constant when operating on this term. The slow undulations of this intensity term are unimportant for holographic diffraction and will be neglected by representing this term as a constant. Further assuming that $I_{ARr}(x,z)$ is approximately constant in the x direction as well, the intenstity term can be written as

$$I_{ARr}(x,z) = \left| \pounds_x \left\{ L_r(x_{do}, z_o) \right\} \right|^2 e^{i(\Delta\alpha x + \Delta\beta z)} = I_{ARr} e^{i(\Delta\alpha x + \Delta\beta z)} \qquad .6.18$$

In the case of the tilted readout beam, the constant intensity is modulated by a phasor $e^{i(\Delta\alpha x + \Delta\beta z)}$. The expression for the diffracted field can now be written as

$$E'_D(x',t) = M_r(t-\tau) \int_0^L \int_{-\infty}^t \pounds_z \left\{ \pounds_{-z} \left\{ E_{BCr}(x_o, z_{do}, t') \right\} I_{ARr} e^{i(\Delta\alpha x + \Delta\beta z)} \right\} M_r^*(t'-\tau) dt' dz \qquad 6.19$$

where the additional phasor term $e^{i\Delta\alpha x}$ arises as a result of the propagation of the deviated readout beam, and $\Delta\alpha \approx \Delta\beta^2/2k_o$ .and $M_r(t-\tau)$ and $M_r^*(t'-\tau)$ have been moved outside of the $\pounds_z$ operator because they have no spatial dependence. At this point it is evident that the output is temporally modulated by the desired signal with no additional delay. Both of the $\pounds_z$ and the $\pounds_{-z}$ operators now operate on $E_{BCr}(x_o, z = z_{do}, t')$, although the argument of the $\pounds_z$ operator contains the additional phasor term $e^{i(\Delta\alpha x + \Delta\beta z)}$. From the definition of the $\pounds_z$ operator given by equation 6.9, it is seen that the integration portion of the operator is over the variable x_o, and hence the $e^{i\Delta\beta z}$ portion of the phasor can be moved outside of the operator, so that a tilted

140

wavefront maintains the tilt with propagation. The $e^{i\Delta\alpha x}$ portion of the phasor must be dealt with more carefully. The paraxial approximation of the beam propagation invoked by the Fresnel operators necessitates that $\Delta\beta$ is small, and for a small deviation away from the wavevector k_o, $\Delta\alpha$ will vary quadratically with $\Delta\beta$ according to $\Delta\alpha \approx \Delta\beta^2/2k_o$. Because $\Delta\alpha$ is small, its effect on the Fresnel operator $\mathcal{L}_z$ can be considered just to be a small angular shift in angle of the diffracted wave. This assumption allows the $e^{i\Delta\alpha x}$ phasor term to be moved outside of the operator, and the nested operators can be seen to propagate $E_{BCr}(x_o, z_{do}, t')$ backward and then forward again, and invoking the linear operator phase conjugate imaging property it follows that

$$\mathcal{L}_z\left\{\mathcal{L}_{-z}\left\{E_{BCr}(x_o, z = z_{do}, t')\right\}\right\} = E_{BCr}(x_o, z = z_{do}, t').$$ 6.20

Substituting in the expression for the Bragg cell field given by equation 6.7, the definition of $M_r^*(t' - \tau)$ as given from equation 6.15, defining the temporal variable $t'' = t' - \tau$, and cancelling terms yields

$$E_D'(x', t) = R(\tau - x_o/V)\int_0^L I_{ARr} e^{i(\Delta\alpha x + \Delta\beta z)} M_r(t - \tau) e^{i\omega_r(\tau - x_o/V)}\Pi\left[\frac{x_o}{X}\right]dz$$ .6.21

The upper limit of the temporal integral has been extended to $+\infty$, allowing the time integration to be expressed as an exact autocorrelation function of the desired temporal waveform $\tilde{r}(t)$, given by

$$R(\tau - x_o/V) = \int_{-\infty}^{\infty} \tilde{r}(t'' + \tau - x_o/V)\tilde{r}^*(t'')dt''.$$ 6.22

The autocorrelation function will have a peak at a delay time within the aperture of the Bragg cell of $\tau = x_o/V$. This autocorrelation term is proportional to the strength of the holographic grating, and its exact spatial shape and structure throughout the hologram will depend on the waveform $\tilde{r}(t)$ and the illuminating fields. An analytical expression for this autocorrelation term will be presented in Section 6.1.4 for a broadband signal

with a Gaussian autocorrelation, but simply designated as $R(\tau - x'/V)$ for the remainder of this analysis. Using this definition and substituting in the function $M_r(t - \tau)$ results in

$$E'_D(x',t) = \left\{ \tilde{r}(t-\tau)e^{i\omega_r(t-\tau)}e^{i\omega_o t} R(\tau - x'/V)\Pi\left[\frac{x'}{X}\right] \int_0^L I_{AR} e^{i\Delta\beta z} dz \right\} * \delta(x' - \Delta\alpha^2/2k_o).6.23$$

The tiny shift due to the final convolution can be neglected. Performing the final integration over z yields a diffracted field with a reduced intensity due to Bragg mismatch of the tilted readout,

$$E'_D(x',t) = \tilde{r}(t-\tau)e^{i\omega_r(t-\tau)}e^{i\omega_o t} R(\tau - x'/V)\Pi\left[\frac{x'}{X}\right] I_{AR} \operatorname{sinc}(\Delta\beta z) \qquad .6.24$$

Equation 6.24 is the fundamental result of this section and demonstrates the holographic reconstruction process. The result given by equation 6.24 shows that the delayed, desired signal $\tilde{r}(t-\tau)$ on RF carrier $e^{i\omega_r(t-\tau)}$ has been recovered. Furthermore, the autocorrelation term $R(\tau - x'/V)$ appears at the image plane of the Bragg cell, with a tiny spatial shift resulting from the Bragg mismatched readout which can be ignored because of its 4*th* order dependence on $\Delta\beta$. Finally, the diffracted field is multiplied by $\operatorname{sinc}(\Delta\beta z)$, which indicates an angularly dependent weighting term due to phase-mismatched readout, which for the Bragg matched read out of the desired signal becomes unity.

6.1.3 Holographic Beam-Forming Process for both Desired Signal and Interfering Jammers

The derivation for the holgraphic beam-forming operation done in the previous section assumed that only a single desired signal was incident upon the RF array, although the capability to incorporate Bragg mismatched readouts from other AOAs incident on the array was included in the analysis. More generally, there will be

additional interference signals incident upon the array, such as jammers or broadband noise. The beam-forming derivation can be extended to the case of simultaneous, multiple jammers, by modifying the array field signal given by equation 6.6 to include the jamming terms. An array signal $E_{AR}(x = x_{do}, z_o, t)$ is defined so as to include a desired term $E_{ARr}(x = x_{do}, z_o, t)$ (equation 6.6) and a term composed of M, narrowband jammers, $E_{ARj}(x = x_{do}, z_o, t)$. The total optical field launched by the fiber array will then be

$$E_{AR}(x = x_{do}, z_o, t) = E_{ARr}(x = x_{do}, z_o, t) + E_{ARj}(x = x_{do}, z_o, t) \qquad 6.25$$

where the desired term is

$$E_{ARr}(x = x_{do}, z_o, t) = e^{i\omega_o t} e^{i\Phi(z_o)} \tilde{r}(t - \tau) e^{i\omega_r \left[t - \tau - z_o a \sin(\theta_{rf})/cD\right]} \Pi\left[\frac{z_o}{ND}\right] \text{comb}\left[\frac{z_o}{D}\right] * g\left[\frac{z_o}{d}\right] \qquad 6.26$$

and the interference terms are

$$E_{ARj}(x = x_{do}, z_o, t) = e^{i\omega_o t} e^{i\Phi(z_o)} \sum_{j=1}^{P} A_j e^{i\omega_j \left[t - z_o a \sin(\theta_j)/cD\right]} \Pi\left[\frac{z_o}{ND}\right] \text{comb}\left[\frac{z_o}{D}\right] * g\left[\frac{z_o}{d}\right] \qquad 6.27$$

The A_j, ω_j, and θ_j are the amplitude, frequency, and the incident angle (in the RF domian) of the jth jammer. Again, noting the space and time separability of the functions given by equations 6.26 and 6.27, the final diffracted field can now be written as

$$E_D'(x', t) =$$

$$\int_0^L \int_{-\infty}^t \mathcal{L}_z \left\{ \begin{array}{l} \mathcal{L}_x\left\{L_r(x=x_{do}, z_o)M_r(t - \tau) + L_j(x=x_{do}, z_o)e^{i\Delta\beta_j z}M_j(t)\right\} \cdot \\ \left[\left[\mathcal{L}_x\left\{L_r(x=x_{do}, z_o)M_r(t' - \tau) + L_j(x=x_{do}, z_o)M_j(t')\right\}\right]^* \mathcal{L}_{-z}\left\{E_{BC}(x_o, z=z_{do}, t')\right\}\right] \end{array} \right\} dt' dz$$

$$6.28$$

where $L_r(x = x_{do}, z_o)$ and $M_r(t - \tau)$ for the desired signal are defined by equations 6.14 and 6.15 respectively, and the corresponding interference terms according to

$$L_j(x = x_{do}, z_o) = e^{i\Phi(z_o)} e^{-i\omega_j z_o a \sin(\theta_j)/cD} \Pi\left[\frac{z_o}{ND}\right] \text{comb}\left[\frac{z_o}{D}\right] * g\left[\frac{z_o}{d}\right] \qquad 6.29$$

and

$$M_j(t) = A_j e^{i\omega_j t} e^{i\omega_o t}.$$

6.30

The phasor term $e^{i\Delta\beta_j z}$ in equation 6.28 indicates the the *jth* jammer is arriving at a different angle than the desired signal, and the desired signal component of the read-out beam is undeviated from the write beam component, with $\Delta\beta_j = \dfrac{a}{cD}\left[\omega_r \sin(\theta_r) - \omega_j \sin(\theta_j)\right]$. Carrying out the multiplication of the operator terms of equation 6.28 yields

$$E'_D(x',t)=\int_0^L \int_{-\infty}^t \pounds_z \left\{ \pounds_{-z}\left\{E_{BC}\left(x_o, z=z_{do}, t'\right)\right\} \begin{bmatrix} I_{ARr}M_r^*(t'-\tau)M_r(t-\tau) + \\ \displaystyle\sum_{j=1}^P I_{ARj}e^{i(\Delta\alpha_j x'+\Delta\beta_j z)}M_j^*(t')M_j(t) \\ +\displaystyle\sum_{j=1}^P \Gamma^*_{ARrj}e^{i(\Delta\alpha_j x'+\Delta\beta_j z)}M_j(t)M_r^*(t'-\tau) \\ +\displaystyle\sum_{j=1}^P I_{ARrj}e^{i(\Delta\alpha_j x'+\Delta\beta_j z)}M_j^*(t')M_r(t-\tau) \end{bmatrix}\right\}dt'dz$$

6.31

where the following definitions have been made,

$$I_{ARr}(x,z)=\left|\pounds_x\left\{L_r\left(x=x_{do}, z_o\right)\right\}\right|^2$$

6.32

$$I_{ARj}(x,z)=\left|\pounds_x\left\{L_j\left(x=x_{do}, z_o\right)\right\}\right|^2$$

6.33

$$\Gamma^*_{ARrj}(x,z)=\left[\pounds_x\left\{L_r\left(x=x_{do}, z_o\right)\right\}\right]^* \pounds_x\left\{L_j\left(x=x_{do}, z_o\right)\right\}$$

6.34

$$I_{ARrj}(x,z)=\pounds_x\left\{L_r\left(x=x_{do}, z_o\right)\right\}\left[\pounds_x\left\{L_j\left(x=x_{do}, z_o\right)\right\}\right]^*.$$

6.35

As in the previous section, it is assumed that the $e^{i(\Delta\alpha_{rj} x'+\Delta\beta_{rj} z)}$ phasor term can be moved outside of the $\pounds_x$ operator. Again assuming that the intensity terms of equations 6.32 through 6.35 are approximately constant in x and z, and that the angular shift due to the phasor term $e^{i\Delta\alpha_j x}$ is small, the four terms in the interior square brackets of equation 6.31 can be moved outside of the nested $\pounds_z$ operators. The nested $\pounds_z$

144

operators can then be collapsed, and the diffracted field $E'_D(x',t)$ can then be written as the sum of four separate integrals;

$$E'_D(x',t) = \int_0^L I_{ARr} e^{i(\Delta\alpha_r x + \Delta\beta_r z)} M_r(t-\tau) \int_{-\infty}^{\infty} E_{BC}(x_o, z=z_{do}, t') M_r^*(t'-\tau) dt' dz$$

$$+ \int_0^L M_j(t) \sum_{j=1}^P I_{ARj} e^{i(\Delta\alpha_j x + \Delta\beta_j z)} \int_{-\infty}^{\infty} E_{BC}(x_o, z=z_{do}, t') M_j^*(t') dt' dz +$$

$$\int_0^L M_j(t) \sum_{j=1}^P I_{ARrj}^* e^{i(\Delta\alpha_{rj} x' + \Delta\beta_{rj} z)} \int_{-\infty}^{\infty} E_{BC}(x_o, z=z_{do}, t') M_r^*(t'-\tau) dt' dz + \qquad .6.36$$

$$\int_0^L M_r(t-\tau) \sum_{j=1}^P I_{ARrj} e^{-i(\Delta\alpha_{rj} x' + \Delta\beta_{rj} z)} \int_{-\infty}^{\infty} E_{BC}(x_o, z=z_{do}, t') M_j^*(t') dt' dz$$

The four integrals will be evaluated separately. Allowing the upper limit of the temporal integrals to go to infinity, the first integral is the holographic reconstruction of the desired signal, and yields the same result as given in equation 6.24,

$$d(t) = \tilde{r}(t-\tau) e^{i\omega_r(t-\tau)} e^{i\omega_o t} R(\tau - x'/V) I_{ARr} \Pi\left[\frac{x'}{X}\right] \qquad 6.37$$

where the sinc function is equal to unity because of perfect Bragg matching. Substituting in the expressions for $E_{BCr}(x_o, z_{do}, t')$ and $M_j(t)$, the second integral of equation 6.36 becomes,

$$C_1(t) = \int_0^L \sum_{j=1}^P I_{ARj} e^{i(\Delta\alpha_j x + \Delta\beta_j z)} \Pi\left[\frac{x_o}{X}\right] |A_j|^2 e^{i\omega_j t} e^{i\omega_o t} e^{i\omega_r(\tau - x_o/V)} \int_{-\infty}^{\infty} \tilde{r}(t'' + \tau - x_o/V) e^{it''(\omega_r - \omega_j)} dt'' dz \; 6.38$$

where $t'' + \tau = t'$. The cross-correlation between the jammer signal and the desired signal will be assumed to be small, and hence the contribution of equation 6.38 to the total diffracted field will be considered negligible. This assumption is based on the fact that the jammer is very narrowband, and the shared frequency content with the reference signal spectrum, if any, will become vanishingly small as the integration time becomes large. Only if a harmonic component of the desired signal matches the jammer will any significant grating be written that the jammer can diffract off of.

The third integral can be written as

$$C_2(t) = \int_0^L \sum_{j=1}^P I^*_{ARrj} e^{i(\Delta\alpha_j x' + \Delta\beta_j z)} \Pi\left[\frac{x_o}{X}\right] A_j e^{i\omega_j t} e^{i\omega_o t} e^{i\omega_r(\tau - x_o/V)} \int_{-\infty}^\infty \tilde{r}(t'' + \tau - x_o/V) \tilde{r}^*(t'') dt'' dz .6.39$$

The temporal term is the autocorrelation of the desired signal, which as in equation 6.37, will have a peak at $\tau = x_o/V$. This portion of the diffracted field can then be written as

$$C_2(t) = \sum_{j=1}^P A_j e^{i\omega_j t} e^{i\omega_o t} R(\tau - x'/V) \Pi\left[\frac{x'}{X}\right] I^*_{ARrj} \operatorname{sinc}(\Delta\beta_j L) * \delta(x' - \Delta\alpha_j^2/2k_o). \quad 6.40$$

This result is quite similar to the result of equation 6.37, and indicates that the jammer signals are also diffracted off of the holographic grating formed by the desired signal, but weighted by a sinc function with an argument equal to the momentum mismatch between the desired signal and each particular jammer.

The fourth and final integral can be written as

$$C_3(t) = \int_0^L \sum_{j=1}^P A_j^* \tilde{r}(t-\tau) e^{i\omega_r(t-x_o/V)} e^{i\omega_o t} \Pi\left[\frac{x_o}{X}\right] I_{ARrj} e^{-i(\Delta\alpha_j x' + \Delta\beta_j z)} \int_{-\infty}^\infty \tilde{r}(t'' + \tau - x_o/V) e^{it''(\omega_r - \omega_j)} dt'' dz$$

6.41

This term represents the diffraction of the desired signal off of the weak gratings formed betwen the jammers and the corresponding frequency components of the reference in the AOD. This term is usually small and can be neglected, but for very large jammers it can produce a significant diffracted component, but since it produces the desired signal waveform, it can be safely neglected. In fact, this situation is that of "piggy-back" signals discussed in Chapter 7, and these signals which diffract off of gratings written by signals at a different frequency are eliminated with a Fabry-Perot etalon filter. The total diffracted field will then be the sum of the first and third integral terms,

146

$$E'_D(x',t) = R(\tau - x'/V)\Pi\left[\frac{x'}{X}\right]\left\{\begin{array}{l}\tilde{r}(t-\tau)e^{i\omega_r(t-\tau)}e^{i\omega_o t}I_{ARr}\\ +\sum_{j=1}^{P}A_je^{i\omega_j t}e^{i\omega_o t}\Gamma^*_{ARrj}\,\mathrm{sinc}(\Delta\beta_j L)*\delta(x'-\Delta\alpha_j^2/2k_o)\end{array}\right\}.6.42$$

This result demonstrates the holographic beamforming process leading to the reconstruction of not only the desired signal as in the previous section, but the jammers which also diffract off of the array sidelobes of the grating formed by the desired signal. It is these jammers of course which corrupt the SNR of the desired signal return, and provide the motivation for the jammer-nulling processor of the following chapter.

6.1.4 Analytic Expression for the Adaptively Formed Holographic Grating

The results of the prior two sections demonstrate that the holographically reconstructed field is proportional to the strength of the temporal autocorrelation of the desired signal, which has been represented by $R(\tau - x_o/V)$. The operator notation allowed the convenient manipulation of the interacting fields, and dramatically simplified the spatio-temporal nature of these fields. In this section, an analytic expression of the spatio-temporal holographic grating formed in the PRC will be derived, based on a simplified model of holographic imprinting.

The interacting optical fields will consist of the reference signal from the Bragg cell, $E_{BC_r}(x_o, z = z_{do}, t')$, which is modulated by the desired signal $\tilde{r}(t - x_o/V)$, and the signal from the array, $E_{ARr}(x = x_{do}, z_o, t)$, which is also modulated by the desired signal, at some fixed range delay. These two fields were given by equations 6.7 and 6.6, and are shown again below.

$$E_{ARr}(x=x_{do}, z_o, t)$$
$$=e^{i\omega_o t}e^{i\Phi(z_o)}\tilde{r}(t-\tau-z_o a\sin(\theta_{rf})/cD)e^{i\omega_r[t-\tau-z_o a\sin(\theta_{rf})/cD]}\Pi\left[\frac{z_o}{ND}\right]\mathrm{comb}\left[\frac{z_o}{D}\right]*g\left[\frac{z_o}{d}\right] \quad 6.6$$

$$E_{BCr}(x_o, z = z_{do}, t) = e^{i\omega_o t} \Pi\left[\frac{x_o}{X}\right]\tilde{r}(t - x_o/V)e^{i\omega_r(t - x_o/V)}. \qquad 6.7$$

where the broadband nature of the time delay has been included as a delay term on the desired signal envelope. The analysis begins by writing out explicitly the expression for the holographic grating given by equation 6.10,

$$g(x,z,t) = \int_{-\infty}^{t}\left[\pounds_x\{E_{ARr}(x = x_{do}, z_o, t')\}\right]^* \pounds_{-z}\{E_{BCr}(x_o, z = z_{do}, t')\}dt'. \qquad 6.10$$

Expanding out the operators in equation 6.10 for the fields 6.6 and 6.7 yields

$$g(x,z,t) = \frac{e^{-ik(x+z)}}{-\lambda^2 xz}\iint\left[\int_{-\infty}^{t} E_{ARr}^*(x = x_{do}, z_o, t')E_{BCr}(x_o, z = z_{do}, t')dt'\right]e^{\left[\frac{-ik(x-x_o)^2}{2z}\right]}e^{\left[\frac{-ik(z-z_o)^2}{2x}\right]}dx_o dz_o$$

$$6.43$$

Substituting in the fields given by equations 6.6 and 6.7, the holographic grating becomes,

$$g(x,z,t) =$$

$$P_1(x,z)\iint\left\{\begin{array}{l}\left[\int_{-\infty}^{t}\tilde{r}^*(t' - \tau - z_o a\sin(\theta_{rf})/cD)\tilde{r}(t' - x_o/V)dt'\right]e^{-i\omega_r(x_o/V - \tau - z_o a\sin(\theta_{rf})/cD)} \\ \cdot e^{i\Phi(z_o)}\Pi\left[\frac{z_o}{ND}\right]\text{comb}\left[\frac{z_o}{D}\right] * g\left[\frac{z_o}{d}\right]\Pi\left[\frac{x_o}{X}\right]P_2(x_o, z_o)\end{array}\right\}dx_o dz_o \qquad 6.44$$

The functions $P_1(x,z)$ and $P_2(x_o, z_o)$ result from the expansion of the quadratic exponential functions in equation 6.43, and are defined as

$$P_1(x,z) = \frac{e^{-ik(x+z)}}{-\lambda^2 xz}e^{\frac{-ik}{2}(x^2/z + z^2/x)} \qquad 6.45$$

$$P_2(x_o, z_o) = e^{ikx_o x/z}e^{ikz_o z/x}e^{\frac{-ik}{2}(x_o^2/z + z_o^2/x)}. \qquad 6.46$$

Since the photorefractive integration time is usually many milli-seconds, and the reference signal repetition time is on the order of micro-seconds, the evaluation of the

temporal integral can be simplified by allowing the upper limit of the integral to be extended to $+\infty$, and then treating the integral as an autocorrelation of the signal $\tilde{r}(t')$. Instead of choosing a specific waveform for the signal $\tilde{r}(t')$, a Gaussian autocorrelation function will be assumed, resulting in

$$\int_{-\infty}^{\infty} \tilde{r}^*\left(t'-\tau-z_o a\sin\left(\theta_{rf}\right)/cD\right)\tilde{r}\left(t'-x_o/V\right)dt' = r_{11}\exp\left[\frac{-\pi}{2\sigma^2}\left(\tau-x_o/V-z_o a\sin\left(\theta_{rf}\right)/cD\right)^2\right].6.47$$

where r_{11} is proportional to the product of the amplitude of the reference signal (which is fixed) and the desired signal (which can vary), and $\sigma = \sigma_d\sqrt{\pi}$ where σ_d is the desired signal bandwidth. The expression given by equation 6.47 is the tilted correlation peak that represents the AOA of the array input by the tilt angle. The grating $g(x,z,t)$ can now be expressed as the product of two integrals,

$$g(x,z,t)=$$
$$P_1(x,z)r_{11}\left\{\begin{array}{l}\int e^{\left[\frac{-\pi}{2\sigma^2}\left(\tau-x_o/V+z_o a\sin\left(\theta_{rf}\right)/cD\right)^2\right]}e^{i\omega_r\left(\tau-x_o/V\right)}\Pi\left[\frac{x_o}{X}\right]e^{-ikx_o^2/2z}e^{ikx_o x/z}dx_o \cdot \\ \int e^{i\Phi(z_o)}e^{i\omega_r z_o a\sin\left(\theta_{rf}\right)/cD}\Pi\left[\frac{z_o}{ND}\right]\text{comb}\left[\frac{z_o}{D}\right]*g\left[\frac{z_o}{d}\right]e^{-ikz_o^2/2x}e^{ikz_o z/x}dz_o\end{array}\right\}\quad 6.48$$

At this point, a narrowband assumption will be made, which removes the angularly dependent delay term $z_o a\sin\left(\theta_{rf}\right)/cD$ from the argument of the Gaussian in equation 6.48. This allows the grating to be written as a seperable function of the form

$$g(x,z,t)=P_1(x,z)r_{11}\int Q(x_o)dx_o\int S(z_o)dz_o \qquad 6.49$$

where each of the integrals can now be evaluated separately. The integral $\int Q(x_o)dx_o$ over the variable x_o will be evaluated first. This integral can be written in terms of that of a complex Gaussian,

$$\int Q(x_o)dx_o = e^{i\omega_r\tau}e^{(-\pi\tau^2/2\sigma^2)}\int e^{(bx_o^2+ax_o)}e^{ik(cx_ox+dx_o+gx_o^2)}dx_o$$

$$= e^{i\omega_r\tau}e^{(-\pi\tau^2/2\sigma^2)}f_1(x) \qquad\qquad 6.50$$

where the aperture function $\Pi[x_o/X]$ has been neglected since for a large aperture it's effect in the far field will only be that of a convolution with a delta function. The integral portion of equation 6.50 can be evaluated using the method of stationary phase[2], with the result that the complex Gaussian integral function $f_1(x)$ can be approximated by

$$f_1(x) = \int e^{(bx_o^2+ax_o)}e^{ik(cx_ox+dx_o+gx_o^2)}dx_o$$

$$= \int h(x_o)e^{ik\mu(x_o)}dx_o \approx e^{ik\mu(X_o)}h(X_o)\sqrt{\frac{2\pi i}{k\mu''(X_o)}} \qquad 6.51$$

where $h(x_o) = e^{(bx_o^2+ax_o)}$, $\mu(x_o) = e^{(cx_ox+dx_o+gx_o^2)}$, and

$$a = \tau\pi/\sigma^2 V \qquad\qquad 6.52 \qquad\qquad b = -\pi/2\sigma^2 V^2 \qquad\qquad 6.53$$

$$c = 1/z \qquad\qquad 6.54 \qquad\qquad d = -\omega_r/kV \qquad\qquad 6.55$$

$$g = -1/2z \qquad\qquad 6.56$$

The term $\mu''(X_o)$ in equation 6.51 is the second derivative of $\mu(x_o)$ evaluated at the stationary point X_o, where

$$\mu'(x_o)\big|_{X_o} = 0 \qquad\qquad 6.57$$

and $\mu'(x_o)$ is the first derivative of $\mu(x_o)$, and it is found that $X_o = -(cx+d)/2g$. Using the approximation given in 6.51, and after much algebra, the function $f_1(x)$ can be approximated by

$$f_1(x) \approx e^{\pi(x+x')^2/w_x^2}e^{-\pi(z+z')^2/w_z^2}e^{\pi\tau^2/2\sigma^2}e^{ik(\omega_r^2z/2k^2V-\omega_r/kV-x^2/z)}e^{i\pi/4}\sqrt{2\pi z/k} \qquad 6.58$$

where $w_x = \sqrt{2}\sigma V$, $w_z = kV^2\sigma/\omega_r$, $x' = (\tau kV^2 + z\omega_r)/kV$, and $z' = \tau kV^2/\omega_r$. Note that the term x' is actually a function of z, and x' and z' contain the range delay τ.

150

With these substitutions, $\int Q(x_o)dx_o$, the integral over x_o given in equation 6.50 becomes

$$\int Q(x_o)dx_o \approx e^{\pi(x+x')^2/w_x^2} e^{-\pi(z+z')^2/w_z^2} e^{ik\left(\omega_r^2 z/2k^2 V - \omega_r/kV - x^2/z\right)} e^{i\omega_r \tau} e^{i\pi/4} \sqrt{2\pi z/k} \qquad 6.59$$

The integral over z_o of equation 6.48, $\int S(z_o)dz_o$, can be solved by assuming that the individual fiber apertures of diameter d are very small, and therefore for essentially any plane x within the PRC, the field profile due to each aperture will be the appropriately scaled Fraunhoffer diffraction pattern[3]. This assumption is valid under the condition[4] that $x \gg \pi d^2/\lambda$, and for $d \approx 5\mu m$, and $\lambda \approx .5\mu m$, a distance of $x \gg 50\mu m$ satisfies the Fraunhoffer condition. Because the array is made up of many (N), very small apertures, it is reasonable to express the array field as a discrete sum of N small apertures. In addition, the random phase profile across the aperture due to the discrete fibers of different lengths given by $e^{i\Phi_n}$ has been approximated by $e^{i\Phi(z_o)} \text{comb}[z_o/D]$. Thus the approach will be to discretize the z_o integral, take the Fourier transform of the initial field profile, and take this expression to be the field as a function of z, at a propagation distance x throughout the crystal. From equation 6.48, the initial field profile is taken to be

$$f_2(z_o) = e^{i\omega_r z_o a \sin(\theta_{rf})/cD} \Pi\left[\frac{z_o}{ND}\right] \text{comb}\left[\frac{z_o}{D}\right] * g\left[\frac{z_o}{d}\right]. \qquad 6.60$$

Taking the Fourier transform and substituting the result back into equation 6.48 yields

$$\int S(z_o)dz_o \approx dD\sum_{n=1}^{N} e^{i\Phi_n} \text{comb}\left[\frac{zD}{\lambda x} - \xi_o\right] g\left[d\left(\frac{zd}{\lambda x} - \xi_o\right)\right] e^{-ikn^2 D^2/2x} e^{iknDz/x} \qquad 6.61$$

where $\xi_o = \omega_r a \sin(\theta_r)/2\pi cD$. Finally, the expression for $g(x,z,t)$ given in equation 6.48 is

$$g(x,z,t) = -\left\{ \begin{array}{l} dDr_{11}\dfrac{\sqrt{2\pi z/k}}{\lambda^2 xz}\displaystyle\sum_{n=1}^{N} e^{i\Phi_n} \, \mathrm{comb}\left[\dfrac{zD}{\lambda x}-\xi_o\right]\left|g\left[d\left(\dfrac{zd}{\lambda x}-\xi_o\right)\right]e^{\pi(x+x')^2/w_x^2}e^{-\pi(z+z')^2/w_z^2} \\ e^{-ikn^2D^2/2x}e^{iknDz/x}e^{ik\left(\omega_r^2 z/2k^2 V-\omega_r/kV-z^2/2x-3x^2/2z-x-z\right)}e^{i\omega_r\tau}e^{i\pi/4} \end{array} \right\} .6.62$$

The result in equation 6.62 is difficult to interpret, in part due to the several mixed x and z variable terms. However, there are several features which can be pointed out. For example, the upper row of the equation shows that the strength of the grating is directly proportional to the amplitude of the desired signal, r_{11}. An amplitude scaling term then multiplies the sum of N Gaussian fiber apertures, each with a unique phase. The next term is an x and z variable Gaussian-like amplitude weighting term whose width varies inversely with the desired signal bandwidth σ. This weighting term is then multiplied by a z-varying Gaussian weighting term, whose width also varies inversely with desired signal bandwidth. The lower row of equation 6.62 is composed of all phasor terms, the last being a fixed term, preceeded by a phasor which is both signal frequency and delay dependent. The remaining phase terms indicate a complicated family of chirped and curved fringes formed throughout the PRC, which are responsible for diffracting the array inputs towards the image plane of the AOD.

6.2 Beam-Forming Processor Computer Simulation

The derivation of the Section 6.1 treated the photorefractive material as a strictly linear material in that the grating strength was directly proportional to the time-integrated intensity of the write beams. As discussed in Chapter 4, photorefractive materials are very non-linear, and their holographic response varies with incidence angle, and grating spatial frequency. Adding these effects to the analysis of Section 6.1, in addition to such phonomena as fanning and two-wave-mixing, would have made the analysis virtually intractable. Even when assuming the PRC is linear with intensity, the analytic result for the holographic grating given by equation 6.62 makes

simple interpretation difficult. While the grating profile formed in the main-beam processor has been measured experimentally as a function of angle (reported later in this chapter), this measurement represents the integrated result of the entire grating volume, and information about the actual volumetric grating distribution is lost. In order to gain insight into the structure of these gratings, computer simulations of the main-beam forming processor were completed to provide not only a spatial mapping of the holographic gratings within the PRC, but also a useful tool for investigating various experimental configurations. Moreover, these simulations take into account the photorefractive responses to spatial frequency, and include grating nonlinearities, fanning and two-wave-mixing.

The simulations begin with a definition the optical mapping of the phased-array antenna, and the diffracted output of the acoustooptic Bragg cell. These fields are propagated via a split-step Fourier transform beam-propagation algorithm[5] and imaged onto the PRC in order to write the hologram. The holographic gratings within the PRC produced by these fields are calculated using a finite-difference algorithm[6, 7]. The hologram is then read out using the optical phased-array input, and the diffracted field is then propagated and focused onto a detector, and the incident RF waveform is extracted as the real part of the complex field, simulating single quadrant heterodyne detection. The simulation is executed in discrete time steps; for a given RF waveform sampled with N time steps, a field corresponding to the nth time step is formed and propagated through the optical system and the crystal. After N steps the index grating is fully evolved, and it is then read out by the optical phased-array field using the same propagation routine. We simulate a continuous, linear antenna array made up of 1500 sample points (the discrete fibers are ignored), and an AO Bragg cell made up of 500 discrete delays.

6.2.1 Split-Step Beam Propagation Algorithm

The split-step beam-propagation algorithm propagates the electro-magnetic fields in discrete steps by accounting for free-space propagation in the Fourier domain and media inhomogeneities and nonlinearities in real space. Consider an electric field $E(x)$ propagating in the z direction, in a (2-D) medium with index $n(x,z) = n_o + \Delta n(x,z)$, where n_o is the background refractive index and $\Delta n(x,z)$ is an index perturbation. The split-step algorithm can be summarized as: the Fourier transform of the field is taken with respect to the transverse dimension of the incident field (x direction here), and then multiplied by a free-space propagation transfer function to account for free-space diffraction, the inverse Fourier transform is taken, and multiplied by a transmittance function which describes the integrated effects of the inhomogeneous media between z and $z + \Delta z$. The media transmittance function is proportional to $n(x,z)$, and will be unity in the case of free-space, but more generally it can be a lens, a grating structure such as a hologram or perhaps a random index perturbation describing turbulent media. The field at the $m + 1$ propagation step can be expressed algorithmically as[5]

$$E_x\big[x,(m+1)\Delta z\big] = e^{i\Delta n(x,m\Delta z)k_o\Delta z}\,\mathcal{F}^{-1}\left\{\mathcal{F}\{E_x(x,m\Delta z)\}e^{i\Delta z\sqrt{k^2-k_x^2}}\right\}. \qquad 6.63$$

where the discretely sampled index perturbation is taken to be

$$\Delta n(x,m\Delta z) = \int_{(m-1)\Delta z}^{m\Delta z} \Delta n(x,z)dz \qquad 6.64$$

This algorithm is then implemented for M discrete spatial steps of length Δz, and the final field is the field at the plane $z = M\Delta z$.

6.2.2 Finite-Difference Photorefractive Grating Model

The photorefractive gratings formed within the crystal are calculated using a Crank-Nicholson[8] finite difference algorithm. The simulations presented here used an existing

PRC finite-difference program developed by Steve Blair for photorefractive two-beam coupling and fanning studies[9, 10].

The index calculation used in the finite-difference algorithm is based on an analytical expression for the spatio-temporal evolution of photorefractive space-charge field[6, 7, 11], expressed as a function of incident beam geometries and intensities, and material parameters. From reference 11, the spatio-temporal evolution of the normalized photorefractive space-charge field $\tilde{E}^{sc}$ is described by

$$\left(\tau\frac{\partial}{\partial t}+1\right)\tilde{E}^{sc} = \frac{\partial^2 \tilde{E}^{sc}}{\partial \tilde{x}^2} - \frac{\partial I/\partial \tilde{x}}{(I+I_d)} \qquad 6.65$$

where $\tilde{E}^{sc} \equiv E/E_q$, and $E_q = qN_A/(\varepsilon_{DC}k_D)$ is the trap density limited space-charge field with q being the electron charge, N_A is the crystal acceptor dopant density, ε_{DC} is the DC dielectric constant, and k_D is the Debye screening vector given by $K_D = q\sqrt{N_A(N_D-N_A)/(N_D\varepsilon_{dc}k_B T)}$ for crystal doping density N_D and temperature T, where k_B is the Boltzman constant. In equation 6.65, τ is the dielectric relaxation time constant given by $\tau \approx \tau_o/[I(x)+I_d]$ where τ_o is a function of material parameters[12], $I(x)$ is the the spatially varying incident optical intensity, and I_d is an effective background illumination that accounts for the thermal excitation of charge carriers. The equation as shown is written in terms of the normalized transverse spatial variable $\tilde{x}$, given by $\tilde{x} \equiv k_D x$. The space-charge field is coupled to the amplitude of the electric field according to

$$2ik\frac{\partial A(x,z)}{\partial z} + \frac{\partial^2 A(x,z)}{\partial x^2} + 4k\gamma_o \tilde{E}^{sc} A(x,z) = 0 \qquad 6.66$$

where $E(x,z,t) = A(x,z)e^{i(kz-\omega t)}$, and the coupling constant is given by $\gamma_o = 2\omega n^3 r_{eff}/c$.

The Crank-Nicholson finite difference algorithm is implemented in the PRC by first making discreet approximations to the derivatives in equation 6.65. At each time step $n\Delta t$, the space-charge field is calculated along the transverse direction x in discreet

spatial steps $i\Delta x$, at a given spatial propagation step $m\Delta z$ in the PRC. The optical field amplitudes are modified by the interaction with the space-charge field induced index perturbation, and then propagated via the beam-propagation algorithm to the next step $(m+1)\Delta z$. This process is continued through the entire crystal, and then repeated for the next time step $(n+1)\Delta t$, where $\Delta t/\tau = 0.01$, and the total number of simulation steps is 200, corresponding to 2 photorefractive time constants. The spatial sampling parameters used were $\Delta z/\lambda = 6$ in the propagation dimension, and $\Delta x/\lambda = 0.25$ for the transverse dimension.

6.2.3 Simulation Results

The main-beam forming processor simulation results presented here are based on a geometry where both the optical signal from the phased-array and the reference Bragg cell are imaged onto the entrance face of the PRC. Plane wave inputs to the array have been chosen only for simplicity; curved or more complicated wavefronts could also be accomodated. The overall optical phased-array profile is weighted by a gaussian to eliminate the high spatial frequency terms which are associated with a rectangular aperture. This should yield an array function with reduced sidelobes.

Figure 6.4a shows the simulation output of the main-beam processor optical architecture. The Bragg cell and the phased-array ouputs are imaged with a four-f optical system onto the input face of the PRC, where the input and output faces are designated by the dashed vertical lines shown in the figure. Figure 6.4b shows the interaction between the two fields in the crystal, and figure 6.4c shows the resulting holographic grating formed within the crystal (both images rotated by 90 dgrees). The angle between the two fields is approximately 15 degrees, the crystal is 1.2 mm thick, and the RF input is on array boresight. The grating structure formed within the crystal is much more complex than the simple slice description used in the previous

156

(a)

(b)   (c)
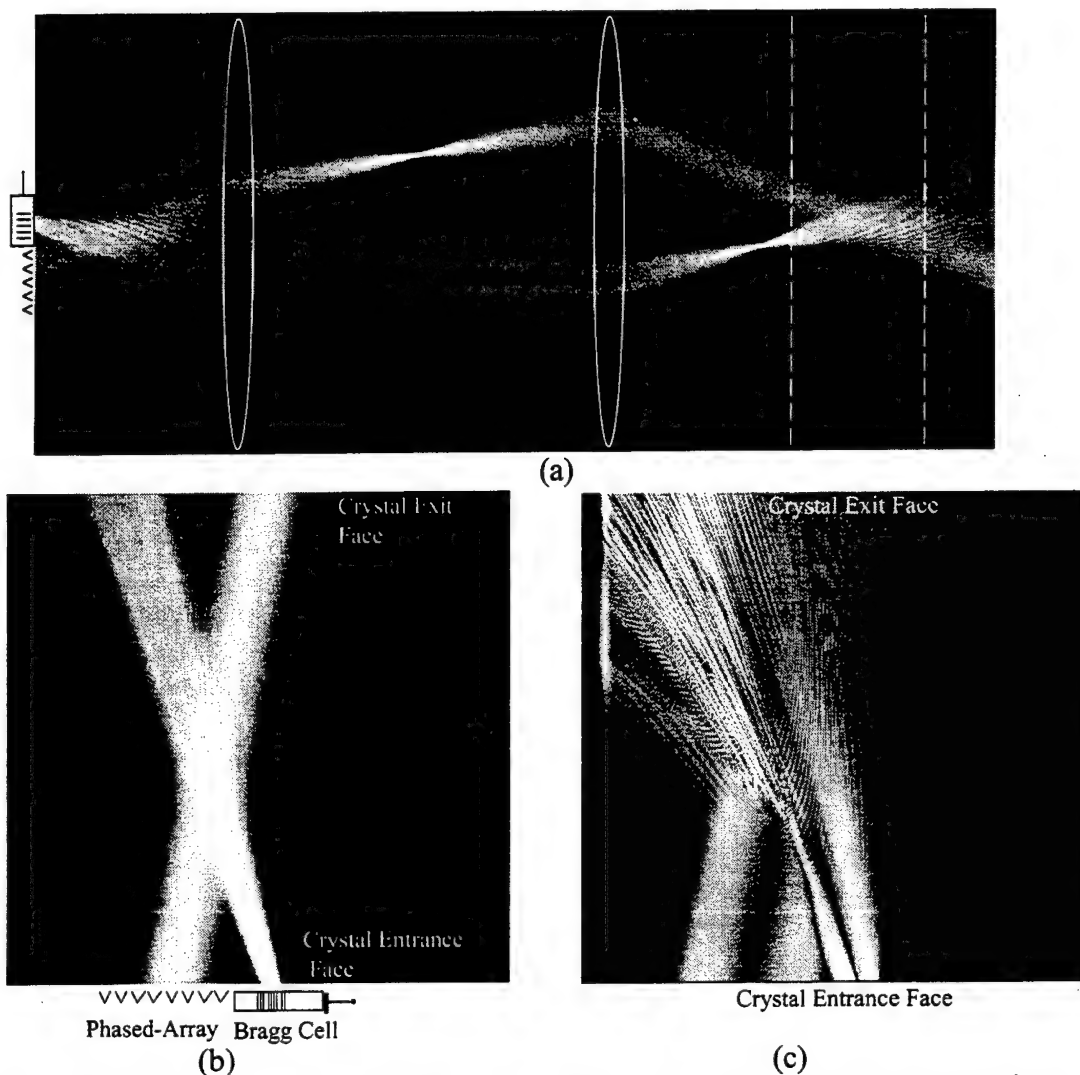
Figure 6.4. Optical architecture of main-beam forming processor shown in (a), field interaction within the crystal shown in (b), and resulting holographic grating shown in (c). Figures (b) and (c) are rotated by 90 degrees. With each time step the diffraction from the Bragg cell slides along by one pixel, the array signal evolves, and the grating is updated.

sections,due to the derivative bandpass photorefractive response, photorefractive nonlinearities, and fanning.

After the grating is formed, it is stored and subsequently read out by the phased-array optical signal. This is shown in figure 6.5a, where the diffracted field is seen to be diverging slightly, and originating from a virtual source location of the original AO reference beam write field at the focus behind the crystal corresponding to the autocorrelation time delay between the phased-array and AO signals. A cross-

157
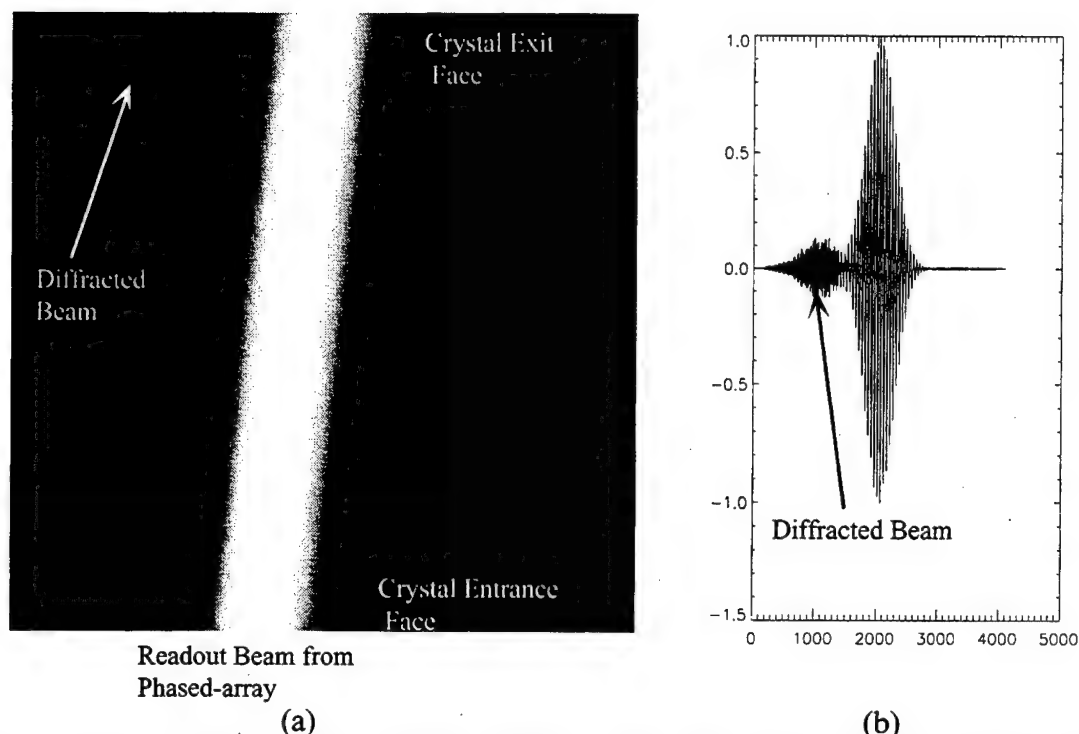
Figure 6.5. Readout of holographic grating with phased-array field and resulting diffracted field shown in (a). Cross-section of the field at the crystal ouput face in (b).

section of the field at the crystal output face is shown in figure 6.5b. The outputs shown in figure 6.5c represent only one of approximately 200 time samples from the readout field; propagating each of these temporal samples through the grating, focusing the diffracted field and measuring the peak value for each allows the input RF chirp to be recovered.

The holographic grating has been read out with an umodulated plane wave as a function of angle in order to examine the Bragg selectivity of the hologram. The results of this simulation are shown in figure 6.6. Figure 6.6 indicates that the angular selectivity resembles a sinc function response convolved with a Gaussian to some extent, although somewhat assymetrical with a subtle lobe structure. This assymetry is probably due to the assymetrical fanning gain evident in figure 6.4c. The -3 dB width is approximately 0.0075 rad, or 0.43 degrees, which is appropriate for a 1.2 mm crystal.
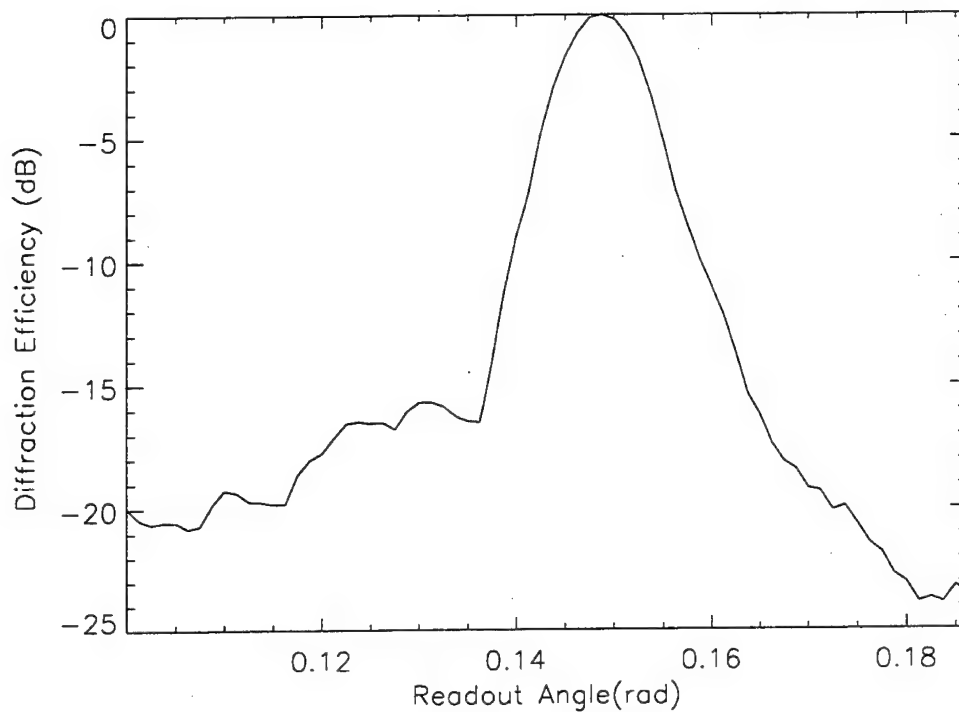
Figure 6.6. Angular selectivity of hologram formed in the PRC.

This result shows that an angular selective grating is being formed, and that adaptive beam-forming has been accomplished.

The more interesting beam-forming scenario is when there is interference present as well. Figure 6.7 shows the interaction within the PRC where in addition to the desired signal on array boresight, there is a narrowband jammer present at approximately 1.5 (0.025 rad) degrees (optical) from boresight, and also random noise across the array. The desired signal, which is a chirp, is shown in figure 6.8a. The jammer corrupted chirp is shown in figure 6.8b, where for this example the jammer has the same power as the desired signal. The random noise is 20 dB lower than the desired and jammer signals. After forming the grating and reading it out with the beam from the phased-array, the desired chirp signal is recovered as shown in figure 6.9. Although somewhat corrupted by the jammer, which is clearly visible during the off portion of the chirp, the SINR of the recovered signal is dramatically improved over the input

159
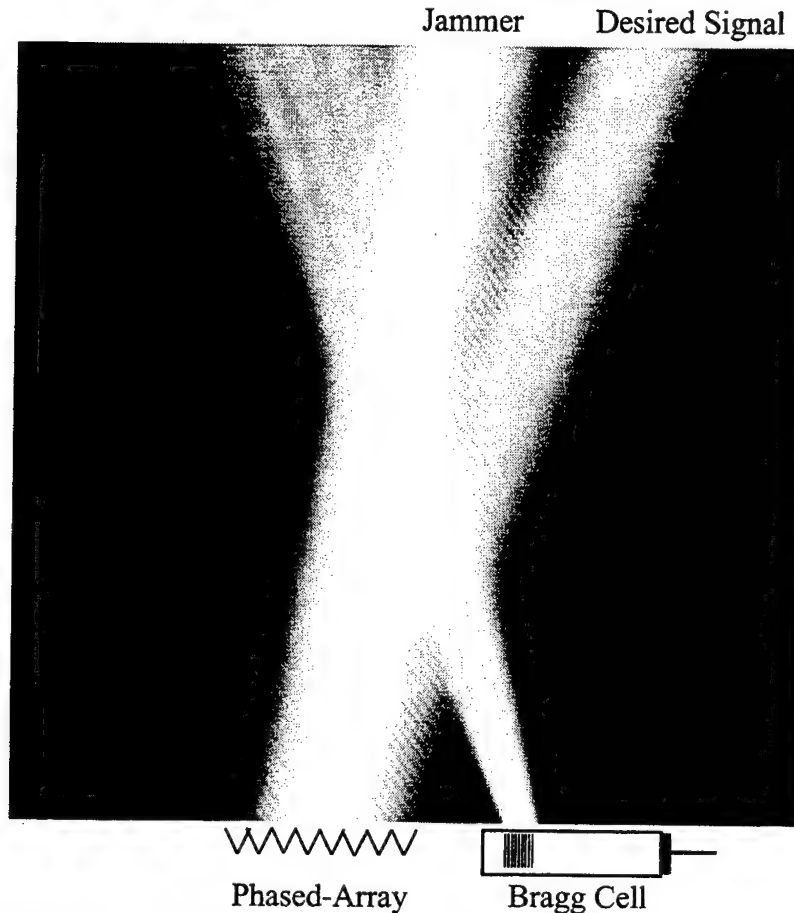
Figure 6.7. Beam interaction within PRC for beam-forming simulation in the presence of a narrowband jammer and random noise across the array.

signal shown in figure 6.8b. The SINR has been improved by approximately 24 dB (in power), which agrees reasonably well with the attenuation expected due to the angular selectivity shown in figure 6.6.

Increasing the power of the jammer much further introduced some difficulties with the simulations. In particular, the simulations needed to be run for many more cycles in order to write an adequate grating, and thus became very time-intensive. The requirements for many more simulation cycles is because there is always a finite amount of correlation between the jammer and and the desired signal when calculated over a finite temporal window. For example in the lab, the repetitive chirp is being presented to the hologram at a pulse repetition frequency of approximately 100 kHz,

(a)   (b)
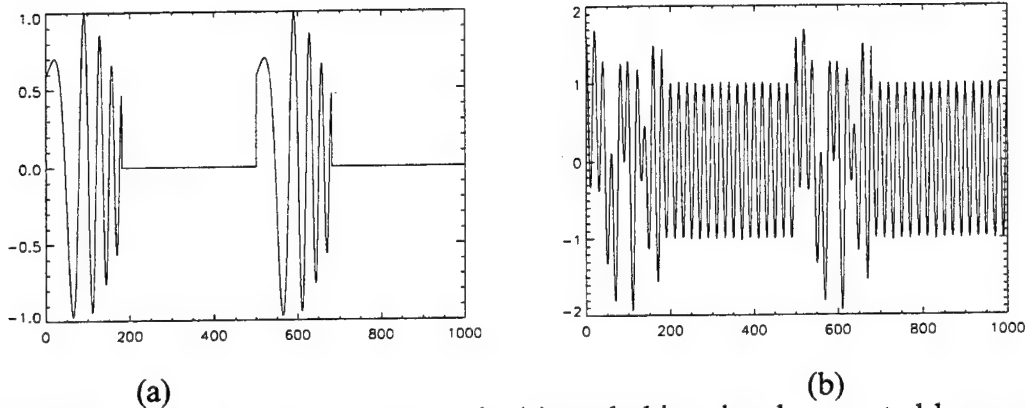
Figure 6.7. Desired chirp signal shown in (a), and chirp signal corrupted by equal strength jammer shown in (b).
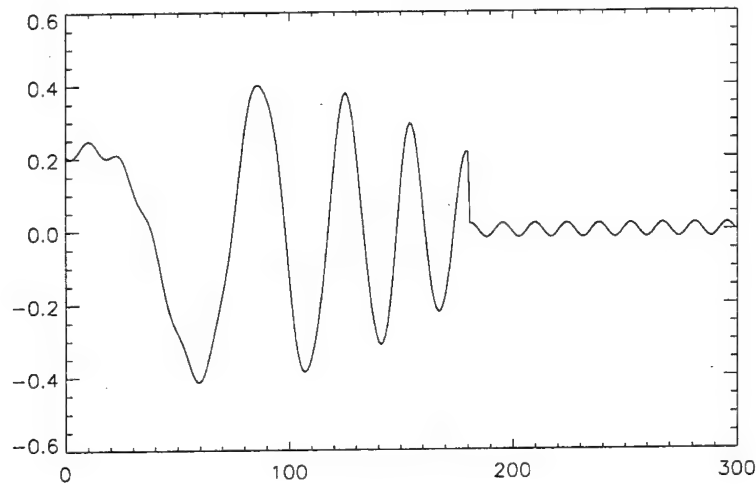
Figure 6.9. Recovered desired chirp signal with residual jammer, demonstrating an SINR improvement of approximately 24 dB.

which corresponds to many chirp presentations over a single time-constant of the PRC (1 sec) or the feedback (10 msec). Thus, writing a grating for only a few chirp cycles allows for grating terms to be written between the desired signal and the jammer.

Results of a simulation with the jammer 10 dB greater than that of the desired signal are shown in figure 6.10. As shown in figure 6.10a, the desired signal input from the array is severely corrupted, although the recovered chirp shown in 6.10b has an SINR improvement again of approximately 24 dB. Figure 6.10b suggests that the lower frequency components of the recovered chirp have been degraded the most

161

(a)   (b)
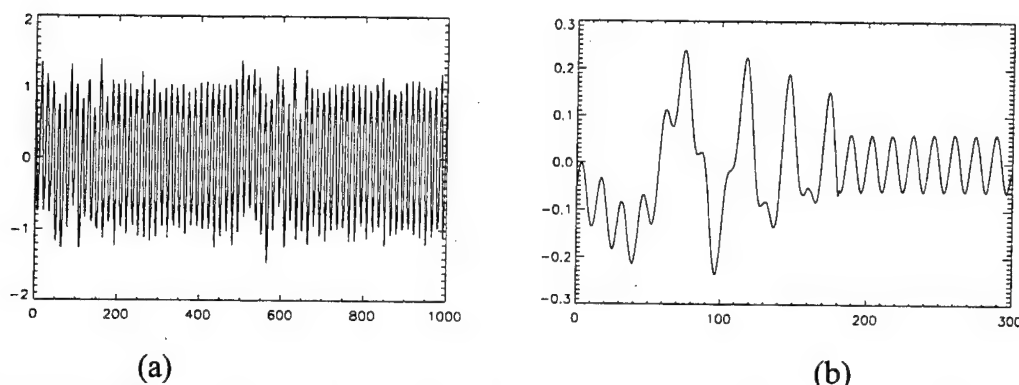
Figure 6.10. Corrupted desired chirp input signal shown in (a), and recovered desired signal in (b) demonstrating an SINR improvement of approximately 24 dB in the presence of a strong jammer.

severely. This may be due to the fact that the low frequency grating terms written by the strong jammer have washed-out the lower frequency grating terms produced by the weaker desired signal.

The simulation results of Section 6.2 demonstrate the adaptive beam-forming process in the presence of interference, using a beam-propagation model which includes diffraction, and a dynamic holographic grating model which takes into account the nonlinear and non-ideal behavior of photorefractive materials.

6.3 Experimental Demonstration

6.3.1 Overview of experimental set-up

The electro-optically upconverted signals from far-field radar sources which are incident on a phased-array are simulated in our laboratory experimental system using multiple acousto-optic modulators in the back focal plane of a lens as shown in figure 6.11. Several sources can be input into the processor at three different AOAs simultaneously, while two sources can be scanned in angle using motorized translation stages. A diffuser can be placed at the front focal plane to simulate the complex phase front that would result from fibers of unequal length, as well as a Ronchi ruling to simulate the sampled nature of the phased array and fiber bundle.

162
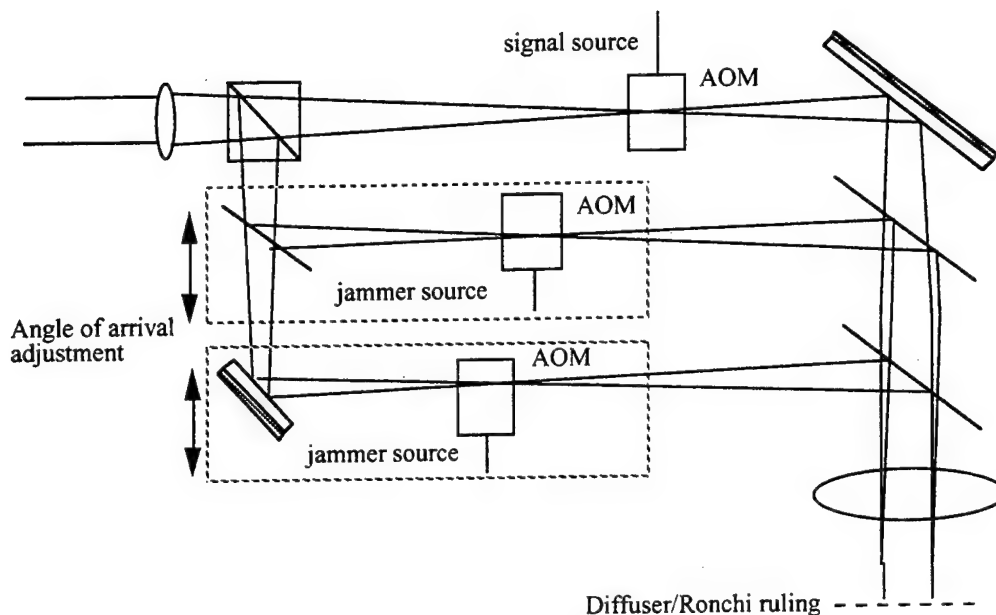
Figure 6.11. The phased-array simulator consists of three AOMS in the back focal planeof a collimating lens, which simulate the electrooptically upconverted signal from far-field radar returns.

The optical layout of the beam-forming phased-array radar processor is shown in figure 6.12. The 514 nm argon source is spatially filtered, collimated, and incident on the first beam-splitter (BS1). Light exiting one port of BS1 is sent to the phased array simulator where it is divided into three paths, one for each AOM. As described above, the AOMs are in the back focal plane of a lens, thus translation in the back focal plane changes the effective AOA of the source at the front focal plane. The front focal plane is approximately at the front of the PRC, with the signal at the PRC consisting of two vertically diverging replicas of the simulator output necessary for the Bragg degeneracy write/read technique described in Chapter 5. The replicas are produced using the combination of polarizing elements shown in the figure. The horizontally polarized diffracted output of the AOMs is passed through the first 45 degree $\lambda/4$ plate which produces circular polarization and then through the Rochon prism to produce two linear, orthogonally polarized beams diverging at approximately 0.2 degrees.
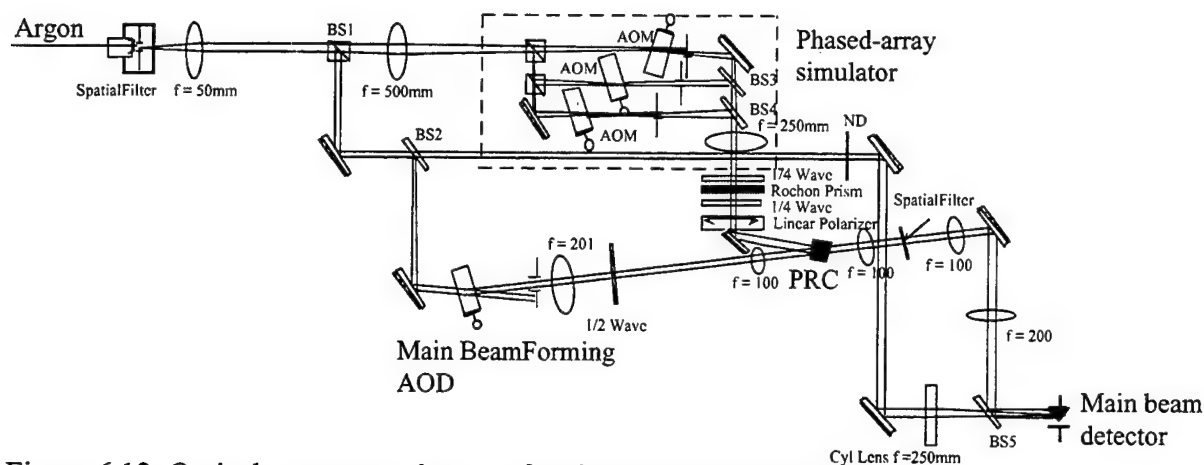
Figure 6.12. Optical component layout of main-beam forming phased-array radar processor.

These two beams then pass through the second $\lambda/4$ plate to produce two circularly polarized beams, and after passing through the final linear polarizer become two horizontally polarized beams, both of which are incident on the PRC as extraordinary polarized waves. As described in Chapter 5, this technique allows the diffracted term from the hologram to be separated from the incident write beam. Rotating the first $\lambda/4$ plate chnages the beam ratio r, between reading and writing beams. The other output of BS1 is sent to BS2 where the reflected beam is sent to the main-beam forming Bragg cell, a TeO_2 slow-shear wave polarization-switching Bragg cell. The diffracted component from the Bragg cell is rotated back to a horizontal polarization with a $\lambda/2$ plate, demagnified with a 2:1 telescope, and incident upon the PRC to write gratings with the phased-array simulator output. The transmitted component of BS2 is sent to the main-beam photodetector for use as a heterodyne reference, and is usually focused to a slit with a cylindrical lens to have good overlap with the 1-D slit image of the Bragg cell produced by the diffracted beam from the PRC. The diffracted component from the PRC is separated from the write beams using the Bragg degeneracy technique and is then incident on the main-beam photodetector which is placed in the Fourier plane of the AOD . The Fabry-Perot bandpass filter array is not installed in this system, so this system is essentially a narrowband beam former with no time delay.

164
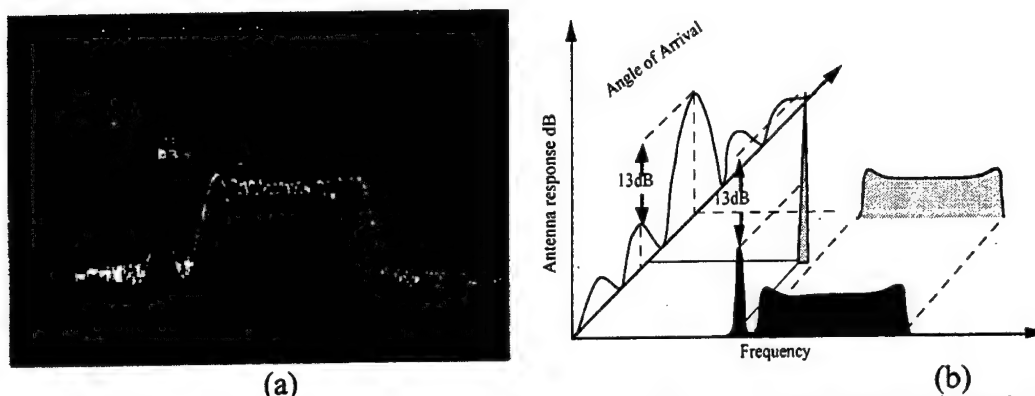
Figure 6.13. Frequency spectrum of processor output demonstrating beam formation in the direction of broadband signal of interest as viewed on a spectrum analyzer in (a) (1 MHz/.div, 10 dB/div). The received radar signal scenario is shown in (b).

6.3.2 Main-Beam Formation

Experimental results from the beam forming processor are shown in figure 6.13. Figure 6.13a shows the frequency spectrum of the output of the processor after adaptively steering the main beam towards the desired signal, and figure 6.13b depicts the radar scenario of the received signals. As shown in figure 6.13b, there is a broadband signal of interest (4 MHz wide sweep) and a strong narrowband jammer (76.8 MHz) incident at different AOAs. The AOA-frequency plane can be viewed as a slice out of the 3-D RF signal environment for 2-D arrays discussed in chapter 1. The beam-forming processor forms an antenna array function centered on the broadband signal of interest, while the jammer AOA is adjusted to fall on the first antenna sidelobe in this case. After weighting by the array function the processor signals can be projected onto the frequency axis as shown in 6.13b, which corresponds qualitatively to the spectrum analyzer plot shown in 6.13a. It is important to note that the spatial processing achieved by forming an array function pointed toward the desired signal has by itself reduced the jammer power due to the fact that it is arriving on an antenna sidelobe (a reduction of approximately 13 dB in this case). This jammer power reduction before detection reduces the required dynamic range of the detector.

165

<div align="center">(a)   (b)</div>
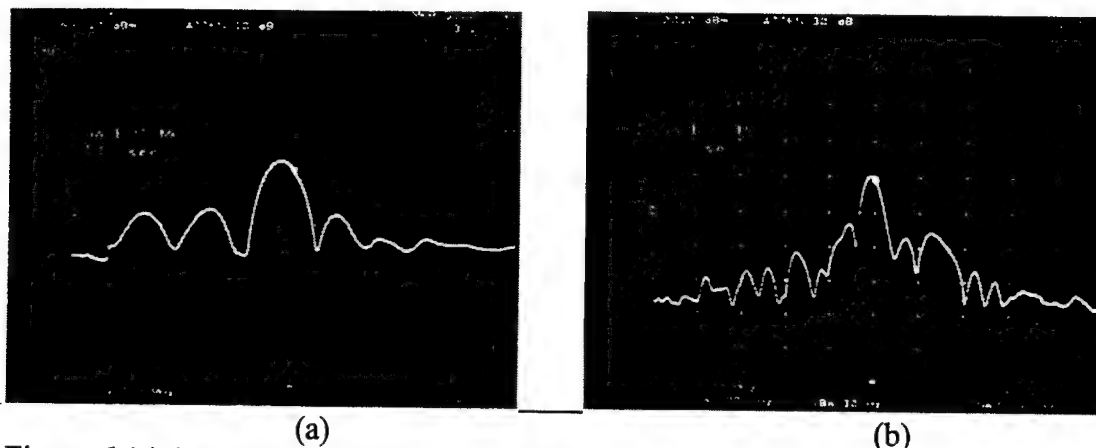
Figure 6.14. Measured antenna array pattern from beam-forming phased-array radar processor in (a), with diffuser in optical phased-array simulator (10 dB/div).

6.3.3 Measured Antenna Array Function

The antenna array function formed on the 4 MHz wide sweep signal has been experimentally measured by detecting the diffraction efficiency of the holographic grating as a function of angle. The results of this measurement are shown in figure 6.14a, where the horizontal axis corresponds to the AOA. Figure 6.14b shows the array function formed on the same signal of interest, where a diffuser has now been placed at the output of the phased-array simulator in order to simulate the effects of a complex phase front resulting from fibers of unequal length. Note that the scale of figure 6.14b is 50% larger than that of 6.14a. It is evident from both 6.14a and 6.14b that in general both antenna functions have the expected sinc-like structure, with the lobe structure being more complex in 6.14b. Non-ideal beam geometries and overlap, gaussian wavefronts, and photorefractive fanning and spatial frequency response, and processor instabilities during the long mechanical scan-time to make this measurement contribute to deviations away from the ideal sinc pattern.

References

[1]   J.W. Goodman, *Introduction to Fourier Optics*. (McGraw-Hill, 1968), chap. 2, pp. 10.

[2]   A. Papoulis, *Signal Analysis*. (McGraw-Hill, 1977), chap. 8, pp. 271-273.

[3]   K. Wagner and D. Psaltis, "Multilayer optical learning networks," Appl. Opt. **26**, no. 23, 5061-5076 Dec. (1987).

[4]   J.W. Goodman, *Introduction to Fourier Optics.* (Mcgraw-Hill, 1968), chap. 4, pp. 61.

[5]   J. A. Fleck, J. R. Morris and M.D. Feit, "Time dependent propagation of high energy laser pulses through the atmosphere," Appl. Phys. **10**, 129-160 (1976).

[6]   A. A. Zozulya, M. Saffman and D.Z. Anderson, "Propagation of light beams in photorefractive media- fanning, self-bending, and formation of self-pumped 4-wave mixing phase-conjugation geometries," Phys. Rev. Letts. **73**, no. 6, 818-821 (1994).

[7]   A. A. Zozulya, M. Saffman and D.Z. Anderson, "Double phase-conjugate mirror: convection and diffraction," J. Opt. Soc. Am. B **12**, no. 2, 255-264 Feb. (1995).

[8]   W. H. Press, W. T. Vettering, S. A. Teukolsky, B. P. Flannery, *Numerical Recipes in C.* (Cambridge University Press, 1992), chap. 19, pp. 848.

[9]   A. W. Sarto, K. Wagner, R. T. Weverka, S. Blair, and S. Weaver, "Photorefractive phased-array antenna beam-forming processor," in *Radar Processing, Technology, and Applications,* SPIE **2845**, (1996).

[10]   S. Blair, *Personal Communication,* 1995

[11]   M. Saffman, "Self-Organized Formation of Image Representations in Photorefractive Oscillators," Ph.D. thesis, University of Colorado, 1994.

[12]   G.C. Papen, B.E.A. Saleh and J.A. Tataronis, "Analysis of transient phase conjugation in photorefractive media," J. Opt. Soc. Am. B **5**, no. 8, 1763-1774 August (1988).

7. Jammer-Nulling Processor, and Combined Main-Beam Forming Jammer-Nulling Processor

The jammer-nulling processor computes the angles-of-arrival of interfering narrowband radar jamming signals and adaptively steers nulls in the antenna angular response in the direction of these jammers in order to extinguish them. This chapter begins with an overview of the operation of the jammer-nulling processor, followed by the development of a theoretical model which provides analytical expressions relating system parameters, such as feedback gain and phase, to performance metrics such as suppression depth and convergence rate. The model addresses the general jammer scenario of multiple narrowband interference sources of arbitrary spatial profile and is used to model system behavior for single and multiple jammers. The dynamical model which is developed is then used to derive an expression for the signal-to-interference-noise-ratio (SINR) of the system in the presence of a desired broadband signal and noise sources. The SINR derivation leads to insights for optimizing the processor performance based on system parameters such as relative strength between optical beams, electronic gain settings, and the physical constants of devices. A straightforward derivation develops a direct analogy between this dynamical model and the traditional, Widrow-Hopf LMS algorithm presented in Chapter 2. The latter portion of the chapter presents experimental results of convergence behavior for single and multiple jammers, pulsing jammers, and the processor jammer nulling bandwidth. The experimental results obtained are compared with the behavior predicted by the theoretical model. The final section of the Chapter presents experimental results of the combined jammer-nulling and beam-forming processor, which integrates the jammer-nulling processor of this Chapter and the beam-forming processor of the previous Chapter into a single adaptive processor.

7.1 Theory of Operation

The phased-array-radar jammer-nulling processor is depicted in figure 7.1. Incident radar signals are coherently converted to the optical domain and imaged onto a photorefractive crystal (PRC). The portion of the signal which passes undiffracted through the crystal is heterodyne detected, delayed, amplified and passed on to the output of the processor to form a staring main beam estimate. In this implementation the jammer-nulling processor is a completely independent system from the beam-forming processor; the main beam is not steered by this processor. The main beam signal is formed along a particular direction of interest, such as along the array boresight. This is accomplished by heterodyne detection of the portion of the phased-array simulator output which is transmitted directly through the PRC. Steering of the main beam is accomplished by varying the angle of the reference beam. This simplified beam-forming method is implemented here because the relevant aspects of the jammer-nulling processor performance are independent of the beam-forming mechanism, and partly because historically, the jammer-nulling processor was implemented in this manner initially.

The processor output is formed as the difference between the main-beam signal and the jammer estimate, and is fed back to the acoustooptic Bragg cell in order to calculate correlation weights in the form of holographic gratings in the PRC. If the received radar signal contains a narrowband jammer as well as a broadband signal of interest, the delayed version of the signal diffracted from the Bragg cell will produce stationary fringes only with the incident narrowband jammer when interfered with the array input in the PRC. Broadband signals are decorrelated after the feedback delay and hence produce moving fringe patterns which result in no stationary gratings. For an incoming jammer at frequency ω_j, possibly composed of multiple spatial modes l,
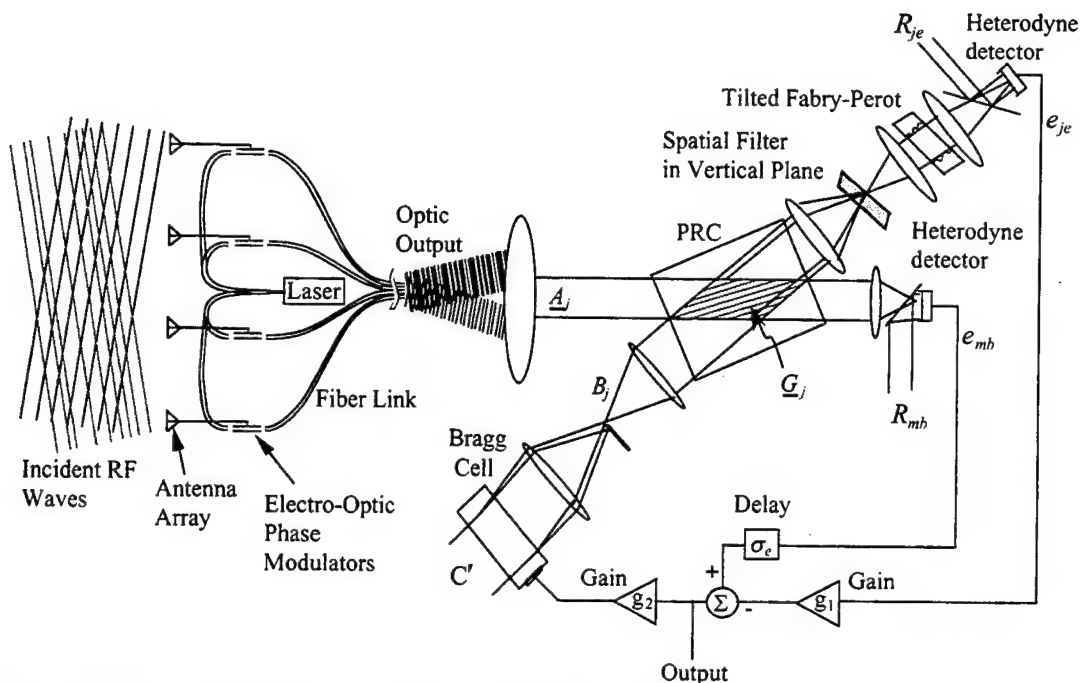
Figure 7.1. Schematic of adaptive jammer-nulling processor.

(denoted as spatio-temporal jammer vector $\underline{A}_j$ in figure 7.1) a stationary fringe pattern will form at the PRC and begin creating the holographic grating $\underline{G}_j$ whose fringe modulation depth is proportional to the strength of the correlation between the delayed jammer signal and the incident signal from the array. This grating is Bragg matched to the AOA of the incident jammer and will produce a diffracted beam which propagates in the direction corresponding to the same angle of diffraction associated with that frequency in the AOD feedback. As the gratings build up, a portion of the incident light from the jammer is diffracted off of the gratings, and onto the jammer estimate photodetector where it is heterodyne detected and produces the electronic jammer estimate signal. This jammer estimate signal is amplified and electronically subtracted from the undiffracted signal, thus creating an error signal after the difference node shown in the figure. This error signal is the amount of residual jammer contained in the processor output signal. At the onset of a jammer, before the holographic gratings are formed, this error signal is at its maximum value. As the gratings build up, the diffracted component of the jammer signal increases, decreasing the error signal after

170
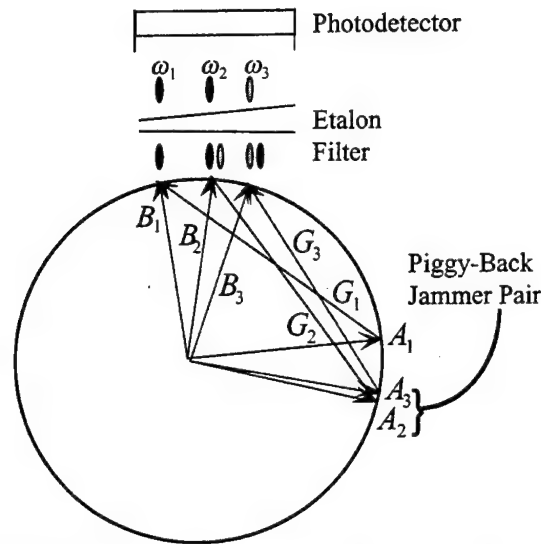
Figure 7.2. Jammers A_2 and A_3 have narrowly separated optical AOAs and hence diffract off of each gratings. This piggy-back diffraction of A_2 off of the grating written by A_3, and A_3 off of the grating written by A_2 produces spurious frequency terms, which are consequently blocked by the etalon filter before photodetection.

the difference node. This reduces the amplitude of the signal applied to the feedback Bragg cell, thereby causing the gratings to build up more slowly. The gratings continue to build up, reducing the jammer content in the output. At steady state the residual jammer content in the output has been reduced by the reciprocal net gain around the feedback loop. These Bragg selective time-integrated gratings formed in the PRC are the adaptive weights used to modify the array pattern by producing nulls corresponding to the AOA of incoming jammers. Angularly resolvable inputs to the phased-array are Bragg mismatched to each other's gratings so they are not affected by gratings which arise from other input signals. The tilted Fabry-Perot etalon located before the jammer estimate detector is in an image plane of the Bragg cell and serves to discriminate between signals incident at the same AOA (in either one or two dimensions) but at different frequencies. Alternatively, a wedged etalon could be implemented in a Fourier plane. More specific design issues associated with these two types of etalon filters are discussed in Chapter 8. A possible scenario demonstrating the need for this AOA-frequency discrimination is shown in figure 7.2. Figure 7.2 is a momentum space

representation showing the two narrowband jammers A_1 and A_2 writing gratings G_1 and G_2 respectively between their corresponding frequency upshifted signals from the Bragg cell, B_1 and B_2. For simplicity, the two jammers are considered to be plane waves, and hence represented as delta functions in momentum space. These two jammers have distinctly different AOAs and temporal frequencies, and can be assumed to have significant Bragg mismatch, therefore negligible mutual diffraction, or cross-talk, between them. However, when a third jammer A_3 is very close in optical AOA to jammer A_2, or may even share the same optical AOA as A_2. In this situation, jammers A_2 and A_3 can be partially Bragg matched to each others gratings and can thus diffract off of each others grating, or "piggy-back" off of each other because the grating will diffract beams at either temporal frequency. If there were no etalon filter, all the jammer components would be collected by the jammer estimate detector and be nulled by the adaptive processor. At first thought this seems favorable enough, but where the situation becomes deleterious to operation is when a broadband signal of interest is near the same AOA as a jammer, allowing the desired signal to diffract off of the jammer grating, and subsequently be nulled. Inserting the etalon filter and calibrating the frequency dispersion relationship between the feedback Bragg cell and the etalon, there will be a unique passband frequency versus position on the etalon which corresponds to the frequency dispersion relationship of the Bragg cell (shown as the angular distribution of B_1, B_2, and B_3 in figure 7.2). Thus, as shown in figure 7.2, only those signals at *both* the specific jammer AOA and frequency will pass through the etalon and be detected by the jammer estimate detector. In addition, most of the frequency components of a broadband signal of interest will not pass through the Fabry-Perot filter, while those of a narrowband jammer will pass through and be nulled by the processor. This structure implements the optical array processing algorithm discussed in Section 2.3

172

7.2 Jammer Dynamics
7.2.1 Main-Beam and Jammer Estimate Signals

The analysis of the processor dynamics begins by calculating the electronic signal produced by an incident jammer at the main-beam forming detector. In the dynamical analysis which follows, it will be assumed that the main-beam has been steered towards a desired signal of interest, either adaptively using the beam-forming processor of the previous section, or heterodyne detection of the portion of the signal from the phased array transmitted directly through the crystal shown in figure 7.1 and by adjusting the angle of the heterodyne reference wave at the main-beam photodetector. It is important to point out that the latter approach, which is invoked in this Chapter, is not truly adaptive, and in contrast to the main-beam forming processor, requires a coherent, phase-conserved fiber feed input from the array. To investigate the jammer dynamics, having an actual desired signal is not necessary because ideally the desired signal has no effect of the jammer dynamics. However, it is important to have a formed main-beam, or antenna response pattern to elucidate the directional effect on incoming jammers, consistent with the inherent spatial processing gain of the phased-array. A desired signal along with electrical and optical noise terms are added later in the chapter when the SINR of the processor is discussed.

The signal transduced from the phased-array and incident on the PRC for the *jth* incoming jammer $\underline{A}_j$ at RF frequency ω_j , will be considered to be propagating nominally in the $\hat{x}$ direction, with arbitrary spatial profile expressed as a sum over l spatial modes each with a particular amplitude and phase. The optical representation of such a single frequency RF jammer which consists of multiple plane wave components (due to such effects as multipath reflections, near field curvature, random phase delays, or topological transformations) in the fiber-feed network (approximated as a smooth function here) can be expressed in vectorial form as

$$\underline{A}_j \equiv \sum_l A_{jl} e^{-ik_l z} e^{-i\sqrt{k_o^2 - k_l^2}\, x} e^{i\omega_j t} e^{i\omega_o t} \qquad\qquad 7.1$$

where A_{jl} is the amplitude of the *jlth* spatio-temporal mode of the jammer with RF

frequency ω_j, ω_o is the optical carrier frequency, and $k_o = 2\pi/\lambda$, k_l is the transverse

optical wave vector component which is equal to the transverse incident RF wavevector

times the ratio of antenna spacing to fiber spacing. To simplify the analysis, the optical

mapping of the phased-array and all of the following grating and diffracted terms are

confined to the x-z plane. This corresponds to a one-dimensional optical mapping of the

antenna array, which can be either one or two dimensional. For a coherent fiber feed,

the planewave components can be associated with corresponding RF planewaves. For

random phase fiber feeds, this is a more general decomposition, for example with a

Fourier lens the signals A_{jl} correspond to the wave from each fiber aperture. Using a

coherent fiber feed, beam forming can be accomplished by simply heterodyne detecting

(either with a planewave reference or a large area detector in the fiber feed image plane,

or using a spot reference on a tiny detector in the Fourier plane).

For a strong jammer and small diffraction efficiency, the optical signal incident

on the main-beam photodetector can be approximated by equation 7.1, and heterodyne

detection in the image plane of this signal with a large Gaussian apodized reference

beam of amplitude R_{MB} having a tilt represented by transverse momentum k_r, and

phase $\phi_{R_{MB}}$ produces electrical signal e_{MB}, given by

$$e_{MB} = \int_a \left| \begin{array}{l} \Pi\!\left(\dfrac{z}{L}\right) \sum_{jl} A_{jl} e^{-ik_l z} e^{-i\sqrt{k_o^2 - k_l^2}\, x} e^{i\omega_j t} e^{i\omega_o t} \\[2mm] + R_{MB} e^{i\phi_{R_{MB}}} e^{i\omega_o t} e^{-\pi(z/\sigma_r)^2} e^{-ik_r z} e^{-i\sqrt{k_o^2 - k_r^2}\, x} \end{array} \right|^2 \Re dz \qquad\qquad 7.2$$

where $e^{-\pi(z/\sigma_r)^2}$ represents the Gaussian apodization of width $\sigma = \sigma_r/\sqrt{\pi}$ of the

reference beam, and the integration is over the variable z. $\Re$ is the responsivity of the

photodetector in units of amps/watt. The function $\Pi(z/L)$ represent the finite aperture

174

of the initial wavefront transduced from the array. The analysis has been generalized to allow for multiple jammers by introducing the sum over j in equation 7.2. Equation 7.2 can be evaluated by setting the plane of the photodetector to correspond to $x = 0$. Expanding out the magnitude-squared operation results in

$$e_{MB} = \Re \int_a \Pi\left(\frac{z}{L}\right)\left\{\begin{array}{l}|R_{MB}|^2 e^{-2\pi(z/\sigma_r)^2} + I_{\Psi A} + \\ R_{MB}e^{-i\phi_{RMB}}e^{-\pi(z/\sigma_r)^2}e^{-ik_r z}\sum_{jl}A_{jl}e^{i(\omega_j t - k_l z)} + c.c.\end{array}\right\}dz \qquad 7.3$$

where

$$I_{\Psi A} \equiv \sum_{jl}\left|\Psi_{jl}A_{jl}e^{-ik_l z}e^{i\omega_j t}e^{i\omega_o t}\right|^2 = \sum_{jl}\left|\Psi_{jl}A_{jl}\right|^2 \qquad 7.4$$

is a DC intensity with contributions from *all* incident jammers (all frequencies), and Ψ_{jl} is the array function weighting term to be derived shortly. This DC term, as well as the DC term of reference beam, $|R_{MB}|^2$, can be neglected based on that they will be below the bandwidth of the octave bandwidth photodetector. Carrying out the integration of the remaining terms in equation 7.3 yields an electrical signal given by

$$e_{MB} = R_{MB}e^{-i\phi_{RMB}}\sum_{jl}A_{jl}e^{i\omega_j t}\left\{L\sigma_r\,\text{sinc}[k_l L] * e^{-\pi\sigma_r^2(k_l - k_r)^2}\right\} + c.c.. \qquad 7.5$$

This result indicates that the electrical signal output of the main-beam photodetector is the sum of the amplitudes of j jammers, each at RF frequency ω_j, and each multiplied by the amplitude and phase of the heterodyne reference beam. The more interesting term of equation 7.5 is the array function weighting term Ψ_{jl} which appears in brackets and multiplies each term. This weighting term describes the effects of the jammers coming in at different AOAs than the signal of interest, and having their amplitudes correspondingly suppressed by the main-beam antenna response. The antenna function weighting is seen to be a sinc function apodized by a gaussian centered at k_r, which produces a squinted, main-beam array function with reduced sidelobes compared to an unapodized sinc antenna response. When the Gaussian width goes to infinity, this

175

degenerates to the conventional $\text{sinc}\left[(k_l - k_r)L\right]$ mainbeam of an unapodized array. As equation 7.5 indicates, each of the l components of the j jammers will be weighted according to their AOA with respect to the AOA of the desired signal.

For beams that are not on boresight the array function is squinted as becomes apparent by examining the terms k_r and k_l. The term k_r is the transverse momentum component of the heterodyne reference wave,

$$k_r = \frac{\omega_o}{c} \sin(\theta_r).$$

7.6

This term is seen to be fixed in both frequency and angle, positioned to optimize the response of the desired signal at some AOA. When a coherently remoted array is implemented, the term k_l is given by

$$k_l = \frac{a\omega_j}{cD} \sin(\theta_l)$$

7.7

which is seen to be a function of both the AOA of the *lth* spatial mode, and the frequency of the *jth* jammer, ω_j. The significance of this, and how each jammer is ultimately weighted by the array function is better understood with the use of figure 7.3, which plots the transverse optical momentum verses the frequency parameterized by equispaced angles, with an overlay of the beam forming response. As shown in the figure, there is an array function formed at a position k_r on the transverse momentum axis. The straight lines on the figure are lines of constant angle θ, and are seen to compress as θ increases due to the fact that the slope of the $\sin(\theta_l)$ term in equation 7.7 decreases with increasing θ. Indicated on the figure is the intersection point between a desired signal frequency ω_{mb}, and the projection of the array function along the line of constant k_r, which intersects a line of constant θ corresponding to its AOA. This particular point corresponds to the position a main-beam is formed. Also shown is

176

a jammer of frequency ω_1 higher than ω_{mb}, at an angle θ_1, where the frequency-angle relationship is such that this particular jammer falls on the first sidelobe of the formed
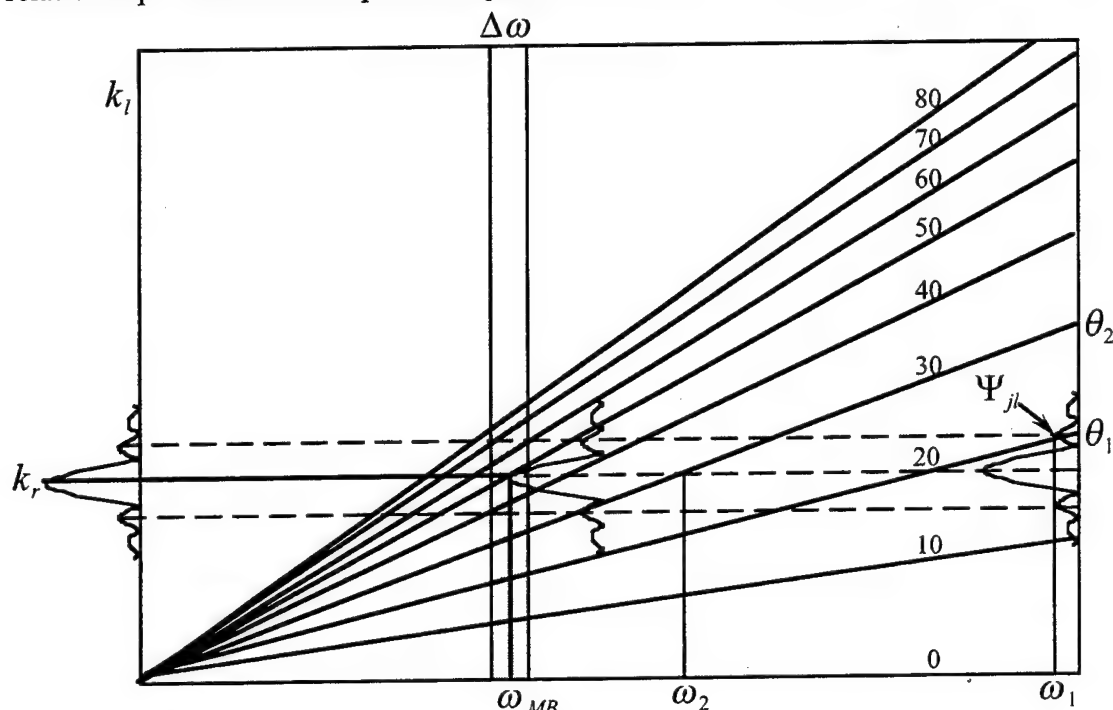
Figure 7.3. Frequency-momentum space showing weighting function Ψ_{jl} in incident jammers.

main-beam antenna function. The projection of this point onto the array function is the weighting function Ψ_{jl}, which affects each spatial mode of each jammer differently. Thus, the spatial processing gain produced by the array is seen to initially reduce the received jammer strength.

Also shown in the figure is a second jammer at ω_2, at such an angle that it falls on the peak of the array function, as though it were at the same angle of the jammer even though it is not so in radar space. Because there is no etalon installed in this version of the main-beam formation process, this squint is inherent to this processing scenario. This shortcoming of the processing technique essentially means that without the etalon, the system is appropriate for narrowband processing only. For example, the shaded region in figure 7.3, denotes a reduced system bandwidth of $\Delta\omega$. Over this

reduced system bandwidth, squint is negligible and there is a unique relationship between k_t and θ. This bandwidth issue is consistent with what was shown in Section
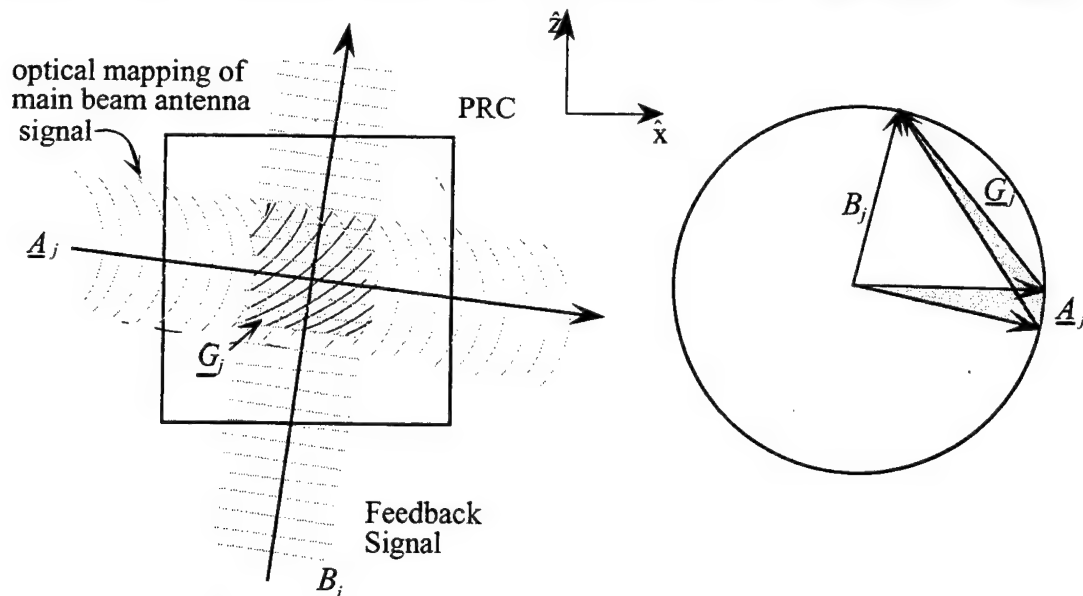
Figure 7.4. Interference at photorefractive crystal between the *jth* single frequency jammer $\underline{A}_j$ of arbitrary spatial profile and feedback beam B_j containing frequency content of $\underline{A}_j$. The real space representation is shown at the left of the figure illustrating near field curvature, and the momentum space representation is on the right illustrating two distinct jammers.

2.3, in that the etalon filter effectively provides the necessary time delays to enable broadband processing.

In order to form the jammer estimate, a portion of the *jth* jammer $\underline{A}_j$ is diffracted off of the Bragg-matched family of gratings in the photorefractive crystal. The optical wavefront corresponding to an incident RF jammer after upconversion to the optical domain at the PRC is shown in figure 7.4, both in real space and momentum space, along with the resulting holographic gratings $\underline{G}_j$ and feedback signal B_j, discussed further below. As shown in figure 7.4, the collection of spatial modes of the jammer $\underline{A}_j$ writes a corresponding family of gratings denoted by $\underline{G}_j$. This diffraction can ideally be considered an inner product of the incident signal in equation 7.1 with the appropriate Bragg-matched set of gratings $\underline{G}_j$, which are expressed in vectorial form as

178

$$\underline{G}_j \equiv \sum_l G_{jl} e^{-ik_{jl}^{Gz} z} e^{+ik_{jl}^{Gx} x} \qquad 7.8$$

The G_{jl} are the grating amplitudes, $k_{jl}^{Gz} = k_l - \sqrt{k_o^2 - K_j^2}$ are the grating wavevector components in the $\hat{z}$ direction, and $k_{jl}^{Gx} = K_j + \sqrt{k_o^2 - k_l^2}$ are the components in the $\hat{x}$ direction, and $|K_j| = \omega_j / V$ is the acoustic wave vector at the frequency ω_j with acoustic velocity V in the feedback Bragg cell. The inner product between $\underline{G}_j$ and $\underline{A}_j$ is defined as

$$\langle \underline{A}_j, \underline{G}_j \rangle = \sum_l A_{jl} G_{jl}^* . \qquad 7.9$$

It is important to note that the weighting function Ψ_{jl} is not included for the jammer estimate signals derived from the diffracted beam, which is detected at the jammer estimate detector. This is because in contrast to the main-beam array function which is steered towards the desired signal, each jammer input diffracts off of its own grating and is therefore always on boresight for its own grating. This is a restatement of the fact that the jammer-nulling processor builds up and steers array functions in the directions of the jammers, in accordance with the fact that the jammer-nulling processor is essentially a sidelobe canceller. The process of beam forming towards the jammers is essentially identical to the main-beam forming process described in Chapter 6, however because the jammers are narrowband, there will be a strong correlation over many time delays, and gratings will be formed over a greater volume throughout the PRC than with a broadband desired signal.

The electrical jammer estimate signal, e_{JE}, is generated by the coherent detection of this diffracted component using a plane wave heterodyne reference of amplitude R_{JE} with phase $\phi_{R_{JE}}$, which will be assumed to uniformly illuminate the photodetector area. The signal e_{JE} for this single jammer case can be written as an integral over the surface area a of the photodetector in terms of this inner product as

$$e_{JE} = \int_a \left| w(x) \langle \underline{A}_j, \underline{G}_j \rangle e^{i\omega_j t} e^{i\omega_o t} e^{iK_j x} e^{i\sqrt{k_o^2 - K_j^2} z} + R'_{JE} e^{i\omega_o t} e^{i\phi_{R_{JE}}} e^{-ik_o z} \right|^2 \Re dx \qquad 7.10$$

179

where because of the 1-D analysis, the integration is over x only. The term $w(x)$ is the holographic reconstruction of the Fourier plane impulse response of the AO device, given by the Fourier transform AO device aperture, and it has an effective width of $1/N$ of the detector aperture assuming that the detector aperture is equal to the reference beam width. The jammer estimate current then becomes

$$
\begin{aligned}
e_{JE} &= \left| R'_{JE} \right|^2 \Re + \left| \langle \underline{A}_1, \underline{G}_1 \rangle \right|^2 \Re + \frac{\Re R'_{JE} e^{i\phi_{R_{JE}}} e^{i\omega_1 t}}{N} \sum_l \langle \underline{A}_1, \underline{G}_1 \rangle + c.c. \\
&= \Re R_{JE} e^{i\phi_{R_{JE}}} \sum_l \left(A_{1l} e^{i\omega_1 t} G_{1l}^* \right) + c.c.
\end{aligned}
\qquad 7.11
$$

where $R_{JE} = R'_{JE}/N$, and the DC terms can be dropped because of the detector capacitive coupling (highpass), and the resulting output oscillates with a strength proportional to the jammer and gratings.

More generally there may be multiple jammers present, each at a different frequency ω_j, and each with a unique set of spatial modes. Due to potential partial Bragg matching between gratings written by different jammers (the piggy-back jammers of the previous section), the relation for the photocurrent given by equation 7.10 must be extended to accommodate the multiple jammer scenario. Consider first the situation where there are two jammers present, A_1 and A_2, of frequency ω_1 and ω_2 respectively, and each made up of only one spatial mode (planewave jammers). This scenario is shown in figure 7.5, and the four resulting diffracted terms, W, are written out in equation 7.12,

$$
W = A_1 G_1 e^{i(\omega_1 t + K_1 x)} + A_2 G_2 e^{i(\omega_2 t + K_2 x)} + \eta_{12} A_1 G_2 e^{i\left[\omega_1 t + \left(K_2 - \Delta k_x^{12}\right)x\right]} + \eta_{21} A_2 G_1 e^{i\left[\omega_2 t + \left(K_1 - \Delta k_x^{12}\right)x\right]} . 7.13
$$

where $\Delta \bar{k} = \bar{k}_1 - \bar{k}_2$, $\Delta k_x^{12} = \Delta \bar{k} \cdot \hat{x}$, and K_1 and K_2 are the propagation vectors for the acousto-optically diffracted beams of jammers A_1 and A_2, in the directions of B_1 and

180

$$\Delta \bar{k} = \bar{k}_1 - \bar{k}_2 \qquad \Delta k_x^{12} = \Delta \bar{k} \cdot \hat{x}$$
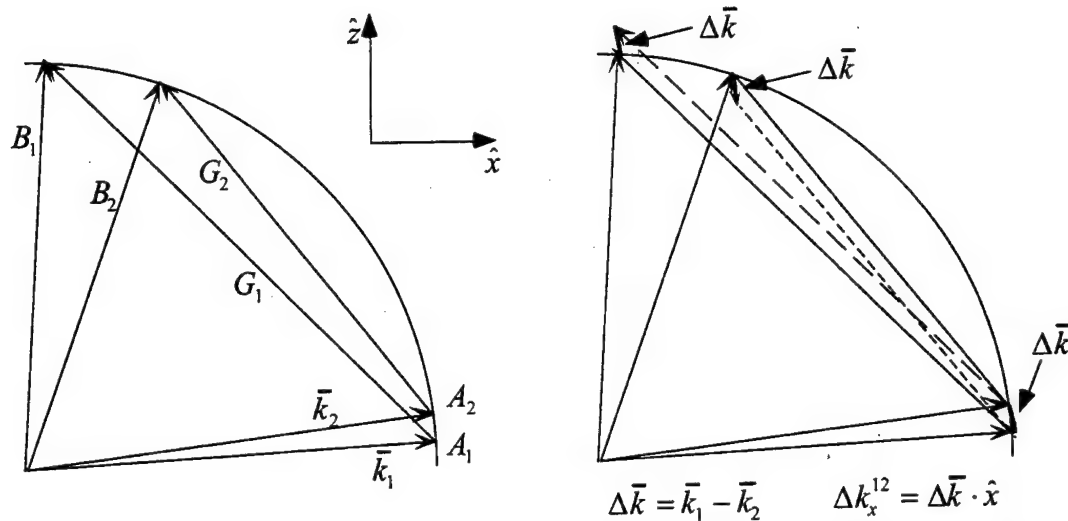
Figure 7.5. Two planewave jammers, A_1 and A_2, of frequency ω_1 and ω_2 respectively, shown in momentum space, write independent gratings G_1 and G_2. Each jammer can diffract off of the grating written by the other jammer, with momentum mismatch $\Delta \bar{k}$.

B_2 as shown in figure 7.5. As shown in the figure each of the input beams is capable of diffracting off the grating written by the other jammer, with resulting momentum mismatch $\Delta \bar{k}$. The second two terms of equation 7.13 represents the cross-talk terms between the gratings, and the terms η_{12} and η_{21} are weighting terms which account for the Bragg mismatched diffraction efficiency resulting from each jammer reading out the other jammer's grating. It is important to note that although the Bragg mismatch may be large, resulting in small η weighting terms, if the jammer(s) are very strong, the diffracted component may still be large. Equation 7.13 can be written more explicitly as

$$W = \langle A_1, G_1 \rangle e^{i(\omega_1 t + K_1 x)} + \langle A_2, G_2 \rangle e^{i(\omega_2 t + K_2 x)} + \int A_1 G_2 e^{i \Delta \bar{k}_{12} \cdot \bar{r}} d\bar{r} + \int A_2 G_1 e^{i \Delta \bar{k}_{21} \cdot \bar{r}} d\bar{r} \quad 7.14$$

where the inner product notation has been used in writing the first two diffracted terms, even though in this case they have been assumed to be planewaves for which $\sum A_{jl} G_{jl}^* = A_{jj} G_{jj}^* \equiv \underline{A}_j \cdot \underline{G}_j^* \equiv \langle \underline{A}_j, \underline{G}_j \rangle$. The integral of momentum mismatch $\Delta \bar{k}$ over the crystal interaction volume will be assumed to yield a weighting term of the form $\eta \approx \mathrm{sinc}(\Delta k_x L)$, assuming an interaction region with transverse dimensions y and z

much greater than the nominal propagation direction x. By symmetry $\eta_{ij} = \eta_{ji} \equiv \eta$, and the diffracted terms of equation 7.14 can be written as a sum of inner products, the latter two appropriately weighted to account for Bragg mismatching on readout,

$$W = \langle A_1, G_1 \rangle e^{i(\omega_1 t + K_1 x)} + \langle A_2, G_2 \rangle e^{i(\omega_2 t + K_2 x)}$$
$$+ \eta \langle A_1, G_2 \rangle e^{i\left[\omega_1 t + \left(K_2 - \Delta k_x^{12}\right)x\right]} + \eta \langle A_2, G_1 \rangle e^{i\left[\omega_2 t + \left(K_1 - \Delta k_x^{12}\right)x\right]}. \qquad 7.15$$

As discussed in the previous section, the Fabry-Perot etalon filter functions as a position (or angle) dependent frequency bandpass filter, ideally insuring that only those frequencies corresponding to the unique frequency-position (or angle) relationship between the etalon and the Bragg cell pass through the etalon. Thus, ideally the etalon filter would completely filter out and remove the last two terms of equation 7.15. In reality however, there will be some leakage due to the fact that the etalon will not have infinitely narrow, unique passband functions for each frequency. Again, if the jammer is strong enough, significant leakage may occur for a piggy-back jammer pair passing through the etalon. The frequency response of the etalon can be represented by another weighting function, Δ_{12}, which is a function of the frequency separation between the two jammers. This weighting function is of the form

$$\Delta_{12} = \left(\frac{1 - r^{2N} e^{iN\delta_{12}}}{1 - r^2 e^{i\delta_{12}}} \right). \qquad 7.16$$

The phase factor δ_{12} is the phase shift between each of the N bounces inside the etalon, and takes into account the frequency spacing between the first and second jammers, upshifted to optical frequencies by ω_o,

$$\delta_{12} = \frac{h}{\pi c} \left(\omega_o + \omega_1 + \frac{\omega_1 - \omega_2}{2} \right). \qquad 7.17$$

Multiplying the cross-talk terms of equation 7.15 by the etalon weighting factor yields

$$W = \langle A_1, G_1 \rangle e^{i(\omega_1 t + K_1 x)} + \langle A_2, G_2 \rangle e^{i(\omega_2 t + K_2 x)}$$
$$+ \eta \Delta_{12} \langle A_1, G_2 \rangle e^{i[\omega_1 t + (K_2 - \Delta k_x^{12}) x]} + \eta \Delta_{21} \langle A_2, G_1 \rangle e^{i[\omega_2 t + (K_1 - \Delta k_x^{12}) x]} \qquad 7.18$$

where again by symmetry $\Delta_{jm} = \Delta_{mj}$. Equation 7.16 can now be extended to account

for an arbitrary number of jammers, each denoted by j,

$$W = \sum_j \left[\langle A_j, G_j \rangle e^{i(\omega_j t + K_j x)} + \sum_{m, m \neq j} \eta_{jm} \Delta_{jm} \langle A_j, G_m \rangle e^{i[\omega_j t + (K_m - \Delta k_x^{jm}) x]} \right] \qquad 7.19$$

where the dummy subscript, m, has been introduced to enumerate the cross-talk terms.

As the number of bounces in the etalon, N, approaches infinity, equation 7.16

approaches Airy's formula[1],

$$\Delta_{12} \big|_{N \to \infty} \approx \left(\frac{1}{1 - r^2 e^{i\delta_{12}}} \right) \qquad 7.20$$

which describes the bandpass amplitude transmittance function of a plane, parallel

Fabry-Perot etalon. The tilted or wedged nature of the etalons invoked here may induce

beam walkoff, and hence provide a smaller number of bounces than a comparable plane

parallel etalon. For this analysis however, N will be assumed large, as will the cavity

finesse, and the etalon will be considered to have an appropriately narrow frequency

response so as to provide adequate resolution and isolation between jammer

frequencies. In addition, when the Bragg mismatch between jammers is sufficiently

large (or the array is appropriately apodized with, for example, Gaussian weighting to

substantially decrease the sidelobes), then the contribution from the piggy-back jammer

terms in equation 7.19 may be neglected. Thus, the selective capability provided by

both Bragg matching and the etalon filter can enforce only the inner products with

common subscripts in equation 7.19. For this case of multiple, planewave jammers, the

jammer estimate current e_{JE} becomes

$$e_{JE} = |R_{JE}|^2 \Re + \sum_j \left| \langle A_j, G_j \rangle \right|^2 \Re + \Re R_{JE} e^{i\phi_{RJE}} \sum_j e^{i\omega_j t} \langle A_j, G_j \rangle + c.c.$$

$$= \Re R_{JE} e^{i\phi_{RJE}} \sum_j \left(A_j e^{i\omega_j t} G_j^* \right) + c.c.$$
7.21

where the DC terms of equation 7.21 have been dropped due to bandpass filtering by the photodetector. Thus the photodetected output consists of a weighted linear superposition of each of the jammers, oscillating at the corresponding frequencies. Each jammer has its own degree-of-freedom in the corresponding grating diffraction efficiencies, G_j. It will be shown in the following analysis how the jammer-nulling processor uses correlation cancellation loop feedback to adaptively estimate main-beam corruption by each jammer and drive the gratings G_j to the appropriate amplitude and phase to subtract out and eliminate all of the jammers from the system output.

Having multiple jammers present on the photodetector raises an interesting aspect to this method of processing. Recall that the reference beam uniformly illuminates the jammer estimate photodetector. This is necessary because the adaptive nature of the processor means that the frequency of the jammers, and hence the position in the Fourier plane of the AO which is assumed to be the detector plane, are not known *a priori*. For this reason the reference beam must be available to, and hence spread out, linearly across the photodetector to interact with all possible jammer frequencies simultaneously. Because the reference beam is spread out to interact with N possible jammers, there is a $1/N$ reduction in heterodyne processing gain, where N is the time-bandwidth product of the feedback Bragg cell, and the width of the Fourier plane impulse response $w(x)$ is $1/N$ of the reference beam width.

Finally, the most general case is when there are multiple jammers, each with a unique set of individual spatial modes denoted by l. The situation is now complicated by the fact that there could conceivably be coupling between the different spatial modes of different jammers. To simplify the situation dramatically, it will be assumed that each jammer has the same group of spatial modes, and that coupling will occur only between

corresponding spatial modes. We can analytically represent the corresponding diffracted terms of equation 7.19 with vector modes instead of scalars, resulting in

$$W = \sum_j \left[\left\langle \underline{A}_j, \underline{G}_j \right\rangle e^{i\left(\omega_j t + K_j x\right)} + \sum_{m, m \neq j} \eta_{jm} \Delta_{jm} \left\langle \underline{A}_j, \underline{G}_m \right\rangle e^{i\left[\omega_j t + \left(K_m - \Delta k_x^{jm}\right)x\right]} \right]. \qquad 7.22$$

The assumption of minimal Bragg matching and an ideal etalon filter will again however be invoked here, and the high-pass filtered jammer estimate current will then be the vectorial version of equation 7.21,

$$\begin{aligned} e_{JE} &= \Re R_{JE} e^{i\phi_{RJE}} \sum_j e^{i\omega_j t} \left\langle \underline{A}_j, \underline{G}_j \right\rangle + c.c. \\ &= \Re R_{JE} e^{i\phi_{RJE}} \sum_{jl} \left(A_{jl} e^{i\omega_j t} G_{jl}^* \right) + c.c. \end{aligned} \qquad 7.23$$

The similarity between equations 7.21 and 7.23 should be pointed out, although the inner product terms have a vectorial nature and the additional summation over the spatial modes, l, the two equations are essentially the same. This similarity is to be expected, because any jammer with multiple spatial modes, could alternatively be considered as multiple planewave jammers, but all of the same frequency ω_j.

7.2.2 Feedback Analysis

The RF feedback signal applied to the feedback Bragg cell contains the signal spectrum produced by the difference between e_{JE} amplified by g_1, and a delayed version of e_{MB}. This difference signal is then amplified by g_2 and applied to the Bragg cell. The DC terms in equations 7.21 are blocked by the transducer bandpass function of the feedback acousto-optic Bragg cell and therefore do not contribute to the acoustic interaction in the Bragg cell. The resultant single sideband diffraction from the Bragg cell with amplitude B incident at the photorefractive crystal is given by

$$B = R_{MB} \Re \eta g_2 C \sum_{jl} A_{jl} e^{-is_j} e^{i\left(\omega_j t - K_j x\right)} e^{-i\sqrt{k_o^2 - K_j^2} z} e^{i\omega_o t} \left[\Psi_{jl} - g_1 \left(R_{JE}/R_{MB} \right) G_{jl}^* e^{ip_j} \right] \qquad 7.24$$

where C is the amplitude strength of the incident illumination at the Bragg cell, and η is the Bragg cell efficiency in units of %/amp. In addition, phase terms have been combined by defining

$$p_j \equiv \phi_{R_{MB}} - \phi_{R_{JE}} - \omega_j \sigma_e \qquad s_j \equiv \phi_{R_{MB}} - \phi_C - \omega_j \sigma_e - \omega_j \sigma_a \qquad 7.25$$

where σ_a is the acoustic delay at the Bragg cell transducer, and σ_e is the electrical delay around the feedback loop which serves to decorrelate broadband signals of interest.

The photorefractive material responds to the incident optical intensity by writing a grating proportional to the spatially varying component of the intensity which in turn suffers a temporal decay due to the spatially constant (DC) component of the intensity. As discussed in Chapter 4, the time evolution of the grating G can be written in terms of these two intensity components and the material constants α and β,

$$\frac{\partial}{\partial t} G = -\alpha I_{DC} G + \beta I_{grating} \qquad 7.26$$

where α and β are given by equations 4.50 and 4.55. Calculation of the incident intensity from $I = |A + B|^2$ yields the DC and the spatially varying components of the intensity, given by

$$I_{DC} = I_A + |R_{MB}|^2 \eta^2 \Re^2 g_2^2 |C|^2 \sum_{jln} A_{jl} A_{jn}^* \left[\Psi_{jl} - g_1(R_{JE}/R_{MB}) G_{jl}^* e^{ip_j} \right] \left[\Psi_{jn} - g_1(R_{JE}/R_{MB}) G_{jn} e^{-ip_j} \right]$$

$$7.27$$

where

$$I_A \equiv \sum_{jl} \left| A_{jl} e^{-ik_l z} e^{-i\sqrt{k_o^2 - k_l^2} x} e^{i\omega_j t} e^{i\omega_o t} \right|^2 = \sum_{jl} |A_{jl}|^2 \qquad 7.28$$

is a D.C. component with contributions from all jammers present, and

$$I_{grating} = \sum_{jln} A_{jl} A_{jn}^* e^{-ik_{Gzlj} z} e^{ik_{Gxjl} x} e^{is_j} \left[\Psi_{jn} - g_1(R_{JE}/R_{MB}) G_{jn} e^{-ip_j} \right] R_{MB} \Re \eta g_2 C \qquad .7.29$$
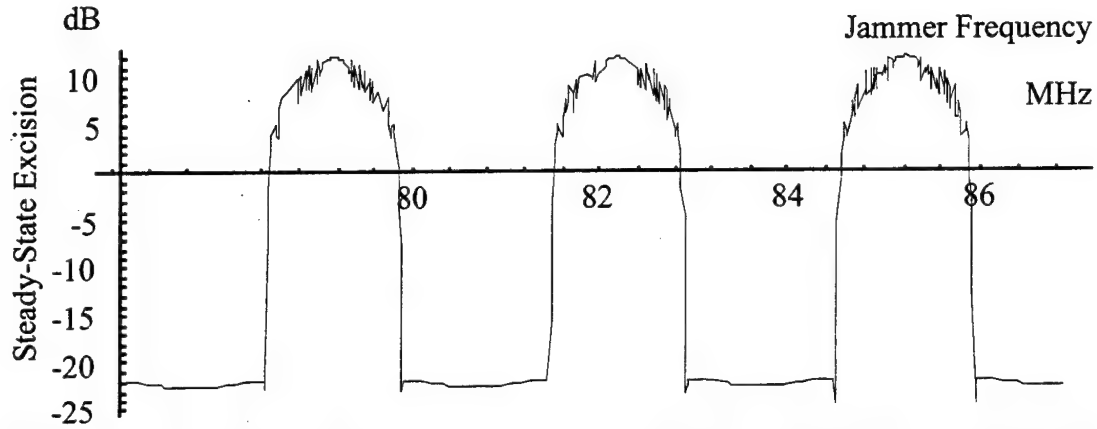
Figure 7.6. Plot of theoretical jammer nulling bandwidth obtained from a numerical solution of equation 7.32 for the plane wave jammer case, where $a = 1$, $b = 12.6$, and $t' = 8$ seconds.

Using equations 7.26, 7.27, and 7.29, the expression for the time evolution of the *jth* grating, expressed in vectorial form is then

$$\frac{\partial}{\partial t}\underline{G}_j = \beta e^{is_j}\, A_j\left(\underline{A}_j^* \cdot \underline{\Psi}_j - \underline{A}_j^* \cdot \underline{G}_j g_1\left(R_{JE}/R_{MB}\right)e^{-ip_j}\right)R_{MB}\eta\Re g_2 C$$
$$-\alpha\left(\begin{array}{c} I_A + \left|R_{MB}\right|^2 \eta^2 \Re^2 g_2^2 |C|^2 \cdot \\ \sum_{j,l,n} A_{jl}A_{jn}^*\left[\Psi_{jl} - g_1\left(R_{JE}/R_{MB}\right)G_{jl}^* e^{ip_j}\right]\left[\Psi_{jn} - g_1\left(R_{JE}/R_{MB}\right)G_{jn}e^{-ip_j}\right]\end{array}\right)\underline{G}_j \qquad .7.30$$

An intuitive metric for quantifying the jammer nulling performance of the processor is in terms of the jammer excision E. The excision is a complex, dynamical, dimensionless variable, and is defined to be the residual jammer content in the processor output normalized by the initial jammer amplitude. Transforming 7.30 using the excision E yields the vectorial expression

$$\underline{E}_j \equiv \underline{\Psi}_j - g_1 e^{-ip_j}\,\underline{G}_j\,R_{JE}/R_{MB} \qquad 7.31$$

Substituting 7.31 into 7.30 results in the dynamical equation for the excision

$$\frac{\partial}{\partial t'}\left(\underline{E}_j\right) = \left(a + \frac{1}{I_A}\sum_{jln} A_{jl}A_{jn}^* E_{jl}^* E_{jn}\right)\left(\underline{\Psi}_j - \underline{E}_j\right) - \frac{b}{I_A}e^{-i\sigma_o\left(\omega_c - \omega_j\right)}\underline{A}_j\left(\underline{A}_j^* \cdot \underline{E}_j\right) \qquad 7.32$$

187
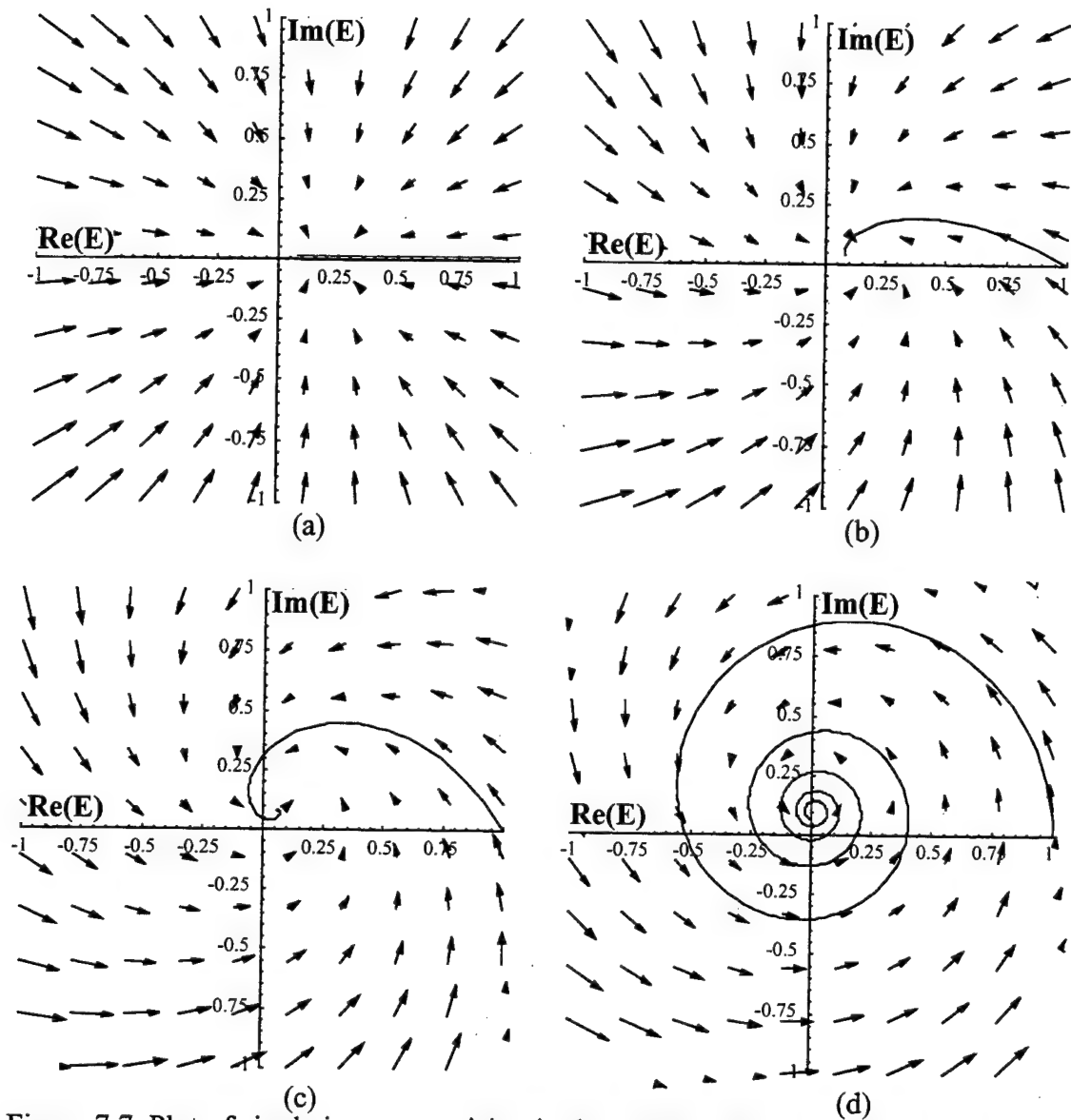
Figure 7.7. Plot of single jammer excision in the complex plane, superimposed over a vector-velocity-field (time interval of 3 seconds), for $a = 1$, $b = 20$. The phase difference increases from 0 to $\pi/2$ by $\pi/6$ for each plot in the sequence.

where the following unitless definitions have been made:

$$t' = t\left(\alpha I_A |R_{MB}|^2 \eta^2 \Re^2 g_2^2 |C|^2\right)$$ 7.33

$$a = 1 \Big/ \left(|R_{MB}|^2 \eta^2 \Re^2 g_2^2 |C|^2\right)$$ 7.34
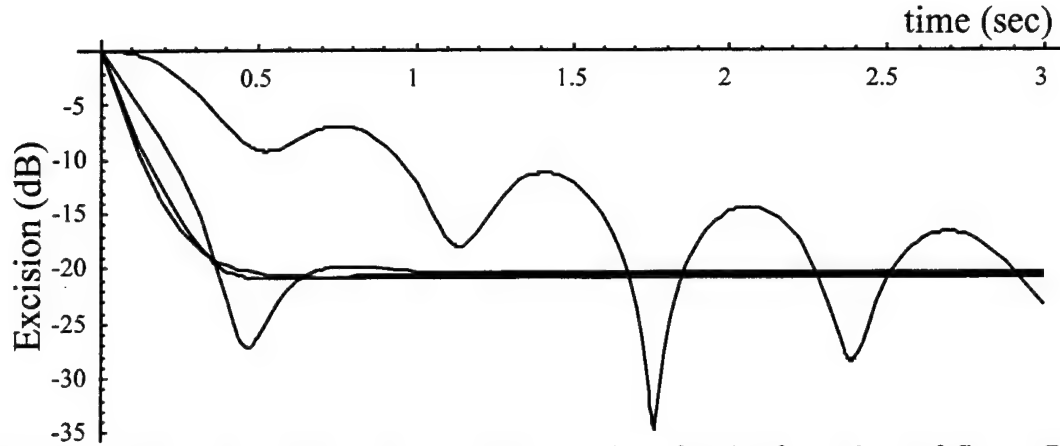
Figure 7.8. Magnitude of the excision versus time for the four plots of figure 7.7, again, $a = 1$, $b = 20$.

$$b = g_1 R_{JE} \beta \Big/ \left(\alpha |R_{mb}|^2 \eta \Re g_2 C \right) \qquad 7.35$$

and the system center frequency ω_c is defined according to

$$\omega_c = \frac{\phi_{R_{JE}} - \phi_C}{\sigma_a}. \qquad 7.36$$

This term represents the phase difference between the two inputs of the summing node. It will be shown that for convergence to jammer suppression it is necessary that $-\pi/2 \le \sigma_a \left(\omega_c - \omega_j \right) \le \pi/2$. When the phase difference is increased by an increment of 2π, the nulling behavior repeats, i.e. a periodic nature of the nulling behavior is evident. This range of allowed phase values for jammer suppression translates directly into a frequency nulling bandwidth, as shown in figure 7.6. The figure shows a plot of the steady-state jammer excision bandwidth obtained from a numerical solution of equation 7.32 for the single plane wave jammer case with parameters estimated from the experimental set-up of the following section. A nulling bandwidth of approximately 1.7 MHz with a null depth of 22 dB repeating every 3 MHz is obtained. Note that outside the nulling bandwidth the system oscillates with moderate gain of 5 to 10 dB.

Alternatively, the behavior of equation 7.32 can be plotted as a dynamical variable in the complex excision plane. The excision of a single jammer as a function of time is plotted in the complex plane in figure 7.7 a-d (t = 0 to 3 seconds). A net phase

189
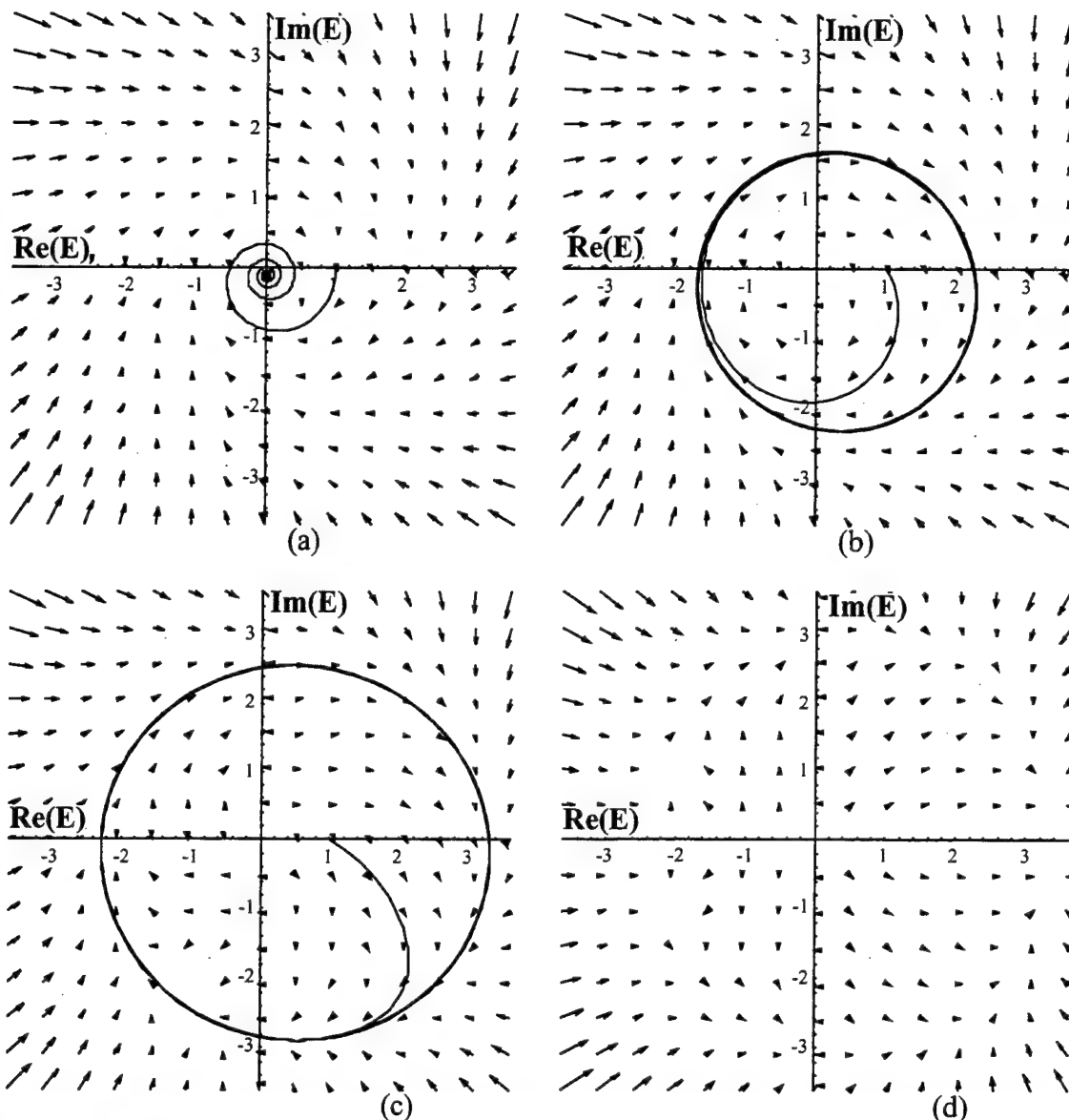
Figure 7.9. Plot of single jammer excision in the complex plane, superimposed over a vector-velocity-field (time interval of 3 seconds). The phase difference increases from $\pi/2$ to π by $\pi/6$ for each plot in the sequence. The simulation parameters are the same as those for figure 7.7.

difference due to a frequency shift from the processor center frequency increases from 0 to $\pi/2$ by $\pi/6$ for each plot in the sequence. Superimposed over each plot is a vector-velocity-field plot of the excision. Thus, given any excision value, the motion of the excision can be predicted by following the direction indicated by the arrows in the figure. In figure 7.7a, the jammer is at the center frequency and the phase shift is zero.
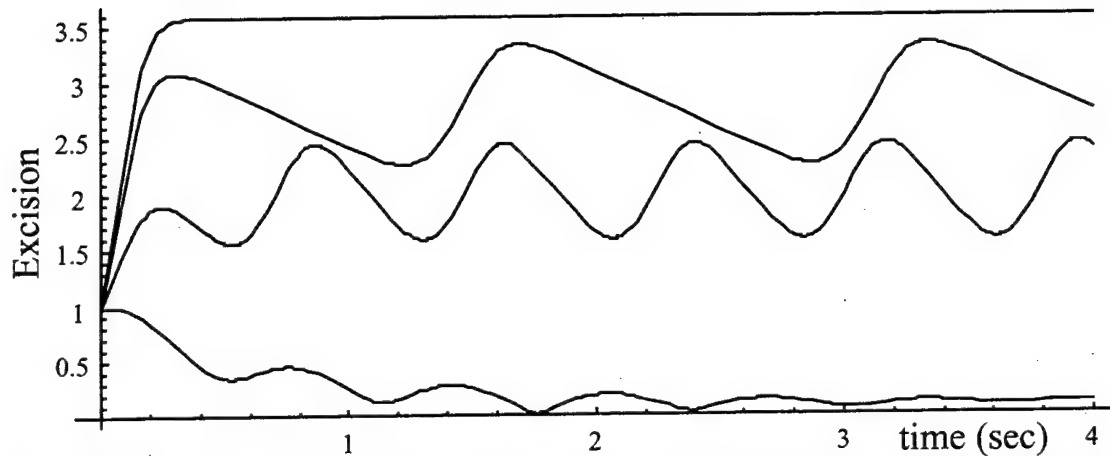
Figure 7.10. Magnitude of the excision versus time for the four plots of figure 7.9. The simulation parameters are the same as those for figure 7.9

The excision is reduced from its initial value of 1 to a steady-state value of approximately of 0.05, or -26 dB. Because the phase shift is zero, the excision is entirely real, and remains real as it travels along the real axis towards the steady-state value, as shown in the figure. As the phase difference is increased, the convergence of the excision becomes more and more oscillatory. Figure 7.7d is the marginally convergent case, where the phase difference is equal to $\pi/2$. For these convergent cases, the magnitude of the steady-state excision value is unchanged, as shown in figure 7.8. The four curves in the plot of excision versus time correspond to the four plots of figure 7.7. Note that after 3 seconds the marginally convergent case has still not converged.

Increasing the phase difference beyond $\pi/2$ results in non-convergent behavior, as shown in figure 7.9 a-d. Figure 7.9a is again the marginally convergent case, and the remaining three plots correspond to phase differences of $2\pi/3$, $5\pi/6$, and π respectively. The remaining plots are clearly non-convergent, the last plot, that when the phase difference is π, is somewhat difficult to interpret but indicates that the excision is driven towards a value of approximately 3.5, or +11 dB. The magnitude of these same four cases is shown in figure 7.10, plotted from $t = 0$ to 4 seconds. As will

191

be shown later in this Chapter, noise sources can also induce oscillatory behavior in the jammer suppression.

7.3 Jammer Scenarios

An analytical solution for the third order nonlinear equation for the excision has not been found, although a solution to the second order can be found. However, under the assumption that the excision becomes small ($\omega_j \approx \omega_c$, $a << b$), a linearized version of equation 7.32 is more useful for discussing some simple jammer scenarios. The time evolution of the excision for the *jth* jammer in this linear regime can be approximated by

$$\frac{\partial}{\partial t'}\left(\underline{E}_j\right) \cong (a)\left(\underline{\Psi}_j - \underline{E}_j\right) - \frac{b}{I_A}\underline{A}_j\left(\underline{A}_j^* \cdot \underline{E}_j\right). \qquad 7.37$$

At the onset of the *jth* jammer, $G_j = 0$, and from equation 7.31 we have that $\underline{E}_j\big|_{t'=0} = \underline{\Psi}_j$. This demonstrates that initially the excision is limited to the amount provided by the spatial processing gain of the phased-array. After transforming back from the change of variables of equations 7.33 - 7.35, equation 7.37 yields a jammer decay rate of

$$\frac{\partial}{\partial t}\underline{E}_j\bigg|_{t=0} = -\underline{A}_j\left(\underline{A}_j^* \cdot \underline{E}_j\right)\gamma' e^{-i\sigma_a\left(\omega_c - \omega_j\right)} \qquad 7.38$$

where a lumped factor has been defined as

$$\gamma' = g_1 R_{je}\beta\eta\Re g_2 C \qquad 7.39$$

with units of $(\text{watt} \cdot \text{second})^{-1} = \text{joules}^{-1}$. The result of equation 7.38 illustrates that the excision is decreasing in the direction of the incident jammer as expected, at a rate proportional to both jammer strength and feedback loop gain, in accordance with the LMS algorithm discussed in Chapter 2. The steady-state excision can be obtained by setting the time derivative in equation 7.37 equal to zero,

192

$$\left.\underline{\hat{A}}_j^* \cdot \underline{E}_j\right|_{t\to\infty} \cong a\left(\underline{\hat{A}}_j^* \cdot \underline{\Psi}_j\right) \Big/ \left(a + \left(\underline{A}_j^* \cdot \underline{A}_j\right) b e^{-i\sigma_a(\omega_c-\omega_j)}/I_A\right) \tag{7.40}$$

where $\underline{\hat{A}}_j$ indicates a unit vector in the $\underline{A}_j$ direction. The result given by equation 7.40 demonstrates once again that the excision is in the direction of the interference as desired, but in contrast to a true LMS-based algorithm in which the suppression depth depends on the jammer strength, the steady-state suppression value of the *jth* jammer depends on the ratio of the power in the *jth* jammer to the total amount of interference power I_A. As shown below, for a single jammer this ratio is unity, and the suppression depth is independent of jammer strength.

7.3.1 Single Jammer Dynamics

Consider a single incident jammer at center frequency ω_c, which yields $\underline{A}_1^* \cdot \underline{A}_1 = I_A$. In the limit of $a/b \ll 1$ (implying large feedback gain) equation 7.38 yields an initial decay rate of

$$\left.\frac{\partial}{\partial t}\left(\underline{\hat{A}}_1^* \cdot \underline{E}_1\right)\right|_{t=0} = -\left(\underline{\hat{A}}_1^* \cdot \underline{E}_1\right)I_A\gamma' \tag{7.41}$$

and for the steady-state suppression equation 7.40 yields

$$\underline{\hat{A}}_1^* \cdot \underline{E}_1 \cong a\underline{\hat{A}}_1^* \cdot \underline{\Psi}_1/b = \underline{\hat{A}}_1^* \cdot \underline{\Psi}_1 \, \alpha/\gamma'. \tag{7.42}$$

The most simple single jammer scenario to consider is that of a single frequency, plane wave jammer. In this case the spatio-temporal jammer vector $\underline{A}_1$ is reduced to a single spatial mode with amplitude A_0 at frequency ω, given by

$$A = A_o e^{i\omega t} e^{ik_1 x}. \tag{7.43}$$

Similarly, $\underline{\Psi}_1$, the suppression due to the main-beam array function evaluated at the jammer's transverse wavevector, is collapsed to a scalar value, denoted as Ψ_1. For this

case, equations 7.41 and 7.42 are dramatically simplified. In fact, for this case, equation 7.37 can be solved analytically[2] yielding

$$E(t') = E_o e^{-\left[a + be^{i\sigma_a(\omega_c - \omega_1)}\right]t'} + \frac{a\Psi_1}{a + be^{i\sigma_a(\omega_c - \omega_1)}} \qquad 7.44$$

which for a jammer at center frequency ω_c yields a steady-state excision given by

$$E(t')\big|_{t \to \infty} \approx {a\Psi_1}\Big/{b} = \frac{\alpha\Psi_1}{g_1 R_{je}\beta\eta\Re g_2 C} = {\alpha\Psi_1}\Big/{\gamma'} \qquad 7.45$$

and decay time constant of

$$\tau = \frac{1}{I_A g_1 R_{je}\beta\eta\Re g_2 C} = \frac{1}{I_A \gamma'}. \qquad 7.46$$

Note that in equation 7.45, as in equation 7.42, for a single jammer the steady-state suppression depends on the ratio a/b, which is independent of jammer power and the total interference power.

A less intuitive result is obtained from a solution to the second order approximation of equation 7.32. The second order approximation is given by

$$\frac{\partial}{\partial t'}\left(\underline{E}_j\right) = a\left(\underline{\Psi}_j - \underline{E}_j\right) + \frac{\Psi_j}{I_A}\sum_{jln} A_{jl}A_{jn}^*E_{jl}^*E_{jn} - \frac{b}{I_A}e^{-i\sigma_a(\omega_c - \omega_j)}\underline{A}_j\left(\underline{A}_j^* \cdot \underline{E}_j\right) \qquad 7.47$$

For a single plane wave jammer this becomes

$$\frac{\partial}{\partial t'}(E) = a(\Psi - E) + \Psi E^2 - be^{-i\sigma_a(\omega_c - \omega_j)}E \qquad 7.48$$

with an analytical solution given by[3]

$$E(t) = \frac{\sqrt{4a\Psi - \kappa^2}}{2}\tan\left[\frac{t\sqrt{4a\Psi - \kappa^2}}{2} - \tan^{-1}\left(\frac{\kappa - 2}{\sqrt{4a\Psi - \kappa^2}}\right)\right] + \frac{\kappa}{2} \qquad 7.49$$

where $\kappa = a\Psi + be^{-i\sigma_a(\omega_c - \omega_j)}$. While an analytic solution to the third order differential equation for the time evolution of the excision has not been found, it is interesting to note that the second order approximation does have a solution. However, the solution

based on the linear approximation has proven adequate for the limiting cases examined, and the more complex solution given by equation 7.49 has not been used.

7.3.2 Dynamics of Multiple Jammers

7.3.2.1 Two Jammers of Equal Strength

Consider next the case of two incident jammers of equal strength denoted as $\underline{A}_1$ and $\underline{A}_2$, but having different AOAs and frequencies both near ω_c. Since both jammers have the same power of $I_A/2$, from equation 7.38 it is clear that the excision begins to decrease in the appropriate direction for each jammer at a rate proportional to jammer strength,

$$\frac{\partial}{\partial t}\left(\hat{\underline{A}}_1^* \cdot \underline{E}_1\right)\Bigg|_{t=0} = -\left(\hat{\underline{A}}_1^* \cdot \underline{E}_1\right) I_A \gamma'/2 \qquad 7.50$$

$$\frac{\partial}{\partial t}\left(\hat{\underline{A}}_2^* \cdot \underline{E}_2\right)\Bigg|_{t=0} = -\left(\hat{\underline{A}}_2^* \cdot \underline{E}_2\right) I_A \gamma'/2 \qquad 7.51$$

while from equation 7.40 the steady-state excision values become

$$\hat{\underline{A}}_1^* \cdot \underline{E}_1 \cong 2a\underline{\hat{A}}_1^* \cdot \underline{\Psi}_1/b = 2\hat{\underline{A}}_1^* \cdot \underline{\Psi}_1(\alpha/\gamma') \qquad 7.52$$

and

$$\hat{\underline{A}}_2^* \cdot \underline{E}_2 \cong 2a\underline{\hat{A}}_2^* \cdot \underline{\Psi}_2/b = 2\hat{\underline{A}}_2^* \cdot \underline{\Psi}_2(\alpha/\gamma'). \qquad 7.53$$

Note the factor of two present in equations 7.52 and 7.53 as compared to equation 7.42. This result illustrates a simple example of how the steady-state suppression value of the *jth* jammer depends on the ratio of the power of the *jth* jammer to the total amount of interference power I_A. In this particular case, a factor of two in amplitude between the excision of a single incident jammer and the excision of each of the two equal strength jammers.

7.3.2.2 Strong and Weak Jammer

Next consider the case of two jammers of different frequencies and different AOAs, where one (jammer $\underline{A}_1$) is much stronger than the other (jammer A_2). In this case we can assume that $I_A \cong \underline{A}_1^* \cdot \underline{A}_1$. For the strong jammer, the initial rate of excision given by equation 7.38 becomes

$$\frac{\partial}{\partial t}\left(\hat{\underline{A}}_1^* \cdot \underline{E}_1\right)\bigg|_{t=0} \cong -\left(\hat{\underline{A}}_1^* \cdot \underline{E}_1\right)I_A\gamma' \qquad 7.54$$

and the steady-state suppression from equation 7.40 is

$$\hat{\underline{A}}_1^* \cdot \underline{E}_1 \cong a\hat{\underline{A}}_1^* \cdot \underline{\Psi}_1 / b = \hat{\underline{A}}_1^* \cdot \underline{\Psi}_1 \, \alpha/\gamma' . \qquad 7.55$$

Thus, for the strong jammer the results correspond approximately to the case of the single jammer as considered previously in equations 7.41 and 7.42. The rate of excision for the weaker jammer, A_2, is slower than that of A_1, and is proportional to $\underline{A}_2^* \cdot \underline{A}_2$, as shown in equation 7.56:

$$\frac{\partial}{\partial t'}\left(\hat{\underline{A}}_2^* \cdot \underline{E}_2\right)\bigg|_{t'=0} \cong -b\left(\hat{\underline{A}}_2^* \cdot \underline{E}_2\right)\left(\underline{A}_2^* \cdot \underline{A}_2/I_A\right) \qquad 7.56$$

The steady-state suppression of the weaker jammer is now reduced in comparison to the stronger jammer, in particular by the ratio of the power in $\underline{A}_2$ to the total interference power $I_A = \underline{A}_1\underline{A}_1^* + \underline{A}_2\underline{A}_2^*$,

$$\hat{\underline{A}}_2^* \cdot \underline{E}_2 \cong a\hat{\underline{A}}_2^* \cdot \underline{\Psi}_2 \Big/ \left(a + b\left(\underline{A}_2^* \cdot \underline{A}_2\right)/I_A\right) . \qquad 7.57$$

7.3.2.3 Two Jammers with the Same Optical Angle-of-Arrival

A special case to consider is when jammers of differing frequencies share the same optical AOA in the adaptive processor, as would occur with the piggy-back jammers discussed in previous sections of this Chapter when there is no etalon filter installed. This situation arises when two jammers of different frequencies share the

196
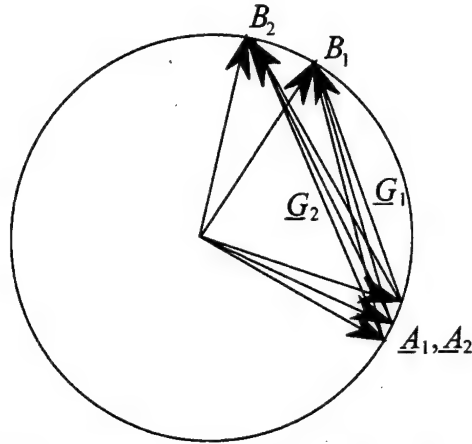
Figure 7.11. Momentum space representation of two multiple spatial mode jammers $\underline{A}_1$ and $\underline{A}_2$ of different temporal frequencies which share the same optical angle of arrival.

same RF transverse momentum vector component, and hence the same transverse optical wavevector component. Note that because the jammers have different frequencies but the same RF transverse momentum vector component, they have different RF AOAs. The optical scenario is depicted in momentum space in figure 7.11. The figure depicts a particular case of two different temporal frequency jammers, $\underline{A}_1$ and $\underline{A}_2$, each consisting of three overlapping spatial modes, along with the corresponding sets of gratings $\underline{G}_1$ and $\underline{G}_2$ written between the jammers and their corresponding feedback beams, B_1 and B_2.

Although gratings will not be written between the different temporal frequencies, i.e. between $\underline{A}_1$ and B_2, the gratings can be read out by both frequencies. Without the Fabry-Perot etalon installed the excision for the *jth* frequency jammer can be supplemented by diffractions from other gratings which were written by other frequencies. The excision for the *jth* jammer then takes the form

$$\underline{E}_j \equiv \underline{\Psi}_j - g\, R_{je}/R_{mb}\, e^{-ip_j} \sum_m \underline{G}_m \,. \qquad 7.58$$

This result suggests that the jammers will be nulled together, and that they will be suppressed by the same amount, regardless of the relative power between them, in

contrast to the previous cases examined for jammers with different AOAs. If the $\underline{\Psi}_j$ are equal, then the jammers will all have the same steady-state suppression level.

The results from the above jammer scenarios indicate that the jammer nulling processor performance is analogous to a processor based on the LMS algorithm in the sense that the decay rate of the jammer(s) depends on jammer strength and feedback gain. Except for the special case of a mutual AOA, the steady-state suppression results indicate a dependence upon the total interference power, in contrast to that predicted by traditional LMS based algorithms. These results are compared to those predicted by the narrowband, Widrow-Hopf, single adaptive loop in the following section.

7.4 Comparison to the LMS Adaptive Loop

The basic operation of the single narrowband Widrow-Hopf LMS adaptive loop was presented in Chapter 2. In addition, the equivalence of the optically implemented jammer-nulling and beam-forming algorithms to the broadband, Widrow-Hopf, true-time-delay algorithm was presented. It is instructive to investigate the similarity of the jammer-nulling processor algorithm to the simple Widrow-Hopf LMS adaptive loop within the context of the physical system variables introduced in the previous section using the standard nomenclature used to describe the Widrow-Hopf LMS loop in Chapter 2. The derivation which follows is for single, narrowband LMS feedback loops, for forming single adaptive weights. The fact that the loop itself is narrowband does not imply that the resulting analogies developed are applicable only to a narrowband scenario, one can consider this single loop as one of many which make up a broadband system. Specifically, the equivalent feedback gain constant k of the LMS algorithm will be derived, as will an expression for the optimal set of weights for the processor which minimize the excision.

$$x_n(t) = D_n(t)e^{-ik_x^D nd} + A_n(t)e^{-ik_x^A nd}$$

Signals From Other Elements

$$s(t) = \sum_n^N x_n(t)W_n$$

W_n

Output

k

$$\varepsilon(t) = r(t) - \sum_n^N x_n(t)W_n$$

Reference Signal $r(t) \propto D(t)$
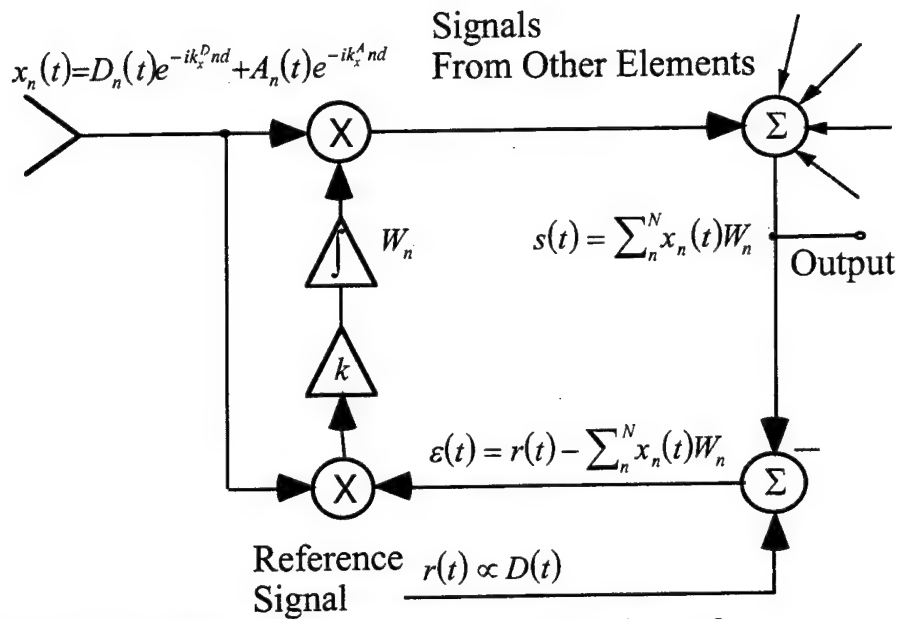
Figure 7.12. Single LMS adaptive loop as discussed in Chapter 2.

The narrowband, Widrow-Hopf adaptive LMS loop for a single antenna array element from chapter 2 is shown in figure 7.12, and the adaptive loop for a single array element of the jammer nulling processor is shown in figure 7.13 with no photorefractive erasure term present. It is important to note that in figure 7.13, some signals are optical, and some are electrical. It has been assumed that the electrooptic upconversion of the received array signal has already been implemented at this point of the discussion. The signals shown in the standard LMS loop of figure 7.12 are all electrical. As discussed in Chapter 2, while algorithmically the two systems are the same, there are some significant differences between them.

In particular, the output of the jammer-nulling processor is *after* the difference node, instead of before as with the standard LMS loop of Chapter 2. Thus the output of the jammer-nulling processor is actually the "error" signal, in which the jammer content has been reduced and the broadband signal of interest passes through the jammer-nulling loop unaffected. It follows that a second difference is that the reference signal
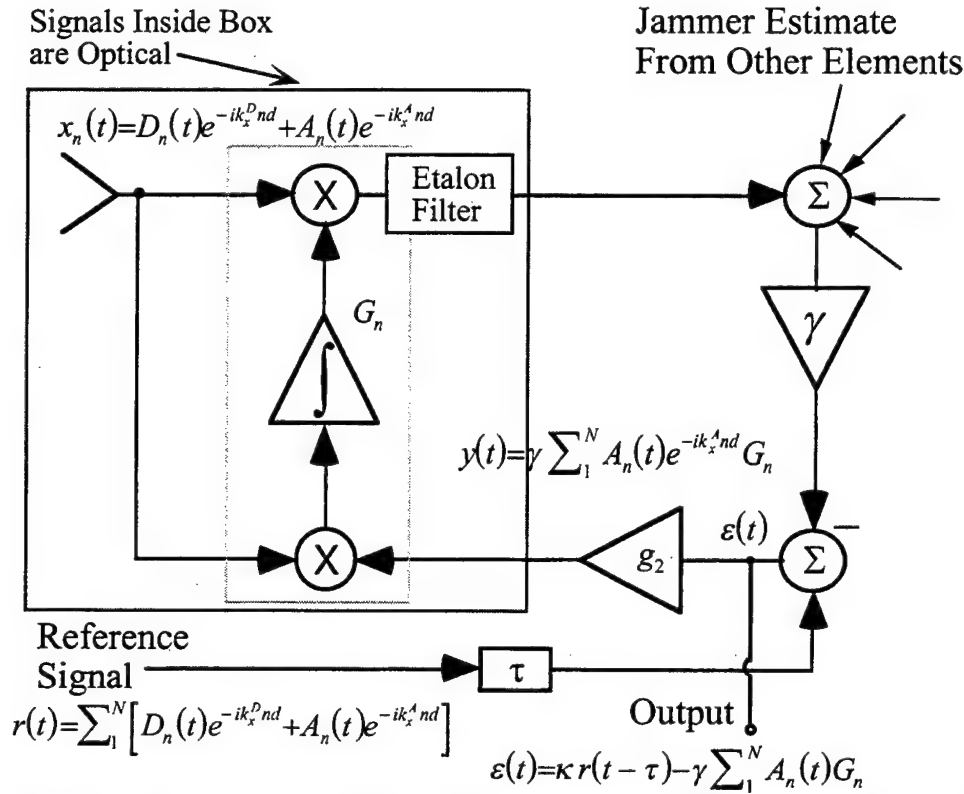
Figure 7.13. LMS adaptive loop for a single array element of the adaptive phased-array jammer nulling processor.

input into the difference node is *the signal to be nulled,* i.e. the interfering jammer. This contrasts with the standard loop implementation in which the correlation-cancellation-loop is configured to maximize the array output for the desired signal. The reference signal r of the standard LMS implementation is a temporal waveform which is required to correlate well with the signal of interest, and the output is taken before the difference node. In the jammer-nulling processor the reference signal is the output of the main-beam estimate photodetector, or the steered main-beam forming processor. This main-beam signal contains both the desired signal and the corrupting jammer signals. The desired signal is broadband and much weaker than the jammer, therefore the reference signal for interference cancellation is essentially the interfering signal itself.

An additional, more fundamental difference between the jammer-nulling processor and the Widrow-Hopf LMS loop is related to the fact that (ideally) no portion of the desired signal gets collected by the jammer estimate detector due to the spatially selective bandpass filter array. As will be shown, while the jammer-nulling processor still follows an LMS minimization rule, this difference has a fundamental impact on the expressions for the optimal weights and steady-state weight values as compared to the results of Chapter 2. In particular, it is found that when the jammer-nulling processor is modeled as an ideal LMS algorithm (i.e. neglecting photorefractive weight erasure), the excision of a particular jammer depends on its power ratio to the total interference power, and is not related to the power of the broadband signal of interest. However, for a single jammer it is found that the excision level is *independent* of jammer power. These results are consistent with the jammer suppression scenarios discussed in the previous section in which weight erasure was included, but the desired signal and noise were not included. As will be shown in Section 7.5, the effects of noise and the broadband desired signal reveal themselves primarily through their impact upon the grating erasure terms, and because erasure has been ignored in this analysis, their significance is minimal here.

The fact that because the interference serves as the correlation reference, and this makes the jammer-nulling processor analogous to the traditional sidelobe cancellor was reviewed in Chapter 2. However, in a sidelobe cancellor the suppression depth of a signal is proportional to its incident power, therefore a strong desired signal can actually null itself. The Bragg selective gratings and the etalon bandpass filter array in the jammer-nulling processor essentially act as an excisor filter for the broadband desired signal. This feature makes the jammer-nulling processor even more robust than a traditional sidelobe canceller in that suppression does not occur even if the desired signal is strong.

Consider a single, electro-optically upconverted planewave jammer of frequency ω_A, represented by $A(t) = Ae^{i\omega_A t}$ and a broadband desired signal $D(t) = De^{i[\omega_D t + \phi(t)]}$, shown as a phase-modulated signal, both of which are incident on an N element array. The total optical signal contributed to the processor by the nth element is taken to be $x_n(t) = D_n(t)e^{-ik_x^D nd} + A_n(t)e^{-ik_x^A nd}$, where k_D^x and k_A^x are the transverse propagation vector components for the desired and jammer signals respectively, and d is the fiber core spacing. As shown in figure 7.13, this is multiplied by a Bragg-matched "gratinglet" G_n, sent to a summing node, and amplified by an effective gain γ. This summing node is optically implemented as the jammer estimate heterodyne photodetector, and gathers contributions from all the other antenna elements as shown in the figure. Due to the feedback delay τ, the broadband signal component at the element output and that from the difference node are decorrelated, and as discussed earlier there is no weight buildup due to this signal. Due to the finite integration time over which the adaptive weights are formed, no correlation between these signals is only an approximation, and in actuality some partial correlation sidelobes between the delayed and undelayed versions of the broadband desired signal will exist. However, the correlated component will be considered negligible in this analysis. The fact that there are no gratings created due to the desired signal combined with the spatially selective etalon frequency filter, ensures that only jammer components will be both diffracted and collected at the jammer estimate heterodyne detector. Noise at the fiber input is ignored because it can be considered to be broadband, and the majority of its power will not be passed by the bandpass filter array. Thermal noise generated at the detectors is neglected in this analysis, but will be included in section 7.5. The summed output signal is then written as

$$y(t) = \gamma \sum_1^N A_n(t)e^{-ik_x^A nd} G_n \qquad\qquad 7.59$$

where the time variable t now contains the intrinsic delay of the etalon filter array. Note the distinction between the summed output signal for the jammer nulling processor given by equation 7.59 which is now assumed to consist *only* of the product of the jammer signal and the grating weights, and the summed weighted output result of the Widrow-Hopf LMS loop shown below in equation 7.60. In particular, Widrow-Hopf signal consists of *all* incoming signals contained in the X vector of the unadapted array output multiplied by the adaptive weights,

$$s(t)_{WH\,LMS} = \sum_1^N x_n(t)W_n.$$

7.60

The summed signal of equation 7.59 can be represented by the product of two (complex) vectors,

$$y(t) = \gamma\, \underline{G}^T \underline{A}(t) = \gamma\, \underline{A}^T(t)\underline{G}$$

7.61

where the complex vectors are given by

$$\underline{A} = \left[A_{1_R} \cdots A_{N_R}\right] + i\left[A_{1_I} \cdots A_{N_I}\right]$$

7.62

and

$$\underline{G} = \left[G_{1_R} \cdots G_{N_R}\right] + i\left[G_{1_I} \cdots G_{N_I}\right]$$

7.63

where the subscripts R and I represent real and imaginary parts respectively. The other input into the difference node is the reference signal $r(t-\tau)$, which is the delayed, steered, main-beam signal which contains both the desired signal and the corrupting jammer signal,

$$r(t) = D(t) + \Psi_{MB}A(t) = \sum_1^N\left[D_n(t)e^{-ik_x^D nd} + A_n(t)e^{-ik_x^A nd}\right]$$

7.64

where the jammer signal is seen to be weighted by Ψ_{MB}, the main-beam antenna function, to account for the fact that the array has formed a beam in the direction of the desired signal $D(t)$. The second equality reflects the fact that the reference signal is actually formed by summing the output from all of the antenna array elements. The

error signal at the output of the difference node is the difference between equations 7.61 and 7.64. This error signal is also the processor output, and can be written as

$$\varepsilon(t) = \kappa r(t - \tau) - \gamma \sum_{1}^{N} A_n(t) G_n = \kappa r(t - \tau) - \gamma \underline{A}^T \underline{G}_j. \qquad 7.65$$

The effective gain constant κ multiplying the reference signal accounts for photodetector responsivities, optical powers, and material parameters. From chapter 2, the generic form of the complex LMS algorithm was given as

$$\frac{\partial}{\partial t} \underline{W} = -k \nabla_W E\left[\varepsilon \varepsilon^*\right] = 2kE\left[\underline{X}^* \varepsilon\right] \qquad 7.66$$

where $E[\bullet]$ is the expectation operator and ∇_W is the gradient operator with respect to the weight, W. The corresponding steady-state weight values for the Widrow-Hopf LMS algorithm were given by $\underline{W} = \underline{S} \underline{\underline{\Phi}}^{-1}$, where the reference correlation vector $\underline{S}$ is

$$\underline{S} = E\left[x_1^*(t) r(t), \cdots, x_N^*(t) r(t)\right]^T \qquad 7.67$$

and the covariance matrix $\underline{\underline{\Phi}}$ is

$$\underline{\underline{\Phi}} = E \begin{bmatrix} x_1^* x_1 & x_1^* x_2 & \cdots & x_1^* x_N \\ x_2^* x_1 & x_2^* x_2 & & \vdots \\ \vdots & & \ddots & \\ x_N^* x_1 & & & x_N^* x_N \end{bmatrix}. \qquad 7.68$$

Written in terms of the holographic grating diffraction efficiency G_j, corresponding to the *jth* jammer, the LMS algorithm for the jammer-nulling processor can be written as

$$\frac{\partial}{\partial t} \underline{G} = -k \nabla_G \left[\varepsilon \varepsilon^*\right] \qquad 7.69$$

where k is the feedback gain constant. Note that the expectation operator, $E[\bullet]$, has been dropped, because in actuality, as with the Widrow-Hopf implementation, the optical implementation discussed here is based on approximating expectation values by instantaneous values. By determining the three parameters k, κ, and γ in terms of the

system parameters of the processor, the standard LMS algorithm and its associated notation can be directly related to the optically implemented jammer-nulling processor.

The optimum weights are found by setting the gradient of the sum-squared error equal to zero,

$$\nabla_G \left[\varepsilon \varepsilon^* \right] = 0 \qquad\qquad 7.70$$

which is equivalent to

$$\nabla_G \left[\varepsilon \varepsilon^* \right] = \nabla_G \left[\varepsilon_R^2 \right] + \nabla_G \left[\varepsilon_I^2 \right]. \qquad\qquad 7.71$$

Carrying out the gradient operation is done with respect to both the real and imaginary parts, which when using equation 7.65 for the error ε results in

$$\nabla_{G_R} \left[\varepsilon \varepsilon^* \right] = \left[\varepsilon \nabla_{G_R} \varepsilon^* \right] + \left[\varepsilon^* \nabla_{G_R} \varepsilon \right] = -\gamma \varepsilon \underline{A}^* - \gamma \varepsilon^* \underline{A} \qquad\qquad 7.72$$

and

$$\nabla_{G_I} \left[\varepsilon \varepsilon^* \right] = \left[\varepsilon \nabla_{G_I} \varepsilon^* \right] + \left[\varepsilon^* \nabla_{G_I} \varepsilon \right] = i\gamma \varepsilon \underline{A}^* - i\gamma \varepsilon^* \underline{A} \qquad\qquad .7.73$$

It follows that the sum of the two above equations can be expressed as[4]

$$\nabla_{G_R} \left[\varepsilon \varepsilon^* \right] + \nabla_{G_I} \left[\varepsilon \varepsilon^* \right] = -2\gamma \varepsilon \underline{A}^* \qquad\qquad 7.74$$

which allows equation 7.69 to be written as

$$\frac{\partial}{\partial t} \underline{G} = -k\nabla_G \left[\varepsilon \varepsilon^* \right] = 2k\gamma \underline{A}^* \varepsilon. \qquad\qquad 7.75$$

Note that the second equality of the above LMS rule and the second equality of equation 7.66 differ in the term which multiplies the error. The $\underline{X}$ vector of equation 7.66 contains all incident signals, while the $\underline{A}$ vector in equation 7.75 contains only jammer signals. Setting equation 7.74 equal to zero and substituting in equation 7.65 for the error yields

$$\left[\kappa r(t-\tau) - \gamma \underline{G}_{opt}^T \underline{A} \right] \underline{A}^* = 0. \qquad\qquad 7.76$$

205

Solving for $\underline{G}_{opt}$ results in an expression for the optimum weights

$$\underline{G}_{opt} = \frac{\Psi_{MB}\kappa\underline{S}_A\underline{\underline{\Phi}}_A^{-1}}{\gamma} \qquad 7.77$$

where the constants κ and γ will be derived shortly. A vector $\underline{S}_A$ analogous to the correlation vector of equation 7.67 is defined as

$$\underline{S}_A \equiv \underline{A}^* r(t-\tau) = \underline{A}^*\left[\sum_1^N D_n(t-\tau)e^{-ik_x^D nd} + A_n(t-\tau)e^{-ik_x^A nd}\right]. \qquad 7.78$$

Again, under the assumption that over the finite integration time which the adaptive weights are formed, the correlation between the desired signal and the jammer is negligible, the reference correlation vector $\underline{S}_A$ simplifies to

$$\underline{S}_A = \underline{A}^*\left[\sum_1^N A_n(t-\tau)e^{-ik_x^A nd}\right]. \qquad 7.79$$

Under the same negligible correlation assumption, the matrix $\underline{\underline{\Phi}}_A$, analogous to the covariance matrix of equation 7.68 also contains only jammer signals,

$$\underline{\underline{\Phi}}_A = \underline{A}^* \underline{A}^T. \qquad 7.80$$

In the single plane wave jammer analysis of the previous section, the grating vector $\underline{G}$ was actually treated as a single, spatially uniform weight throughout the holographic crystal. This corresponds to straightforward phase steering with a uniform weight value and a linear phase-shift across the array, which is all that is necessary to steer an antenna beam in the direction of a single narrowband jammer. For this simplified case, the optimum weight value given by equation 7.77 reduces to

$$G_{n,opt} = \frac{\Psi_{MB}\kappa}{\gamma}. \qquad 7.81$$

The convergence to the optimum weight can also be shown by returning to equation 7.75 and computing the time evolution of a single weight, which is described by

$$\frac{\partial}{\partial t} G = -k \nabla_G \left[A(t) \left(\kappa r(t-\tau) - \gamma A(t) G \right) \right].$$ 　　　7.82

Carrying out the gradient operation, and noting that the cross-correlation of the desired signal and the jammer is zero, it follows that

$$\frac{\partial}{\partial t} G = k\gamma \left(\Psi_{MB}\kappa - \gamma G \right) A^2 = k\gamma \Psi_{MB}\kappa A^2 - k\gamma^2 A^2 G.$$ 　　　7.83

This differential equation can be solved by standard techniques[5] to yield

$$G(t) = \left[G(0) - \Psi_{MB}\kappa/\gamma \right] e^{-k\gamma^2 A^2 t} + \Psi_{MB}\kappa/\gamma$$ 　　　7.84

where $G(0)$ is the initial weight value at $t=0$. It is evident that as t approaches infinity, the weight does indeed converge to the steady-state optimum value of $\underline{G}_{ss} = \Psi_{MB}\kappa/\gamma$ in accordance with equation 7.81.

Expressions for κ and γ can be determined by noting that the error signal ε is equivalent to the optical feedback signal B given by equation 7.24. Thus for the case of a single planewave jammer it follows that

$$\kappa = R_{MB}\eta\Re g_2 C e^{i\omega(\sigma_a + \sigma_e)}$$ 　　　7.85

and

$$\gamma = g_1 R_{JE}\Re \eta g_2 C e^{i\omega\sigma_a}.$$ 　　　7.86

Substituting these equations into equation 7.81 yields

$$G_{ss} = \Psi_{MB}R_{MB}e^{-ip}/g_1 R_{JE}$$ 　　　7.87

where $p = \phi_{R_{MB}} - \phi_{R_{JE}} - \omega\sigma_a$. This result is consistent with the desired behavior of the excision given by equation 7.31, in that these optimum weight values set the excision to zero. Moreover, this result is independent of jammer strength and does not depend on

207

the broadband desired signal. Having determined κ and γ, the optimum weight vector given by equation 7.76 can be written as

$$\underline{G}_{opt} = \frac{\Psi_{MB} R_{MB} e^{-ip}}{g_1 R_{JE}} \underline{S}_A \underline{\underline{\Phi}}_A^{-1}.$$ 7.88

Finally, the feedback gain constant k can be determined by substituting equation 7.24 into the LMS algorithm expressed by equation 7.69. This substitution results in

$$\frac{\partial}{\partial t} G = -\beta |R_{mb}|^2 \Re^2 \eta^2 g_2^2 |C|^2 \nabla_G A \left[\Psi_{MB} - g_1 \left(R_{JE}/R_{MB} \right) G \right] A \left[\Psi_{MB} - g_1 \left(R_{JE}/R_{MB} \right) G \right].$$ 7.89

Expanding out the terms and taking the gradient yields

$$\frac{\partial}{\partial t} G = 2\beta g_1 R_{JE} \Re \eta g_2 C[A\varepsilon].$$ 7.90

Referring to equation 7.75, the feedback gain constant in terms of the system parameters of the jammer nulling processor is then

$$k = g_1 R_{JE} \beta \eta \Re g_2 C = \gamma'$$ 7.91

where γ' is the lumped constant defined in equation 7.39. From equations 7.84, 7.87, and 7.91, it is evident that for both rapid and high jammer suppression the system parameter to be maximized is γ', which has just been shown to be equal to the feedback constant k of Chapter 2. The product of terms which make up the constant γ' appear in both the steady-state excision expressions and the decay-rate expressions of the previous section. These equations are shown again below, where the subscript j refers to the jth jammer,

$$\left. \frac{\partial}{\partial t} \underline{E}_j \right|_{t=0} = -\underline{A}_j \left(\underline{A}_j^* \cdot \underline{E}_j \right) \gamma' e^{-i\sigma_a(\omega_c - \omega_j)}$$ 7.38

$$\underline{\hat{A}}_j^* \cdot \underline{E}_j \cong a \underline{\hat{A}}_j^* \cdot \underline{\Psi}_j / b = \underline{\hat{A}}_j^* \cdot \underline{\Psi}_j \, \alpha / \gamma'.$$ 7.42

208

It is evident that the decay-rate given by equation 7.38 of the previous section is directly proportional to k and the steady-state excision given by equation 7.42 is inversely proportional to k. This performance is consistent with the performance predicted by the traditional LMS algorithm.

7.5 Effects of Additive Noise and Desired Signal

A realistic dynamical analysis of the jammer-nulling processor requires the presence of a broadband desired signal in addition to additive noise, and an interpretation of how the excision is affected by these factors. In particular, detector noise should be considered, as well as optical noise terms unique to the jammer-nulling processor. Moreover, it is important to also examine the behavior of the signal-to-interference plus noise ratio (SINR) of the processor output. The SINR is a practical figure-of-merit with which to assess and quantify the processor performance.

7.5.1 Derivation of Steady-State Excision and SINR in the Presence of Noise and Desired Signal

The analysis follows closely to that presented in Section 7.2, where for simplicity a single planewave jammer is incident upon the array. The incident jammer signal $\underline{A}_j$ of equation 7.1 is therefore collapsed to single jammer, composed of only one spatial propagation mode l, but it has been shown that the results would not change for a more complex near-field or multipath jammer. A broadband desired signal $D(t)$ is also present. The optical noise terms to be included consist of front-end detector noise at the array which has been upconverted to the optical domain, and optical feedthrough resulting from the holographic multiplexing scheme. The multiplexing feedthrough can consist of both a fanning-induced scattering term and the double-diffraction term discussed in Section 5.3.2 when the technique of angle multiplexing using Bragg degeneracy is used. Use of the orthogonal polarization multiplexing scheme eliminates

this troublesome double-diffraction term. The analysis is developed in terms of the Bragg degeneracy multiplexing technique, and reduces to the case when the orthogonal polarization multiplexing technique is used. It should be noted that although the analysis presented here corresponds directly with the single crystal implementation of the phased-array radar processor shown in figure 7.1, it is not specific to this architecture and is directly applicable to the experimentally demonstrated combined processor configuration which uses two separate PRCs.

The total electrooptically upconverted optical signal incident on the PRC is taken to be

$$F = \left(Ae^{i\omega t} + D + U\right)\frac{\left(1 + re^{i\phi_r}e^{-ik_{rp}y}\right)}{\sqrt{1 + r^2}} \qquad 7.92$$

where $Ae^{i\omega t}$ is the signal from the incident jammer, and $D(t)$ is the desired signal, and U represents the summed front-end array detector noise, which is taken to be a uniformly distributed zero-mean random variable. The term $\left(1 + re^{i\phi_r}e^{-ik_{rp}y}\right)\big/\sqrt{1 + r^2}$ accounts for the fact that there are actually two incident beams from the Rochon prism, whose relative amplitudes are determined by the factor r, and the spatial phase factor in the y direction indicates that these Rochon outputs are displaced in the direction of Bragg degeneracy (see figure 5.4). This scenario is more realistic than that presented in section 7.2, where it was assumed that there was only one beam present, A, that of the jammer only. The second set of beams produced by the Rochon prism will add significantly to erasure, add no processing gain, but are merely a necessity of the holographic multiplexing technique. Because in this sense there is literally an extra set of beams at the crystal, the problem is treated as such. In particular, compared to the results of section 7.2, just as there is a desired signal and additive noise in this analysis, there is additional erasure due to the multiplexing technique. The signal F is diffracted off of holographic grating G_2 (see figure 5.4) and passed through the etalon filter array. The selectivity of the holographic grating and the etalon array result in only the

components of F near the jammer frequency and angle reaching the heterodyne detector. Also incident on the detector is the multiplexing feedthrough term discussed above, which is modeled as a coefficient f multiplying the feedback beam B. The coefficient f is composed of two terms, the scattering term f_o due to fanning, and the double diffraction coefficient f_2 multiplied by the double diffraction efficiency as derived in Section 5.2.3. The two gratings written, G_1 and G_2, can be related by noting that each shares the common write beam B. In particular, $G_1 \propto AB^*$, $G_2 \propto A^*B$, where A_1 and $Ae^{-ik_{rp}y}$ are the two signals produced from the Rochon prism, and the ratio is r, leading to an expression for f given by

$$f = f_o + f_2 G_1^* G_2 = f_o + f_2 r |G|^2 e^{-i\phi_r} \qquad 7.93$$

where G_1 and G_2 are the two individual gratings, and the second equality is in terms of the factor r. After combining with the jammer estimate heterodyne reference R_{je}, which uniformly fills the photodetector, the current at the output of the jammer estimate detector is given by

$$e_{JE} = \left| rAGe^{i\omega t} + fB + R_{JE}e^{i\phi_{RJE}} + U/\Im \right|^2 \Re \qquad 7.94$$

where $\Re$ is the photodetector responsivity, and $\Im$ is proportional to the etalon filter finesse. After expanding and bandpass filtering to eliminate the D.C. and higher harmonic terms, equation 7.94 becomes

$$e_{JE} = rAGR_{JE}\Re e^{i\omega t - i\phi_{RJE}} + fBR_{JE}\Re e^{-i\phi_{RJE}} + N_{JE} + UR_{JE}e^{i\phi_{RJE}} \Re/\sqrt{N}\Im + c.c. \qquad .7.95$$

The random, uncorrelated front-end detector element noise term adds in proportion to $1/\sqrt{N}$ where N is the number of detector elements. In the following, the $U/\Im$ noise term will be neglected because the etalon finesse is assumed to be large, and combined with the $1/\sqrt{N}$ reduction, the net result is taken to be small. A thermal noise current term N_{JE} has also been added to the detector output.

The main beam heterodyne photodetector signal is given by

$$e_{MB} = \int_a \left| \Pi\left(\frac{z}{L}\right)\left(Ae^{i\omega t} + D + U\right) + R_{MB}e^{-\pi(z/\sigma_r)^2}e^{i\phi_{RMB}} \right|^2 \Re dz \qquad 7.96$$

which results in

$$e_{MB} = \Psi A R_{MB}\Re e^{i\omega t - i\phi_{RMB}} + DR_{MB}\Re e^{-i\phi_{RMB}} + R_{MB}\Re e^{-i\phi_{RMB}} U/\sqrt{N} + N_{MB} + c.c. \; .7.97$$

A thermal noise term N_{MB} has also been added, and Ψ is the normalized array function defined in previous sections. The D.C. signals have been dropped, as well as those outside of an octave bandwidth. The RF feedback signal sent to the Bragg cell is composed of the difference between e_{MB} and $g_1 e_{JE}$, and this difference is then amplified by g_2. Illuminating the Bragg cell with an optical signal with amplitude C and phase shift $e^{i\phi_c}$, the diffracted optical signal from the Bragg cell propagating towards the PRC is then

$$B(t - x/V) = R_{MB}\eta\Re g_2 Ce^{i\phi_c} \left\{ \begin{array}{l} Ae^{-is}e^{-i\phi_c}e^{i\omega(t - x/V)}\left[\Psi - g_1\left(R_{JE}/R_{MB}\right)Gre^{ip}\right] \\ +U/\sqrt{N}\left(t - \sigma_a - \sigma_e - x/V\right)e^{-i\phi_{RMB}} \\ +D\left(t - \sigma_a - \sigma_e - x/V\right)e^{-i\phi_{RMB}} \\ -g_1 fB\left(t - \sigma_a - x/V\right)R_{JE}/R_{MB}\,e^{-i\phi_{RJE}} \\ +N_{MB}/\Re R_{MB}\left(t - \sigma_a - \sigma_e - x/V\right) \\ -g_1 N_{JE}/\Re R_{MB}\left(t - \sigma_a - x/V\right) \end{array} \right\} \qquad 7.98$$

where V is the acoustic velocity of the Bragg cell, η is the diffraction efficiency of the Bragg cell in units of diffraction efficiency/amp, and σ_a and σ_e are the feedback acoustic and electrical delays respectively. Due to the multiplexing feedthrough term, the signal B occurs on both sides of the equality, with two different temporal arguments. In order to solve for B, the Fourier transform of equation 7.98 is taken, and using the shift theorem and inverse transforming, the phaseshifts are converted into time delays. Thus the feedback signal B becomes

212

$$B(t - x/V) = R_{MB}\eta\Re g_2 Ce^{i\phi_c}\left\{\frac{Ae^{-is}e^{-i\phi_c}e^{i\omega(t-x/V)}\left[\Psi - g_1\left(R_{JE}/R_{MB}\right)Gre^{ip}\right]}{\left(1 + g_1 fe^{-i\omega'(\sigma_a)}R_{JE}\eta\Re g_2 Ce^{i\left(\phi_c - \phi_{RJE}\right)}\right)}\right\} + \quad 7.99$$

$$R_{MB}\eta\Re g_2 Ce^{i\phi_c}\sum_{m=0}^{\infty}\left[\left(-g_1 fR_{JE}\eta\Re g_2 Ce^{i\left(\phi_c - \phi_{RJE}\right)}\right)^m\right]\begin{Bmatrix} N_{MB}/\Re R_{MB}\left(t-\sigma_e-x/V-\tau_m\right) \\ -g_1 N_{JE}/\Re R_{MB}\left(t - x/V - \tau_m\right) \\ +D\left(t - \sigma_e - x/V - \tau_m\right)e^{-i\phi_{RMB}} + \\ U/\sqrt{N}\left(t-\sigma_a-\sigma_e-x/V\right)e^{-i\phi_{RMB}} \end{Bmatrix}$$

where the substitution of

$$\left(1 + g_1 fR_{JE}\eta\Re g_2 Ce^{i\varrho}\right)^{-1} = \sum_{m=0}^{\infty}\left(-g_1 fR_{JE}\eta\Re g_2 Ce^{i\varrho}\right)^m \qquad 7.100$$

has been made based on the assumption that $g_1 fR_{JE}\eta\Re g_2 C < 1$. The delay time τ_m which appears in the multiplexing feedthrough terms represents the accrual of acoustic delays from the mth pass around the loop. In particular, for the mth pass, $\tau_m = \sigma_a + m\sigma_a$. In accordance with prior definitions (equation 7.25), the time evolution of the photorefractive grating amplitude diffraction efficiency evolves according to

$$\frac{\partial}{\partial t}G = -\alpha I_{D.C.}G + \beta I_{grating} = -\alpha\left(|F|^2 + |B|^2\right)G + \beta AB^*. \qquad 7.101$$

Equation 7.101 elucidates the fact that while all the components of F contribute to the DC erasure, only the jammer component, A, contribute to the grating writing process. Using equations 7.92 and 7.99 for the signals F and B respectively, the average intensity, $I_{D.C.}$, becomes

$$I_{DC} = \left(|A|^2 + |D|^2 + |U|^2\right) \qquad 7.102$$

$$+|R_{mb}|^2\eta^2\Re^2 g_2^2|C|^2\left\{\begin{array}{l} |A|^2\left[\Psi - g_1\left(R_{JE}/R_{MB}\right)Gre^{ip}\right]\left(1 + g_1 fR_{JE}\eta\Re g_2 Ce^{-i\omega\sigma_a}e^{i\left(\phi_c - \phi_{Rje}\right)}\right)^{-1}\Big|^2 \\ +\dfrac{\left(\langle N_{MB}\rangle^2/\Re^2|R_{MB}|^2 + g_1^2\langle N_{JE}\rangle^2/\Re^2|R_{MB}|^2 + |D|^2 + |U|^2/N\right)}{1 - \left(g_1 fR_{JE}\eta\Re g_2 C\right)^2} \end{array}\right\}$$

where the $\langle N_{MB} \rangle$ and $\langle N_{JE} \rangle$ represent the time averages of these noise terms, and the resonance factors γ_o and $\gamma_1(\omega)$ are defined as

and

$$\gamma_o \equiv 1 - |g_1 f R_{JE} \eta \Re g_2 C|^2 \qquad 7.103$$

$$\gamma_1(\omega) \equiv \left(1 + g_1 f R_{JE} \eta \Re g_2 C e^{i\sigma_o(\omega - \omega_c)}\right). \qquad 7.104$$

Both of these resonance factors are a result of the multiplexing feedthrough and are ideally kept near unity. When the values of these terms are near unity, this implies small leakage terms, f. Also note that $\gamma_1(\omega)$ is frequency dependent. The grating intensity pattern is given by

$$I_{gr} = \frac{A R_{MB} \eta \Re g_2 C e^{i\phi_c} e^{-iKx}}{\sqrt{1+r^2}} \left\{ \begin{array}{l} A e^{-is} e^{-i\phi_c}\left(\Psi - g_1 Gr e^{ip} R_{JE}/R_{MB}\right)\gamma_1^{-1}(\omega) \\ + \sum\limits_{m=0}^{\infty} \left[\left(-g_1 f R_{JE} \eta \Re g_2 C e^{i(\phi_c - \phi_{RJE})}\right)^m \left(\begin{array}{l} \dfrac{N_{MB}|_{\omega,m} + g_1 N_{JE}|_{\omega,m}}{\Re R_{MB}} \\ + D|_{\omega,m} + \dfrac{U|_{\omega,m}}{\sqrt{N}} \end{array}\right)\right] \end{array} \right\} 7.105$$

where the notation $D|_{\omega,m}$, N_{JE}, N_{MB}, and $U|_{\omega,m}$ indicates the signal contribution at frequency ω, on the *mth* pass around the loop. These narrowband noise terms can be assumed to write weak gratings with themselves, and with the other signals present in the PRC because each individual narrowband frequency component of the noise spectra will be assumed to be small. These terms will then be neglected and the grating intensity term is simplified to

$$I_{gr} = \frac{A^2 R_{MB} \eta \Re g_2 C e^{-is} e^{-iKx}}{\sqrt{1+r^2}}\left(\Psi - g_1 Gr e^{ip} R_{JE}/R_{MB}\right)\left(1 + g_1 f R_{JE} \eta \Re g_2 C e^{i\sigma_o(\omega - \omega_c)}\right)^{-1} 7.106$$

making the same change of variables using t', a, and b, as in equations 7.33 - 7.35, the time evolution of the grating becomes

214

$$\frac{\partial}{\partial t'}G = -\left(\begin{array}{l} \frac{a}{|A|^2}\left(|A|^2+|D|^2+|U|^2\right) \\[2mm] \left|\Psi - g_1\frac{R_{JE}}{R_{MB}}Gre^{ip}\right|^2 |\gamma_1(\omega)|^{-2} \\[2mm] \frac{P_{A=0}}{|A|^2|R_{MB}|^2\Re^2}\gamma_o^{-1} \end{array}\right)G + b\frac{R_{MB}}{\gamma_1(\omega)g_1R_{JE}\sqrt{1+r^2}}e^{-is}\left(\Psi - g_1Gre^{ip}\frac{R_{JE}}{R_{MB}}\right)\quad 7.107$$

where the term containing all signal powers before jammer turn has been defined as

$$P_{A=0} = \left(\langle N_{MB}\rangle^2 + g_1^2\langle N_{JE}\rangle^2 + |R_{MB}|^2\Re^2|D|^2 + |R_{MB}|^2\Re^2|U|^2/N\right). \qquad 7.108$$

The excision is defined as

$$E = \Psi - g_1Gre^{ip}\,R_{JE}/R_{MB} \qquad\qquad 7.109$$

and substituting this into equation 7.107 and linearizing in E, produces

$$\frac{\partial}{\partial t'}E = \left(\begin{array}{l} -\frac{a}{|A|^2}\left(|A|^2+|D|^2+|U|^2\right) \\[2mm] +|E|^2|\gamma_1(\omega)|^{-2} + \frac{P_{A=0}}{|A|^2|R_{MB}|^2\Re^2}\gamma_o^{-1} \end{array}\right)(\Psi-E) - \frac{rbe^{i\sigma_a(\omega-\omega_c)}E}{\gamma_1(\omega)\sqrt{1+r^2}} \quad . \qquad 7.110$$

Here the effects of γ_o and $\gamma_1(\omega)$ on the excision become somewhat apparent. Should either of these resonant terms be driven towards small values, their reciprocal becomes quite large. In particular, the resonant denominators will affect the D.C. erasure term and introduce a frequency dependent oscillation term through $\gamma_1(\omega)$. Setting the temporal derivative equal to zero results in the somewhat cumbersome expression for the steady-state excision,

$$E_{ss} = \frac{\dfrac{a\Psi}{|A|^2}\left(|A|^2+|D|^2+|U|^2\right)+\dfrac{P_{A=0}}{|A|^2|R_{MB}|^2\Re^2}\gamma_o^{-1}}{\left[\begin{array}{c}\dfrac{P_{A=0}}{|A|^2|R_{MB}|^2\Re^2}\gamma_o^{-1}+\dfrac{rbe^{i\sigma_a(\omega-\omega_c)}}{\gamma_1(\omega)\sqrt{1+r^2}}\\[4mm]+\dfrac{a}{|A|^2}\left(|A|^2+|D|^2+|U|^2\right)\end{array}\right]}.$$

$$7.111$$

The analytic expression for the steady-state suppression given by equation 7.111 is not very intuitive. An enlightening first case to examine is for a single plane wave jammer. Setting f equal to zero, neglecting all noise components, and assuming that the jammer is much stronger than the desired signal essentially reduces the problem to the scenario of section 7.3. Recall, however, that the analysis of this section includes the effects of the second jammer signal beam produced by the Rochon prism. The steady-state excision then becomes

$$E_{ss} = \frac{a\Psi}{rb}\sqrt{1+r^2} = \frac{\Psi\alpha\sqrt{1+r^2}}{r\beta g_1 R_{JE}\eta\Re g_2 C} = \frac{\Psi\alpha}{\gamma' r}\sqrt{1+r^2}$$

$$7.112$$

where γ' was defined in equation 7.39. Assuming that these two beams are equal, or setting r equal to 1, results in a steady-state excision of

$$E_{ss} = \frac{\sqrt{2}a\Psi}{b} = \frac{\sqrt{2}\Psi\alpha}{\gamma'}.$$

$$7.113$$

Setting r equal to 1 is what is typically done in the lab, and in addition has been shown to be the optimum value for jammer excision[6]. Equation 7.113 shows for this case, that with all noise and feedthrough sources removed, the excision is degraded by an additional factor of $\sqrt{2}$ compared to the results of section 7.3.1 due to the second beam produced by the Rochon prism when using the Bragg degeneracy multiplexing technique. This degradation arises because of the added erasure the PRC suffers when there is an additional optical beam present. The situation is effectively the same for the

orthogonal polarization multiplexing scheme, because again there is a second (readout) beam present which acts as an erasure mechanism of the photorefractive grating.

At this point the SINR can be defined as

$$SINR \equiv \frac{\text{Desired Signal Power}}{\text{Interference Power} + \text{Noise Power}} \qquad 7.114$$

which for the jammer-nulling processor becomes

$$SINR \equiv \frac{|D|^2 |R_{MB}|^2 \mathfrak{R}^2}{|E_{ss}|^2 |A|^2 |R_{MB}|^2 \mathfrak{R}^2 + \langle N_{MB} \rangle^2 + g_1^2 \langle N_{JE} \rangle^2 + fB |R_{JE}|^2 \mathfrak{R}^2 g_1^2 + |U|^2 |R_{MB}|^2 \mathfrak{R}^2 / N} \qquad 7.115$$

where E_{ss} is the steady-state excision value. In the following section, the excision and SINR behavior will be examined as a function of system parameters.

7.5.2 Excision and SINR in the presence of Noise and Desired Signal

The excision and SINR behavior will now be examined as a function of system parameters, and expressions corresponding to several important limiting cases will be derived. In addition to gaining insight into the behavior of the steady-state excision and the SINR, an effort towards determining relationships between system parameters which optimize performance will be made. As will be shown, and as equation 7.111 suggests, with the introduction of noise and feedthrough the jammer-nulling processor behavior becomes quite complicated.

As has been shown several times throughout this chapter, minimizing the excision requires maximizing the quantity γ', given by equation 7.39. The obvious way to maximize this term is to increase the electrical gain terms g_1 and g_2, the jammer estimate reference beam R_{JE}, and the feedback Bragg cell input optical field amplitude C. However, while the dynamical analysis of section 7.2 yields results which suggest that these electrical gains can be increased without bound, the addition of a desired signal and noise will place limits on the amount of system gain which can be applied.

For example, examination of the third and fourth terms in the denominator of equation 7.115 as well as the definition of the excision in equation 7.31 indicates a trade-off between the SINR and the excision with respect to electrical amplification term g_1. The noise terms in the SINR expression suggest g_1 should be small. However, the definition of the excision suggests that to drive the excision to small values, g_1 should be large when considering realistic values of R_{JE}/R_{MB} and moderate grating diffraction efficiencies G. The steady-state excision given by equations 7.113 and 7.112 also indicates that g_1 should be large.

Plots of the excision and SINR given by equations 7.111 and 7.115 respectively are shown in figures 7.14 (a) and (b). The plot in figure 7.14 shows the excision plotted versus the gain term g_1, parameterized in the quantity $g_2 C$. The gain parameter $g_2 C$, is the product of electrical post-summing-node gain and the feedback Bragg cell input optical field amplitude. This parameter was chosen because except for g_1, all the other quantities in equation 7.112 are bounded by material or device limits. Material and device parameters were set to $\alpha = 0.5$, $\beta = 5$, both with units of joules^{-1}, $\Re = 0.5$ with units of amps/watt, and $\eta = 0.9$ with units of %/amp, for all simulations in this section. The remaining simulation parameters are listed in the figure caption. The important point to note from figure 7.14 is that for the range of system variables chosen, the quantity $g_1 g_2 C$ is approximately conserved. This implies that the excision can be minimized by increasing either g_1 or g_2 in the presence of a desired signal and noise (feedthrough is omitted at this point of the analysis) as predicted, and as demonstrated in figure 7.14(a). In contrast, the plot of the SINR shown in figure 7.14 (b), also plotted versus the gain term g_1, and parameterized in the quantity $g_2 C$, shows that SINR improves for smaller values g_1 and larger values of $g_2 C$. In previous works discussing jammer suppression and dynamics[7,2], it had been proposed that g_1 should be large in order to maximize the excision. While a large value of g_1 does indeed
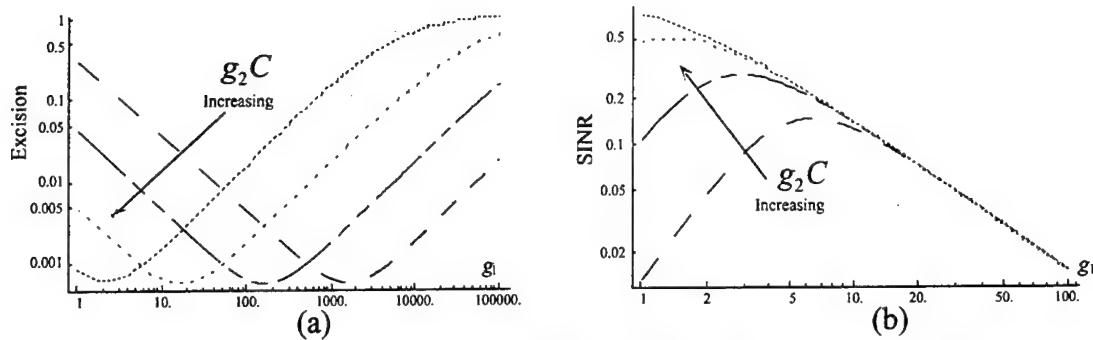
Figure 7.14. Excision versus g_1 parameterized in g_2C, with units of volts/meter ($g_2C = 10^1, 10^2, 10^3, 10^4$) in (a), and SINR versus g_1 parameterized in g_2C ($g_2C = 10^2, 10^{2.5}, 10^3, 10^{3.5}$) in (b). The simulation Parameters were: $A = 0.1$, $R_{JE} = 0.1$, $R_{MB} = 0.005$, $D = 10^{-3}$, $U = 10^{-7}$, all with units of volts/meter and $r = 1$, $N_{JE} = N_{MB} = 10^{-5}$ with units of amps, and $f = 0$, which is unitless.

increase excision, it correspondingly degrades the SINR. Thus it follows that the factor to be increased is g_2C, and it is satisfactory to set g_1 equal to unity for this analysis.

The quantity g_2C cannot be increased without bound however. The amount of gain which can be applied is limited by the amount of electrical detector noise, and to a much lesser extent by the amplitude of the desired signal. A plot of the excision, E, versus electrical detector noise terms in the jammer estimate and main-beam detectors N_{JE} and N_{MB} (both assumed to be equal here), parameterized in g_2C is shown in figure 7.15(a), where r has been set equal to 1. It is clear that for a given g_2C value the excision is compromised as the detector noise increases. As the gain is further increased, the point at which the excision is compromised occurs at smaller values of noise, and the excision is also seen to pass through a minimum near $g_2C = 10^3$. Ultimately, all of the curves saturate at the value of one, corresponding to no excision at all. The same saturation behavior is seen to occur in the excision versus desired signal amplitude plot shown in figure 7.15 (b). The primary difference between this and the detector noise case is that the effects do not occur until g_2C has reached much larger values. The front-end array noise terms were held at constant, small values for both of
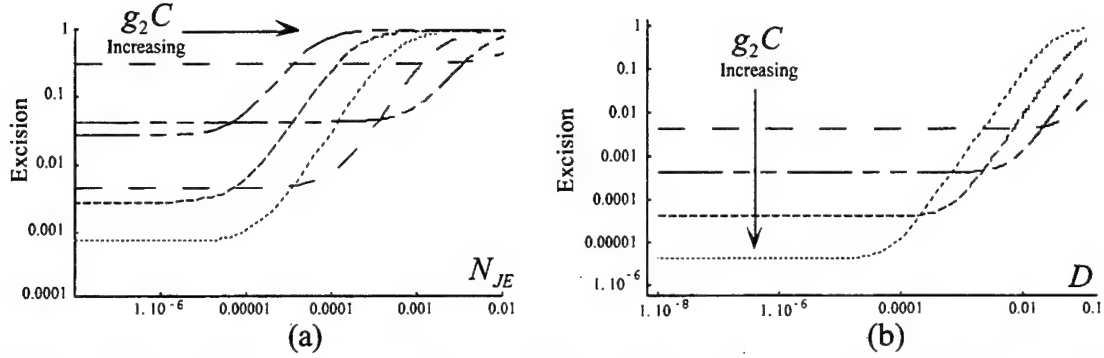
Figure 7.15. Excision versus detector noise N_{JE} parameterized in gain g_2C ($g_2C = 10^1, 10^2, 10^3, 10^4, 10^5, 10^6$ and desired signal $D = 10^{-3}$) in (a), and excision versus desired signal D parameterized in g_2C ($g_2C = 10^3, 10^4, 10^5, 10^6, 10^7$ and $N_{JE} = N_{MB} = 10^{-8}$) in (b). The simulation Parameters were: $A = 0.1$, $R_{JE} = 0.1$, $R_{MB} = 0.005$, $U = 10^{-7}$, all with units of volts/meter and $r = 1$, $f = 0$, and $g_1 = 1$, both unitless.

these plots. According to equation 7.111, the excision behavior for U is the same as for the desired signal, but further reduced by the number of array elements N, demonstrating spatial processing gain.

For the detector electrical noise term limited case (neglecting array element noise) the steady-state excision given in equation 7.111 becomes

$$E_{ss} = \frac{a\Psi\left(|A|^2+|D|^2\right)+ \frac{1}{\left|R_{mb}\right|^2 \Re^2}\left(\langle N_{mb}\rangle^2+g_1^2\langle N_{je}\rangle^2+\left|R_{mb}\right|^2\Re^2|D|^2\right)}{\left[\frac{1}{\left|R_{mb}\right|^2 \Re^2}\left(\langle N_{mb}\rangle^2 + g_1^2\langle N_{je}\rangle^2 + \left|R_{mb}\right|^2\Re^2|D|^2\right)+ \frac{|A|^2 be^{i\sigma_a(\omega-\omega_c)}}{\sqrt{1+r^2}} \atop +a\left(|A|^2+|D|^2\right)\right]}. \qquad 7.116$$

The corresponding expression for the SINR becomes

$$SINR = \frac{|D|^2\left|R_{mb}\right|^2\Re^2}{\left|E_{ss}\right|^2|A|^2\left|R_{mb}\right|^2\Re^2 + \langle N_{mb}\rangle^2 + g_1^2\langle N_{je}\rangle^2}. \qquad 7.117$$

220

7.5.3 Excision in the Presence of Noise, Desired Signal, and Optical Feedthrough due to Multiple Diffraction.

The most volatile parameter of all to be considered is the optical feedthrough term f. Recall the resonance factors γ_o and $\gamma_1(\omega)$ defined in equations 7.103 and 7.104. Both of these definitions introduce a constraint that $1 > f^2 g_1^2 |R_{je}|^2 \eta^2 \Re^2 g_2^2 |C|^2$ in order for these terms to remain bounded. This inequality effectively defines a constraint upon the maximum gain $g_2 C$, determined by the feedthrough parameter f, from the standpoint that the amount of feedthrough will determine how much the system gain can be increased before the resonance terms cause the system to go into oscillation or saturation. Plots of the excision, E, versus gain term $g_2 C$, parameterized in feedthrough, f, are shown in figure 7.16. Note that the first (bottom) two curves of the figure have an excision that is reasonably behaved. There is a general tendency for the excision to be compromised as the feedthrough is increased, however the most significant effect is that excision becomes unstable, in this case for the third and fourth curves of the family. This unstable behavior is caused by the resonant denominator terms γ_o and $\gamma_1(\omega)$, even though the jammer frequency has not been varied here.

The feedthrough parameter f was initially defined by equation 7.93, and is repeated below

$$f = f_o + f_2 r |G|^2 e^{-i\phi_r} \qquad\qquad 7.118$$

where f_2 was shown in Chapter 5 to be equal to 1/2. One first limiting case to consider is when the scattering term $f_o \ll 1$, and therefore $f \approx \frac{r}{2} |G|^2 e^{-i\phi_r}$. Noting that at steady-state the excision goes to zero, therefore from equation 7.109, for a single jammer $|G|^2_{ss} \to \Psi^2 R_{mb}^2 / g_1^2 r^2 R_{je}^2$. Substituting this steady-state expression for G into equation 7.118, it follows that the constraint introduced above requires that $1 > g_2 C \eta \Re \Psi^2 R_{mb}^2 / (2 g_1 r R_{je})$. Thus the product $g_2 C$ is limited by
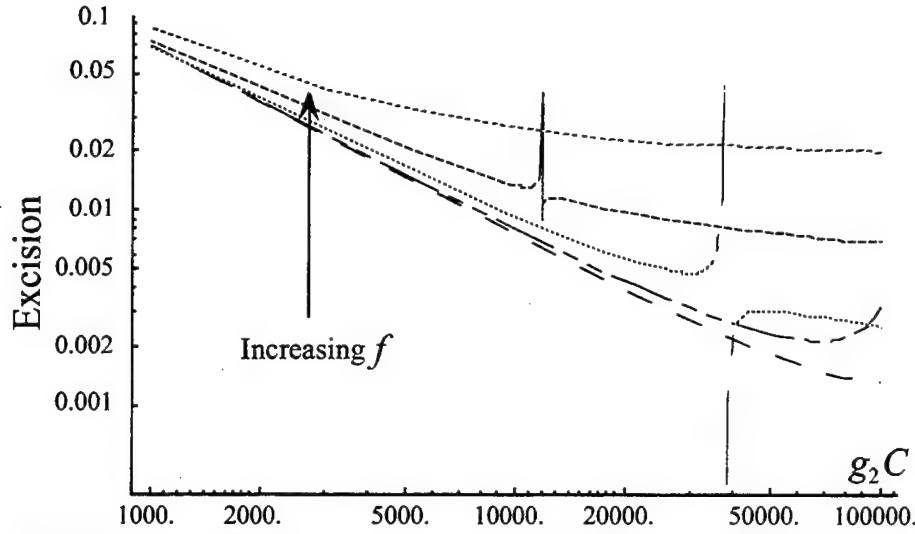
Figure 7.16. Plot of excision versus g_2C, parameterized in optical feedthrough f, which is unitless, where $f = 10^{-3}, 10^{-2.5}, 10^{-2}, 10^{-1.5}, 10^{-1}$. The simulation parameters were: $A = 0.1$, $R_{JE} = 0.1$, $R_{MB} = 0.005$, $D = 10^{-3}$, $U = 10^{-5}$ all with units of volts/meter and $r = 1$, and $N_{JE} = N_{MB} = 10^{-5}$, in units of amps.

$$g_2C < \frac{2g_1 r R_{je}}{\Psi^2 R_{mb}^2 \eta \Re}. \qquad 7.119$$

The condition given by 7.119 imposes a severe constraint on jammer suppression. Substituting the value for g_2C given in equation 7.119, it follows that the steady-state excision of $E_{ss} = \sqrt{1+r^2}\, a\Psi/b$ will be limited by

$$E_{ss} > \sqrt{1+r^2}\, a\Psi/b > \frac{\sqrt{1+r^2}\,\alpha\Psi^3 R_{mb}^2}{2\beta R_{je}^2 g_1^2 r}. \qquad 7.120$$

Common experimental conditions result in the two signals from the Rochon prism being equal ($r = 1$), as well as $R_{JE} \approx R_{MB}$. Under these simplified conditions that $r = 1$, $g_1 = 1$, $R_{JE} \approx R_{MB}$, and assuming that the AOA of the jammer is near that of the desired signal so that $\Psi \approx 1$, equation 7.120 further simplifies to

$$E_{ss} \approx \frac{\alpha}{\beta\sqrt{2}}. \qquad 7.121$$

222

Where α and β are the photorefractive material parameters derived in Section 4.3.3. At unity modulation depth the ratio β/α is approximately $1/2\pi$ times the number of Kogelnik orders that a PRC can provide, which is typically less than 5. Therefore, for this case where the multiplexing feedthrough is significant, the suppression depth appears to be limited to unacceptably poor performance by material parameters. The limit of 5 Kogelnik orders results in a limit of approximately 30dB of jammer suppression. Choosing a more favorable ratio of R_{JE}/R_{MB} may optimize the excision somewhat, although practically R_{JE} cannot be increased past the point where the photodetector saturates. The optimum value of r has in fact been shown to be equal to 1.

7.5.4 Excision in the Presence of Noise, Desired Signal, and Optical Feedthrough due to Scattering.

As discussed in Chapter 5, one of the primary motivations for implementing the orthogonal polarization multiplexing scheme was to eliminate the multiple diffraction feedthrough term f_2. When f_2 is eliminated, the feedthrough term f is limited to the scattering term f_o, and the restriction on g_2C now leads to $g_2C \approx 1/2\eta\Re R_1 f_o$. The resulting steady-state excision for this f_o limited case is then

$$E_{ss} > \frac{\sqrt{1+r^2}\,a\Psi}{b} \rightarrow \frac{2\sqrt{2}\,\alpha\Psi f_o}{\beta} \qquad 7.122$$

where the last expression corresponds to the case when $r = 1$. Because f_o is small, this case represents a significant improvement in suppression depth compared to the case limited by f_2. For example, if the scattering term is considered to be dominated by photorefractive fanning, the fanning can be considered to go uniformly into a number

of modes, N_{modes}, typically given by $N_{modes} \approx \left(Area/\lambda^2\right)\left(\Omega/2\pi\right) \approx 10^6$. If it is assumed that only one mode is matched to the detection system, then $f_o \approx 10^{-6}$.

7.5.5 Excision and SINR with Desired Signal and Jammer only.

The last case to consider is when all noise terms, as well as the feedthrough are negligible. The signals present are then only a strong jammer signal and a desired signal of interest. The steady-state excision can then be approximated by

$$E_{ss} = \frac{a\Psi\left(|A|^2 + |D|^2\right) + |D|^2}{|D|^2 + \dfrac{rb|A|^2}{\sqrt{1+r^2}}} \qquad\qquad 7.123$$

which clearly demonstrates that the excision of the jammer is reduced due to the presence of the desired signal. The SINR for this case can be approximated by

$$SINR = \frac{|D|^2}{|E_{ss}|^2|A|^2} \quad = \quad \frac{|D|^2\left(\dfrac{rb|A|^2}{\sqrt{1+r^2}} + |D|^2\right)^2}{a^2\Psi^2\left(|A|^2 + |D|^2\right)^2|A|^2}. \qquad\qquad 7.124$$

7.5.6 System Parameter Tradeoffs

A useful set of parameter tradeoffs to investigate is the heterodyne reference signal levels. While in actuality the heterodyne reference signal levels R_{JE} and R_{MB} will be limited by photodetector saturation levels, it is instructive to investigate the relative importance of these signals on the excision and SINR levels. Consistent with the fact that minimizing the excision requires maximizing γ', inspection of equation 7.112 for the steady-state excision suggests that for small values of excision, E, R_{JE} should be maximized. This is demonstrated in figure 7.17a, where the excision is driven to smaller values as R_{je} is increased, while it is independent of the signal R_{MB}, as predicted by equation 7.112 when there is no desired signal D. The addition of a
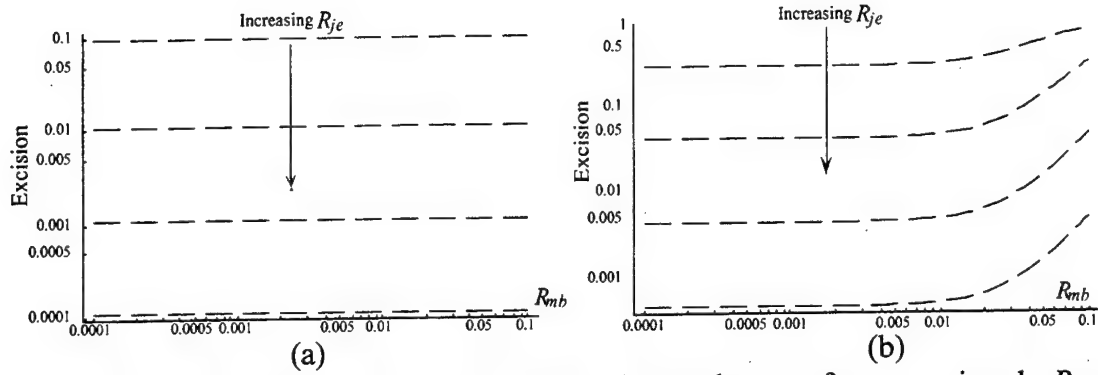
Figure 7.17. Excision versus main-beam heterodyne reference signal R_{MB}, parameterized in jammer estimate heterodyne reference signal R_{JE}, where $R_{JE} = 10^{-4}, 10^{-3}, 10^{-2}, 10^{-1}$. There is no desired signal in (a), and there is a desired signal of amplitude $D = 10^{-3}$ in (b). The simulation parameters were: $A = 0.1$, $U = 10^{-7}$, with units of volts/meter, and $r = 1$. $N_{JE} = N_{MB} = 10^{-7}$ in units of amps, $g_2 C = 4 \times 10^4$, with units of volts/meter, and $f = 0$, which is unitless.

desired signal introduces a significant change a shown in figure 7.17(b). Beyond a critical value of R_{MB}, the excision is compromised. This behavior is first indicated in equation 7.123, where the a/b term is seen to affect the jammer and desired signals differently, but more explicit when equation 7.123 is expanded out,

$$E_{ss} = \frac{\dfrac{\Psi\left(|A|^2 + |D|^2\right)}{g_2^2 |C|^2 |R_{mb}|^2 \eta^2 \Re^2} + |D|^2}{|D|^2 + \dfrac{r g_1 R_{je} \beta |A|^2}{\alpha g_2 C |R_{mb}|^2 \eta \Re \sqrt{1 + r^2}}}$$
7.125

The SINR demonstrates a similar trend, decreasing after approximately the same value of R_{mb}, as shown in figure 7.18.

It is useful to conclude this section by reviewing several other trade-offs for minimizing the excision and maximizing the SINR. There are the obvious issues such as reducing the noise terms and optical feedthrough, as well as optimizing photorefractive material parameters α and β. Improved device performance such as acousto-optic diffraction efficiency η and photodetector responsivity $\Re$ is always
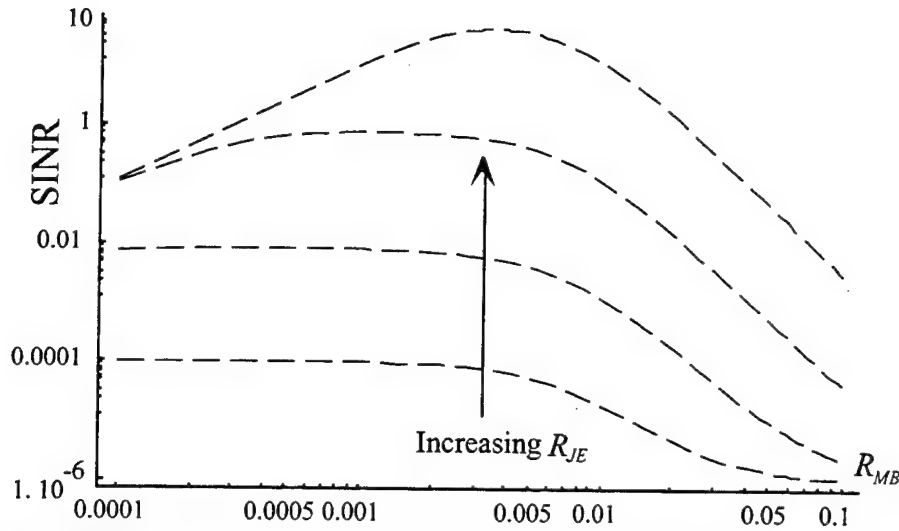
225

Figure 7.18. SINR versus main-beam heterodyne reference signal R_{MB}, parameterized in jammer estimate heterodyne reference signal R_{JE}, where $R_{JE} = 10^{-4}, 10^{-3}, 10^{-2}, 10^{-1}$. The simulation parameters were: $A = 0.1$, $U = 10^{-7}$, with units of volts/meter, $N_{JE} = N_{MB} = 10^{-7}$, with units of amps, $g_2 C = 4 \times 10^4$ with units of volts/meter, and $f = 0$, which is unitless.

advantageous. Nevertheless, in general these parameters are either practically or fundamentally limited. In a practical sense, in order to simultaneously minimize the excision and maximize the SINR, it is advantageous to maximize the gain term γ', but moreover to maximize the term $g_2 C$, keep the gain term g_1 near unity, and to make the amplitude of the jammer estimate detector heterodyne reference signal R_{JE} large. As discussed in the following section, the experimental setup enabled the ratios of the optical beams to be varied using variable beamsplitters. There is of course a fixed amount of laser power introduced into the system, in particular

$$I = |C|^2 + |R_{JE}|^2 + |R_{MB}|^2 + |F|^2. \qquad 7.126$$

As mentioned, the reference beams cannot be increased beyond the point of detector saturation, and the main-beam reference signal R_{MB} actually has little impact. Experimentally, C and F were kept as large as possible, and set to be approximately equal at the turn on time of a jammer.

226

7.6 Experimental Results

Experimental results are presented for each of the jammer scenarios discussed above. In particular, results are obtained for the steady-state suppression values and convergence rates for single plane-wave jammers, a pulsing single planewave jammer, and two jammers of different frequencies at both different and identical AOAs. In addition, a straightforward experimental demonstration of the linear relationship of jammer suppression with system feedback gain as predicted in section 7.3 is presented. The jammer nulling bandwidth predicted by equation 7.44 is also experimentally verified.

7.6.1 Experimental Set-up

The initial experimental configuration of the jammer-nulling processor is shown in figure 7.19. This configuration uses the Bragg degeneracy write/read beam multiplexing technique described in Chapter 5, and has been used to acquire the majority of the experimental results presented here. The argon laser illumination is split at beamsplitter (BS-1) to form the feed forward and feedback beams. The feedback beam is applied to the feedback Bragg cell, and spatial filtering allows only the +1 order to be incident at the PRC. The feed forward beam illuminates a phased array input simulator. This subsystem of the processor is intended to simulate the superposition of the electro-optically modulated, fiber remoted signals of the antenna array elements[8]. At present the simulator consists of three acousto-optic modulators (AOMs) at the back focal plane of a lens. The +1 diffracted signal from each AOM is passed through the lens and they overlap at the PRC, which is placed approximately one focal length away from the lens. Two of the AOMs and input beams can be translated linearly in the direction perpendicular to the axis of the lens and in the plane of the table using a motorized stage. This changes the angle of the beam with respect to the PRC, which simulates a signal in the far field at a variable AOA. The output of the simulator is
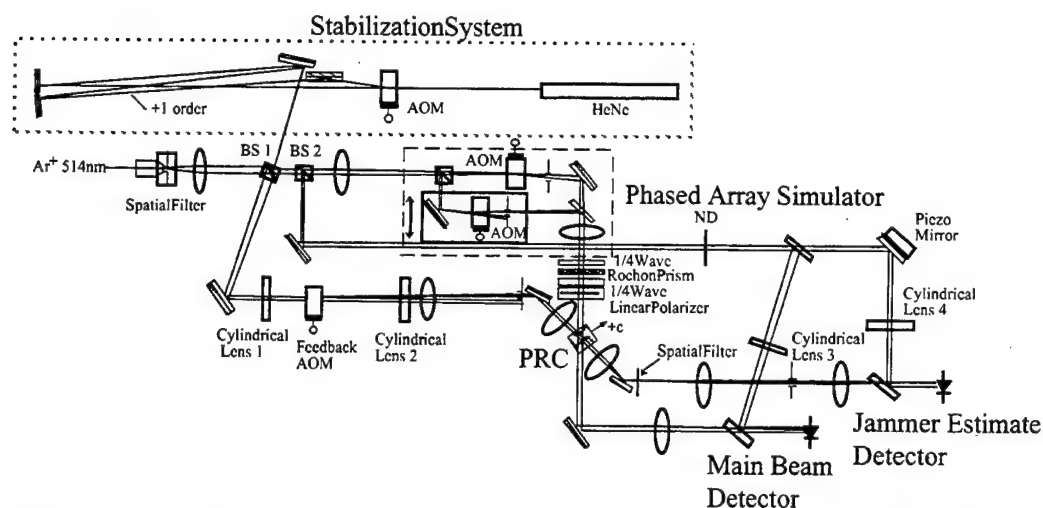
227

Figure 7.19. Optical component layout of jammer nulling processor using Bragg degeneracy for write/read separation.

passed through a 1/4 wave plate, a 0.1° Rochon prism, a second 1/4 wave plate, and finally a linear polarizer to produce two degenerate, vertically diverging beams (of the same polarization) incident at the PRC, implementing the Bragg degeneracy write/read beam separation technique. Rotating the waveplate allowed the ratio of the two write beams incident on the crystal to be varied, corresponding to changing the parameter r. The beam ratio was set to unity for all of the experiments reported here. BS-2 is used to produce the heterodyne reference beams for the jammer estimate and signal detectors shown in the lower right of the figure. The phase critical feedback path of the processor is actively stabilized using a HeNe laser interferometer with a phase tracking piezoelectric actuated mirror to eliminate long-term drift. Phase drifts at the other interferometric paths in the processor, such as at the photorefractive crystal and the main beam signal detector are adaptively compensated for by the processor. In this configuration the jammer estimated detector is used to also detect the HeNe optical stabilization signal. At present, the Fabry-Perot bandpass filter array is not installed in the system.

The associated RF schematic with two phased-array signal sources is shown in figure 7.20. As shown in the figure, one of the sources drives an AOM, loops through
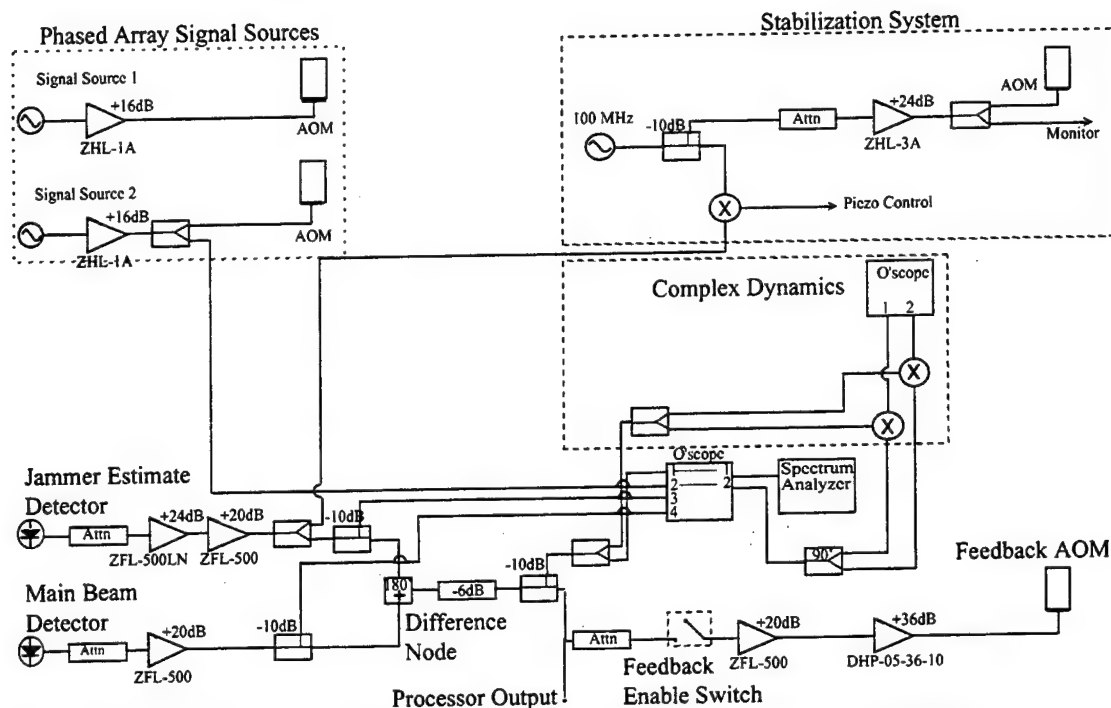
228

Figure 7.20. RF schematic of phased-array radar jammer-nulling processor.

channel 2 of an oscilloscope to provide a trigger source, and then serves as an in-phase

and quadrature mix-down reference for measuring the complex dynamics of the output

signal. The amplified output from the jammer estimate detector is subtracted from the

amplified main-beam detector signal at the difference node, which forms both the

processor output and the RF input to the feedback AOM. The processor output is also

split off for complex dynamics analysis into both an oscilloscope and a spectrum

analyzer.

At the upper right of figure 7.20 is the RF portion of the active path length

stabilization system. As shown in the figure, the 100 MHz signal is extracted from the

jammer estimate detector and mixed down against the 100 MHz reference source. As

the optical path length between the feedback path and the detector heterodyne reference

beam varies, the output at the jammer estimate detector varies in amplitude. This

amplitude actually varies cosinusoidally but the stabilization circuit gain is set-up so as

to remain biased in the linear regime of this response. As shown in figure 7.21, after
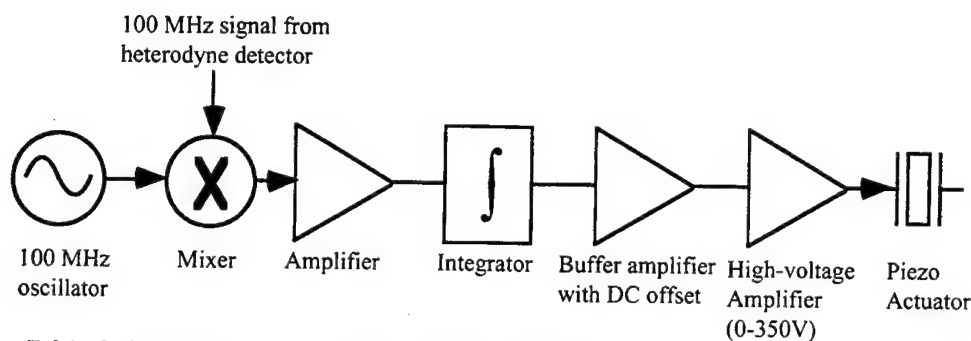
Figure 7.21. Schematic of first piezo actuator driver circuit.

mixing this signal down against the 100 MHz reference signal, the varying DC voltage is sent into an integrator, followed by an inverter and amplifier, and finally fed back to the piezo driven mirror. The frequency response of the feedback circuit was designed to compensate for slowly varying path length drift only. A shortcoming of this system is that the feedback signal to the integrator is not strictly phase information, but also depends upon the magnitude of the product of the signals because of the mix-down process. In general this is not a problem; however, given that the HeNe beam is going through the AOM, it can be Bragg matched, and therefore some energy can be coupled out of this beam, and even worse, couple the jammer dynamics into the stabilization system, which is highly undesirable. A second stabilization system was later implemented using a commercial (Stanford Research Systems SRS 850) lock-in amplifier. Internal DSP capabilities of the lock-in amplifier allowed generation of a strictly phase dependent voltage which was fed to the piezo driver circuit. This second stabilization system is shown in figure 7.23. An 80 kHz reference signal for the lock-in amplifier was generated by taking the difference frequency from the mix-down process of the two phase locked oscillators shown in the figure. The 70.000 MHz oscillator was also used as the RF input to the stabilization AOM shown in the upper right of figure 7.22. The dynamic phase shift of the optical beam exiting from the experiment is maintained by heterodyne detection, and the resulting RF signal is sent through a bandpass filter to reduce noise and feedthrough from any jammers, amplified, and
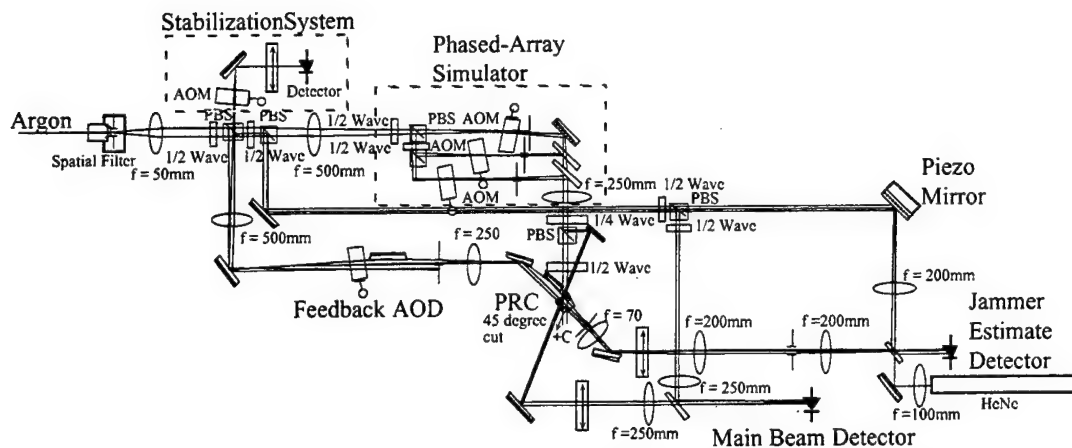
Figure 7.22. Optical component layout of jammer nulling processor using orthogonal polarizations for write/read separation.
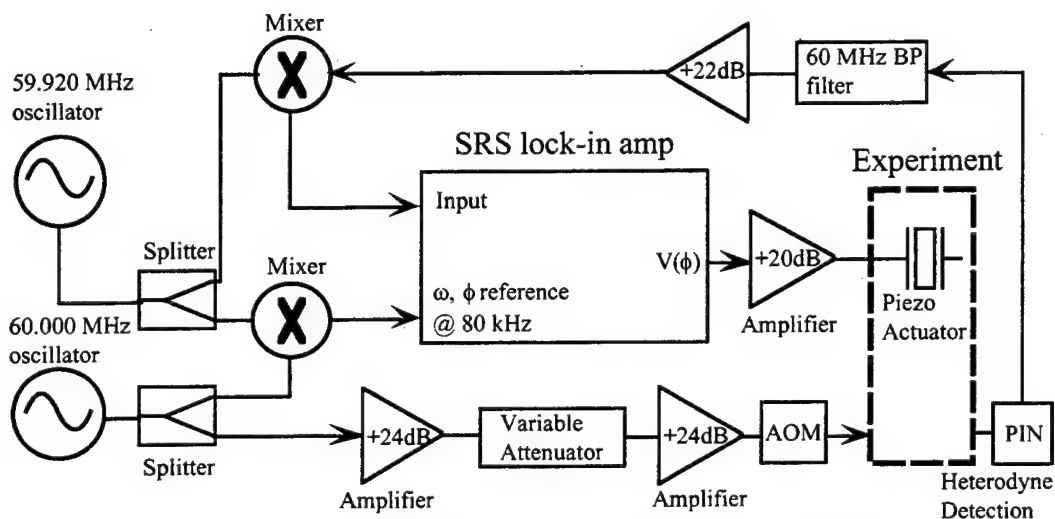
Figure 7.23. Stabilization system using commercial lock-in amplifier to generate a phase dependent error voltage to drive piezo actuator.

finally mixed-down against the 59.920 MHz oscillator to produce a difference signal at 80 kHz for comparison to the lock-in reference. The phase-dependent voltage provided as an output by the lock-in amplifier was then amplified and applied to piezo actuator and mirror. The kilohertz down conversion was necessary in order to match the frequency processing capabilities of the SRS-850, which is limited to 100 kHz. Figure 7.22 shows an improved configuration of the jammer nulling processor which uses the orthogonal polarization write/read technique described in chapter 4. The λ/4 plate and

231

PBS after the phased-array simulator create the two orthogonally polarized write and read beams. The transmitted ordinary polarized write beam is blocked by the aperture just after the PRC and before the 70 mm lens. It should also be noted that the HeNe stabilization laser is now going backwards through the system with its path more closely matched to that of the actual processor, as well as now having its own dedicated optical detector.

7.6.2 Single Jammer Results

Experiments were conducted investigating steady-state suppression values and jammer decay rates for a single frequency plane-wave jammer. Spectrum analyzer trace photos demonstrating suppression of a single narrowband jammer are shown in Figure 7.24, and were obtained using the experimental set-up shown in figure 7.19. Figure

7.24a shows the processor output before suppression (open loop) with an incident 70MHz jammer signal shown at screen center. The DC component at left and second harmonic component at right are outside of the system bandwidth. Figure 7.24b is the processor output after the feedback loop is closed, showing jammer suppression of 35dB. The output of the processor is mixed down electrically with both in-phase and quadrature components of a reference signal taken from the jammer input. This allows measurement of the complex excision, E. Figure 7.25 shows the experimental measurements of E from the onset of the jammer. Figure 7.25a shows the motion of E in the complex plane superimposed over a fit to a numerical solution of equation 7.32 for a single plane wave jammer, using fit parameters of a = 0.206, b = 2.09, $\sigma_a(\omega_c - \omega_j)$ = -0.61. Figure 7.25b shows the decay of the log magnitude of E, also superimposed on a fit of the magnitude of equation 7.32 using the same fit parameters. This experiment used different parameters than that showed in figure 7.24, and achieved only -26 dB steady-state excision. Note that because of the log scaling the jitter away from the theoretical solution is larger at deeper excision. These experimental

232

10 dB/div

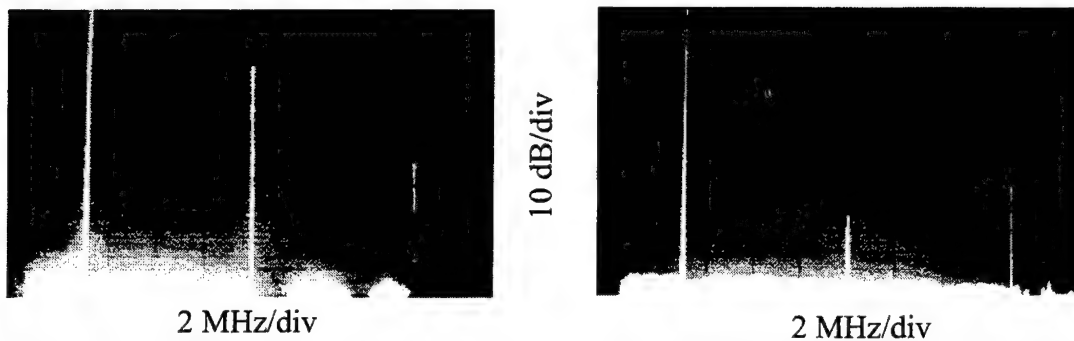2 MHz/div   2 MHz/div

Figure 7.24. Photos of the spectrum analyzer display showing a single narrowband jammer of 70 MHz (at screen center) before suppression at left, and suppressed by 35 dB at right. The spectrum analyzer was used in averaging mode, yielding an accurate reading of E_{ss}. Traces at either side of jammer are the DC component and second harmonic respectively, which are outside of the system bandwidth.
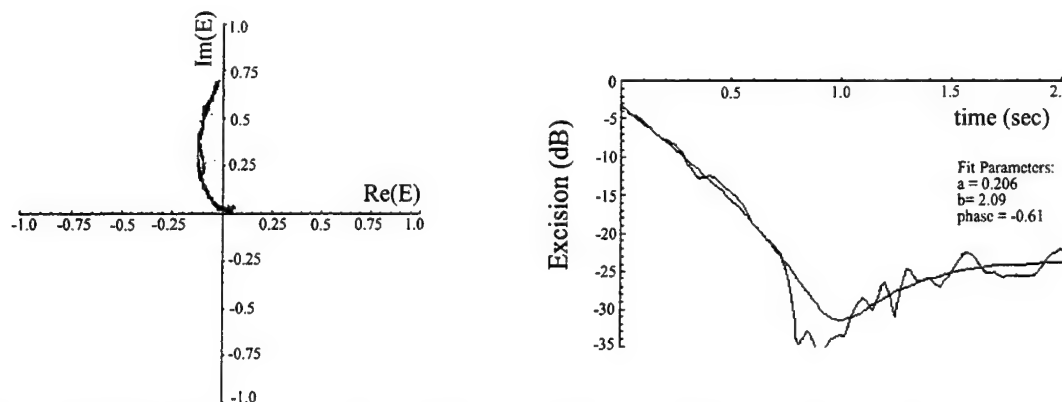
Figure 7.25. (a) Experimental data of excision plotted in complex plane, superimposed over fit of theoretical model, (b) magnitude of excision versus time, also with theoretical fit.

results are in excellent agreement with the theory developed in Section 7.2., in particular the numerical results shown in figures 7.7 and 7.8.

Experimental results are shown in figure 7.26 for a pulsing single narrow-band jammer. The figure shows two superimposed traces of processor output versus time: one trace is the processor output showing the unsuppressed jammer pulsing at 3.3 Hz (feedback off), and the other trace is the output with the jammer suppressed (feedback on) by approximately 25 dB. Note the slightly increased noise floor of the processor output when the jammer is being suppressed. The result shown in figure 7.26 demonstrates that the long photorefractive grating decay time constant is advantageous

233

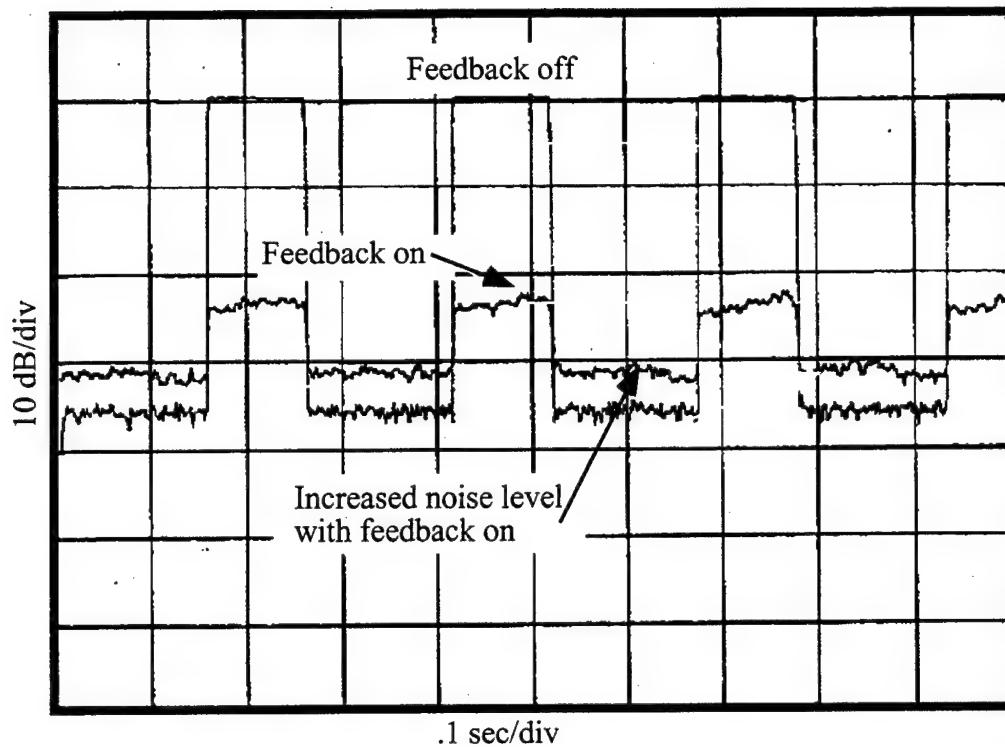Figure 7.26. Two superimposed oscilloscope traces of processor output versus time, one is the processor output showing the unsuppressed jammer pulsing at 3.3 Hz (feedback off), and the other is the output with the jammer suppressed (feedback on) by approximately 25 dB.

in the pulsing jammer scenario. The processor builds up an initial grating at the onset of the jammer, and as long as the pulse repetition rate of the jammer is shorter than the inverse decay time constant the grating remains, providing almost instantaneous jammer suppression to a blinking jammer as shown in the figure. This is in marked contrast to processors that must re-adapt at every turn-on transient of a blinking jammer.

Significantly higher single planewave jammer suppression results have been obtained using the processor illustrated in figure 7.22, employing the orthogonal polarization write/read technique. In addition, variable polarizing beamsplitters were used to more optimally distribute the optical power as determined by the analysis in Section 7.5. These results shown in figure 7.27 demonstrate 45 dB of suppression for a 75.8 MHz narrowband jammer. This method of write/read isolation, discussed in
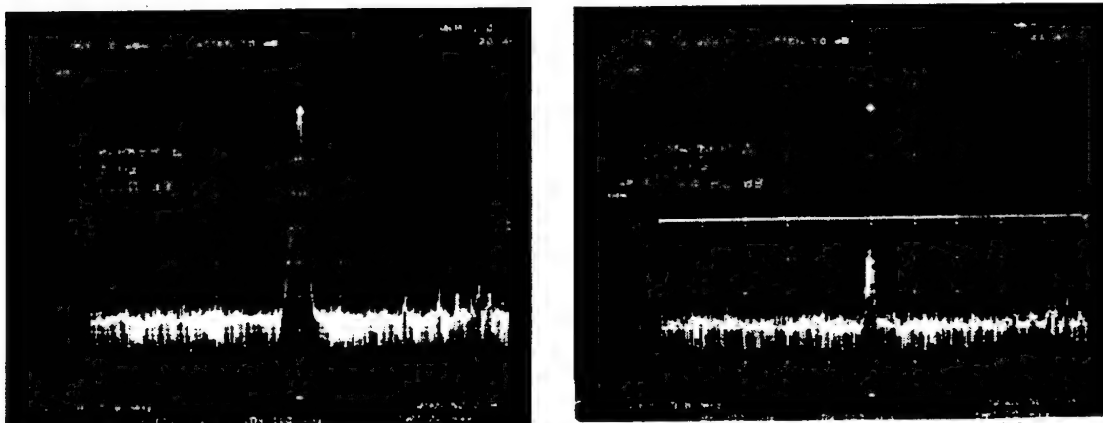
Figure 7.27. Photos of spectrum analyzer display showing single narrowband jammer of 75.8 MHz (at screen center) before suppression at left, and steady-state suppression by 45 dB at right.

Chapter 5, has allowed a significant increase of the feedback gain, and corresponding increased suppression depth and decreased response time.

7.6.3 Multiple Jammer Results

7.6.3.1 Two Jammers of Equal Strength

Experiments were conducted for two equal amplitude plane wave jammers of different temporal frequencies and AOAs. The emphasis of the experiments of this section was on investigating the relationships between jammers for different scenarios, and not on maximizing suppression depth or convergence time. Figure 7.28a shows the two jammers, at 75.45 MHz and 76.7 MHz, before suppression. Figure 7.28b shows the two jammers after suppression, each suppressed by the same amount (approximately 14dB), in agreement with equations 7.50 and 7.51. The decay time constants can be estimated from figures 7.28c and 7.28d, which show the decay of the jammer strengths on a log-linear scale. From this data the time constants are estimated to be .17 $\sec^{-1}$ and .15 $\sec^{-1}$ for jammers 1 and 2 respectively. When one of the jammers is turned off, an increase of 6 dB in suppression is expected for the remaining jammer, in accordance with the factor of two difference between equations 7.50 and
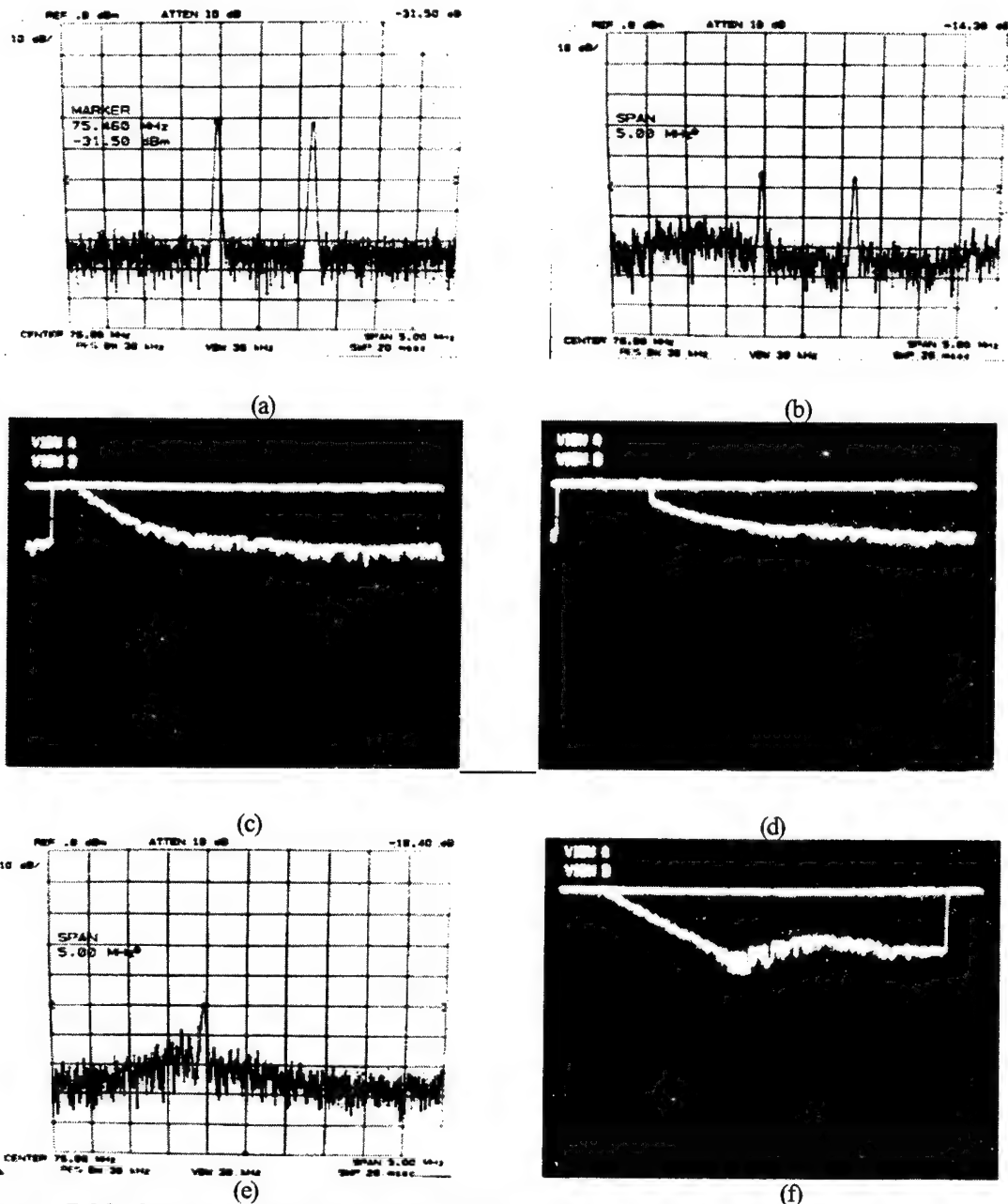
Figure 7.28. Spectrum analyzer trace of two equal strength narrowband jammers at 75.5 and 76.7 MHz: (a) before suppression, and (b) suppressed by 14.3 dB, (.5 MHz/div, 10dB/div). Figures (c) and (d) show the suppression time dynamics (decay rate) of 75.5 and 76.7 MHz jammers respectively (.2 sec/div, 10 dB/div). A single 75.5 MHz jammer is shown in (e) with increased suppression of 4 dB after turning off second jammer, while suppression rate is unaffected as shown in (f). Figures (c), (d), and (f) were obtained by using the spectrum analyzer in zero-span mode.

7.42. However, the time constant should remain the same due to the fact that it depends only on individual jammer strength as shown in equation 7.38. Figure 7.28e shows the
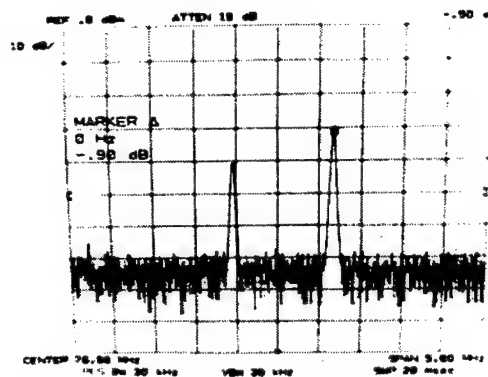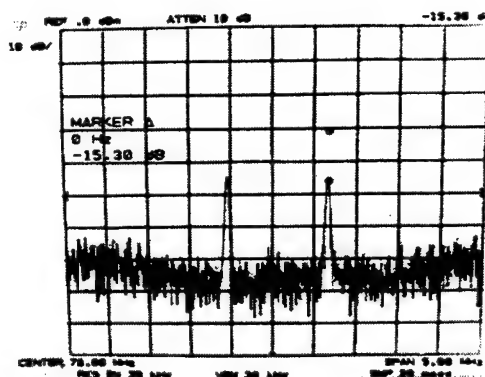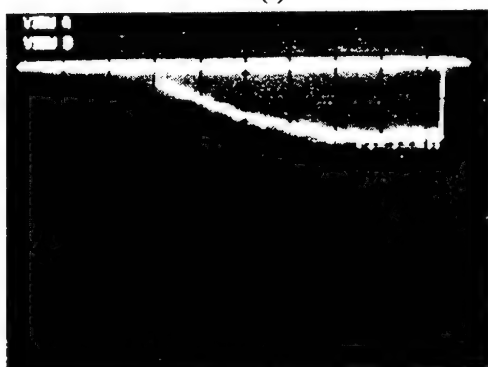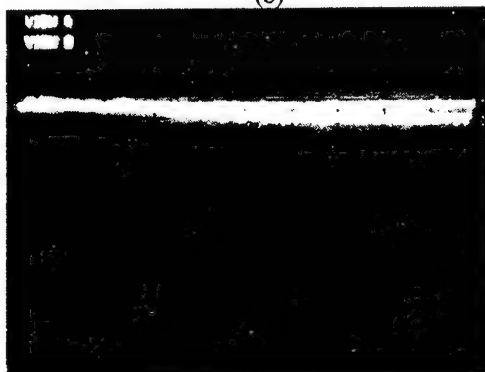
Figure 7.29. (a)two jammers differing by 10 dB before suppression, and (b) asymmetric suppression (.5 MHz/div, 10dB/div). Figures (c) and (d) demonstrate power dependent suppression dynamics for the two jammers; in (c) strong jammer, and (d) weaker jammer (.2 sec/div, 10 dB/div).

single jammer at 75.45 MHz, now being suppressed by an additional 4dB, while figure 7.28f still yields a decay time constant of .15 sec^{-1}. Both of these results are in good agreement with the theoretical predictions.

7.6.3.2 Two Jammers; one Strong, one Weak

The next case to consider is when one jammer is much stronger than the other. Figure 7.29a shows two jammers at 75.45 MHz and 76.7 MHz before suppression, but with jammer 1 now 10 dB less than jammer 2. Figure 7.29b shows the two jammers being suppressed; the stronger jammer suppressed by 15 dB and the weaker by only 5 dB. This asymmetric suppression is in excellent agreement with the scenario described above for one strong and one weak jammer (equations 7.54 - 7.57). It is

237
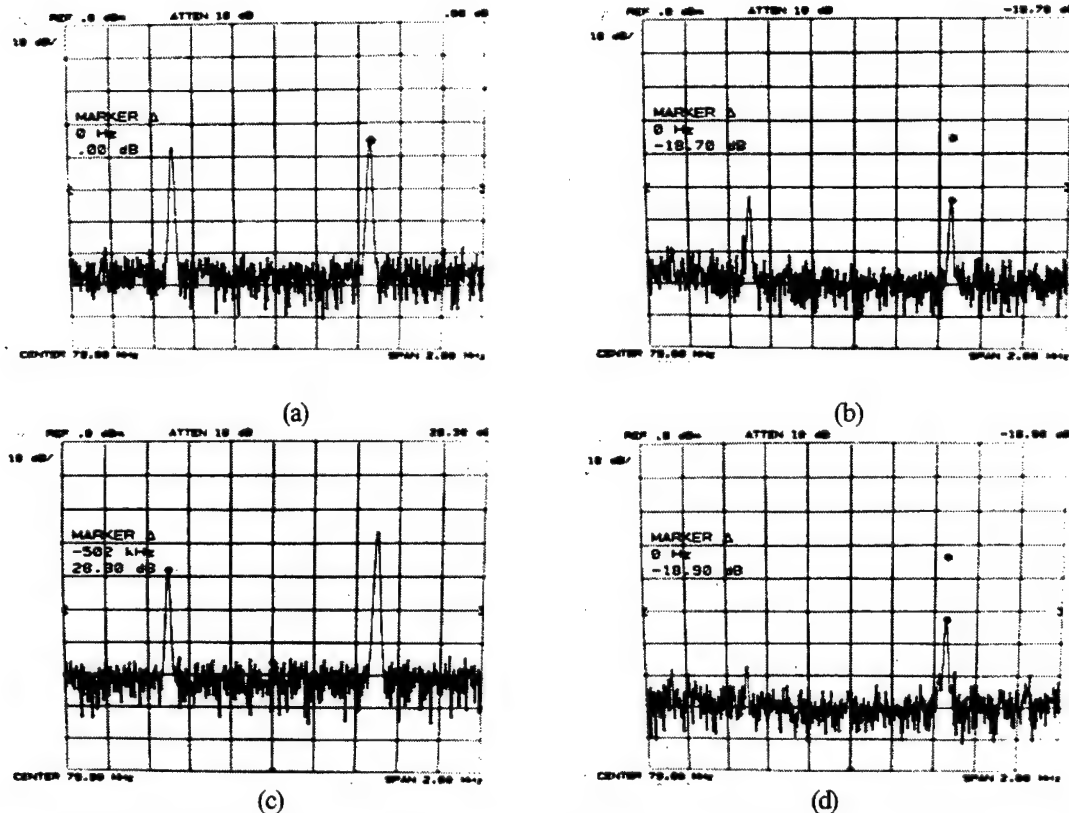
Figure 7.30. Two equal strength jammers with the same AOA (a) before suppression, (b) suppressed by 18.7 dB (.5 MHz/div, 10dB/div). (c) the same two jammers as in (a), with one reduced in power by 10 dB, (d) suppression of both jammers 18.9 dB.

expected that the suppression level of the stronger jammer is essentially unchanged, while the weaker jammer suppression level is reduced by the ratio of its power to the total interference power, in this case approximately 10 dB. The suppression time constant behavior for this scenario can be estimated from figures 7.29c and 7.29d. Figure 7.29c yields a suppression time constant of 0.67 $\sec^{-1}$ for the weaker jammer and 7.29d yields 0.23 $\sec^{-1}$ for the stronger. These results agree only moderately well with the expected results; equations 7.54 and 7.56 predict a ratio of 10 between the two time constants for this case, but the time constant is difficult to estimate for figure 7.29d.

7.6.3.3 Two Jammers with the Same Angle-of-Arrival

Finally, the special case of two plane wave jammers of different temporal frequencies sharing the same AOA is investigated. Equation 7.58 predicts the same amount of suppression for both jammers, regardless of their relative amplitudes. This prediction is confirmed experimentally as shown in figure 7.30. Figures 7.30a and 7.30b show two equal strength jammers at the same AOA before and after suppression by -18.7 dB. Figure 7.30c shows the jammers before feedback, with one jammer 10 dB lower in power than the other. After turning the feedback on, both jammers are equally suppressed, again by more than -18 dB. This is in marked contrast to the previous two jammer cases at different AOAs examined earlier.

7.6.4 Processor Characterization

7.6.4.1 Jammer Suppression versus Feedback Gain

The dynamical analysis of Section 7.3 (equation 7.45) predicts a linear increase in jammer suppression with increasing feedback gain parameters g_1 and g_2. This linear relationship will hold only below a certain gain value, because eventually the response of some component in the feedback loop will saturate. A straightforward experiment was performed to investigate the linearity of the jammer-nulling processor of figures 7.19 and 7.20. In particular, the set-up shown in figure 7.31 was used to measure the linearity of the output power versus the open-loop gain of the processor, and the linearity of jammer suppression versus feedback gain. As shown in the figure, output power versus open-loop gain parameter data was acquired by varying the attenuation of the RF power applied to the feedback Bragg cell (varying g_2) and measuring the output power at the difference node. Jammer suppression data was acquired by performing the same procedure with the switch closed as shown in the figure.
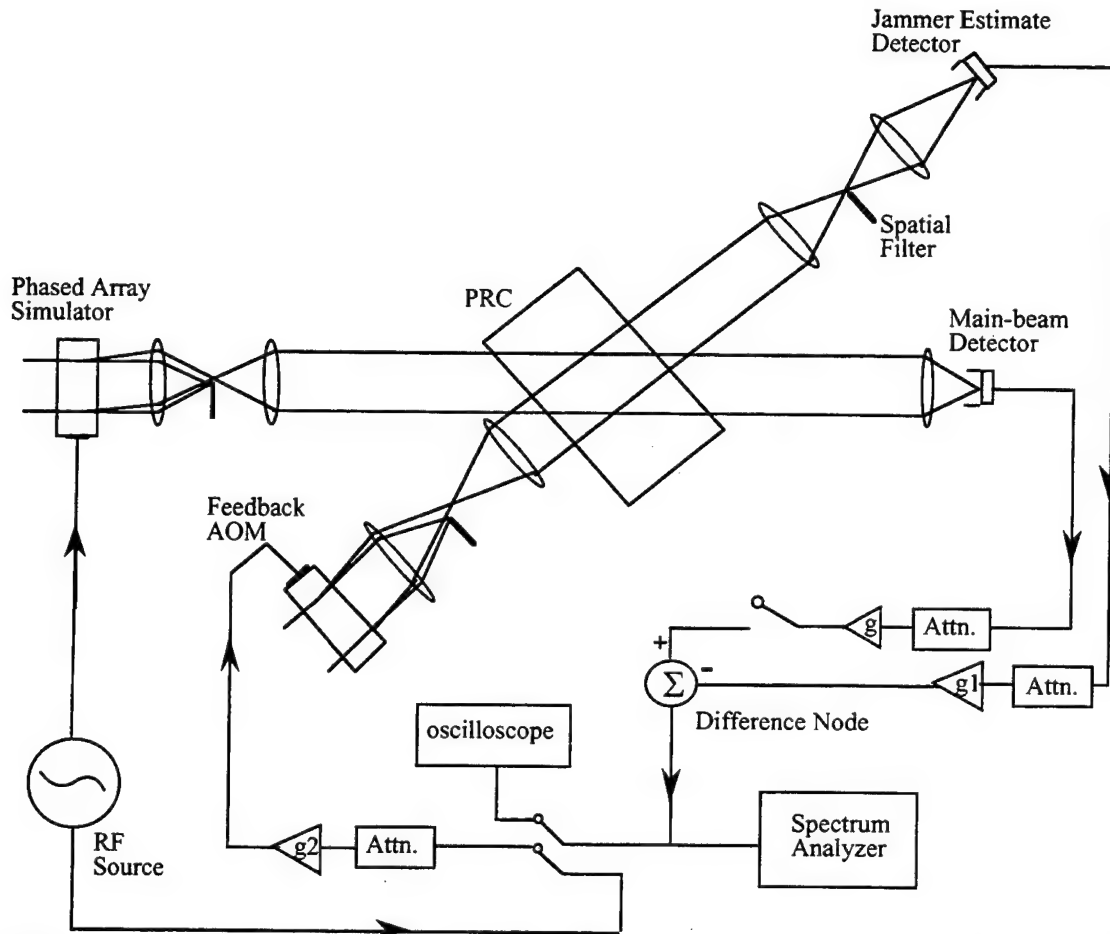
Figure 7.31. Schematic of experimental set-up for measurement of open-loop gain (measured at oscilloscope) in adaptive phased-array processor. For jammer suppression versus feedback gain measurements, the switches are closed to complete feedback loop.

The output power versus open-loop gain data is plotted in figure 7.32(a). The large upper and lower bounds evident in the measurements indicate that some instability was present in the system at the time of measurement. Nevertheless, the data obtained exhibits a definite rolloff in output power, indicating that saturation of one or more system components is occurring. The jammer suppression versus gain data in figure 7.32(b), exhibits a similar rolloff near the same gain region. Additional gain would likely send the processor into oscillation. At the time this data was taken the Bragg degeneracy multiplexing technique was being used, therefore it is likely that significant optical feedthrough was present. Evaluation of these data sets demonstrates the

240
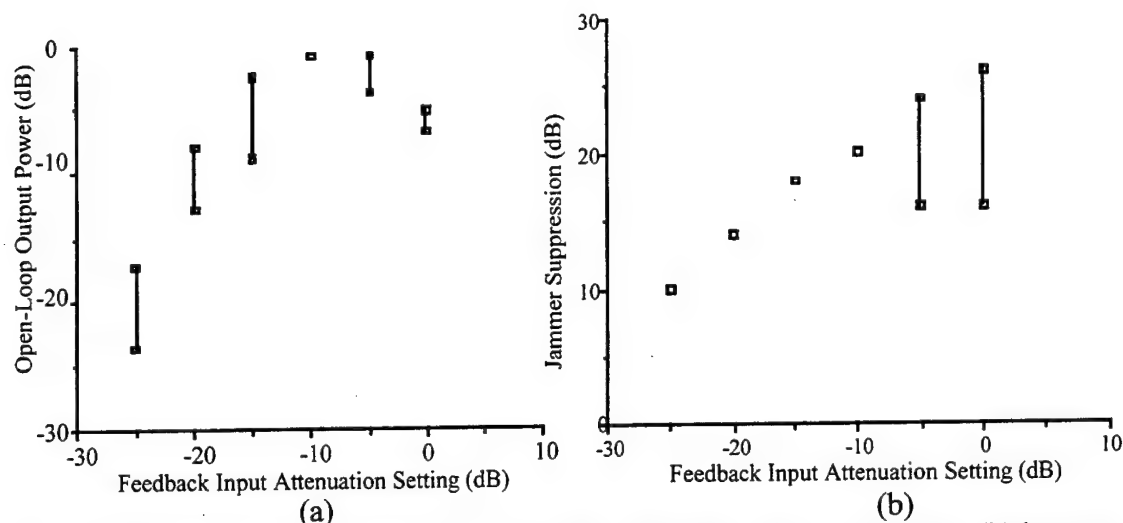
Figure 7.32. (a) Open-loop output power versus feedback input attenuation, (b) jammer suppression verses feedback attenuation setting (varying gain parameter g_2).

encouraging conclusion that if the upper bound of operable open loop gain can be extended, increased jammer suppression follows.

7.6.4.2 Periodic Jammer Nulling Bandwidth

Equation 7.44 predicts that the jammer suppression level is dependent upon the phase difference $\sigma_a(\omega_c - \omega_j)$ around the feedback loop. This was derived in Section 7.2, and shown in figure 7.6. Experimental results which demonstrate the periodic nulling behavior of the processor were obtained by sweeping a single narrowband jammer over a several MHz bandwidth and using the max-hold display feature of the spectrum analyzer. Figure 7.33 is a photo of a spectrum analyzer trace of an experimental result showing periodic jammer suppression behavior over a 10MHz bandwidth. Approximately 25 dB nulls are observed over a 3 MHz bandwidth, suggesting a feedback delay of approximately 160 nanoseconds, which is primarily limited by the transducer delay in the Bragg cell. The transducer delay is related to the fact that one can position the beam which illuminates the Bragg cell only so close to the actual transducer. As a result, there is small amount of non-illuminated AO material which the acoustic column must propagate through before interacting with the optical beam. The

241
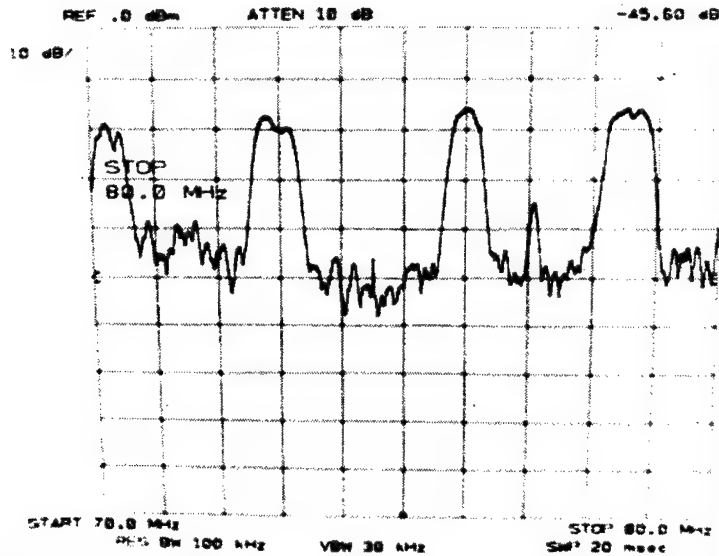
Figure 7.33. Spectrum analyzer trace showing experimental result demonstrating periodic nulling behavior over 10 MHz wide frequency sweep.

time it takes the acoustics to propagate through this non-illuminated region is what is referred to as transducer delay. This result agrees well with the results shown in figure 7.6, which shows periodic jammer nulling bandwidth as calculated from equation 7.32. Note that outside the regions of nulling, the system oscillates with moderate gain (the signal portion above -20 dBm) in agreement with the numerical simulations. The asymmetric relationship between the widths of the nulling and non-nulling regions in the experimental results is not fully understood, but suggests the presence of an additional nonlinear phenomena in the experimental results.

7.7 Combined Beam-Forming and Jammer-Nulling Processor

The final experimental objective of this thesis is to combine the jammer-nulling processor described in this chapter with the main-beam forming processor described in Chapter 6 into a single processor. This combined processor which performs simultaneous main-beam formation and jammer suppression is shown schematically in figure 7.34. This processor is the superposition of the two previously described processors, each with its own PRC, in which the output of the beam-forming processor
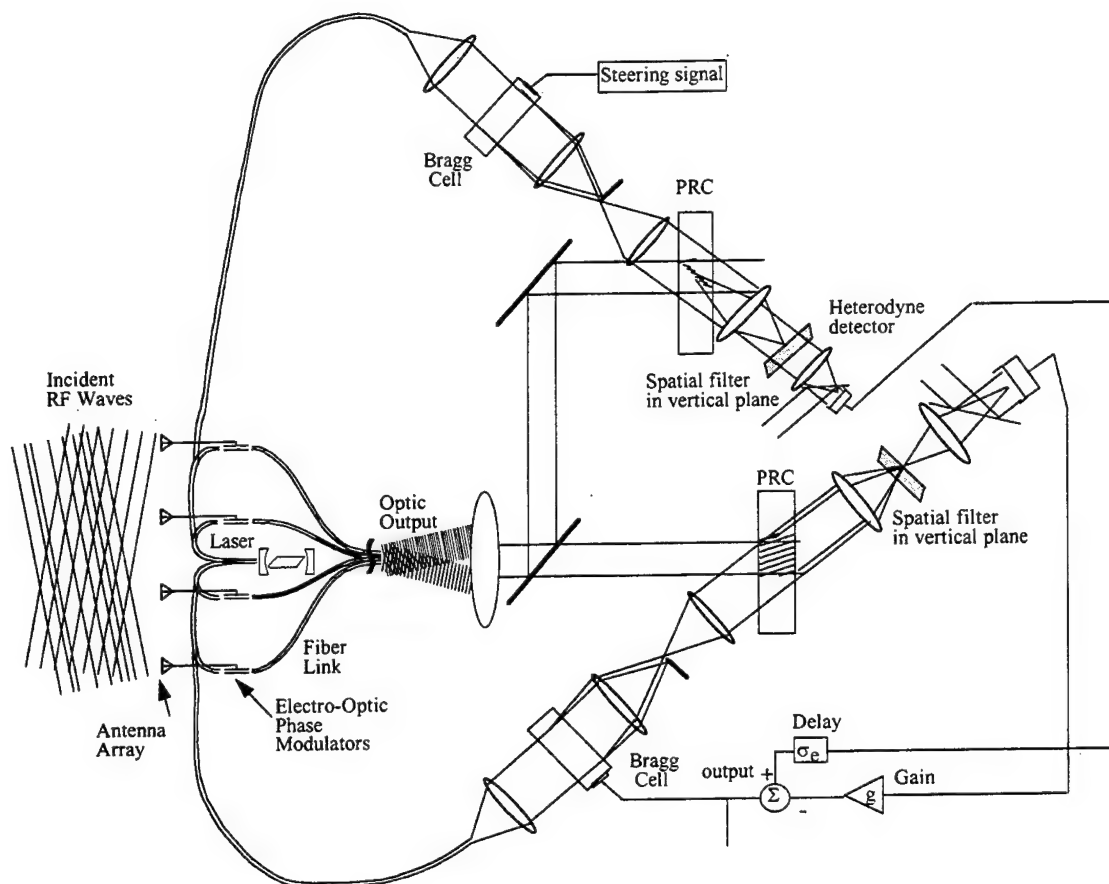
Figure 7.34. Schematic representation of beam-forming jammer-nulling phased-array radar processor.

is used as the main-beam input into the jammer-nulling processor. The optical layout of

the combined processor as built in the lab is shown in figure 7.35. In addition to the

phased-array simulator and the two, interacting main-beam and jammer-nulling

processors, there is an active stabilization system included in the processor. The system

relies on interferometric detection at several places in the processor, in particular at both

PRCs and at both photodetectors. Phase shifts due to mechanical path length variation

and thermal effects are compensated for automatically at three of the aforementioned

locations by adaptively shifting the photorefractive grating; this adaptivity corresponds

to the processor responding to a changing radar signal environment. Referring to figure

7.35, the only phase critical path relationship is between the diffracted component of

the jammer-nulling PRC and the reference beam. This diffracted signal becomes the
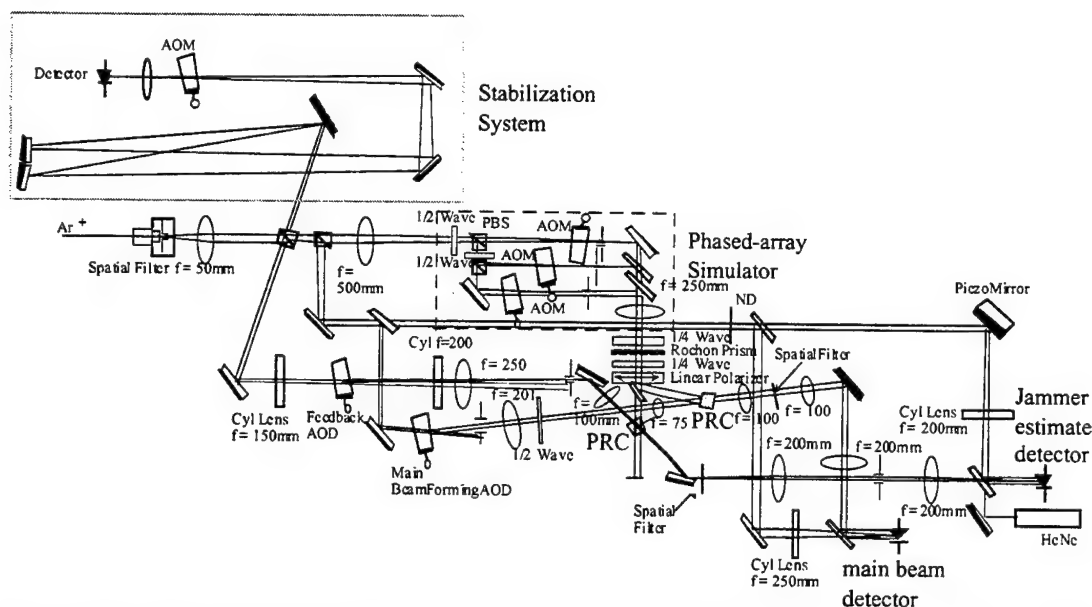
Figure 7.35. Optical component layout of combined main-beam and jammer -nulling phased-array radar processor

negative input to the difference node, thus its phase with respect to the main beam (the positive input at the difference node) must be preserved. The active stabilization system in the processor preserves this phase relationship by using the auxiliary HeNe laser to monitor path length differences between the reference and jammer-nulling feedback paths of the processor, as described in Section 7.6.1.

Experimental results demonstrating simultaneous beam formation and jammer suppression[9] are shown in figure 7.36. Figure 7.36a shows the frequency spectrum of the output of the processor, which has formed a main beam in the direction of the desired broadband signal, with a strong narrowband jammer simultaneously incident on the first antenna sidelobe as shown in figure 7.36b. After closing the feedback loop, the jammer is suppressed by an additional 20 dB from the 13 dB suppression which occurs due to its arrival on the first antenna sidelobe, giving a total jammer suppression of 33 dB. The final adapted beam pattern for the above scenario is depicted schematically in figure 7.37, which shows the main antenna lobe in the direction of the desired signal, a jammer nulling beam pointed towards the jammer and adaptively weighted to the

244

(a)   (b)
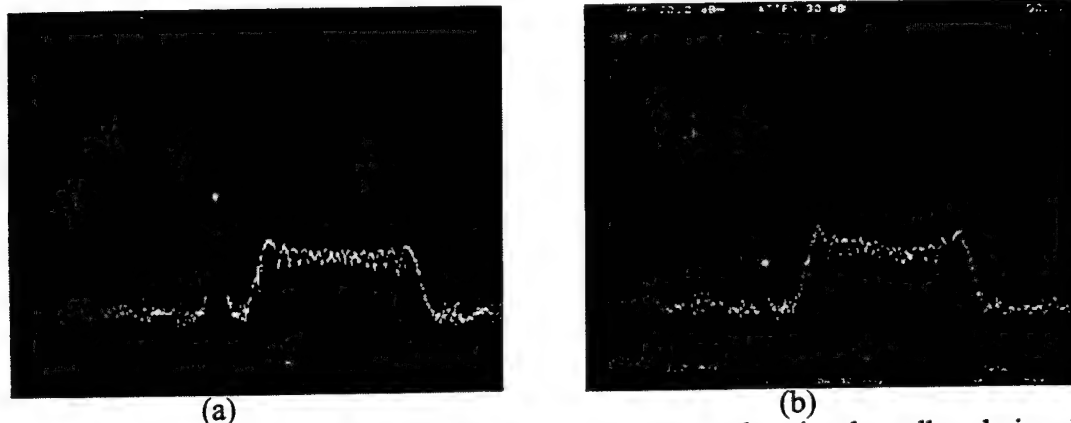
Figure 7.36. Frequency spectrum of processor output showing broadband signal of interest and strong jammer on antenna sidelobe before implementing jammer nulling feedback in (a), after suppression in (b) demonstrating additional 20 dB of suppression (1 MHz/div, 10 dB/div).

corresponding main-beam sidelobe, and the difference beam pattern showing an antenna null rotated to correspond to the AOA of the incident jammer. In the presence of multiple jammers (as discussed in Section 7.2.1), a similar jammer estimate beam will be pointed towards each arriving jammer and adaptively weighted to the correct amplitude to produce a deep null towards each jammer.

The jammer signal was chosen to be out of the frequency band of the desired signal simply to allow the jammer suppression behavior to be observed. If it were the case that the jammers were always out of the desired signal frequency band, the entire jammer-nulling processor could be replaced by a frequency filter. Jammers which fall within the desired signal bandwidth are also nulled, but more difficult to observe on a spectrum analyzer. As indicated in figure 7.36b, the main-beam signal is slightly corrupted when jammer-nulling occurs. It is likely that because there is no Fabry-Perot etalon installed in the jammer-nulling processor, there was a small amount of desired signal diffracted of the jammer grating which was detected and consequently there was a small amount of desired signal suppression.

The simultaneous main-beam and jammer-nulling results presented in this Chapter demonstrate the ability of this adaptive processor to successfully perform in a
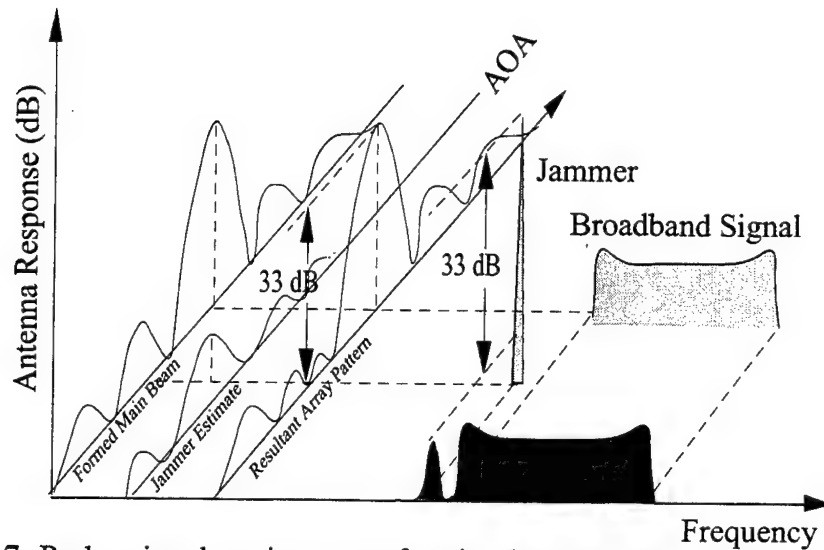
Figure 7.37. Radar signal environment for simultaneous main-beam formation and jammer-nulling experiment.

complex, multi-dimensional signal environment. Furthermore, these are the first known examples of optically processed phased-array radar experimental results demonstrating simultaneous main-beam and jammer-cancellation.

7.8 Chapter Summary

Many significant aspects of the Jammer-nulling processor have been discussed in this Chapter, as well as experimental results of the combined jammer-nulling and beam-forming processor, and it is useful to summarize these results here. Section 7.1 described the basic theory of operation of the jammer-nulling processor. The dynamical analysis of the jammer-nulling processor were then derived for the general case of multiple jammers with multiple spatial modes in section 7.2, and then simplified to several cases involving 1 and 2 planewave jammers in section 7.3. These same planewave jammer scenarios, including just a single jammer, two jammers of the same powers and different powers, and jammers at the same and different AOAs, were experimentally verified in section 7.6. The highest steady-state suppression achieved was 45 dB, for a single planewave jammer. Section 7.4, the comparison of the jammer-

nulling processor to the simple narrowband LMS loop, is intended to provide some insight to the processor operation in the context of the large existing body of work pertaining to the Widrow-Hopf LMS algorithm. It allows a direct comparison of the processor parameters to the feedback gain parameter defined in the standard literature. Section 7.5 consisted of an extended derivation of the jammer-nulling processor dynamics, which included a desired signal, optical and electrical noise, optical leakage in the feedback loop, both from scattering and multiple diffractions, and the photorefractive erasure penalty resulting form the holographic read/write techniques. By examining both the jammer excision and the processor SINR, appropriate with the addition of a desired signal, it was found that maximizing the feedback gain parameter $g_2 C$ is the most direct method to optimizing both jammer suppression and SINR. Simulations of the derived excision and SINR equations under various limiting assumptions help to identify desirable experimental operating conditions. Finally, the combined jammer-nulling and beam-forming experimental results presented in section 7.6 are the first known reported results of adaptive, simultaneous beam forming and jammer cancellation, and demonstrate the ability of this adaptive processor to successfully perform in a complex, multi-dimensional signal environment.

References

[1]   M. Born and E. Wolf, *Principles of Optics*, 6. (Pergamon, 1980), chap. 7.

[2]   A.W. Sarto, R.T. Weverka, and K. Wagner, "Photorefractive phased-array radar processor dynamics," in *Photonics for Processors, Neural Networks, and Memories,* Proc. Soc. Photo-Opt. Instrum. Eng. **2026**, July 310-324 (1993).

[3]   *Standard Mathematical Tables*. Chemical Rubber Publishing, 1957.

[4]   B. Widrow, J. McCool, and M. Ball, "The complex LMS algorithm," Proc. IEEE 719-720 April (1975).

[5]   E. Finizio and A. Ladas, *An Introduction to Differential Equations*. Wadsworth, 1982.

[6]   R.T. Weverka, "Personal Communication," 1995.

[7]   R.T. Weverka and K. Wagner, "Adaptive phased-array radar processing using photorefractive crystals," in *Optoelectronic Signal Processing for Phased-Array Antennas II,* B.M. Hendrickson and G.A. Koepf, ed. Proc. Soc. Photo-Opt. Instrum. Eng. **1217**, 173-182 (1990).

[8]   R.T. Weverka, K. Wagner, and A.W. Sarto, "Adaptive phased-array radar processing using photorefractive crystals," Appl. Opt. **35**, no. 8, 1344-1366 March (1995).

[9]   A.W. Sarto, R.T. Weverka, and K. Wagner, "Beam-steering and jammer-nulling photorefractive phased-array radar processor," in *Optoelectronic Signal Processing for Phased-Array Antennas IV,* Proc. Soc. Photo-Opt. Instrum. Eng. **2155**, 378-388 (1994).

8. Resonator Structures for Signal Processing

Fabry-Perot etalons are well known for their applications in high-resolution optical spectrum analysis, and have also been implemented as frequency channelizers for electronic signal processing. Such a channelization approach can result in a very compact, real-time method of channelization for large bandwidth signals. In addition the output of these channelizers are optical, and therefore can be used for further processing in the optical domain. The tilted and wedged Fabry-Perot etalons discussed in Section 1 of this Chapter also play an important role in the implementation of the true-time-delay versions of the adaptive phased-array processor, as discussed in Chapter 2. A similar structure to the Fabry-Perot etalon is the Herriott cell, a multiple pass optical resonator which functions as a discretely sampled optical delay-line by allowing each round-trip pass within the cavity to be individually sampled. This type of resonator structure provides another method of achieving true-time-delay in the phased-array processor. Section 2 of this chapter briefly presents Herriott cell theory and some simple, yet instructive simulations, followed by experimental results obtained from a demonstration Herriott cell.

8.1 Etalon Frequency Channelizers for Phased-Array Processing

8.1.1 Background and Implementation

The tilted and wedged Fabry-Perot etalons are methods of implementing the linear array of bandpass filters with linearly increasing center frequency required for the fully independent spatio-temporal optical implementation of the Widrow algorithm[1] as shown in Chapter 2. In this context, because of the intrinsic delay induced by the etalons, these etalons may be interpreted as providing the multiple time-delayed taps required for broadband processing. However, the most straightforward manner in which to view their processing role is as RF channelizers. Fabry-Perot etalons have been proposed[2,3] as a method of RF channelization because of their ability to

implement highly resolved multiple RF channels in parallel in a physically compact manner. Analogous systems done at RF frequencies would require an extensive amount of bulky and often expensive RF hardware. When the processing is done at optical frequencies, even bandwidths of many GHz are still only a small fraction of the optical carrier frequency. The two approaches discussed in this chapter are the tilted etalon which performs channelization by having a different bandpass frequency versus incident angle, and the wedged etalon which has a position dependent bandpass frequency along the aperture of the etalon.

The three key elements for optical channelization are a method of modulating the optical signal with the RF spectrum to be investigated, a method for dispersing the modulated spectrum into resolvable channels, and a method of detecting the amount of signal in each channel. For the work discussed in this thesis, an acousto-optic Bragg cell has been chosen as the means of modulating the optical carrier, because the same Bragg cell implements the continuous tap-in delay line in the adaptive phased-array processor. The Bragg cell also provides a frequency dependent diffraction angle with frequency, which is utilized in the application of both the tilted and wedged Fabry-Perot etalons. An alternative modulation source is an electro-optic (EO) modulator where some frequency/angle dependency must be introduced. For example, in [3], an EO modulator was used to modulate the optical carrier, the modulated beam was focused into a plane-parallel etalon, and detection of each channel was done with a linear array of detectors. In [2], an EO modulator was again used for modulation, and a collimated output beam was input into a wedged etalon with a movable frequency channel mask and a small area detector. In contrast, for the true-time delay applications discussed in this thesis, the output of the tilted and wedged etalons in the phased-array processor are spatially integrated onto a single photodetector, and the sum of the individual channelized frequencies are then used in the calculation of the adaptive weights.

One implementation of a tilted etalon as a spatially dependent frequency filter in the jammer-nulling processor is shown in figure 8.1. While the details of the jammer-nulling processor have been discussed in Chapter 6, the significant function of the etalon in the jammer-nulling implementation is to eliminate any broadband desired signal components from contributing to the jammer estimate signal, which would result in the nulling of the desired signal as well. The jammer-nulling processor steers an antenna function in the direction of a jammer by building up a corresponding grating Bragg matched to the AOA of the jammer and the frequency dependent angle from the feedback Bragg cell. If the desired signal is at or near the same AOA as the jammer, or at an angle corresponding to an antenna sidelobe, errant diffraction of the desired signal off of the holographic grating could occur, causing some desired signal to be present in the jammer estimate signal. As shown in figure 8.1, the Bragg cell is imaged onto the PRC, and then re-imaged onto the tilted etalon which is tilted so as to have the same frequency versus angle as that of the Bragg cell. The left beam stop in the figure blocks the DC component from the Bragg cell, and the beam stop at the right (which is actually in the vertical dimension as explained in Chapter 5) blocks the directly transmitted portion of the diffracted grating writing beam from the Bragg cell. The combination of the frequency dependent diffraction angle from the Bragg cell and the angular dependent pass-band characteristic of the tilted etalon defines a unique frequency-angle passband relationship for signals diffracting off of the holographic grating. Functionally, any signal which has diffracted off of the holographic grating but is not of the same frequency which wrote the grating will not pass through the etalon and will therefore not contribute to the jammer estimate signal. The wedged etalon would be implemented in a similar fashion, where instead a Fourier plane of the Bragg cell would be imaged through the PRC and onto the etalon, where the frequency versus position relationship of the Bragg cell and that of the etalon would be matched.

251
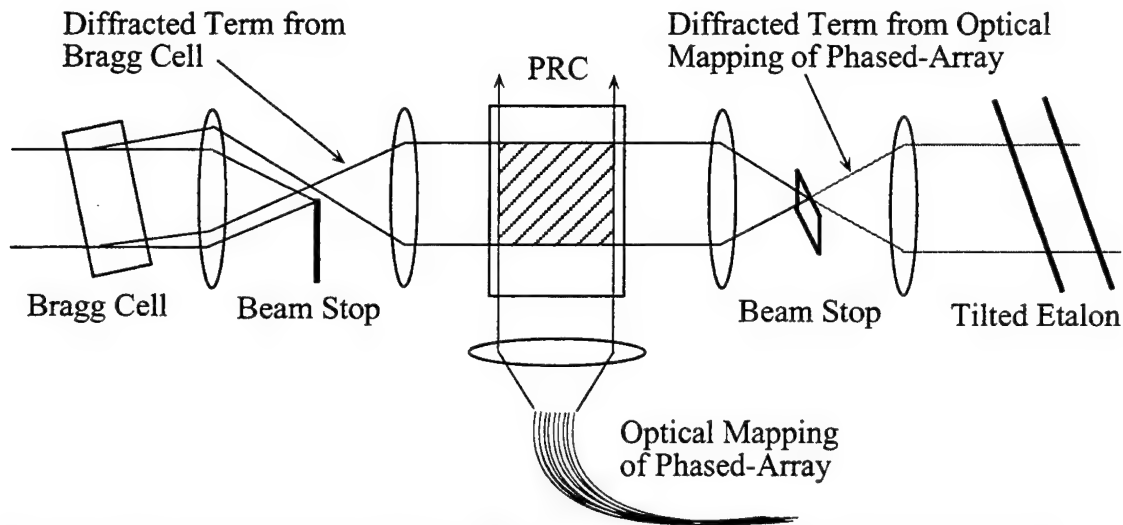
Figure 8.1. Schematic diagram of a tilted etalon performing as an angularly selective frequency filter in the jammer-nulling processor

In the beam-forming subsystem of the processor, the etalons are implemented in essentially the same manner as for the jammer-nulling processor. The significant difference in the beam-forming case is that the holographic grating is Bragg matched to the desired signal of interest, and the jammer signals constitute the errant diffractions. At first glance it may seem that because of the etalon filter the jammers are extinguished, and that the jammer-nulling portion of the processor is not necessary. However, the jammers are in general much stronger than the desired signal, and therefore the formed main-beam signal can still be significantly corrupted.

8.1.2. Tilted Fabry-Perot Etalon

In this Section, a set of four equations which couple the frequency dispersion function of the Bragg cell and a tilted etalon will be used to obtain an analytical relationship between the etalon tilt angle, etalon dimensions, and magnification of the imaging system for a given system bandwidth and number of resolvable channels. The same set of equations are used to numerically determine a 3dB ripple solution for the RF bandwith for a given Bragg cell and tilted etalon combination.

The plane parallel Fabry-Perot etalon tilted by angle θ_{bias} away from normal incidence has an angularly dependent passband frequency characteristic. Recalling that an untilted plane parallel, lossless etalon of cavity spacing d will have a transmitted intensity component I_t given by the Airy formula[4]

$$I_t = \frac{I_i}{1 + \frac{4R\sin^2(\delta/2)}{(1-R)^2}}$$

8.1

where I_i is the incident intensity, R is the reflectivity of the cavity mirrors, and

$$\delta = \frac{4\pi nd\cos(\theta)}{\lambda} = 2m\pi \qquad m \text{ an integer}.$$

8.2

In equation 8.2, n is the refractive index in the cavity, and λ is the optical wavelength. There will then be a maximum transmission of the etalon at frequency ν_m whenever

$$\nu_m = m\frac{c}{2nd\cos(\theta)}.$$

8.3

These resonances are separated in frequency by the free-spectral range *(FSR)* of the cavity, given by

$$FSR = \frac{c}{2nd\cos(\theta)}$$

8.4

and the cavity will have a frequency resolution of

$$2\Delta\nu_{1/2} = \frac{FSR}{F_R} = \frac{c}{2ndF_R\cos(\theta)}$$

8.5

where the reflectivity finesse, F_R, is defined as

$$F_R = \frac{\pi\sqrt{R}}{1-R}$$

8.6

and $\Delta\nu_{1/2}$ is the frequency half-width at the half-power point of the etalon transmission function.

253

By matching the frequency dispersion with incidence angle of the etalon given by equation (8.3) to the frequency dispersive property of the diffracted component of the Bragg cell, the required angle/frequency filtering operation will be achieved. The scan angle of the deflected beam from a Bragg cell, assuming isotropic acousto-optic interaction, due to an RF frequency f is given by

$$\theta_f = 2\sin^{-1}\left(\frac{f\lambda}{2V}\right)$$

8.7

where λ is the optical carrier frequency and V is the acoustic velocity of the Bragg cell. For an RF bandwidth of Δf, and assuming small angles, the total angular scan range $\Delta\theta$ can be approximated by[5]

$$\Delta\theta = \frac{\lambda}{V}\Delta f.$$

8.8

The etalon will be arranged such that its increasing frequency passband with angle will correspond to the increasing diffraction angle with frequency or the Bragg cell as given by equation 8.8.

Using equations (8.3) and (8.8), a set of four equations can be obtained in order to couple the frequency dispersion of the tilted etalon and the Bragg cell over the frequency range of interest. From equation (8.3), it is evident that the passband frequency of the etalon will vary inverse cosinusoidally with etalon tilt angle. This behavior is shown in figure 8.2, where the center curve is the passband frequency v_{cf} of the etalon plotted versus incident angle. The center frequency v_{cf} is the optical carrier frequency v_o plus the RF carrier frequency. The angular scan range of θ_{min} to θ_{max} corresponds to the RF bandwidth of Δf. The upper and lower curves each correspond to $\Delta v_{1/2}$ away from the passband frequency, useful for determining a 3dB ripple bandwidth of a given Bragg cell and etalon combination. From equation (8.3),

254
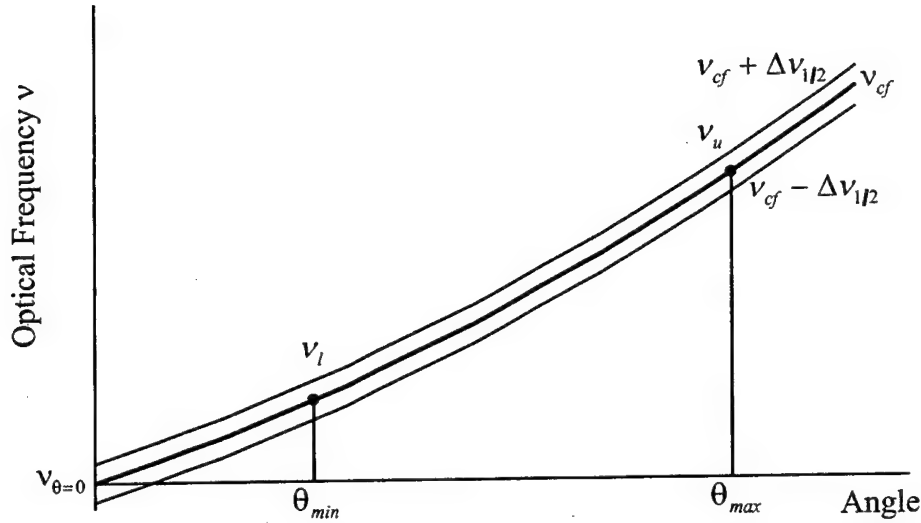
Figure 8.2. Transfer curve of cavity resonant frequency ν_{cf} versus angle θ for tilted Fabry-Perot etalon.

the two passband frequencies at the extremes of the RF bandwith Δf can be expressed as

$$\nu_l = \nu_{cf} - \Delta f/2 = \frac{\nu_{\theta=0}}{\cos(\theta_{min})} \qquad 8.9$$

and

$$\nu_u = \nu_{cf} + \Delta f/2 = \frac{\nu_{\theta=0}}{\cos(\theta_{max})} \qquad 8.10$$

where $\nu_{\theta=0}$ is the passband frequency of the etalon at an incident angle of zero degrees. The Bragg cell angular position at the extremes of the RF bandwith can be determined from equation (8.8) to be

$$\theta_{min}/2 - \theta_{bias} = \frac{c(\nu_{cf} - \Delta f/2 - \nu_o)}{2VM\nu_o} \qquad 8.11$$

and

$$\theta_{max}/2 - \theta_{bias} = \frac{c(\nu_{cf} + \Delta f/2 - \nu_o)}{2VM\nu_o} \qquad 8.12$$

where c is the free-space velocity of light, M is the image magnification of the Bragg cell onto the etalon, and θ_{bias} is the etalon tilt angle away from normal incidence. The angles are illustrated in figure 8.3, where the Bragg cell is shown directly imaged onto

255
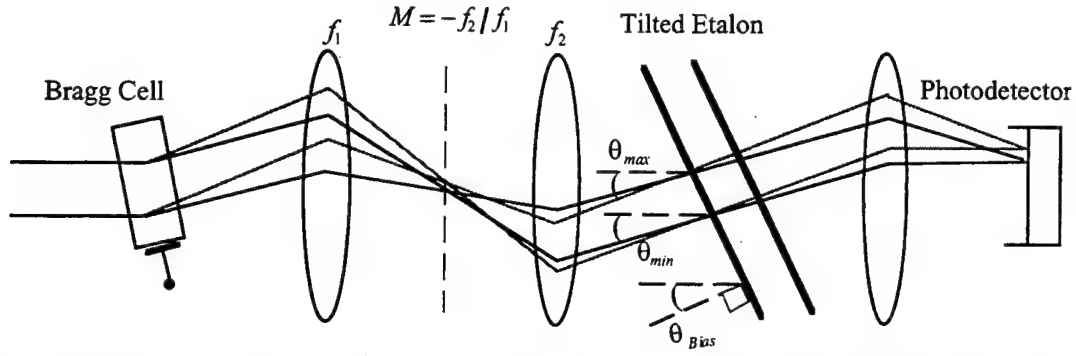
Figure 8.3. Bragg cell shown imaged with magnification M onto etalon tilted by θ_{Bias}. The two diffracted beams from the Bragg cell incident on the etalon at θ_{min} and θ_{max} correspond to optical frequencies $v_l = v_{RFcf} - \Delta f/2$ and $v_u = v_{RFcf} + \Delta f/2$ respectively.

the etalon for simplicity. Equations 8.9 - 8.12 can be used to relate the number of resolvable spots of the Bragg cell, N_{BC}, to the number of resolvable spots in the tilted etalon, N_{FP}. These two quantities are defined as

$$N_{BC} = \Delta f \tau_{BC} \qquad 8.13$$

$$N_{FP} = \frac{FSR}{2\Delta v_{1/2}} \qquad 8.14$$

where τ_{BC} is the time aperture of the Bragg cell. N_{BC} is thus equivalent to the time-bandwith product of the Bragg cell. Ideally the *FSR* of the etalon matches the desired RF bandwidth Δf, and $N_{BC} = N_{FP}$ so that the spectral resolution of the Bragg cell is not degraded by the etalon. The angles θ_{min} and θ_{max} in equations 8.9 and 8.10 are assumed to be small, allowing the approximation to be made of $\cos(\theta) \approx 1 - \theta^2/2$. Using this approximation and substituting the expressions 8.9 and 8.10 into the equations 8.11 8.12 and then taking the difference between the resulting expressions yields

$$\frac{2\Delta f}{v_{\theta=0}} = \theta_{max}^2 - \theta_{min}^2. \qquad 8.15$$

Squaring equations (8.11) and (8.12) yields expressions for θ_{min}^2 and θ_{max}^2 respectively, which after taking their difference and equating to equation (8.15) yields

$$\frac{2}{v_{\theta=0}} = \frac{3c^2 \Delta f}{\left(MVv_o\right)^2} + \frac{2c\theta_{bias}}{MVv_o} \qquad\qquad 8.16$$

where the substitution $v_{cf} - v_o = f_{RFcenter} = 1.5\Delta f$ for an octave bandwidth has been made. Note that the size of the Bragg cell image, W, (which can be taken to be approximately equal to the aperture size of the etalon) is given by $W = \tau_{BC}V|M|$. This relation allows equation (8.16) to be expressed as

$$\frac{N_{FP}}{N_{BC}} = \frac{v_o MV}{3c^2 v_{\theta=0}\Delta f}\left[\left(\frac{|M|}{M}\right)\left(\frac{Wv_o}{\tau_{BC}}\right) - v_{\theta=0}\theta_{bias}c\right]. \qquad\qquad 8.17$$

This result relates the Bragg cell and etalon parameters to the ratio of the number of resolvable spots in the Bragg cell and the etalon. For small tilt angles, $v_{\theta=0} \approx v_o$, and equation 8.17 can be simplified to

$$\frac{N_{FP}}{N_{BC}} \approx \frac{v_o MV}{3c^2 \Delta f}\left[\left(\frac{|M|}{M}\right)\left(\frac{W}{\tau_{BC}}\right) - \theta_{bias}c\right]. \qquad\qquad 8.18$$

As an example, first a specific operating bandwidth Δf is specified, along with a particular Bragg cell with an aperture time of τ_{BC} and an acoustic velocity of V. Imaging the Bragg cell with magnification M onto the etalon aperture W, from equation 8.18, the tilt angle θ_{bias} can be determined. Having determined θ_{bias}, θ_{min} and θ_{max} can then be determined from equations 8.11 and 8.12.

A numeric approach for determining a 3dB ripple solution for the etalon bandpass characteristic has also been implemented. The same set of four equations are simultaneously solved in order to determine θ_{bias}, θ_{min}, θ_{max}, and $v_{\theta=0}$, based on an initial desired magnification, laser and RF center frequencies, and RF bandwidth. An example calculation is plotted in figure 8.4, showing the 3dB ripple solution. This particular example required a magnification of -7.3, but has only a 10 MHz bandwidth on a 100 MHz center frequency ($\theta_{min} = -0.0878$ mrad, $\theta_{max} = -0.205$ mrad), and a
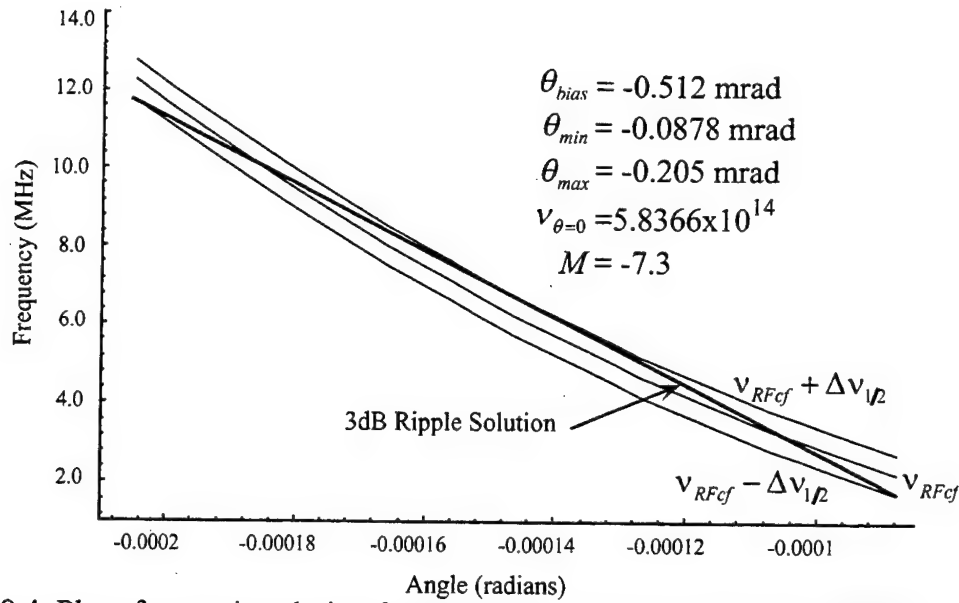
Figure 8.4. Plot of numeric solution for 3dB ripple solution exhibiting 10MHz bandwidth for Bragg cell and tilted etalon combination.

$1\,\mu$sec Bragg cell aperture time which yields only 10 resolvable spots. Increasing the RF bandwidth to 66 MHz in the above example (corresponding to octave bandwidth) results in a required magnification of $M = -48.3$. The magnification of -48 in this solution is a potential problem. A time aperture of 1 μsec and an acoustic velocity of $V = 6$mm/μsec implies a Bragg cell with a 6mm length, and a magnification of 48 yields an image size of 288mm which is very large. From equation (8.4), a *FSR* corresponding to the RF bandwidth of 66 MHz yields a cavity length d of approximately 2.3 meters. From the standpoint of general compactness, as well as maintaining flatness and thermal stability, the above dimensions represent an impractically large etalon.

The above two examples were chosen because all of the phased-array processing experiments presented in this thesis have been done in this frequency range, it is more sensible to consider this etalon channelization method for higher frequencies, such as in the GHz regime. As an example, for a 1 GHz bandwidth signal on a 5 GHz carrier frequency, using a Bragg cell with a time aperture of 100 nsecs, the

258

magnification is 213 (magnification scales with frequency as predicted by equation 8.18). The etalon aperture is now reduced to 135 mm, while the cavity length is 150 mm. These dimensions are more realistic in terms of etalon construction and stability.

The finite number of resolvable channels of the tilted etalon may in addition be further limited by optical beam walkoff within the etalon mirror cavity. The walkoff condition produces beams which do not completely overlap and results in broadened transmission peaks, which limits the finesse to less than that determined by the cavity alone. For plane waves incident on an etalon tilted by angle θ, an effective walkoff finesse can be defined as[3]

$$F_W = \frac{D}{2d\theta}$$

8.19

where D is the beam diameter and d is the cavity spacing. The walkoff finesse is essentially equal to the number of overlapping beams in the etalon. The etalon finesse will then be limited either by the walkoff finesse F_W, or the mirror finesse. The above equation for the walkoff finesse predicts better performance with decreasing cavity size d, further enforcing the advantage of processing at higher frequencies. The mirror finesse is fundamentally limited by mirror reflectivity (equation 8.6) or the mirror flatness, therefore it is reasonable to attempt a design where the walkoff finesse is greater than the mirror finesse.

8.1.3 Wedged Fabry-Perot Etalon

A brief analysis of the applicability of the wedged etalon as a frequency channelizer is presented. The analysis yields approximate dimensions for the etalon, including wedge angle, based on achieving the same frequency resolvability as the input Bragg cell. For bandwidths in the tens of MHz range, it is found that as with the tilted etalon, the cavity dimensions are quite large, and processing GHz bandwidth signals is more sensible.
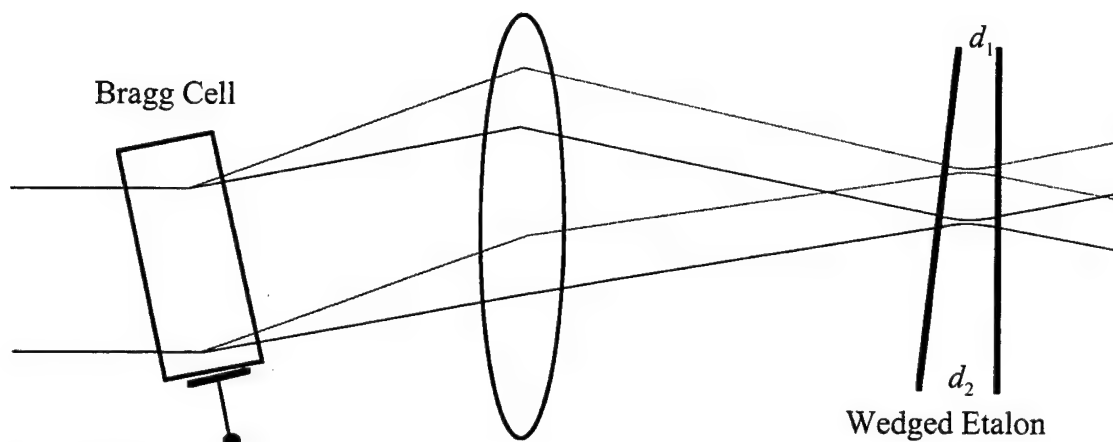
Figure 8.5. Wedged etalon with position dependent frequency bandpass function is placed in the Fourier plane of the Bragg cell.

The wedged Fabry-Perot etalon frequency channelization system for the adaptive phased-array processor functions as an acousto-optic spectrum analyzer followed by a spatially dependent frequency filter. The basic arrangement is shown in figure 8.5, where two frequencies from the Bragg cell are mapped into positions in the Fourier plane which correspond to the correct bandpass frequency position along the linear dimension of the etalon. In the adaptive phased-array system, the Bragg cell shown in figure 8.5 would be an imaged through the PRC, and then onto the etalon.

As with the tilted etalon, the wedged etalon suffers from beam-walkoff and resulting broadened transmission peaks. However, the situation is somewhat worse with the wedged etalon because the wedge angle causes each overlapping wavefront within the cavity to interfere at a slightly different angle and phase shift, which both broadens the transmission peaks and creates an asymmetric spatial impulse response. These two effects in general will reduce the resolution of the etalon to less than that predicted by the cavity finesse[6]. Some additional concerns arise which are specific to the proposed implementation shown in figure 8.5 due to multiple beams focusing down through the etalon. In order to confine the array of spots to a small aperture size, the individual spots should be small. However small spots result in large beam divergence

which is sure to effect the resolvability, and depending upon the cavity length and the wedge angle, a narrow beam may actually walk-off itself entirely after some finite number of bounces less than the number the cavity would normally support based on mirror reflectivity and flatness.

The Bragg cell will scan over a given distance x in the Fourier plane given by

$$x = \frac{F_l \lambda_o \Delta f}{V |M|}$$

8.20

where F_l is the lens focal length, λ_o is the mean optical wavelength, Δf is the RF bandwidth, V is the acoustic velocity of the Bragg cell, and M is the total magnification of the imaging system from the Bragg cell to the etalon. The distance x can be taken to be approximately the length of the etalon aperture. As shown in figure 8.5, d_1 and d_2 are the cavity spacings at either end of the etalon, and the wedge etalon angle will then be

$$\tan(\alpha) = \frac{d_2 - d_1}{x}.$$

8.21

The etalon wedge angle will be shown to be very small, and therefore equation 8.21 will be approximated by

$$\alpha \approx \frac{d_2 - d_1}{x}$$

8.22

Assuming a resonance condition, it follows that at any given position along the etalon aperture, the cavity spacing corresponds to an integral number of wavelengths, thus it follows that $d_2 / \lambda_2 = d_1 / \lambda_1$. Using this relationship between d_1 and d_2, and noting that $\lambda_1 = c/v_1 = c/(v_l + f_1)$ and $\lambda_2 = c/v_2 = c/(v_l + f_2)$, it follows that

$$d_1 = \frac{v_l + f_2}{v_l + f_1} d_2$$

8.23

261

where ν_l is the laser illumination frequency and the bandwidth $\Delta f = f_1 - f_2$.

Substituting equations 8.23 and 8.20 into equation 8.22 yields a wedge angle of

$$\alpha \approx \frac{d_2 V |M|}{F_l (c + \lambda_o f_1)} \approx \frac{dV |M|}{F_l (c + \lambda_o f_1)} \qquad 8.24$$

where d is a mean cavity thickness. For small etalon wedge angles, the *FSR* of the wedged etalon will be assumed to be the same as that for the plane parallel cavity as given in equation 8.4. For example, considering a *FSR* of 66MHz as in the tilted etalon example of the previous section with a magnification of 10, and a lens focal length of 500mm, a value of $\alpha = 0.9$ mrad is obtained from equation 8.24.

An estimate for the maximum allowable wedge angle can be obtained by examining both the wedge induced phase shift and walk-off. Figure 8.6 shows the *pth* bounce of the *ith* channel input, of beam width $W_{p,i}$ incident on a wedged etalon, and the resulting first several transmitted beams. As shown in the figure, subsequent bounces cause each beam to walk along the wedge length, as well as to emerge from the etalon at a slightly different angle on each bounce. The effects of each of these emerging beam properties will be investigated separately. Each of these effects will place a limit on the wedge angle for a given mean cavity spacing.

The increasing phase shift with each subsequent bounce is associated with the increasing emerging angle with each bounce and has been analyzed in [7]. At near normal incidence, neglecting absorption, the phase shift between the first transmitted beam and the *pth* interfering wave at position ρ along x is given by

$$\delta_p = \frac{4\pi}{\lambda} \rho \sin(p-1)\alpha \cos(p-1)\alpha \qquad 8.25$$

An expansion of equation (8.25) in powers of α for a finite number of interfering waves p yields a limit on the wedge angle such that the transmitted intensity does not differ significantly from the Airy formula given by equation (8.1). In particular, for
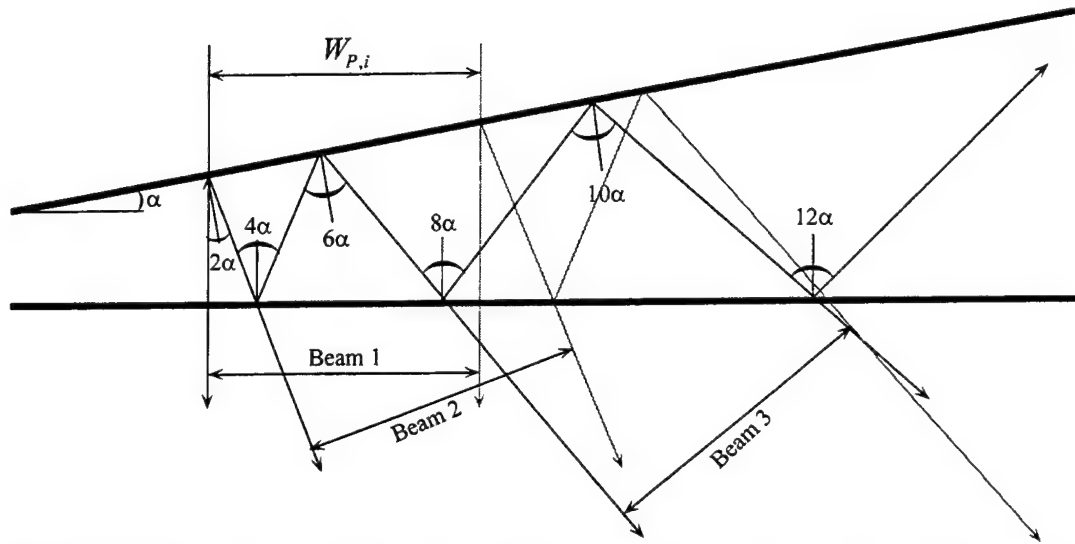
Figure 8.6. Incident beam of width $W_{P,i}$ undergoes lateral walk-off and increasing interference angle with each interfering beam inside a wedged resonator cavity.

$$\alpha^2 < \frac{3\lambda}{8P^3 d} \qquad \text{8.26}$$

the finesse will not be degraded from the plane parallel cavity case (a refractive index of 1 inside the resonator has been assumed).

The effects of lack of spatial overlap due to walk-off can be analyzed by noting that from figure 8.6, as each subsequent interfering beam accumulates an increase in angle with each bounce, the lateral translation increases as well, resulting in increased beam overlap. In particular, the spot $W_{P,i}$ will translate a distance $\delta l \approx d \cdot m$, where d is the mean cavity thickness and m is an integer number of the wedge angle α, and m is a function of the interfering beam number p. For example, from figure 8.6, the second beam $p = 2$ has acquired a total of 2α of angular deviation, beam $p = 3$ has acquired an additional 8α, and beam $p = 4$ has acquired an additional 14α beyond beam $p = 3$. The integer number m for the pth bounce can be expressed as

$$m = \alpha \sum_{p=2}^{P} (6p - 10) \qquad \text{8.27}$$

The total lateral shift of $\delta l \approx d \cdot m$ is used to estimate the spot size for the *ith* channel such that after a desired number of P interfering waves, the spot has just walked off itself, with no more spatial overlap. This spot size is chosen to be

$$W_{P,i} \geq d\alpha \sum\nolimits_{p=2}^{P}(6p-10) \qquad 8.28$$

The sum of the spot sizes $W_{P,i}$ yields an estimate for the value of the required etalon aperture x. The required number of channels should be set equal to the time-bandwidth product N_{BC} of the input Bragg cell, and therefore $x \approx N_{BC}W_{P,i}$, where it is assumed that all of the $W_{P,i}$ can be assumed equal in size. Substituting this expression for x into equation (8.20)yields

$$\alpha^2 < \frac{\Delta f}{\nu N_{BC} \sum\nolimits_{p=2}^{N_{BC}}(6p-10)}. \qquad 8.29$$

An instructive example calculation is the octave bandwidth example presented in the previous section for the tilted etalon. Assuming the RF bandwidth Δf is set equal to the etalon FSR set by the mean cavity spacing d, the 66MHz RF bandwidth again results in a cavity length d of 2.3 meters, which is somewhat large. The time-bandwidth product of $N_{BC} = 66$ leads to bounds of $\alpha \approx 5.4 \times 10^{-7}$ and $\alpha \approx 3.1 \times 10^{-7}$ radians from equations 8.26 and 8.29 respectively. Choosing the smaller of these two extremely small angles results in a spot size of 8mm, and a corresponding etalon aperture length of 0.528 meters. Again, the motivation for this method of channelization at these bandwidths is difficult to justify. Using the parameters from the second example of the previous section of $\Delta f = 1$ GHz and $N_{BC} = 100$, now with the tilted etalon, yields $\alpha \approx 1.1 \times 10^{-6}$ and $\alpha \approx 7.5 \times 10^{-7}$ radians from equations 8.26 and 8.29 respectively. As with the tilted plane-parallel etalon, processing at higher center frequencies and associated larger bandwidths is more promising, and demonstrates the advantages of choosing an optical approach to RF channelization.

8.2 Herriott Optical Time Delay Resonator

A Herriott time delay resonator is essentially a Fabry-Perot resonator where pencil-like beams are launched off-axis into the resonator resulting in a multiple pass cavity which produces multiple output spots, each delayed by the cavity round-trip time. Spherical resonator mirrors refocus the wavefronts so that diffraction spreading is minimized. Because of the multiple, delayed outputs, functionally the Herriott resonator is an optical delay-line, and has applications in optical signal processing. In particular, such a resonator could be used at the input of the phased-array processor to provide tapped, temporally delayed samples of the input signals. The output from each fiber (corresponding to an antenna element) would expanded into a set of discreet, temporal samples for input into the processor. A Herriott time-delay resonator has been built as a proof-of-principle instrument in order to investigate its basic operating characteristics, and to experiment with using the time-delayed outputs to write gratings in a PRC. In this section a brief theory of the Herriott resonator is presented, followed by experimental results.

8.2.1. Herriott Cell as a Transversal Filter

In the early 1960s, D. R. Herriott et al. proposed implementing transversal filters by using optical resonators as folded optical delay lines[8,9]. The concept is to illuminate a spherical or aspherical optical resonator with an off-axis ray of light, and the repeated reflections of the beams between the mirrors where one mirror is a partially reflective output coupler, provides a temporal sampling of the optical input. Each temporal sample is spaced in time by the resonator cavity round-trip time, and depending upon the resonator geometry and input signal launch parameters, each temporal sample can
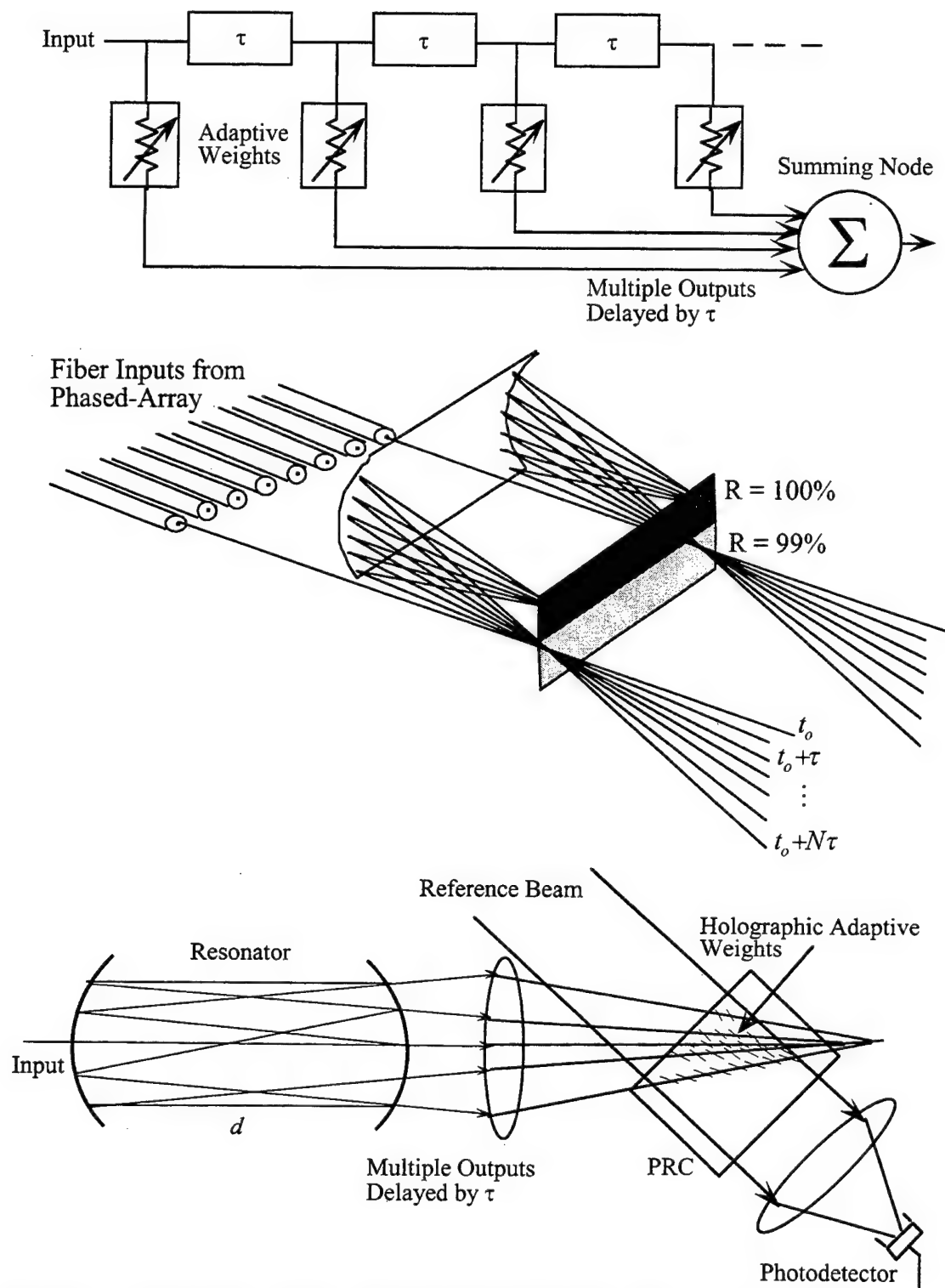
Figure 8.7. Transversal filters; electrically implemented version at top of figure, resonator structure for obtaining multiple tapped delays in figure center, and Herriot resonator architecture using adaptive holographic weights.

be separated in space and/or angle so as to be detectable in an output plane. The net result is a set of discretely spaced temporal samples of an optical signal corresponding to an all optical tapped-delay line or transversal filter. As was shown in Chapter 2, the tapped-delay line can be viewed as performing a discrete Fourier transform on an input signal, providing the multiple degrees of freedom required for processing of broad-band signals.

Figure 8.7 shows three methods for obtaining time-delayed outputs of a broad-band signal. At the top of the figure is the traditional, electrically implemented version discussed in Chapter 2. The summed output of the network is the sum of the discretely sampled outputs, each multiplied by an adaptive weight. Another possible approach is the resonator structure shown in the center of figure 8.7, where a portion of the output from each fiber is allowed to escape after each round trip through the cavity. The result is a 2-D mapping of the antenna array; temporal samples of each fiber output in the vertical dimension, and individual fibers spaced horizontally along the resonator aperture. However, as configured, this particular resonator structure would compensate poorly for diffraction losses. The Herriott resonator approach is shown in the lower portion of the figure. A single optical ray is shown as an input to the cavity, and after each round-trip a portion of the input signal exits. Because these cavities are generally implemented in a stable resonator configuration, diffraction losses are well compensated for. A single such resonator could support multiple fiber inputs simultaneously. As shown in the figure, adaptive weights are formed in the PRC, and multiply each of the sampled outputs of the resonator.

In contrast to typical Fabry-Perot resonator used for spectral analysis and channelization where all reflections are intended to overlap, for the time delay configuration it is desirable to have each bounce either spatially or angularly resolvable so that each delayed sample can be processed uniquely. A resonator with spherical mirrors can be used to generate circular, elliptical, or linear arrays of output samples.

267

Much larger numbers of resolvable output samples can be generated using astigmatic resonator mirrors, which generate Lissajous patterns in the output plane.

8.2.1.1 Herriott Resonator Bandwidth and Frequency Resolution

The design issues to consider are the operating bandwidth of the cell and the available frequency resolution (number of resolvable frequency samples). These are in turn related to the resonator geometry and the number of obtainable round trips, N. Each time sample is delayed by the round-trip time τ, where $\tau = 2d/c$, for a cavity length of d. Correspondingly the resonator will have a Nyquist sampled frequency bandwidth of

$$B \approx \frac{1}{2\tau} = \frac{c}{4d} \qquad\qquad 8.30$$

and a frequency resolution of

$$\Delta v \approx \frac{1}{2N\tau} \qquad\qquad 8.31$$

where N is the number of round-trip cavity trips. The value of N can be quite large, on the order of the finesse of the resonator. As given by equation 6.6 high reflectivity mirrors can have a finesse on the order of several hundred to a few thousand. In practice the finesse is usually limited by mirror flatness to on the order of a few hundred or less. This is particularly important for the typical Fabry-Perot interferometer application where all the reflected waves must add in phase. For example, a mirror flatness of $\lambda/200$ could produce an out of phase wavefront after only 100 bounces. In the time delay application of interest here, each bounce is intended to be spatially or angularly separable and hence not overlap, and therefore the flatness issue is of less concern here. In addition, in the adaptive holographic scheme for calculating the adaptive weights, each individual output spot is used to form a unique hologram, and the precise phase-front of the spot is unimportant.

268

The bandwidth of the resonator varies inversely with cavity spacing d, and as with the etalons of the prior section, the Herriott resonator approach is more sensible for signals with large bandwidth because the cavity length is shorter, making it more stable and compact. For example, for a signal with 100 MHz bandwidth, the cavity spacing is on the order of 1.5 meters, while a signal with 10 GHz bandwidth reduces the cavity spacing to only 1.5 cm.

8.2.1.2 Theory of Off-Axis Ray Paths in Optical Resonators

The ray paths in the Herriot spherical mirror resonator can be described by a simple set of equations, identical to the set of equations describing ray propagation through a series of lenses of focal length f and uniformly spaced by a distance d. As shown in figure 8.8, of interest are the two-dimensional Cartesian coordinates describing the position (x_n, y_n) and slope (x'_n, y'_n) of the nth bounce, denoted by x_n, x'_n, y_n, y'_n for a Cartesian coordinate system. From [8], in a cavity of mirror spacing d and focal length f, the x coordinate of the nth bounce is

$$x_n = A\sin(n\theta + \alpha) \qquad 8.32$$

where

$$\cos(\theta) = 1 - (d/2f) \qquad 8.33$$

$$\tan(\alpha) = \sqrt{\frac{4f}{d} - 1} \bigg/ \left(1 + 2f\frac{x'_o}{x_o}\right) \qquad 8.34$$

and

$$A^2 = \frac{4f}{4f - d}\left(x_o^2 + dx_ox'_o + dfx_o'^2\right). \qquad 8.35$$

An analogous set of expressions exists for the y coordinate, where

$$y_n = B\sin(n\theta + \beta) \qquad 8.36$$

and B and β are defined analogously to equations 8.34 and 8.35. As shown in figure 8.8, the angle θ is the difference in polar angle between the nth and $(n+1)th$ bounce,
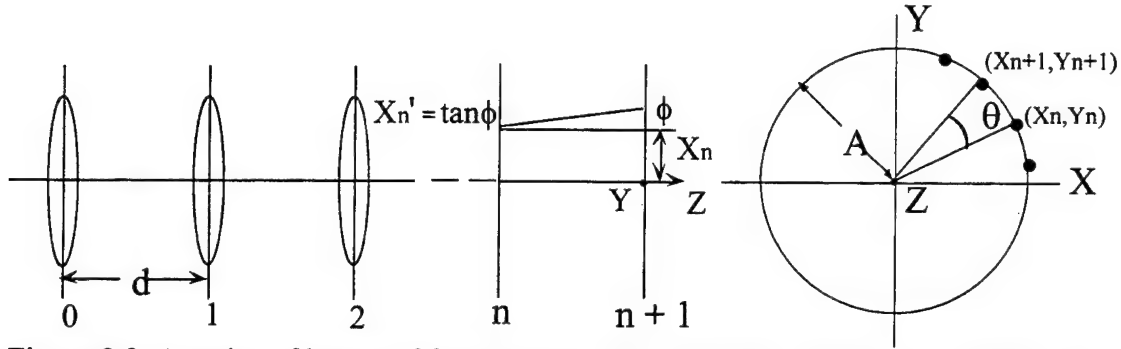
Figure 8.8. A series of lenses of focal length f and uniformly spaced by a distance d form the basis for the simple theory describing ray-propagation in Herriott resonators.

and is solely determined by the cavity geometry, independent of the initial launch parameters x_o, y_o, x_o', and y_o'. The offset angles α and β depend on both the initial launch parameters and the cavity geometry. A and B are the maximum possible excursions of the ray in the x and y directions respectively, and determine the maximum size of the resonator aperture radius. The projection of x_n and y_n onto a plane will in general map out an ellipse, with special cases being a circle when $A = B$ and $\alpha = \beta \pm \pi/2$ (when $\tan(\alpha)\tan(\beta) = -1$), and a straight line when $A = B$ and $\alpha = \beta$. A re-entrant condition exists whenever $2m\theta = 2\pi$, and the spot pattern will reproduce itself after m bounces.

More generally, and of greater interest for the applications discussed in this thesis, the coordinate equations given above can be extended to the case of astigmatic resonator mirrors by explicitly defining mirror focal lengths f_x and f_y for the x and y directions respectively. The astigmatic resonator can produce a plethora of complicated Lissajous patterns, a few of which will be presented in the following sections. The Lissajous patterns can spread the output spots over a large portion of the output plane, which can be advantageous because the spots are more easily separable. The cavity equations (8.32 to 8.36) have been used to calculate different resonator output patterns as a function of cavity and launch parameters. These calculations were done primarily to estimate output spot patterns and sizes as an aid towards choosing optical
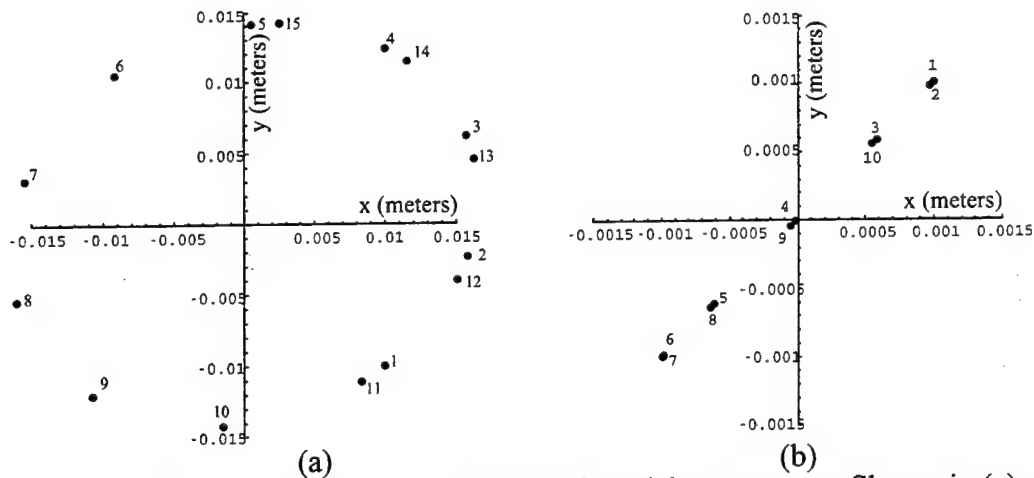
270

Figure 8.9. Output spot patterns of Herriott time-delay resonator. Shown in (a) are the first 15 outputs spots of a near circular output pattern. Input parameters were {d =.353, fx = 3.75, fy = 3.75, xo = .01, x' = .01, yo = .01, y' = -.01}. In (b), the output has collapsed to a nearly a straight line. Input parameters were {d =.353, fx = 3.75, fy = 3.75, xo = .001, x' = .0001, yo = .001, y' = .0001}.

components and resonator configurations for the experimental investigations presented in the following section. Diffraction effects were not included in the calculations, and the input beam was assumed to be mode matched to the cavity.

Figure 8.9a shows a typical pattern calculated for spherical mirrors (no astigmatism). The pattern is near circular in this example because $A \approx B$, and α is approximately $\pi/2$ out of phase with β. The figure shows the first 15 spots which exit the resonator output coupler. Figure 8.9b shows the resonator output where the pattern has now collapsed into nearly a straight line, because now $\alpha \approx \beta$. The output spots walk down the diagonal from the upper right to the lower left and back up again. Arrangements of this type are particularly interesting for phased-array processing applications because a single resonator could simultaneously provide separable output patterns for multiple inputs. For example, appropriate placement of each input signal would map out a diagonal at a unique radial angle.

The astigmatic $\left(f_x \neq f_y \right)$ cases are of interest here because the resulting output patterns make more use of the available resonator aperture. For example, figure 8.10a

(a)   (b)
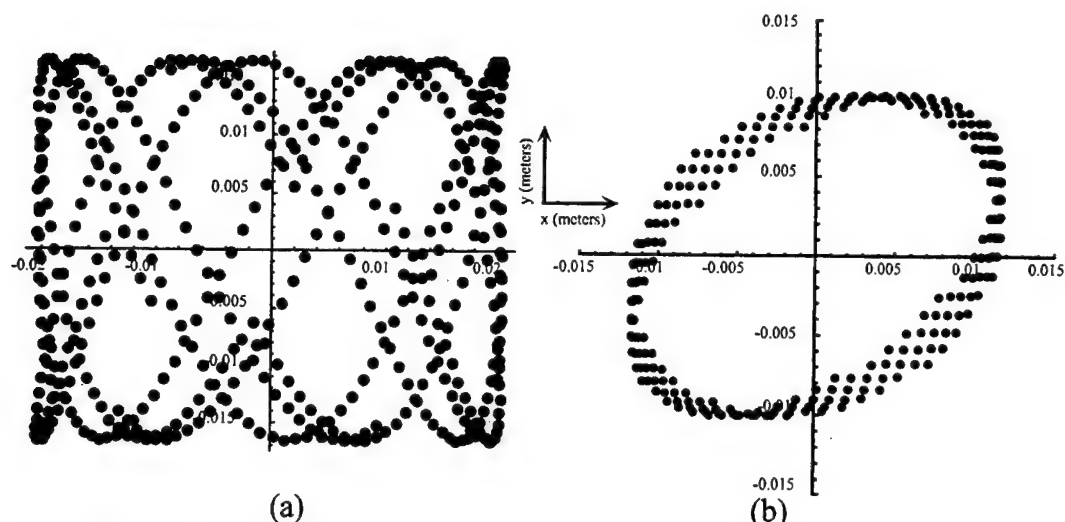
Figure 8.10. Lissajous patterns produced by astigmatic Herriott time-delay resonator. Parameters for (a) were {d =.353, fx = 3.55, fy = 3.75, xo = .015, x' = .01, yo = .01, y' = .01}, and {d =.353, fx = 3.73, fy = 3.75, xo = .0001, x' = .01, yo = .01, y' = 0.0} for (b).

(a)   (b)
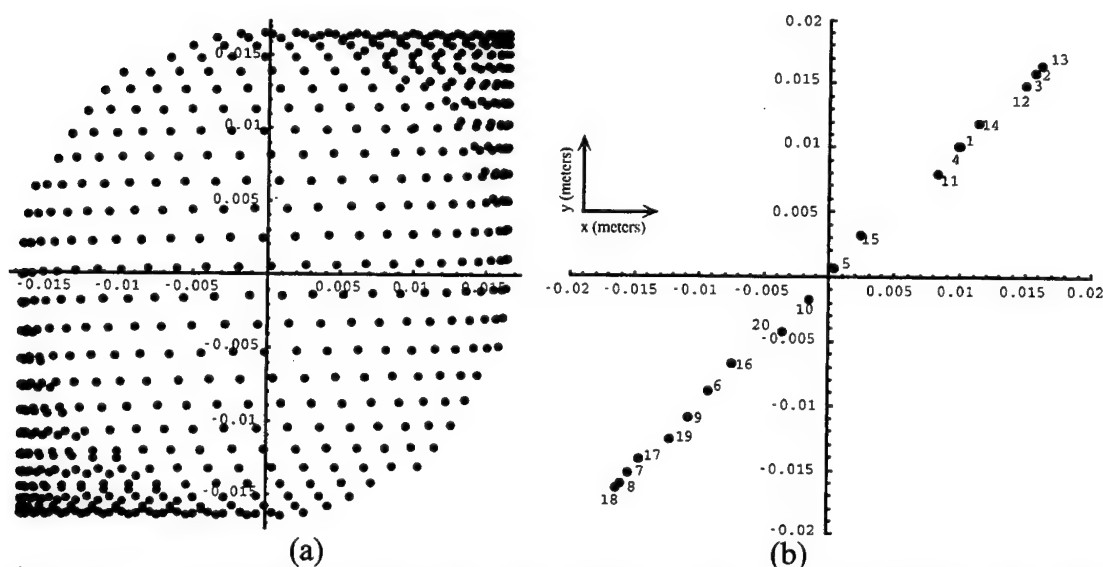
Figure 8.11. Grid-like resonator output spot pattern consisting of 650 spots in (a), and the first 20 output spots of the pattern in (b). Input parameters were {d =.353, fx = 3.72, fy = 3.75, xo = .01, x' = .01, yo = .01, y' = .01}

shows a classic Lissajous pattern produced with a moderate astigmatism of ~ 0.05.

Figure 8.10b shows an elliptical pattern composed of 500 output spots which is

rotating about in its orientation as the spot pattern progresses due to the astigmatism.

A grid-like pattern of 650 output spots shown in figure 8.11a. This pattern is essentially the astigmatic version of that shown in figure 8.9b, as evidenced by the pattern shown figure 8.11b, where the first 20 output spots of the grid-like pattern walk down the diagonal and back up again as in figure 8.9b, only that due to the astigmatism, now the return path is slightly displaced. The line evolves into an ellipse with each pass, slowly opening up each time around, while always passing through the lower left and upper right corners. This is why these two corners have a much higher spot density. Thus, in spite of the intuitive desire to attach a regular numbering sequence to the orderly array of output spots, this is not appropriate. For purposes of using this type of pattern as an input to the optical phased-array processor, the fact that the pattern does not follow an intuitive numbering pattern is immaterial. As explained in Chapters 6 and 7, the holographic beam-forming process does not require the topology of the fielded phased-array to match that of the input optical mapping. Much more important is the fact that the output spots are spread out over the resonator aperture, and that the spots are spatially or angularly resolvable so that they may be individually accessible.

8.2.2 Experimental Demonstration of Herriott Resonator

A Herriott time-delay resonator has been constructed in order to investigate performance issues such as number and arrangement of output spots, resonator optical throughput, and the ability to write holograms in a photorefractive crystal using the output spot pattern.

8.2.2.1 Experimental Set-up

The experimental set-up for the Herriott time-delay resonator is shown in figure 8.12. The doubled Nd:Yag laser (532nm) is spatially filtered, collimated, and focused down through the acousto-optic modulator (AOM). A frequency sweep of
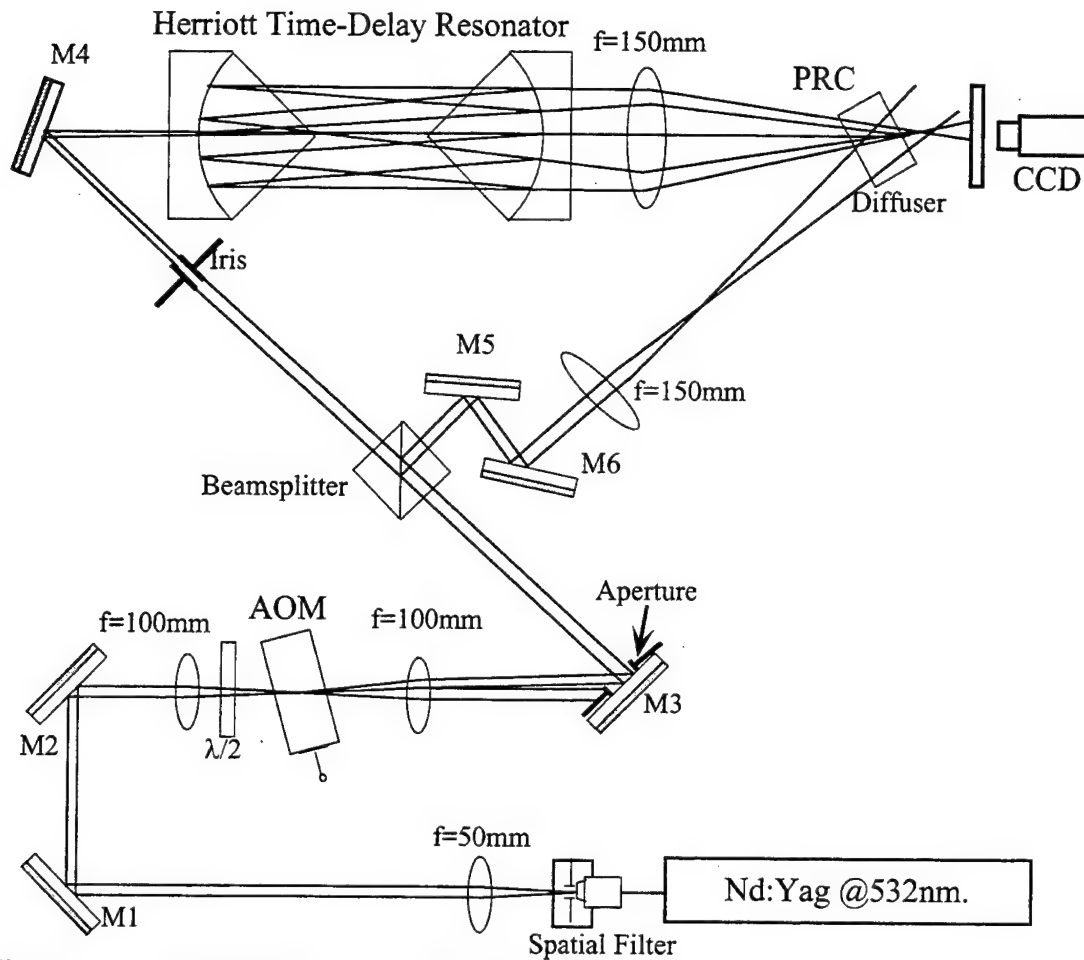
Figure 8.12. Experimental layout of Herriott time-delay resonator experiment.

approximately 20 MHz on an 80 MHz carrier was input into the AOM. The undiffracted

component from the AOM is blocked by the aperture in front of mirror 3 (M3), and the

diffracted component is split by the beamsplitter into a signal and reference arm. The

signal arm is sent through an iris which is set so that the intensity of the signal into the

resonator stays approximately constant as the beam scans about (very little) due to the

AOM deflection with frequency. This modulated beam is then sent via M4 through the

output coupler, and into the resonator. The mirrors of the resonator cavity were 2 inch

diameter, $\lambda/200$, 99.6% reflectivity laser output coupler mirrors. Astigmatism of the

mirrors can be induced by tightening the mounting screw which holds the mirrors in

their mounts. Tightening the screw creates a force on one axis of the mirrors, changing

the radius of curvature of the mirror in the dimension of the axial force. The reference beam is steered with mirrors M5 and M6, brought to a focus with a 150mm lens and allowed to diverge onto the photorefractive crystal (SBN:Cr). When the output of the resonator is blocked, and the PRC is read out with the reference beam, the diffracted output beam propagates to the diffuser. The resonator had a cavity length of 0.353 meters, corresponding to a Nyquist sampling interval of approximately 200 MHz. As discussed below, the cavity seemed to support on the order of 200 output spots, corresponding to a total aperture time of approximately 235 nsec and a frequency resolution of approximately 2 MHz.

8.2.2.2 Experimental Results

The experimental results presented emphasize the large number of output spots and high output spot density available using the Herriott resonator. Figure 8.13 shows an experimental output pattern from the astigmatic resonator, analogous to the calculated result of figure 8.11a. Note that as in figure 8.11a, there are two corners with very high spot density, and the intensity is higher along the primary diagonal formed by the two corners. The lower intensity in the direction orthogonal to this diagonal is consistent with the fact that as in the calculated result, these spots are of a much higher bounce number than those along the primary diagonal, and the intensity is correspondingly reduced due to the less than unity mirror reflectivity.

Attempts to write a photorefractive hologram with the grid-like pattern were met with limited success; only one or two diffracted spots were seen. This was at first attributed to the output intensity of the resonator being extremely low, on the order of several microwatts. The low output intensity was due in part to the fact that coupling into the resonator was done via one of the partially transmitting output couplers as shown in figure 8.12. This low power level prompted an alternate input coupling

275
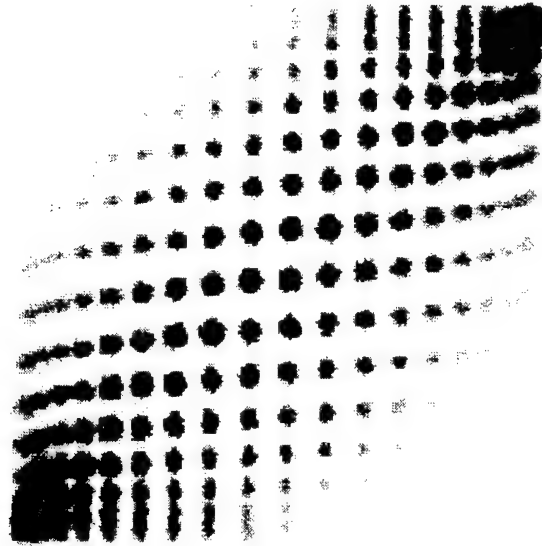
Figure 8.13. Experimental result of grid-like output spot pattern from astigmatic Herriott time-delay resonator

method using a pick-off mirror to couple directly into the cavity rather than through the output coupler. The drawback with this approach is that it limited the available range of achievable input launch parameters. Using the pick-off mirror approach produced the elliptical resonator output pattern shown in figure 8.14, which agrees well with the simulation of figure 8.10b, where the manner in which the intensity decreases confirms the spiral-like progression of the output spots.

Using the pick-off mirror increased the output power to approximately 100 microwatts, however it was found that only the first ring of 10 output spots would write a hologram, corresponding to the first 10 round trips through the cavity. The intensity dependent photorefractive time constant suggested that by waiting long enough, a hologram could be written between many more spots. This was not the case. The question of laser coherence length now arises. The 10 spots recorded in the hologram suggest that during the time of the photorefractive time constant, the
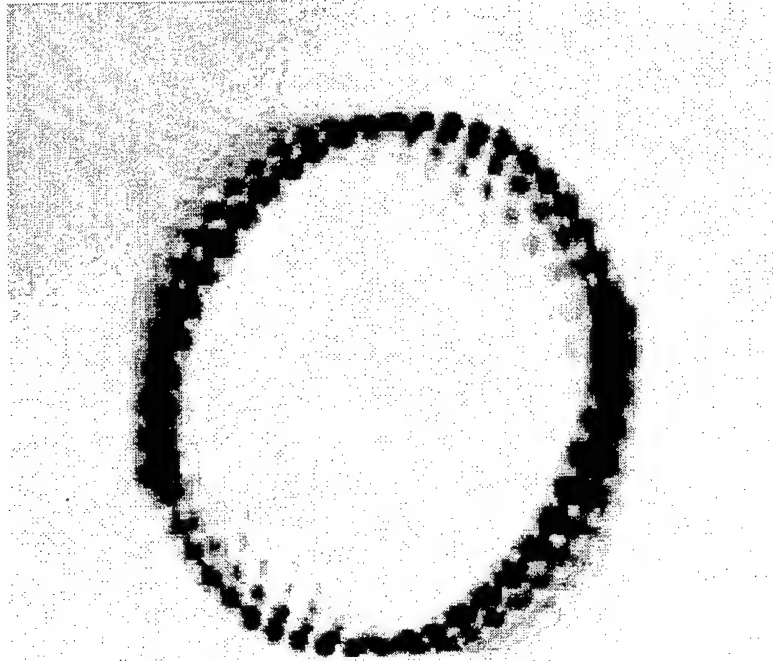
Figure 8.14. Experimental result of output spot pattern from astigmatic Herriott time-delay resonator.

coherence length of the laser was only as long as 20 cavity lengths, about 14 meters instead of the 150m suggested by the manufacturer. To investigate this suspicion, the reference beam path for the hologram was increased by a length approximately equal to a cavity round-trip distance. The 10 spots formed in the hologram all shifted around the ring by one spot, i.e. one round-trip time. By increasing the reference beam path length, the reference beam was now coherent with only 9 of the output spots of the previous ring, and where the 10th output spot was previously at too large of a delay. The suspicion of a dramatically shorter coherence length than assumed was officially confirmed by proper interpretation of the manufacturer's specifications. In particular, a specification of a 150m coherence length was given, however it is only valid for time intervals less than 2μ seconds, which is several orders of magnitude shorter than the photorefractive writing time constant. Thus while the laser has a very narrow linewidth of only 2MHz, the center frequency of that linewidth is moving about at MHz rates,

preventing constructive interference for hologram formation over a time interval even near that of the photorefractive time constant. A laser with better coherence properties is the first step in performing a more useful demonstration of the Herriott time-delay resonator. A faster PRC would also be advantageous. As with the Fabry-Perot resonators of the previous sections, using GHz bandwidth signal inputs would be a better match to the available Nyquist sampling interval and temporal aperture of the Herriot resonator as built.

Despite the shortcoming of a using a laser with an insufficient coherence length, the Herriott resonator experiment did demonstrate the important issues that multiple time-delayed outputs and useful aperture times can be obtained in a compact, straightforward manner, and that these time-sampled signal outputs can be used to form holographic weights for adaptive signal processing.

References

[1]   B. Widrow and S.D. Stearns, *Adaptive signal Processing*. Prentice-Hall Inc, N.J., 1985.

[2]   A. Gabel, L.S. Lee, and I.C. Chang, "Front-end RF channelization using optical techniques," in , SPIE **477**, (1984).

[3]   E.M.Alexander. and R. W. Gammon, "The Fabry-Perot etalon as an RF frequency channelizer," in *Solid State Optical Control Devices,* SPIE **464**, 45-52 (1984).

[4]   A. Yariv, *Optical Electronics*. Saunders College Publishing, 1985.

[5]   J. Xu and R. Stroud, *Acousto-optic Devices: Principles, Design, and Applications*. (Wiley-Interscience, 92), chap. 2, pp. 83.

[6]   M.A. Rob, "Limitations of a wedged etalon for high resolution linewidth measurements," Opt. Lett. **15**, no. 11, 604-606 (1990).

[7]   M. Born and E. Wolf, *Principles of Optics*. Pergamon Press, 87, chap. 7, pp. 351.

[8]   D. Herriott, H. Kogelnik and R. Kompfner, "Off-axis paths in spherical mirror interferometers," Appl. Opt. **3**, no. 4, 523-526 April (1964).

[9]   D.R. Herriott and H.J. Schulte, "Folded optical Delay lines," Appl. Opt. **4**, no. 8, 883-889 August (1965).

9. Conclusion

This thesis has investigated adaptive phased-array processing using photorefractive holograms, both theoretically and experimentally. The demanding, spatio-temporal phased-array signal processing problem was addressed using a unique architecture which exploited the time integrating properties and the large number of accessible degrees-of-freedom available with photorefractive volume holograms. The most significant advantage to the architecture presented is that the required number of processor components used is independent of the number of elements in the phased-array. This attribute allows the processor to scale to processing applications for very large arrays. This is in marked contrast to traditional electronic or acousto-optic approaches, where the hardware complexity of the processor scales in proportion to the size of the array.

The phased-array processor is actually composed of two major processing systems, the main-beam forming processor, and the jammer-nulling processor. The dynamic holographic beam-forming process which these processors are based on, provides a tremendous amount of flexibility in terms of system architecture. For example, as was shown in Chapter 6, the specific mapping of the optical fibers transduced from the antenna array onto the photorefractive crystals is irrelevant, since it is compensated by the holographic diffraction provided that a crystal with an adequate number of degrees-of-freedom is used. When the system architecture uses feedback gain, as in the jammer-nulling processor, the convergence time of the system is determined by the feedback gain, and can be a tiny fraction of the traditionally slow photorefractive time constant.

The operation of both the main-beam processor and the jammer-nulling processor were experimentally investigated, and successfully demonstrated their respective tasks in a robust manner. The beam forming processor was used to steer the array function towards a desired signal of interest, both with a planewave optical input

which simulated a coherent fiber feed, and an input whose phase front was randomized by a diffuser which simulated an arbitrary mapping of the input fibers and fibers of different lengths. The jammer-nulling processor demonstrated the capability of simultaneously suppressing multiple narrowband jammers, and achieved 45 dB of suppression for a single jammer. The most significant results are the simultaneous beam formation and jammer-nulling data obtained with the combined phased-array processor, which demonstrated its capability to process signals received from a complex signal environment. These particular results are the first known results of simultaneous phased-array beam-formation and jammer-suppression using an optical, adaptive phased-array antenna processor.

The dynamical analysis of the jammer-nulling processor led to the conclusion that holographic feed through placed a limit on the amount of jammer suppression. To overcome this limitation, an alternative holographic read-write technique based on orthogonally polarized read-write beams was implemented, as discussed in Chapter 5. The investigation of this multiplexing method was extended to include the wide-angular aperture holographic studies also presented in Chapter 5. By choosing a read-write geometry near the angle of equal curvature of the ordinary and extraordinary momentum surfaces in a 45 degree-cut $BaTiO_3$ crystal, phase-matched holographic readout exceeded 18 degrees in the plane of Bragg selectivity, and 6 degrees in the orthogonal dimension. The ability to simultaneous write and read out holograms over such a wide angular aperture may have applications in optical signal and image processing, as well as in holographic memory. Performing this multiplexing technique using two wavelengths such that the read wavelength is outside of the spectral absorption band of the material, resulting in non-destructive readout, is a possible area of future work with direct applications to holographic memory.

In terms of future work for the phased-array processor, there are several areas which appear worthwhile. The first and most fundamental would be extending the

processor capabilities to include squintless processing of broadband signals. The implementation of the broadband capability could include the time-domain implementations proposed by Wagner et al.[1], or the frequency-domain implementation using the etalon filters discussed Chapters 2 and 8. As was shown in Chapter 8, due to etalon size and stability issues, implementing the frequency-domain approach would be impractical at the current frequency band of processor operation (approximately 100 MHz), although at much higher frequencies it may be feasible. A second issue would be extending the jammer-nulling processor bandwidth by reducing the feedback delay time. Possible approaches to this may include low time-delay acousto-optic devices[2], as well as optimizing cable lengths, amplifier delays, etc. Significant work could also be done in terms of optimizing the performance of the processor with respect to trade-offs between maximizing jammer suppression depth and maximizing the total array signal-to-interference-noise ratio (SINR), in terms of processor system parameters and noise while optimally using laser power as discussed in Chapter 7. It would also be interesting to consider dramatically reducing the size of the processor, while simultaneously designing for improved stability, so that the system could perhaps be made portable and the active path length control system could be eliminated.

In summary, the adaptive phased-array antenna architecture presented in this thesis has sucessfully demonstrated the capabilities and helped to motivate the use of photorefractive, dynamic holographic materials for adaptive signal processing applications in demanding and complex signal environments. It is hoped that the research presented in this thesis may serve as a foundation for future processing architectures for large adaptive phased-arrays, and be recognized as a unique advancement in its field.

References

[1]   K. Wagner, S. Kraut, L. Griffithsaver, R.T. Weverka, and A. W. Sarto, "Efficient true-time-delay adaptive-array processing," in *Radar Processing, Technology, and Applications,* SPIE **2845**, (1996).

[2]   R. T. Weverka and K. Wagner, "Wide angular aperture acoustooptic Bragg cell," in *Devices for Optical Processing,* SPIE **1562**, 66-72 (1991).

10. Bibliography

[1.1]   R.T. Weverka and K. Wagner, "Adaptive phased-array radar processing using photorefractive crystals," in *Optoelectronic Signal Processing for Phased-Array Antennas II,* B.M. Hendrickson and G.A. Koepf, ed. Proc. Soc. Photo-Opt. Instrum. Eng. **1217**, 173-182 (1990).

[1.2]   R.T. Weverka and K. Wagner, "Staring phased-array radar using photorefractive crystals," in *Optical Information Processing Systems and Architectures III,* Proc. Soc. Photo-Opt. Instrum. Eng. **1564**, 676-684 (1991).

[1.3]   A.W. Sarto, R.T. Weverka, and K. Wagner, "Photorefractive phased-array radar processor dynamics," in *Photonics for Processors, Neural Networks, and Memories,* Proc. Soc. Photo-Opt. Instrum. Eng. **2026**, July 310-324 (1993).

[1.4]   A.W. Sarto, R.T. Weverka, and K. Wagner, "Beam-steering and jammer-nulling photorefractive phased-array radar processor," in *Optoelectronic Signal Processing for Phased-Array Antennas IV,* Proc. Soc. Photo-Opt. Instrum. Eng. **2155**, 378-388 (1994).

[1.5]   R.T. Weverka, K. Wagner, A.W. Sarto, and S. Weaver, "3-Dimensional holographic data processing and wavelength readout for range-doppler-angle radar, and synthetic aperture radar," in *Optoelectronic Signal Processing for Phased-Array Antennas IV,* B.M. Hendrickson, ed. Proc. Soc. Photo-Opt. Instrum. Eng. **2155**, 336-347 (1994).

[1.6]   R.T. Weverka, K. Wagner, and A.W. Sarto, "Adaptive phased-array radar processing using photorefractive crystals," Appl. Opt. **35**, no. 8, 1344-1366 March (1995).

[1.7]   A. W. Sarto, K. Wagner, R. T. Wagner, S. Blair, and S. Weaver, "Photorefractive phased-array antenna beam-forming processor," in *Radar Processing, Technology, and Applications,* SPIE **2845**, (1996).

[1.8]   B. Widrow, P.E. Mantey, L.J. Griffiths, and B.B. Goode, "Adaptive antenna systems," in , IEEE Proc. **55**, 2143-2161 (1967).

[1.9]   A.W. Sarto, R.T. Weverka, K.H. Wagner, and S. Weaver, "Wide angular aperture holograms in photorefractive crystals using orthogonally polarized write and read beams," in *Photorefractive materials, effects, and devices,* OSA/NIST, June 214-217 (1995).

[1.10] A. W. Sarto, K. Wagner, R. T. Wagner, S. Weaver, and E. Walge, "Wide angular aperture holograms in photorefractive crystals by the use of orthogonally polarized write and read beams," Appl. Opt. **35**, no. 29, 5765-5775 Oct. (1996).

[1.11] J. A. Fleck, J. R. Morris and M.D. Feit, "Time dependent propagation of high-energy laser beams through the atmosphere," Appl. Phys. **10**, 129-160 (1976).

[1.12] M. Saffman, "Self-Organized Formation of Image Representations in Photorefractive Oscillators," Ph.D. thesis, University of Colorado, 1994.

[2.1] B. Widrow and S.D. Stearns, *Adaptive Signal Processing*. Prentice Hall, 1985.

[2.2] B. Widrow, "Adaptive noise canceling: principles and applications," Proc. IEEE **63**, no. 12, 1692-1719 Dec (1975).

[2.3] S.P. Applebaum, "Adaptive arrays," IEEE Trans. Ant. Prop. **AP-24**, 585-598 (1976).

[2.4] P.W. Howells, "Explorations in fixed and adaptive resolution at GE and SURC," IEEE Trans. Ant., Prop. **AP-24**, no. 5, 575-584 Sept. (1976).

[2.5] J. Capon, R. J. Greenfield and R.J. Kolker, "Multi-dimensional maximum likelihood processing of a large aperture seismic array," Proc. IEEE **55**, 192-211 Feb. (1967).

[2.6] L.J. Griffiths, "A comparison of multi-dimensional Weiner and maximum-likelihood filters for antenna arrays," Proc. IEEE **55**, 2045-2047 Nov. (1967).

[2.7] R.J. Mailloux, "Phased array theory and technology," Proc. IEEE **70**, no. 3, 246-293 March (1982).

[2.8] B. D. Steinberg, and H. M. Subbaram, *Microwave Imaging Techniques*. John Wiley & Sons, 1991.

[2.9] M.I. Skolnik, *Introduction to Radar Systems*. (McGraw-Hill, 1962), chap. 7, pp. 294-329.

[2.10] D. H. Johnson and D.E. Dudgeon, *Array Signal Processing, Concepts and Techniques*. (Prentice Hall, 1993), chap. 3, pp. 84-106.

[2.11] C.L. Dolph, "A current distribution for broadside arrays which optimizes the relationship between beamwidth and sidelobe level," Proc. IRE **34**, 335-345 (1946).

[2.12] T.T. Taylor, "Design of line source antennas for narrow beamwidth and low sidelobes," IEEE Trans. Ant. Prop. **AP-3**, 16-28 (1955).

[2.13] T.T. Taylor, "Design of circular apertures for narrow beamwidth and low sidelobes," IRE Trans. Ant. Prop. **AP-8**, 17-22 (1960).

[2.14] H. W. Yen, M. Wechsberg, J. J. Lee, and A. E. Popa, "EHF fiber-optic based antenna array," in *Optoelectronic Signal Processing for Phased-Array Antennas,* SPIE **886**, 218-222 (1988).

[2.15] A. Goutzoulis and K. Davies, "Compressive 2-D delay line architecture for time steering of phased-array antennas," in *Optoelectronic Signal Processing for Phased-Array Antennas II,* SPIE **1217**, 270-283 (1990).

[2.16] A. P. Goutzoulis, D. K. Davies and J.M. Zomp, "Hybrid electronic fiber optic wavelength-multiplexed system for true time-delay steering of phased array antennas," Opt. Eng. **31**, no. 11, 2312-2322 Nov. (1992).

[2.17] D. Dolfi, F. Michel-Gabriel, S. Bann, and J. P. Huignard, "Two-dimensional optical architecture for time-delay beam forming in a phased-array antenna," Opt. Lett. **16**, no. 4, 255-257 Feb. (1991).

[2.18] N.A. Riza, "Transmit-receive time-delay beam-forming optical architecture for phased-array antennas," Appl. Opt. **30**, no. 32, 4594-95 Nov. (1991).

[2.19] R. D. Esman, M. Y. Frankel, J. L. Dexter, L. Goldberg, M. G. Parent, D. Stilwell, and D. G. Cooper, "Fiber-optic prism true time-delay antenna feed," IEEE Phot. Tech. Lett. **5**, no. 11, 1347-1349 Nov. (1993).

[2.20] A. Molony, C. Edge and I. Bennion, "Fibre grating time delay element for phased array antennas," Elec. Lett. **31**, no. 17, 1485-1486 Aug. (1995).

[2.21] E. N. Toughlian and H. Zmuda, "Variable time-delay system for broadband phased array and other transversal filtering applications," Opt. Eng. **32**, no. 3, 613-617 March (1993).

[2.22] B. Widrow, P. E. Mantey, L. J. Griffiths, and B. B. Goode, "Adaptive antenna systems," Proc. IEEE **55**, no. 12, 2143-2161 Dec. (1967).

[2.23] A. Farina, *Antenna-Based Signal Processing Techniques for Radar Systems.* (Artech House, Inc., 1992), chap. 5.

[2.24] B. Widrow and S.D. Stearns, *Adaptive Signal Processing.* (Prentice Hall, 1985), chap. 12.

[2.25] L.J. Griffiths, "A simple adaptive algorithm for real-time processing in antenna arrays," Proc. IEEE **57**, no. 10, 1696-1704 Oct. (1969).

[2.26] J.W.R. Griffiths, "Adaptive array processing," IEE Proc. **130**, no. 1, 3-10 Feb (1983).

[2.27] R.O. Schmidt, "Multiple emitter location and signal parameter estimation," IEEE Trans Ant. and Prop. **AP-34**, no. 3, 276-280 March (1986).

[2.28] R. Roy and T.K. K., "ESPRIT- estimation of signal parameters via rotational invariance techniques," Opt. Eng. **29**, no. 4, 296-313 April (1990).

[2.29] R. Kumaresan, L. L. Scharf, and A. K. Shaw, "An algorithm for pole-zero modeling," IEEE Trans. Acoust., Speech, Signal Process **34**, 637-640 (1986).

[2.30] R.T. Compton, *Adaptive Antennas.* (Prentice Hall , 1988), chap. 2.

[2.31] R. T. Compton, *Adaptive Antennas.* (Prentice Hall, 1988), chap. 3, pp. 120.

[2.32] D. R. Pape, P. Wasilousky and P.M. Payson, "A high performance apodized phased-array Bragg cell," in *Proc. SPIE vol. 789,* (1987).

[2.33] R. T. Weverka, K. Wagner and A.W. Sarto, "Photorefractive processing for large adaptive phased-arrays," Appl. Opt. **35**, no. 8, 1344-1366 March (1996).

[3.1] J.F. Rhodes, "Adaptive filter with a time domain implementation using correlation cancellation loops," Appl. Opt. **22**, no. 2, 282-287 Jan (1983).

[3.2] S. Haykin, *Adaptive Filter Theory.* (Prentice Hall, 1991), chap. 6.

[3.3] J.D. Cohen, "Optical adaptive linear predictors," Appl. Opt. **24**, no. 23, 4247-4259 Dec. (1985).

[3.4] A.VanderLugt, "Adaptive optical processor," Appl. Opt. **21**, no. 22, 4005-4011 Nov. (1982).

[3.5] A. M. Bardos, W. R. Beaudet and A.VanderLugt, "Stability considerations for adaptive filtering," Appl. Opt. **25**, no. 14, 2314-2325 July (1986).

[3.6] D. Psaltis and J. Hong, "Adaptive acoustooptic filter," Appl. Opt. **23**, no. 19, 3475-3481 Oct. (1984).

[3.7] D. Psaltis and J. Hong, "Adaptive acoustooptic processor," in *Analog Optical Processing and Computing,* SPIE **519**, 62-68 (1984).

[3.8] W. Davenport and W. Root, *Introduction toTheory of Random Processes and Noise.* McGraw Hill, 1967.

[3.9] D. Psaltis, J. Yu and J. Hong, "Bias-free time integrating optical correlator using a photorefractive crystal," Appl. Opt. **24**, no. 22, 3860-3865 Nov. (1985).

[3.10] J. Hong, S. Hudson, J. Yu, and D. Psaltis, "Photorefractive crystals as adaptive elements in acoustooptic filters," in *Optical Technology for Microwave Applications III,* SPIE **789**, 136-144 (1987).

[3.11] P. Kellman, "Time integrating optical signal processing," Opt. Eng. **19**, no. 3, 370-375 May (1980).

[3.12] R.M. Montgomery, "Acousto-optic, photorefractive processor for adaptive antenna arrays," in *Optoelectronic Signal Processing for Phased-Array Antennas II,* SPIE **1217**, 207-217 (1990).

[3.13] R. M. Montgomery and M.R. Lange, "Photorefractive adaptive filter structure with 40-dB interference rejection," Appl. Opt. **30**, no. 20, 2844-2849 July (1991).

[3.14] R. M. Montgomery, W. R. Beaudet and M.R. Lange, "Photorefractive adaptive sidelobe canceler for phased-array antennas," in *Optical Technology for Microwave Applications,* SPIE **1703**, 405-410 (1992).

[3.15] W. Penn, "Optical adaptive array processing," in *Proc. LIA Conf.*, LIA **34**, (1982).

[3.16] W. Penn, R. Wasiewicz and R.M. Iodice, "Optical adaptive multipath canceller for surveillance radar," in *Optoelectronic Signal Processing for Phased-Array Antennas II*, SPIE **1217**, 151-160 (1990).

[3.17] C. W. Keefer, J. E. Malowicki and P.M. Payson, "Wideband operation of a photorefractive based adaptive processor," in *Analog Photonics*, SPIE **1790**, 145-156 (1992).

[3.18] M. C. Budge, R. J. Berinato and M.C. Zari, "Acousto-optic applications for multichannel adaptive optical processor," Tech. Rep., 1992.

[3.19] D. B. Friedman, D. P. Dwyer and R.M. Iodice, "Acousto-optic null steering processor (AONSP)," in *Transition of Optical Processors into Systems*, SPIE **1958**, 83-97 (1993).

[3.20] D. R. Pape, P. Wasilouski and M. Krainak, "A high performance apodized phased-array Bragg cell," in *Optical Technology for Microwave Applications III*, SPIE **789**, 117-126 (1987).

[4.1] P.J. van Heerden, "Theory of Optical Information in Solids," Appl. Opt. **2**, no. 4, 393-400 April (1963).

[4.2] H. Kogelnik, "Coupled wave theory for thick hologram gratings," Bell. Syst. Tech. J. **48**, 2909-2945 (1969).

[4.3] D. Gabor and G.W. Stroke, "The theory of deep holograms," Proc. Roy. Soc. **A304**, 275 (1968).

[4.4] W.C. Sweatt, "Designing and constructing thick holographic optical elements," Appl. Opt. **17**, no. 8, 1220-1227 April (1978).

[4.5] M.R.B. Forshaw, "The imaging properties and aberrations of thick transmission holograms," Opt. Acta **20**, no. 9, 669-686 (1973).

[4.6] J.F. Heanue, M.C. Bashaw, and L. Hesselink, "Volume holographic storage and retrieval of digital data," Science **265**, 749-737 August (1994).

[4.7] E.N. Leith, A. Kozma, J. Upatniks, J. Marks, and N. Massey, "Holographic data storage in three-dimensional media," Appl. Opt. **5**, no. 8, 1303-1311 August (1966).

[4.8] F.H. Mok, "Angle-multiplexed storage of 5000 holograms in lithium niobate," Opt. Lett. **18**, no. 11, 915-917 (1993).

[4.9] J. White and A. Yariv, "Real-time image processing via four-wave mixing in a photorefractive medium," Appl. Phys. Lett. **37**, 5-7 (1980).

[4.10] L. Pichon and J.P. Huignard, "Dynamic joint-Fourier transform correlator by Bragg diffraction in photorefractive Bi12SiO20 Crystals," Opt. Commun. **36**, 277-280 (1981).

[4.11] V. Markov, S. Odoulov, and M. Soskin, "Dynamic holography and optical image processing," Opt. Laser Tech. **11**, 95-99 (1979).

[4.12] P. Yeh, D. Zhang, and C. Gu, "Parallel subtraction of Fourier power spectrum using holographic interferometry," Opt. Lett. **17**, 70-72 (1992).

[4.13] A.E. Chiou and P. Yeh, "Parallel image subtraction using a phase-conjugate Michelson interferometer," Opt. Lett **11**, 306-308 (1986).

[4.14] D.S. Oliver, P. Vohl, R.E. Aldrich, M.E. Behrndt, W.R. Buchan, R.C. Ellis, J.E. Genthe, J.R. Goff, S.L. Hou, and G. m Daniel, "Image storage and optical readout in a ZnS device," Appl. Phys. Lett. **17**, 416-418 (1970).

[4.15] M.P. Petrov, A.V. Khomenko, M.V. Krasin'kova, V.I. Marakhonov, and M.G. Shylyagin, "The PRIZ image converter and its use in optical data processing systems," Sov. Phys.-Tech. Phys **26**, 816-821 (1981).

[4.16] Y. Shi, D. Psaltis, A. Marrakchi, and J. A.R. Tanguay, "Photorefractive incoherent-to-coherent optical converter," Appl. Opt. **22**, 3665-3667 (1983).

[4.17] D.Z. Anderson and J. Feinberg, "Optical Novelty Filters," IEEE J. Quant. Elec. **25**, 635-647 (1989).

[4.18] D.L. Staebler and J.J. Amodei, "Coupled-wave analysis of holographic storage in LiNbO3," J. Appl. Phys. **43**, 1043-1049 (1972).

[4.19] N. Kukhtarev, V. Markov, S. Odoulov, M. Soskin, and V. Vinetski, "Holographic storage in electrooptic crystals. I. Steady-state," Ferroelectrics **22**, 946-960 (1979).

[4.20] N. Kukhtarev, V. Markov, S. Odoulov, M. Soskin, and V. Vinetski, "Holographic storage in electrooptic crystals.II. Beam-coupling-light amplification," Ferroelectrics **22**, 5061-5076 (1979).

[4.21] K. Wagner and D. Psaltis, "Multilayer optical learning networks," Appl. Opt. **26**, 5061-5076 (1987).

[4.22] Y. Owechko, "Cascaded-grating holography for artificial neural networks," Appl. Opt. **32**, 1380-1398 (1993).

[4.23] I.M. Bel'dyugin, M.V. Zolotarev, and K.A. Sviridov, "Optical neural computers based on photorefractive crystals," Sov. J. Quant. Electron. **22**, 384-399 (1992).

[4.24] D. Psaltis, J. Yu, and J. Hong, "Bias free time-integrating optical correlator using a photorefractive crystal," Appl. Opt. **24**, 3860-3865 (1985).

[4.25] J. Khoury, V. Ryan, C. Woods, and M. Cronin-Golomb, "Photorefractive optical lock-in detector," Opt. Lett. **16**, 1442-1444 (1991).

[4.26] J. Khoury, V. Ryan, and M. Cronin-Golomb, "Photorefractive frequency converter and phase-sensitive detector," J. Opt. Soc. Am. B **10**, 72-82 (1993).

[4.27] R.T. Weverka and K. Wagner, "Adaptive phased-array radar processing using photorefractive crystals," in *Optoelectronic Signal Processing for Phased-Array Antennas II,* B.M. Hendrickson and G.A. Koepf, ed. Proc. Soc. Photo-Opt. Instrum. Eng. **1217**, 173-182 (1990).

[4.28] A.W. Sarto, R.T. Weverka, and K. Wagner, "Beam-steering and jammer-nulling photorefractive phased-array radar processor," in *Optoelectronic Signal Processing for Phased-Array Antennas IV,* Proc. Soc. Photo-Opt. Instrum. Eng. **2155**, 378-388 (1994).

[4.29] R.M. Montgomery and M.R. Lange, "Photorefractive adaptive filter structure with 40-dB interference rejection," Appl. Opt. **30**, 2844-2849 (1991).

[4.30] F. Vachss, J. Hong, and C. Keefer, "Adaptive signal processing using a photorefractive time integrating correlator," DARPA/Rome Labs Proc. **PSAA-91**, 127-132 (1991).

[4.31] B. Widrow and S.D. Stearns, *Adaptive signal Processing.* Prentice-Hall Inc, N.J., 1985.

[4.32] R.T. Weverka, K. Wagner, and A.W. Sarto, "Adaptive phased-array radar processing using photorefractive crystals," Submitted to Appl. Opt..

[4.33] J.P. Huignard and P. Gunter, *Photorefractive Materials and their Applications*, vol. 61, Topics in Applied Physics. Berlin: Springer-Verlag, 1989.

[4.34] J.P. Huignard and P. Gunter, *Photorefractive Materials and their Applications*, vol. 62, Topics in Applied Physics. Berlin: Springer-Verlag, 1989.

[4.35] F. Seitz, "Color Centers in Alkali Halide Crystals II," Rev. Modern Phys. **26**, no. 1, 7-94 Jan (1954).

[4.36] T. Huang, "Physics and Applications of Photoanisotropic Organic Volume Holograms," Ph.D. thesis, University of Colorado, 1993.

[4.37] J.J. Amodei and D.L. Staebler, "Holographic pattern fixing in electro-optic crystals," Appl. Phys. Lett. **18**, no. 12, 540-542 June (1971).

[4.38] F. Micheron and G. Bismuth, "Electrical control of fixation and erasure of holographic patterns in ferroelectric materials," Appl. Phys. Lett. **20**, no. 2, 79-81 January (1972).

[4.39] A. Yariv and P.Yeh. , *Optical waves in crystals*. (John Wiley & Sons, N.Y., 1984), chap. ch. 9.

[4.40] J. Feinberg, D. Heiman, J. A. R. Tanguay, and R.W. Hellwarth, "Photorefractive effects and light-induced charge migration in barium titanate," J. Appl. Phys. **51**, no. 3, 1297-1305 March (1980).

[4.41] J.J. Amodei, "Analysis of transport processes during holographic recording in insulators," RCA review **32**, 185-198 June (1971).

[4.42] G.C. Papen, B.E.A. Saleh, and J.A. Tataronis, "Analysis of transient phase conjugation in photorefractive media," J. Opt. Soc. Am. B **5**, no. 8, 1763-1774 August (1988).

[4.43] M.G. Moharam, T.K. Gaylord, and R. Magnusson, "Holographic grating formation in photorefractive crystals with arbitrary electron transport lengths," J. Appl. Phys. **50**, no. 9, 5642-5651 Sept. (1979).

[4.44] L. Young, W.K.Y. Wong, M.L.W. Thewalt, and W.D. Cornish, "Theory of phase holograms in lithium niobate," Appl. Phys. Lett. **24**, no. 6, 264-265 March (1974).

[4.45] P. Yeh, *Introduction to Photorefractive Nonlinear Optics*. New York: (John-Wiley & Sons, 1993), chap. 4.

[4.46] Y. Fainman, E. Klancnik, and S.H. Lee, "Optimal coherent image amplification by two-wave coupling in photorefractive BaTiO3," Optical Engineering **25**, no. 2, 228-234 February (1986).

[4.47] J. Feinberg, D. Heiman, J. A. R. Tanguay, and R.W. Hellwarth, "Photorefractive effects anf light-induced charge migration in barium titanate, erratum," J. Appl. Phys. **52**, no. 1, 537 January (1981).

[4.48] J.O. White, S.K. Kwong, and M. Cronin-Golomb, *Photorefractive Materials and their Applications*, vol. 62, Topics in Applied Physics. (Springer-Verlag, 1989), chap. 4, pp. 106.

[4.49] M. Segev, Y. Ophir, and B. Fischer, "Nonlinear multi two wave mixing, the fanning process and its bleaching in photorefractive media," Opt. Comm. **77**, no. 2.3, 265-274 June (1990).

[4.50] G. Zhang, Q.X. Li, P.P. Ho, S. Liu, Z.K. Wu, and R.R.A. , "Dependence of specklon size on the laser beam size via photo-induced light scattering in LiNbO$_3$:Fe," Appl. Opt. **25**, no. 17, 2955-2958 Sept (1986).

[4.51] N. Kukhtarev, V. Markov, and S. Odulov, "Transient energy transfer during hologram formation in LiNbO3 in external electric field," Opt. Comm. **23**, no. 3, 338-343 December (1977).

[4.52] J.M. Heaton and L. Solymar, "Transient energy transfer during hologram formation in photorefractive crystals," Opt. Acta **32**, no. 4, 397-408 (1985).

[4.53] M. Cronin-Golomb, "Analytic solution for photorefractive two-beam coupling with time-varying signals," in *Digest of Topical Meeting on Photorefractive Materials, Effect and Devices,* Optical Society of America, 142 (1987).

[4.54] M. Horowitz, D. Kligler, and B. Fischer, "Time-dependent behavior of photorefractive two- and four-wave mixing," J. Opt. Soc. Am. B **8**, no. 10, 2204-2217 Oct. (1991).

[4.55] A. Hermanns, C. Benkert, D.M. Lininger, and D.Z. Anderson, "The transfer function and impulse response of photorefractive two-beam coupling," IEEE Journ. Quant. Elec. **28**, no. 3, 750-756 March (1992).

[4.56] F.P. Strohkendl, J.M.C. Jonathan, and R.W. Hellwarth, "Hole-electron competition in photorefractive gratings ," Optics Letters **11**, no. 5, 312-314 May (1986).

[4.57] M. Saffman, "Self-Organized Formation of Image Representations in Photorefractive Oscillators," Ph.D. thesis, University of Colorado, 1994.

[4.58] S. Ducharme and J. Feinberg, "Speed of the photorefractive effect in a BaTiO3 single crystal," J. Appl. Phys. **56**, no. 3, 839-842 August (1984).

[4.59] P. Yeh, *Introduction to Photorefractive Nonlinear Optics*. New York: (John Wiley & Sons, 1993), chap. 1.

[4.60] J.P. Huignard and P. Gunter, *Photorefractive Materials and their Applications*, vol. 62, Topics in Applied Physics. Berlin: (Springer-Verlag, 1989), chap. 6, pp. 205-206.

[4.61] J.E. Ford, Y. Fainman, and S.H. Lee, "Enhanced photorefractive performance from 45 degree-cut BaTiO3," Appl. Opt. **28**, no. 20, 4808 (1989).

[4.62] M.H. Garrett, J.Y. Chang, H.P. Jenssen, and C. Warde, "High photorefractive sensitivity in an n-type 45 degree-cut BaTiO3 crystal," Opt. Lett. **17**, no. 2, 103-105 January (1992).

[5.1] F. Vachss, J. Hong, and C. Keefer, "Adaptive signal processing using a photorefractive time integrating correlator," DARPA/Rome Labs Proc. **PSAA-91**, 127-132 (1991).

[5.2] R.M. Montgomery and M.R. Lange, "Photorefractive adaptive filter structure with 40-dB interference rejection," Appl. Opt. **30**, 2844-2849 (1991).

[5.3] J. Hong, S. Hudson, J. Yu, and D. Psaltis, "Photorefractive crystals as adaptive elements in acoustooptic filters," in *Optical Technology for Microwave Applications III,* SPIE, 136-144 (1987).

[5.4] J. Rhodes, "Adaptive filter with a time-domain implementation using correlation cancellation loops," Appl. Opt. **22**, no. 2, 282-287 January (1983).

[5.5] P.P. Ewald, "Crystal optics for visible light and x-rays," Reviews of modern physics **37**, no. 1, 46-56 January (1965).

[5.6] V.V. Aristov and V.S. Shekhtman, "Properties of three-dimensional holograms," Soviet Physics Uspekhi **14**, no. 3, 263-277 November (1971).

[5.7] R.T. Weverka, K.H. Wagner, R.R. McLeod, K. Wu, and C. Garvin, *Acousto-optic Signal Processing: Theory and Implementation*, 2. (Marcel Dekker, 1995), chap. 15.

[5.8]   R.R. Mcleod, "Spectral-domain analysis and design of three-dimensional optical switching and computing systems," Ph.D. thesis, University of Colorado, Boulder, 1995.

[5.9]   A. Yariv and P. Yeh, *Optical waves in crystals*. (John Wiley & Sons, N.Y., 1984), chap. ch. 4.

[5.10] J.M. Cowley, *Diffraction Physics*. (North-Holland, Amsterdam, 1981), pp. 31.

[5.11] D. Gabor and G.W. Stroke, "The theory of deep holograms," Proc. Roy. Soc. **A304**, 275 (1968).

[5.12] D. Psaltis, X.G. Gu, and D. Brady, *An Introduction to Neural and Electronic Networks*. San Diego: (Academic Press Inc., 1990), chap. 17.

[5.13] D.L. Hecht, "Multifrequency Acoustooptic Diffraction," IEEE Trans. Sonics and Ultrasonics **SU-24**, no. 1.

[5.14] A.W. Sarto, R.T. Weverka, K.H. Wagner, and S. Weaver, "Wide angular aperture holograms in photorefractive crystals using orthogonally polarized write and read beams," in *Photorefractive materials, effects, and devices,* June 214-217 (1995).

[5.15] I.C. Chang, "Noncollinear acousto-optic filter with large angular aperture," Appl. Phys. Lett. **25**, 370-372 (1974).

[5.16] G.A. Coquin, J.P. Griffin, and L.K. Anderson, "Wide-band acousto-optic deflectors using acoustic beam steering," IEEE Trans. Sonics and Ultrasonics **SU-17**, 34-40 (1970).

[5.17] D.A. Pinnow, "Acouto-optic light deflection: Design considerations for first order beam steering," IEEE Trans. Sonics and Ultrasonics **SU-18**, 209-214 (1971).

[5.18] A. Korpel, R. Adler, P. Desmares, and W. Watson, "A television display using acoustic deflection and modulation of coherent light," Appl. Opt. **5**, 1667-1675 (1966).

[5.19] J. Xu and R. Stroud, *Acousto-optic devices*, Wiley series in pure and applied optics. (Wiley-Interscience, 1992), chap. 7, pp. 413-424.

[5.20] R.T. Weverka and K. Wagner, "Wide angular aperture Acoustooptic Bragg cell," in *Devices for Optical Processing,* D.M. Gookin, ed. Proc. Soc. Photo-Opt. Instrum. Eng. **1562**, 66-72 (1991).

[5.21] H. Landolt and R. Bornstein, *Numerical Data and Functional Relationships in Science and Technology, New series: Ferro- and Antoferroelectric Substances*, vol. 3. Berlin: (Springer-Verlag, 1975).

[5.22] M.P. Tarr and M. Cronin-Golomb, "Birefringent phase matching for nonvolatile readout of holographic memories," in *Photorefractive materials, effects, and devices,* 435-438 (1995).

[6.1] J.W. Goodman, *Introduction to Fourier Optics*. (McGraw-Hill, 1968), chap. 2, pp. 10.

[6.2] A. Papoulis, *Signal Analysis*. (McGraw-Hill, 1977), chap. 8, pp. 271-273.

[6.3] K. Wagner and D. Psaltis, "Multilayer optical learning networks," Appl. Opt. **26**, no. 23, 5061-5076 Dec. (1987).

[6.4] J.W. Goodman, *Introduction to Fourier Optics*. (Mcgraw-Hill, 1968), chap. 4, pp. 61.

[6.5] J. A. Fleck, J. R. Morris and M.D. Feit, "Time dependent propagation of high energy laser pulses through the atmosphere," Appl. Phys. **10**, 129-160 (1976).

[6.6] A. A. Zozulya, M. Saffman and D.Z. Anderson, "Propagation of light beams in photorefractive media- fanning, self-bending, and formation of self-pumped 4-wave mixing phase-conjugation geometries," Phys. Rev. Letts. **73**, no. 6, 818-821 (1994).

[6.7] A. A. Zozulya, M. Saffman and D.Z. Anderson, "Double phase-conjugate mirror: convection and diffraction," J. Opt. Soc. Am. B **12**, no. 2, 255-264 Feb. (1995).

[6.8] W. H. Press, W. T. Vettering, S. A. Teukolsky, B. P. Flannery, *Numerical Recipes in C*. (Cambridge University Press, 1992), chap. 19, pp. 848.

[6.9] A. W. Sarto, K. Wagner, R. T. Weverka, S. Blair, and S. Weaver, "Photorefractive phased-array antenna beam-forming processor," in *Radar Processing, Technology, and Applications,* SPIE **2845**, (1996).

[6.10] S. Blair, *Personal Communication,* 1995

[6.11] M. Saffman, "Self-Organized Formation of Image Representations in Photorefractive Oscillators," Ph.D. thesis, University of Colorado, 1994.

[6.12] G.C. Papen, B.E.A. Saleh and J.A. Tataronis, "Analysis of transient phase conjugation in photorefractive media," J. Opt. Soc. Am. B **5**, no. 8, 1763-1774 August (1988).

[7.1] M. Born and E. Wolf, *Principles of Optics*, 6. (Pergamon, 1980), chap. 7.

[7.2] A.W. Sarto, R.T. Weverka, and K. Wagner, "Photorefractive phased-array radar processor dynamics," in *Photonics for Processors, Neural Networks, and Memories,* Proc. Soc. Photo-Opt. Instrum. Eng. **2026**, July 310-324 (1993).

[7.3] *Standard Mathematical Tables*. Chemical Rubber Publishing, 1957.

[7.4] B. Widrow, J. McCool, and M. Ball, "The complex LMS algorithm," Proc. IEEE719-720 April (1975).

[7.5] E. Finizio and A. Ladas, *An Introduction to Differential Equations*. Wadsworth, 1982.

[7.6] R.T. Weverka, "Personal Communication," 1995.

[7.7] R.T. Weverka and K. Wagner, "Adaptive phased-array radar processing using photorefractive crystals," in *Optoelectronic Signal Processing for Phased-Array Antennas II*, B.M. Hendrickson and G.A. Koepf, ed. Proc. Soc. Photo-Opt. Instrum. Eng. **1217**, 173-182 (1990).

[7.8] R.T. Weverka, K. Wagner, and A.W. Sarto, "Adaptive phased-array radar processing using photorefractive crystals," Appl. Opt. **35**, no. 8, 1344-1366 March (1995).

[7.9] A.W. Sarto, R.T. Weverka, and K. Wagner, "Beam-steering and jammer-nulling photorefractive phased-array radar processor," in *Optoelectronic Signal Processing for Phased-Array Antennas IV*, Proc. Soc. Photo-Opt. Instrum. Eng. **2155**, 378-388 (1994).

[8.1] B. Widrow and S.D. Stearns, *Adaptive signal Processing*. Prentice-Hall Inc, N.J., 1985.

[8.2] A. Gabel, L.S. Lee, and I.C. Chang, "Front-end RF channelization using optical techniques," in , SPIE **477**, (1984).

[8.3] E.M. Alexander. and R. W. Gammon, "The Fabry-Perot etalon as an RF frequency channelizer," in *Solid State Optical Control Devices*, SPIE **464**, 45-52 (1984).

[8.4] A. Yariv, *Optical Electronics*. Saunders College Publishing, 1985.

[8.5] J. Xu and R. Stroud, *Acousto-optic Devices: Principles, Design, and Applications*. (Wiley-Interscience, 92), chap. 2, pp. 83.

[8.6] M.A. Rob, "Limitations of a wedged etalon for high resolution linewidth measurements," Opt. Lett. **15**, no. 11, 604-606 (1990).

[8.7] M. Born and E. Wolf, *Principles of Optics*. Pergamon Press, 87, chap. 7, pp. 351.

[8.8] D. Herriott, H. Kogelnik and R. Kompfner, "Off-axis paths in spherical mirror interferometers," Appl. Opt. **3**, no. 4, 523-526 April (1964).

[8.9] D.R. Herriott and H.J. Schulte, "Folded optical Delay lines," Appl. Opt. **4**, no. 8, 883-889 August (1965).

[9.1] K. Wagner, S. Kraut, L. Griffithsaver, R.T. Weverka, and A. W. Sarto, "Efficient true-time-delay adaptive-array processing," in *Radar Processing, Technology, and Applications*, SPIE **2845**, (1996).

[9.2] R. T. Weverka and K. Wagner, "Wide angular aperture acoustooptic Bragg cell," in *Devices for Optical Processing,* SPIE **1562**, 66-72 (1991).